

Study of the magnetic heavy fermions UCoGe and YbRh2Si2 by transport measurements

Mathieu Taupin

▶ **To cite this version:**

Mathieu Taupin. Study of the magnetic heavy fermions UCoGe and YbRh2Si2 by transport measurements. Strongly Correlated Electrons [cond-mat.str-el]. Université Joseph-Fourier - Grenoble I, 2013. English. NNT : . tel-01026388

HAL Id: tel-01026388

https://theses.hal.science/tel-01026388

Submitted on 21 Jul 2014

HAL is a multi-disciplinary open access archive for the deposit and dissemination of scientific research documents, whether they are published or not. The documents may come from teaching and research institutions in France or abroad, or from public or private research centers.

L'archive ouverte pluridisciplinaire **HAL**, est destinée au dépôt et à la diffusion de documents scientifiques de niveau recherche, publiés ou non, émanant des établissements d'enseignement et de recherche français ou étrangers, des laboratoires publics ou privés.

UNIVERSITÉ DE GRENOBLE

THÈSE

Pour obtenir le grade de

DOCTEUR DE L'UNIVERSITÉ DE GRENOBLE

Spécialité : **Physique**

Arrêté ministériel : 7 août 2006

Présentée par

Mathieu TAUPIN

Thèse dirigée par **Jean-Pascal BRISON**
et codirigée par **Dai AOKI**

préparée au sein **du Service de Physique Statistique, Magnétisme et Supracondcutivité (SPSMS) de l'Institut NAnoscience et Cryogénie (INAC), au sein du CEA Grenoble**
et de **l'Ecole Doctorale de Physique de Grenoble**

Etude des fermions lourds magnétiques UCoGe et $YbRh_2Si_2$ par mesures de transport.

Thèse soutenue publiquement le **18 décembre 2013**,
devant le jury composé de :

Marc-Henri JULIEN
CNRS, LNCMI Grenoble, Examinateur, Président
Koichi IZAWA
Graduate School of Science and Engineering, Tokyo Institute of Technology, Rapporteur
Sébastien BURDIN
CNRS, Université de Bordeaux 1, Rapporteur
William KNAFO
CNRS, LNCMI Toulouse, Examinateur
Jean-Pascal BRISON
CEA Grenoble, Directeur de thèse



Remerciements

Après une thèse de trois ans et demi,
De nombreuses personnes sont à remercier.
Tout d'abord, les différents membres du jury:
Marc-Henri JULIEN, pour avoir accepté
D'être président le jour de ma soutenance.
Koichi ISAWA, premier rapporteur,
Pour avoir fait le déplacement jusqu'en France
Afin de me donner le grade de docteur.
Sébastien BURDIN, deuxième rapporteur,
En tant que théoricien, d'avoir corrigé
Et lu le travail d'un expérimentateur.
Et William KNAFO, pour avoir perfectionné
Le contenu physique et la syntaxe anglaise.
Merci à vous d'avoir usé de votre temps
A la lecture de mon manuscrit de thèse
Avec des résultats pas toujours évidents.

Viens ensuite la personne à qui je dois tout
(Bon, peut-être pas, beaucoup de choses en tout cas):
Jean-Pascal, tu m'as accompagné jusqu'au bout
De ce chemin rempli d'embûches et de tracas.
Je n'aurais pu avoir de meilleur encadrant,
L'étendu de tes connaissances n'a d'égal
Que l'écoute et le respect que tu donnes aux gens.
Ces trois années avec toi furent un régal!

Jean-Michel, tu as été pour moi un pilier
Sur lequel je pouvais compter en cas de doutes,
Ta bonne humeur et tes discussions vont manquer...
Durant ton absence, au labo, c'était Beyrouth!

Merci à Jacques, avec ses nombreux coups de gueules,
A Dai, et sa multitude d'échantillons,
A Georg, créant des courants d'air à lui seul,
Et à Alex, ardéchois un peu ronchonchon
Pour vos aides et conseils quand j'en avais besoin.

Je me dois également de mentionner
Daniel et Bernard pour votre soutien;
Iulian pour tes recommandations passionnées;
Jean-Luc, pour ton sens de la sûreté aigüe
Et pour m'avoir fréquemment prêté assistance
Dans la quête de la jauge helium disparue;
Pierre et Fred pour combler mon incompétence
Tant en électronique qu'en informatique.

De nombreux thésards sont également présents,
Ceux qui ont participé à la Golden Week,
Charlène, Benoit et Andreas. Ceux d'avant,
Driss et Caro, et le dernier de la cuvée,
Tristan. On s'est rencontré durant le Master,
Et ce fut un vrai plaisir d'avoir traversé
Avec vous cette épreuve dans la bonne humeur.
Il y a bien entendu mes cobureaux
Mounir, que j'ai gracieusement pris sous mon aile
Pour qu'il connaisse les expressions sans accroc;
Et récemment le nouveau montagnard Gaël
Qui a découvert les joies des ferro supra!
Pour toutes les discussions intéressantes,
Je remercie également Alexandra.
J'ai une petite pensée encourageante
A la nouvelle génération, Adrien
Et Beilun, pour la suite, bonne chance;
A Sheila et Eduardo les brésiliens
Et Yusei, parlant français avec élégance!

Le monde ne s'arrête pas à IMAPEC,
J'ai beaucoup apprécié les différents échanges
avec les thésards et permanents de LaTEQS
("S" muet, sinon pas de rime et j'y perds au change):
Alexander, pour n'avoir jamais essayé
De me faire goûter le fameux Paprika Speck!
Jean-Eudes, et ses discussions diverses et variées,
Paul, avec l'abricotine et ses lointains trecks;
Xavier, qui est dorénavant un concurrent!
Claude, et ses points de vue (parfois très!) passionnés,
Ceux du STM : Toai, Eduard et Vincent,
Marc, François, Louis, Silvano, sans oublier
Christophe et Max pour leurs différentes anecdotes,
Les post-docs Julien et Jean-Pierre, montrant
Que la bonne humeur est sans doute l'antidote
A des projets d'après thèse récalcitrants!

La vie du labo va au-delà du C1,

Marielle répondit toujours à mes questions
Bien que ma réponse fut dans un mail ancien,
Tu m'as bien aidé face à l'administration!
Il y a également les théoriciens
Mike, les Vladimir, Xavier, Julia, Manuel...
Pour vos conseils et votre aide de physicien.
Merci Stéphane, les manips à l'ILL
M'ont montré qu'il est possible concrètement
De n'avoir de résultat strictement aucun
Malgré deux fois 10 jours de mesures à plein temps.
Des expériences qui nous ont en donnés maints
Furent la XMCD à l'ESRF
Menées avec brio par Andrei et Fabrice,
Merci à Jean-Pierre, qui était dans son fief,
Et qui fut une grande source inspiratrice!
Je souhaite remercier l'amabilité
De Karine, Christophe et Gérard, avec qui
J'ai peu, bien qu'agréablement, travaillé.
Je ne serais là où je suis aujourd'hui
Sans vous tous, et vous m'étiez plus que des collègues!
Il ne faut surtout pas oublier les "anciens",
J'ai bien profité de leurs précieux legs
De thésards et post-docs loin d'être béotiens!

La réussite de cette thèse s'est fait
Aussi grâce au soutien de mes "vrais" amis
Qui, pour beaucoup en thèse, connaissaient l'effet
De ce projet qui demande des compromis.
Merci à Alex, répondant toujours présent
A l'appel de la bière du vendredi soir,
Et à Hélène pour nous avoir fréquemment,
Malgré un raté, amenés au Vieux-Manoir!
Merci à Coco, Djé, Ben, Camille, Bobby
Jil, Hana, Ludo, Manue, Emilie, Sylvain
Quentin, sans oublier ceux qui n'ont pas fini:
Antoine, Yannick, Anne, Clément et Adrien
Merci aussi à Luc, le désormais banquier.
Puisque le monde ne s'arrête pas à Gre,
Il ne faut pas oublier les expatriés,
Arthur et Amélie, et leur accueil radieux,
Tim, je suis bientôt ton chef, fais attention!
Grosse pensée à Thomas, François et Gaël,
Les colocs première génération.
Enfin, ce sont avec des excuses réelles
Que je ne vais pas chercher à être exhaustif,
Ainsi, pardon à ceux que je n'ai pas cités.

Le dernier endroit pour prendre l'apéritif,
En ayant une certaine continuité,
Est bien sûr ma nouvelle coloc à Eybens.
Et pour moi, ce fut une des meilleures choses
Que j'ai faite pendant ma thèse, néanmoins
La pire pour ma thèse, difficile osmose...
Merci à mes koloks, ma seconde famille
(En vrac, Gontran, Frank, Benoit, Perrine, Marion,
Charlotte, Dimitri, Florian (pas de Camille...)
Margaux, Sandy, Mathilde, Charlène, Simon).

Ma "vraie" famille mérite aussi un merci:
Ils m'ont toujours supportée, ainsi que mes choix,
Bien que, sans tourner autour du pot de persil,
Ils n'ont jamais compris les travaux de ma voie...

Enfin, une heureuse rencontre a eu lieu
En fin de thèse, grand merci à Iveta
Pour m'avoir fait vivre des moments radieux
Et aussi ceux futurs qu'ensemble l'on vivra.

Merci à vous, lisant ces lignes actuellement,
Prouvant qu'à quelqu'un est utile cet ouvrage,
En espérant qu'au delà des remerciements
Vous réussirez sans mal à tourner les pages...

Introduction en Français

Malgré sa découverte il y a plus de 100 ans, la supraconductivité continue régulièrement de défier la communauté scientifique: il a fallu plus de 40 ans pour comprendre son origine microscopique avec la théorie BCS, les supraconducteurs cuprates ont une température critiques une température critique plus élevée que celle prédite par la théorie BCS, certains systèmes à fermions lourds possèdent une phase supraconductrice coexistent avec un état magnétique... Les interactions électrons-phonons, responsable de la formation des paires de Cooper dans les supraconducteurs conventionnels, ne peuvent être à l'origine de la supraconductivité dans les cuprates et dans les fermions lourds, et, dans certains cas, les fluctuations magnétiques semblent être un bon candidat pour le mécanisme d'appariement.

La physique des fermions lourds se trouvent à basses températures, usuellement en dessous de 10K, avec la présence éventuelle d'une poche supraconductrice, généralement avec une température critique de l'ordre de 1K. Le diagramme de phase typique d'un fermion lourd est similaire à celui du composé $CeRhIn_5$, montré sur la figure 1. En appliquant de la pression, le système passe d'un état magnétique non supraconducteur à un état supraconducteur avec éventuellement coexistence avec l'état magnétique. La température supraconductrice est maximum dans l'état paramagnétique pour ensuite décroître. Le fait que le dôme supraconducteur se situe proche d'une instabilité magnétique supporte l'idée que d'un lien étroit entre supraconductivité et magnétisme. Ce diagramme de phase montre qu'il est expérimentalement réalisable sans techniques expérimentales lourdes de sonder l'état magnétique, ainsi que l'état supraconducteur. Ce contrôle "aisé" (à l'aide de dopage chimique, d'application de pression, de champ magnétique...) de l'état fondamental est un gros avantage des fermions lourds, car cela permet de suivre en détail l'évolution des différents paramètres pour déterminer ce qui est responsable de la supraconductivité.

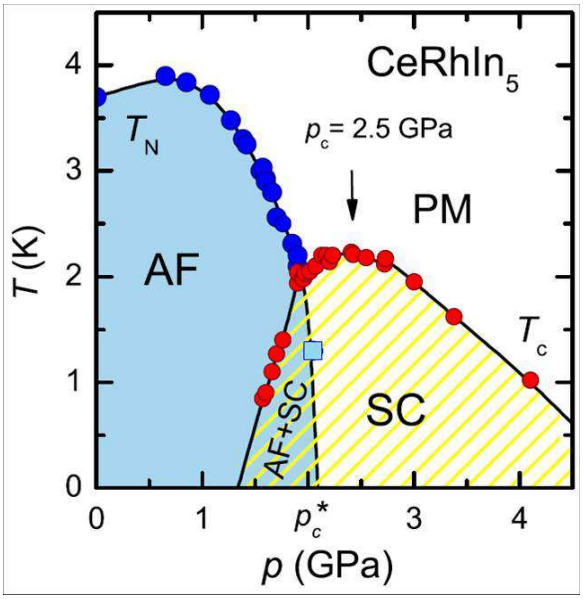


Figure 1 *Diagramme de phase typique d'un fermion lourd, représenté par $CeRhIn_5$ [107]. AF, PM et SC sont les états antiferromagnétique, paramagnétique et supraconducteur respectivement. T_N et T_c sont les températures de Néel et supraconductrice respectivement. p_c and p_c^* sont les pressions critiques, correspondant au maximum de T_c et à la pression à laquelle $T_N \to 0K$ respectivement.*

Un autre intérêt des fermions lourds est le nombre important des différentes propriétés que ces matériaux présentes: la supraconductivité peut coexister avec une phase antiferromagnétique (dans $CeRhIn_5$ par exemple [107]) ou une phase ferromagnétique avec la présence d'une poche supraconductrice induite sous champ dans URhGe [10, 118], existe dans des composés non-centrosymétriques avec un champ critique très élevé (comme dans $CeRhSi_3$ avec H_{c_2}>30T [103]), peut posséder plusieurs énergies caractéristiques (supraconducteur multigap, comme dans $PrOs_4Sb_{12}$ [188]) ou avoir une température critique de 18K dans $PuCoGa_5$ [181]! Il s'agit là d'une liste non exhaustive montrant la quantité d'états fondamentaux différents existant dans les fermions lourds.

Tous les fermions lourds ne sont pas supraconducteurs, comme $YbRh_2Si_2$, et, proche d'un point critique quantique, des propriétés exotiques peuvent apparaître, comme un comportement de non liquide de Fermi. Ce régime non conventionnel représente un défi théorique, car la nature exacte du point critique quantique, ainsi que le rôle des fluctuations quantiques sont toujours en débat.

Ce grand nombre de différentes propriétés fait que les systèmes à fermions lourds sont très intéressants à étudier pour la compréhension des interactions fondamentales impliquant la supraconductivité, et donne la raison pourquoi ces systèmes sont largement étudiés.

Plan de la Thèse

Cette thèse est découpée en cinq chapitres. Le premier donne le contexte scientifique nécessaire pour la compréhension de la physique des fermions lourds, ainsi que les idées générales concernant la supraconductivité. Ensuite, étant donné que cette thèse fut principalement un travail expérimental, le second chapitre recense les techniques expérimentales utilisées. Leur intérêt, ainsi que leurs limites seront donnés, avec une explication plus détaillée sur les mesures de conduction thermique.

Deux composés ont été étudiés: UCoGe et $YbRh_2Si_2$. Le premier composé étudié est le supraconducteur ferromagnétique UCoGe, et les résultats sont montrés dans les chapitres trois et quatre. Le troisième chapitre montre les mesures de champ critique et de XMCD, et le quatrième est dédié aux mesures de conduction thermique. Le second composé, $YbRh_2Si_2$, se trouvant proche d'un point critique quantique, est étudié dans le cinquième chapitre.

Introduction

Despite its discovery 100 years ago, superconductivity continues regularly to challenge the scientific community: the microscopic origin has been understood 40 years after its discovery with the BCS theory, the high superconducting temperature of the cuprates discovered in 1986 is higher than the maximum superconducting temperature predicted in the BCS theory (≈30K), some heavy fermion systems show microscopic coexistence of magnetism and superconductivity... The electron-phonon interaction, which is the pairing mechanism of the formation of the Cooper pairs in conventional superconductors, cannot be responsible for superconductivity in the cuprates and in heavy fermions, but magnetic fluctuations seem a good candidate for pairing mechanism in some cases.

The interesting physics of heavy fermion systems lies at low temperatures (usually below 10K) with a possible superconducting transition, usually in the order of magnitude of 1K. The typical phase diagram of a heavy fermion is similar to the one displayed by the heavy fermion $CeRhIn_5$, shown figure 2. By applying pressure, the system goes from a non-superconducting and magnetic state to a superconducting state with possible coexistence with magnetism. The superconducting temperature is maximum in the paramagnetic phase and then decreases. The fact that the superconducting dome lies close to a magnetic instability in the heavy fermions pledges for a strong link between superconductivity and magnetism. This phase diagram shows that it is experimentally feasible without big facilities to probe the magnetic state as well as the superconducting one. This easy control (via doping, pressure, magnetic field ...) of the ground state of the heavy fermions is a great advantage, as it enables to "follow" the different parameters to see what is responsible for superconductivity.

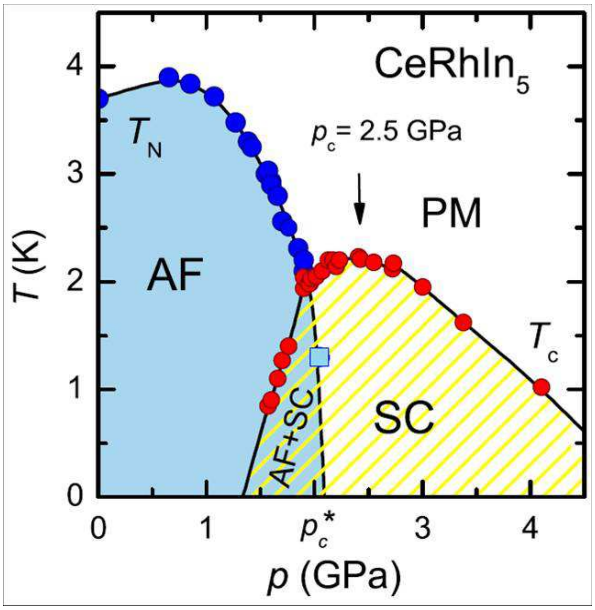


Figure 2 *Typical phase diagram of a heavy fermion, represented by $CeRhIn_5$ [107]. AF, PM and SC are the antiferromagnetic, the paramagnetic and the superconducting states respectively. T_N and T_c are the Néel and the superconducting temperatures respectively. p_c and p_c^* are the critical pressures corresponding to the maximum of the superconducting temperature and to the pressure where $T_N \to 0K$ respectively.*

Another interest for the physics of heavy fermions is the number of different properties exhibited: superconductivity coexists with antiferromagnetism in $CeRhIn_5$ [107], with ferromagnetism in URhGe with a field induced

superconducting pocket [10, 118], exists in the non-centrosymmetric $CeRhSi_3$ with very large H_{c_2} (>30T) [103], has several gaps in $PrOs_4Sb_{12}$ [188] or can even have a superconducting temperature as high as 18K in $PuCoGa_5$ [181]! This non-exhaustive list shows that superconductivity can exist with many different background states.

Some heavy fermions do not exhibit superconductivity, as $YbRh_2Si_2$, and, close to a quantum critical point, other properties can appear, such as non Fermi liquid behaviors. This unconventional regime is also theoretically challenging, as the exact nature of the quantum critical point, as well as the role of the quantum fluctuations are still under debate.

These large numbers of different properties make that the study of the heavy fermion systems is very interesting for the understanding of fundamental interactions implying superconductivity, and explains why these systems are widely studied.

Plan of the thesis

This thesis is separated in five chapters. The first chapter gives the basic theoretical background for understanding heavy fermion physics as well as the general ideas about superconductivity. Then, as it was mainly an experimental work, the second chapter explains the different facilities and probes I used. Each time, I will explain the interest of each probe and their limitations, with a more detailed explanation on the thermal conductivity measurements.

Two different compounds with different properties have been studied during these three years: UCoGe and $YbRh_2Si_2$. The first compound studied is the superconducting ferromagnet UCoGe, and the results are shown in the third and fourth chapters. The third chapter shows the measurements of the upper critical field and the XMCD, and the fourth chapter the thermal conductivity measurements. The second compound is $YbRh_2Si_2$, which lies close to a quantum critical point, and the last chapter is dedicated to it.

Contents

Remerciements ii

Introduction en Français vii

Introduction ix

1 Physical Background 1
- 1.1 Heavy Fermions . . . 1
- 1.2 Superconductivity . . . 3
- 1.3 Superconducting Ferromagnets . . . 7
  - 1.3.1 Introduction . . . 7
    - Theoretical Predictions . . . 7
    - Experimental Results . . . 8
    - Fulde-Ferrel-Larkin-Ovchinnikov State . . . 10
  - 1.3.2 Heavy-Fermion Superconducting Ferromagnets . . . 12
    - General Properties . . . 12
    - Field Induced Superconducting Phases . . . 13
    - Pressure Phase Diagram . . . 14
    - Case of UCoGe . . . 14
- 1.4 Goal of the Thesis . . . 15

2 Experimental Methods 17
- 2.1 Dilution Fridges . . . 17
- 2.2 Resistivity Measurements . . . 20
- 2.3 Thermal Conductivity Measurements . . . 21
  - 2.3.1 Theory . . . 21
    - Principle . . . 21
    - Different Contributions and Wiedemann-Franz Law . . . 21
    - In a Superconductor . . . 22
  - 2.3.2 In Practice . . . 25
    - Principle . . . 25
    - Thermal Conductivity Setup . . . 27
    - Errors Sources . . . 29
- 2.4 X-ray Magnetic Circular Dichroism . . . 29

3 First results on UCoGe **35**
3.1 Measured Samples . . . 35
3.2 Critical Fields . . . 38
3.2.1 How to determine the critical temperature? . . . 38
3.2.2 **H//b** . . . 39
3.2.3 **H//c** . . . 42
3.2.4 Critical Field of Sample S_{47}^{c} . . . 44
3.2.5 Conclusion . . . 47
3.3 XMCD . . . 47
3.3.1 Principle . . . 47
3.3.2 Results . . . 51
H//c . . . 51
H//b . . . 53
3.3.3 Discussion . . . 54
Comparison Between the 1T and 17T Measurements, **H//c** . . . 54
Comparison with Resistivity Measurements . . . 56
Comparison Between the Configurations **H//b** and **H//c** . . . 58
Comparison with XMCD on the Co L-edges . . . 58
3.3.4 Conclusion . . . 60

4 Thermal Conductivity Measurements **63**
4.1 Effect of the Quality (H=0T) . . . 63
4.2 Analysis of the Normal Phase . . . 66
4.2.1 Bare Results . . . 66
H//c . . . 66
H//b . . . 71
4.2.2 Analysis of the Normal Phase . . . 72
4.2.3 Discussion . . . 77
4.2.4 Conclusion . . . 80
4.3 Analysis of the Superconducting Phase . . . 80
4.3.1 Introduction . . . 80
4.3.2 Anisotropy at 0T . . . 81
4.3.3 **H//c** . . . 82
Temperature Dependence . . . 82
Field Dependence . . . 82
4.3.4 **H//b** . . . 84
Temperature Dependence . . . 84
Field Dependence . . . 86
4.3.5 Discussion . . . 87
4.3.6 Conclusion . . . 88

5 $YbRh_2Si_2$ **89**
5.1 Scientific Background . . . 89
Presentation of the System . . . 89
Wiedemann-Franz law and Quantum Critical Point . . . 91
5.2 Description of the Debate . . . 92
5.3 Technical Description . . . 93

5.4 Results of the Very Low Temperature Measurements . . . 94
Comparison between H=0T and H=H_c . . . 94
Field Dependence . . . 95
Study of the Low Temperature Extra Contribution . . . 96
5.5 General Results . . . 99
5.5.1 Description . . . 99
5.5.2 Analysis . . . 102
Resistivity . . . 102
Study of κ at High Temperatures . . . 102
Study of κ above 0.5T . . . 104
Study of κ below 0.5T . . . 107
5.6 Conclusion . . . 110

Conclusion **111**

Perspectives **113**

Conclusion en Français **114**

Appendix **117**
.1 Phenomenological Model of the Normal State of UCoGe . . . 117
.2 Study of κ at High Fields in $YbRh_2Si_2$ . . . 122
.3 Study of the Very Low Temperature Regime in $YbRh_2Si_2$ . . . 124

Bibliography **127**

Résumé des Chapitres en Français **145**

Abstract **149**

Chapter 1

Physical Background

This first chapter reviews the physical background necessary to understand the work done during my thesis. As my subject brings together several big fields of physics, I will not at all do a complete review of these domains, but only emphasize the differences with the existing theoretical models for the simple case.

The first part concerns the physics of heavy fermions (HF). This quite old physics is very rich and groups together some more basic physics (notion of Fermi liquid, Kondo effect, localized/itinerant magnetism...) which will be evoked. Superconductivity (SC) is the next part where basic ideas about unconventional superconductivity are given. As the study of the compound UCoGe was the biggest part of my thesis, the last part concerns the ferromagnetic superconductors, with first the theoretical and experimental advances before discovery of the heavy fermion superconducting ferromagnets, with their description as the last part of the chapter. Presentation of compound $YbRh_2Si_2$ is differed to the introduction of the last chapter.

1.1 Heavy Fermions

The story of the heavy fermions[1] (HF) started with the low temperature measurements of $CeAl_3$ [7] in 1975, where the residual specific heat Sommerfeld coefficient C_p/T is enormous, together with the resistivity behaving as $\rho = \rho_0 + AT^2$, with a very large A coefficient. These two features have the same origin, which characterizes the HF: at low temperature (usually T<10K), HF systems show a strong enhancement of the effective mass of the charge carriers, with the possibility to be described as Landau quasiparticles with Fermi liquid behavior. Soon later the discovery of $CeAl_3$ came the first HF exhibiting superconductivity: $CeCu_2Si_2$ in 1979, discovered by Steglich *et al.* [200]. This discovery challenged the well-established BCS framework, proving that superconductivity can exist in strongly correlated electronic systems and may even be induced by magnetism.

The mechanism leading to the formation of a HF ground state can be different for different compounds, and notably for $4f$ based systems (Ce, Yb or Pr based HF) or $5f$ based systems (U, Np or Pu based HF). The case of the $4f$ compounds is easier due to the more localized character of the f-orbitals, and the Kondo lattice model captures the main ingredient of the problem. At high temperature, the magnetic atoms act as free local moments and the f-electrons are localized. With the "single site" Kondo effect, below the Kondo temperature T_K,

[1] This section was highly inspired by the work of Coleman [34], Bauer [18] and Flouquet [53]

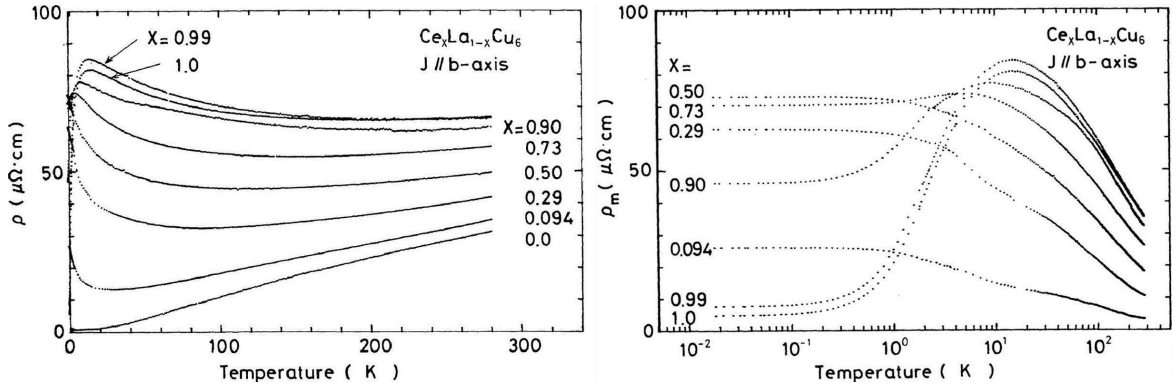


Figure 1.1 *Effect of the chemical doping on the resistivity in $Ce_xLa_{1-x}Cu_6$. A low amount of magnetic impurities (here Ce) gives rise to the Kondo effect, and for high doping ($x > 0.7$), the Kondo lattice is forming with the Ce atoms and coherence appears at low temperature. The Fermi liquid behavior is recovered at high doping (right panel). From [208].*

the magnetic impurities start to be screened on cooling by the conduction electrons, leading to an increase of the electronic resistivity. In HF, this effect happens on each site and it can be balanced by the induced recovery of lattice periodicity upon the decrease of spin disorder: so below a so-called "coherence temperature", the resistivity decreases on cooling. As an example, the figure 1.1 shows the effect of the chemical doping in the HF $Ce_xLa_{1-x}Cu_6$ [208]. In the pure compound $LaCu_6$, the resistivity decreases on cooling in the whole temperature range: it behaves like a normal metal. At low doping (Ce atoms are magnetic), the logarithm increase on cooling of the resistivity at low temperature is due to the Kondo effect, and for $x > 0.7$, the resistivity decreases at low enough temperature, as a consequence of the coherence effects. The right panel shows the magnetic resistivity ($\rho_m = \rho_{Ce_xLa_{1-x}Cu_6} - \rho_{LaCu_6}$): in the HF regime, the Fermi liquid behavior is recovered.

Below the coherence temperature (∼2-50K), the conduction electrons are strongly hybridized with the f-electrons through many body Kondo effects, having for consequence the enhancement of the effective mass $m^\star$ of the quasiparticles (in a normal metal, $m^\star \sim 2-5m_0$, and in HF, $m^\star \sim 10-1000m_0$, with m_0 the bare electron mass). This leads to the renormalized, or "effective" Fermi liquid temperature T_F^*. An unexpected feature is the recovery of the Fermi liquid regime in the coherence state, but with strongly renormalized parameters. This leads to a greater sensitivity of the ground state to external parameters, like magnetic field or pressure.

At low temperature, HF are magnetic or close to a magnetic state, and the application of an external parameter has for effect to bring the system closer to (or to drive it away from) the magnetic instability. If the ground state is magnetic, it can become paramagnetic, and vice-versa. To explain this, a naive picture, giving by Doniach [44], brings face to face the Kondo effect (leading to a non-magnetic state) and the RKKY interaction (controlling the magnetic order). Both are controlled by the coupling exchange between the f-electrons and conduction band (see equations 1.1 and 1.2). By tuning the system with external parameters, this coupling exchange is changed, possibly inducing transition between magnetic and non-magnetic states. Doniach has calculated the dependence of the coherence temperature due to Kondo effect (T_K) and the RKKY temperature (T_{RKKY}) with the exchange coupling constant

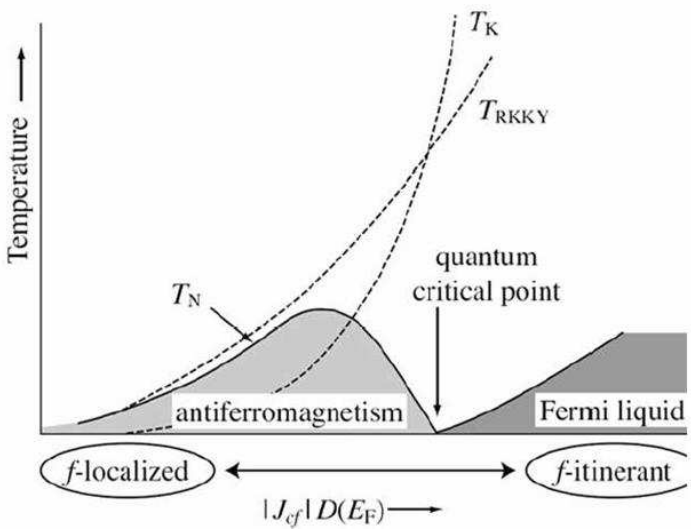


Figure 1.2 *Doniach phase diagram. The abscissa measures the strength of the tuning parameter (pressure, magnetic field...), modifying the coupling constant. The passing from the magnetic phase to the non-magnetic phase goes through a quantum critical point, with the possible existence of an unconventional superconducting pocket. From [44].*

(J) and the electronic density of states ($D(E_F)$):

$$T_K \sim e^{-1/(2JD(E_F))} \tag{1.1}$$

$$T_{RKKY} \sim J^2 D(E_F) \tag{1.2}$$

The figure 1.2 shows the Doniach phase diagram. By applying a tuning parameter (pressure, magnetic field...), the coupling constant changes and the system goes from a magnetic phase to a non-magnetic one (or the inverse) through a quantum critical point (QCP). At this place, unconventional superconductivity with coexistence of magnetic order is possible, as well as non-Fermi liquid behavior in the normal phase. The proximity of the QCP may induce magnetic fluctuations with a large magnetic susceptibility, which can be favorable for superconductivity[2] [129]. The magnetic fluctuations in the HF can be described by Moriya [146], and may be responsible for the anomalous non-Fermi liquid and the unconventional superconductivity around antiferromagnetic QCP. Similar description can be done on the high-T_{sc} cuprates and iron-pnictide superconductors, where the maximum of the superconducting temperature occurs close the QCP.

Around the QCP, deviation of the Fermi liquid regime has been observed in several compounds, the more direct being the resistivity with a non quadratic temperature dependence: $\rho = \rho_0 + AT^n$, with $n < 2$. However, up to now, no theories have succeeded to unify the non-Fermi liquid regime.

1.2 Superconductivity

Superconductivity is an old domain in physics: it has been discovered in Hg in 1911 by Kamerlingh Onnes [154] and despite this, lots of questions are still under debate, like the

[2]For a review about superconductivity in the HF compounds, the reader may read the Pfleiderer's review [165]

microscopic origin of unconventional superconductivity.

In 1957, Bardeen, Schrieffer and Cooper (BCS) [16] have elaborated a microscopic theory to describe the conventional superconductivity. For conventional superconductors, at the superconducting transition, the electrons enter the coherence state and form Cooper pairs via interactions between the charge of the electrons and phonons. The Cooper pairs are formed with electrons of opposite wave vectors and spins (singlet state), are weakly coupled and, at the transition, only the gauge symmetry is broken.

However, Cooper pairs can also be bound in higher orbital states. In such a case, and more generally, the superconducting transition breaks a symmetry (spatial, time reversal...) in addition to the gauge symmetry: one speaks of unconventional superconductivity.

In most of cases, unconventional superconductivity appears due to an unconventional pairing mechanism, i.e. a pairing mechanism not governed by the electron-phonon interactions, but by exchange of spin fluctuations or other "exotic" excitations. Experimentally, unconventional superconductivity has been first discovered with the p-wave superfluidity of ^{3}He [117], and then in heavy fermions systems, an adventure which started with the discovery of the superconductivity of $CeCu_2Si_2$ by F. Steglich in 1979 [200]. A simple picture for non-phononic superconductivity is given by Monthoux *et al.* [144]: the time and space dependent interaction between quasiparticles is divided into the charge-charge and the spin-spin interactions, and given by

$$V_{ind}(\vec{r},t) = -ee' g_n^2 \chi_n(\vec{r},t) - \vec{s}.\vec{s'} g_m^2 \chi_m(\vec{r},t) \tag{1.3}$$

(e, e') and $(\vec{s}, \vec{s'})$ are the charge and the spin of each electron, χ_n is the non-local charge density susceptibility and χ_m the non-local magnetic susceptibility. $g_{n,m}$ are empirical parameters relative to the strength of the coupling to the charge and to the spin. In the case of conventional SC, the first term is dominant and for spin fluctuation mediated SC, the second term is dominant. The figure 1.3 shows a schematic sketch of the charge-charge and the spin-spin interactions with the distance. To be attractive, the charge-charge interaction implies dynamical particles. For spin-spin interactions, it is locally attractive for the ferromagnetism instability (triplet state), whereas it oscillates in space for the antiferromagnetism instability (singlet state).

As FM instability leads only to attractive interactions, it could be expected that unconventional SC is close to this kind of instability. However, the spin-triplet channel is three times less effective than the spin-singlet channel [144]. This ineffectiveness is not valid anymore in anisotropic magnetic systems with fluctuations along one particular axis, suggesting strong magnetic anisotropy is favored for pairing with close to a FM instability [143].

In HF systems, the superconducting temperature is small, usually T_{sc}<2K (with some rare exceptions, as $PuCoGa_5$, with T_{sc}=18.5K [181]), but the upper critical field can be large, higher than 10T. For example, in the non-centrosymmetric HF $CeRhSi_3$, the critical temperature is T_{sc}=0.7K for H_{c_2}>30T [103] (by comparison, for the conventional superconductor Zn, T_{sc}=0.89K for H_{c_2} ≈5mT).

Superconductivity is suppressed by a magnetic field, through two mechanisms:

- the first limitation is the Pauli (or paramagnetic) limit. The magnetic field tends to align the spin, which destroys the Cooper pairs. The Pauli limited critical field, in the

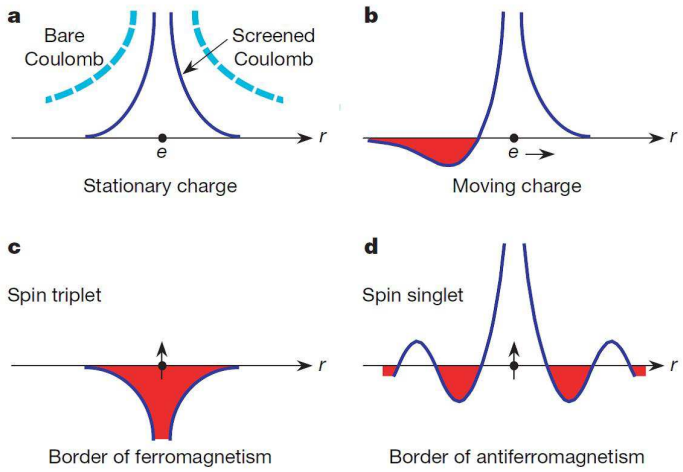


Figure 1.3 *Schematic sketch of the attractive interaction according to its origin versus distance. Panels* ***a*** *and* ***b*** *display the case of charge-charge interaction. For FM instability (panel* ***c****), the attractive interaction is close to the spin whereas it oscillates for the AFM instability (panel* ***d****). From [144].*

Clogston-Chandrasekhar theory [32, 33], is given at T=0K by

$$H_{c_2}^P = 1.84 \frac{g}{2} T_{sc} \tag{1.4}$$

with g the gyromagnetic factor ($g = 2$ for free electrons).

- the second is the orbital limit. The magnetic field acts on the momentum of the electrons. The orbital critical field is given at T=0K by

$$H_{c_2}^{orb} = \frac{\Phi_0}{2\pi\xi_0^2} \tag{1.5}$$

with Φ_0 the quantum flux and ξ_0 the superconducting coherence length.

The large critical field in HF systems can be explained by the large effective mass: the coherence length is proportional to the inverse of the effective mass ($\xi_0 \sim v_F/\Delta \sim \hbar k_F/m^*\Delta$), can thus be very small. From equation 1.5, it appears that $H_{c_2}^{orb} \sim (m^*\Delta/k_F)^2$, leading to a large orbital limit. The Pauli limitation can be suppressed, or raised to higher value, by p-wave pairing, a small (anisotropic) g-factor, strong coupling...

A consequence of the unconventional pairing is that the superconducting order parameter may need to change sign (or phase) on the Fermi surface, leading to nodes of the gap ($\Delta_{\vec{k}}$) imposed by symmetry. The figure 1.4 shows some examples of superconducting gap. The first case is an isotropic s-wave gap, the second is an example of an anisotropic d-wave gap (representation $d_{x^2-y^2}$) with line nodes and the last one is a f-wave gap, with line nodes at the equator and point nodes at the poles. The physical properties are sensitive of the presence of nodes in the superconducting gap, especially thermal conductivity, as it will be explained in the next chapter.

In HF, several Fermi sheets can be present. As a consequence, the quasiparticles can have different pairing strength, depending on the weight of their f-character. In that case,

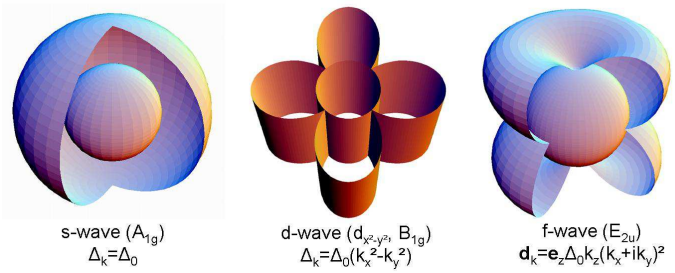


Figure 1.4 *Representation of three superconducting gaps: an isotropic s-wave gap and two anisotropic gaps (d-wave and f-wave) with line nodes and point nodes.*

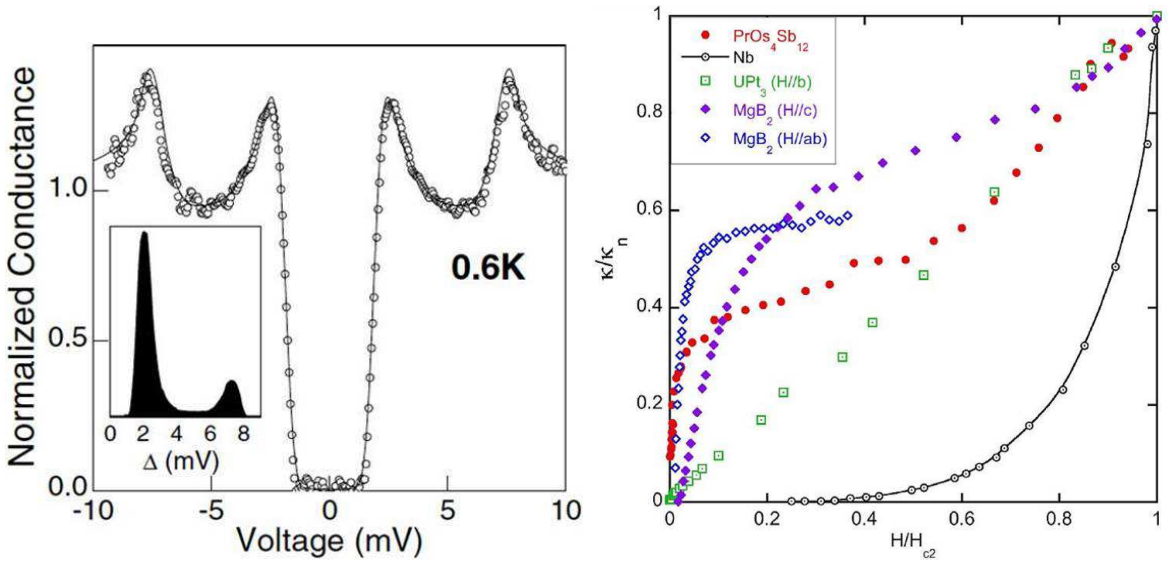


Figure 1.5 *STM spectroscopy in the multigap superconductor MgB_2 [128] (left panel) and thermal conductivity measurements in the multigap superconductors MgB_2 and $PrOs_4Sb_{12}$, and in the one band Nb (conventional SC) and UPt_3 (unconventional SC) [188] (right panel).*

if interband scattering is not "too strong", several superconducting gaps, corresponding to different Fermi sheets, can be present in the superconducting state: this is called multigap superconductivity. It has been theoretically predicted in 1959 by Suhl *et al.* [207] and seen first experimentally in MgB_2 in 2001 [148]. To detect multigap superconductivity, several probes are available, like STM spectroscopy or thermal conductivity. Figure 1.5 shows an example of STM spectroscopy in MgB_2 [128] and the normalized thermal conductivity in different compounds: in the multigap superconductors MgB_2 and $PrOs_4Sb_{12}$, and in the one band Nb (conventional SC) and UPt_3 (unconventional SC) [188] (right panel). The STM spectroscopy shows the condensation of the σ bands at $\pm$8mV and the π bands at $\pm$2mV. The thermal conductivity shows two energy scales: by decreasing the magnetic field, the first decrease below H_{c_2} corresponds to the opening of the large superconducting gap and follows by a plateau. The second decrease is the opening of a smaller gap. Note that multigap superconductivity does not imply necessarily unconventional SC, MgB_2 is an *s*-wave, electron-phonon mediated superconductor (at 39K!).

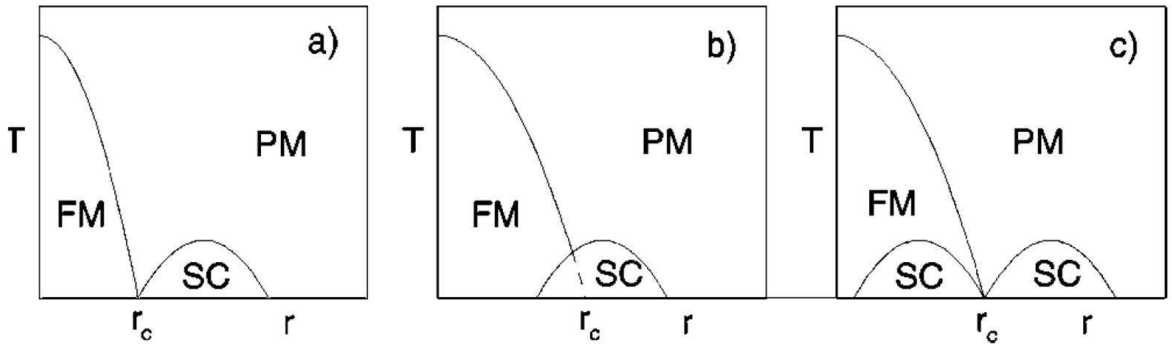


Figure 1.6 *Different scenarios when existence of superconductivity close to a magnetic instability. Panel (a): SC exists only out of the FM phase, like Fe under pressure [192, 183]. The superconductivity exists in both phases, with the vanishing of T_{sc} at the QCP (Panel (c)) or not (Panel (b), case of UCoGe). The panel (c) has been predicted by Fay and Appel [46], and is similar to UGe_2, but no superconductivity has been detected in the PM phase up to now. The parameter r represents the "distance" to the QCP. From [178].*

1.3 Superconducting Ferromagnets

1.3.1 Introduction

The heavy fermion superconducting ferromagnet UGe_2 (its superconductivity has been discovered in 2000 [182]) is the first superconductor where ferromagnetism and superconductivity coexist in a non competitive way and unambiguously. However, the possibility to mix superconductivity and ferromagnetism has been theoretically and experimentally explored since a long time.

Theoretical Predictions

From a BCS point of view, it has been seen that superconductivity is very sensitive to magnetic impurities, and, as the Cooper pairs are formed in opposite spin directions, ferromagnetic spin fluctuations tend to suppress superconductivity [23]. Thus, it is natural to think that coexistence of SC and FM is faintly probable, due to their antagonism. In 1957, Ginzburg has predicted that their coexistence is nevertheless possible, if the internal field due to magnetization is lower than the critical field. However, in some conditions, spin alignment in the superconducting state can lower its energy, leading to coexistence with FM. But the alignment occurs in a very short distance (smaller than the coherence length), and the net magnetization remains zero when averaged over a coherence length. It is so evoked in term of cryptoferromagnetism or modulated ferromagnetism [6, 25]. In ferromagnetic superconductors, the coexistence of FM with SC in a large temperature range is also predicted [95], with a spontaneous vortex phase at zero field [114, 209, 64].

In 1980, Fay and Appel [46] predicted the possibility of p-wave "equal spin pairing" (ESP) superconductivity (Cooper pairs with the same spin $\uparrow\uparrow$ or $\downarrow\downarrow$) with itinerant ferromagnetism (equivalent to the A1 phase in superfluid ^{3}He) close to a magnetic instability, the pairing being induced by longitudinal spin fluctuations. In their theory, SC and FM are carried by the same electrons with triplet pairing, but the superconducting temperature vanishes at the QCP. They predicted that superconductivity is possible in the weak ferromagnet $ZrZn_2$ with

T_{sc} as high as 1K in a very pure system[3]. For a second order ferromagnetic transition, Roussev and Millis predicted the possible coexistence of FM and SC, and, if the ferromagnetism is suppressed by an external parameter (pressure for example), the superconducting pocket can survive in the paramagnetic phase [178]. The different scenarios for superconductivity close to a magnetic QCP are shown figure 1.6. Conventional s-wave superconductivity is also predicted for localized ferromagnets [206, 2] and for weak ferromagnet, if close to a quantum critical point [24, 35].

Experimental Results

So, numbers of theories can predict the coexistence in various systems with different models. From an experimental point of view, a close relationship between FM and SC was early suspected in some rare-earth compounds [133] in 1958, and the first example where coexistence seemed unambiguous is certainly the compound $CeRu_2$ doped with Gd [132]: the superconductivity is not strongly suppressed by the ferromagnetism (see figure 1.7), as expected for a BCS superconductor. The first thought was that the superconductivity was confined in the ferromagnetic domain walls, where the net magnetization is zero [131], but specific heat measurements confirms that SC develops in the whole sample [167]. However, the short range ferromagnetic order (correlation length $r^* \approx 16$Å in $Ce_{0.8}Tb_{0.2}Ru_2$ at 1.5K [177]) made that these compounds are rather "spin glasses". The coherence superconducting length ξ is much larger than r^* ($\xi \approx 100$Å), and so, the superconductivity, carried by the d-electrons, is not affected by the correlations of magnetic moments (carried by the f-electrons) [176].

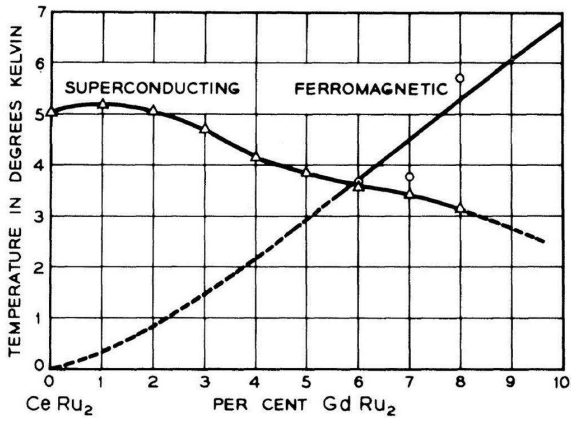


Figure 1.7 *Superconducting phase diagram of the Gd-doped $CeRu_2$ [132].*

In 1962, it has been predicted that ferromagnets can become superconducting when the external field compensates the internal exchange field (Jaccarino-Peter effect [93]). The basic mechanism of the Jaccarino-Peter effect relies on several requirements:

- two separated systems are needed: the magnetic ions and the conduction electrons, coupled by an exchange interaction $-J\vec{S}.\vec{s}$, where J is the exchange integral, $\vec{S}$ the local moment and $\vec{s}$ the conduction electron moment.
- the exchange field should be negative, so that the total field applied to the conduction electron spin: $\mathcal{H} = -J < \vec{S} > .\vec{s} - g\mu_B\vec{H}_{ext}.\vec{s}$, leading to the effective field $\vec{H}_{eff} = \vec{H}_{ext} + J\frac{<\vec{S}>}{g\mu_B}$, and $\frac{<\vec{S}>}{g\mu_B} \approx \vec{m}$. This effective field can be reduced compared to $\vec{H}_{ext}$ and to the internal field.
- the value of the external field compensating the internal field should be smaller than the orbital limitation of the upper critical field: the Jaccarino-Peter effect allows only a suppression of the Pauli limitation due to the exchange field.

[3]Superconductivity was claimed in $ZrZn_2$ [166], but it appears later that it was an experimental artifact [240]

This effect has been seen experimentally in the system $Mo_{1-x}M_xGa_4$ (M=Nb, Ru, Mn, Fe, Co) [52]. It is responsible for very high field superconductors, like in $Pb_{0.7}Eu_{0.3}Gd_{0.2}Mo_6M_8$ with H_{c_2} ≈70T [51], and for field induced superconductivity (e.g. in $Eu_{0.75}Sn_{0.25}Mo_6S_{7.2}Se_{0.8}$ [136]). Some compounds can even show superconductivity only under field (for example, in the organic compound λ-$(BETS)_2Fe_2Cl_4$ [15]). In these compounds, superconductivity can often be described with BCS theory, and one does not speak about ferromagnetic superconductors, as SC exists only when the magnetization is canceled by the applied magnetic field.

In some others classes of rare-earth compounds, superconductivity and ferromagnetism are found together, but in a competitive way. In these compounds, the Curie temperature is smaller than the superconducting temperature, and the superconductivity disappears rapidly in the ferromagnetic state, the coexistence region being only close to T_{Curie}, hence the term cryptoferromagnetism. The first compound discovered were $ErRh_4B_4$ [50] and $HoMo_6S_8$ [92]. The figure 1.8 shows the destruction of superconductivity due to ferromagnetism. In this kind of systems, (localized) ferromagnetism and superconductivity are not carried by the same electrons (rare-earth $4f$ electrons for the FM and $4d$ electrons for the SC [96]), and interact destructively.

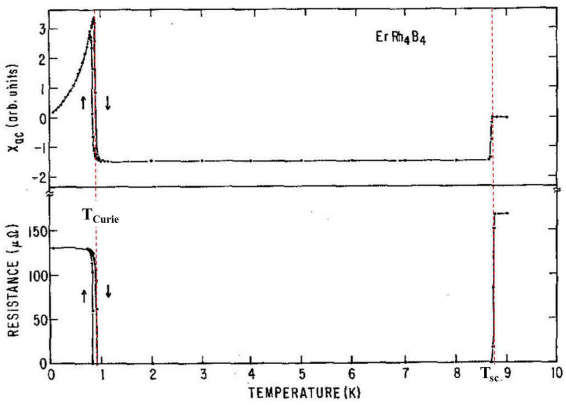


Figure 1.8 *AC susceptibility (top) and resistivity (bottom) of $ErRh_4B_4$. The system becomes superconductor at 8.8K and ferromagnet at 0.8K, which destroys superconductivity. Both properties coexist in a very narrow region close to T_{Curie}. From [50].*

Shortly afterwards, superconductivity was found in Y_9Co_7 (or Y_4Co_3) [110], with strong magnetic correlations, which appear to be a mix of itinerant and localized ferromagnetism, carried by Co atoms [236], with T_{Curie} ≈4.5K and T_{sc} ≈2.5K. Contrary to the heavy fermion superconducting ferromagnets, SC appears to be described by the conventional BCS theory (mediated by phonons), and the PM and FM states are described by spin fluctuation theory. Recent experiments seem confirm, after a long debate, that there would be a homogeneous coexistence of both orders [111]. It would be the first case of coexistence of superconductivity and itinerant ferromagnetism, and the only one for d-electron systems.

The high-T_c superconductor $R_{1.5}Ce_{0.5}RuSr_2Cu_2O_{10}$ (R=Eu and Gd) shows coexistence of ferromagnetism (T_{Curie} ≈130K for R=Eu) and superconductivity $T_{sc} \approx 33K$ [48, 47] with possible spontaneous vortex phase at zero field [198]. However, the superconductivity emerges from the CuO_2 whereas the ferromagnetism comes from the SrO layers [147]. A phase separation is evoked, even if the magnetism in these compounds seems rather complicated [104]. A large part of the lack of knowledge comes from the difficulty to grow good and large single crystals.

Recently, coexistence of ferromagnetism and superconductivity has been found in the iron-pnictide $EuFe_2(As_{1-x}P_x)_2$, where an ordered moment appears at 20K on the Eu site [174]. The parent compound exhibits antiferromagnetism, and for $x > 0.2$, ferromagnetism appears, accompanied by superconductivity (carried by Fe electrons) when $0.2 < x < 0.4$, with T_{sc}^{max} ≈30K. The existence of the SC in the FM state is attributed to the large upper critical field in the non-magnetic parent compound (≈60T in $BaFe_2As_2$ [243]) compared to the hyperfine field of the Eu atoms (≈28T [150]), and the $3d$-electrons responsible for

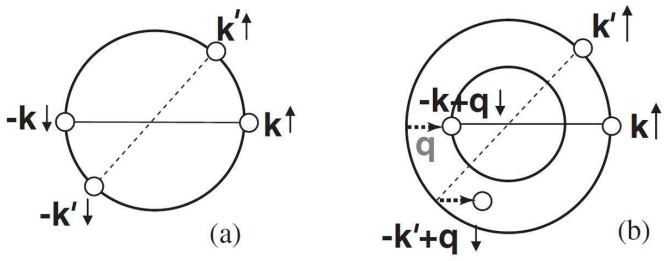


Figure 1.9 *Panel (a): $(\vec{k}\uparrow, -\vec{k}\downarrow)$ pairing predicted by the BCS theory. Panel (b): FFLO pairing state $(\vec{k}\uparrow, -\vec{k}+\vec{q}\downarrow)$ between two Fermi surfaces (spin ↑ band and spin ↓ band), resulting a non vanishing momentum of the Cooper pairs. The Cooper pair $(\vec{k'}\uparrow, -\vec{k'}+\vec{q}\downarrow)$ cannot form, as the state is not at the border of the Fermi surface.*

superconductivity and for the RKKY interactions are different [29].

The coexistence of FM and SC has also been observed at the interface of ferromagnetic/superconductor junctions, by proximity effects (induced superconductivity in the ferromagnet, see, e.g. [41]) and, very recently, in nanoparticles. Coexistence has been observed, for example, in $La_{2-x}Sr_xCuO_4$ [242], in YBCO powders [59] and in Bi_3Ni nanostructures [77]. In the two former systems, superconductivity and ferromagnetism do not coexist homogeneously, which means that FM is certainly not responsible for SC. In the latter system, SC survives up to high fields and seems related to the magnetic ground state, but further experiments are needed to conclude unambiguously.

All the examples cited here show that the coexistence of ferromagnetism and superconductivity has already been believed to be observed. It appears however that either there is a phase separation, or that the magnetic state is more complicated than ferromagnetism, and often SC and FM are competitive phenomena. The uniqueness of the HF-SC comes from the fact that FM and SC are carried by the same electrons, which means that FM and SC are cooperative properties instead of competitive (see the next section). Note that the Jaccarino-Peter effect is not possible in the HF superconducting ferromagnets, as it occurs in localized ferromagnets. Moreover, in these compounds, pairing could well be mediated by ferromagnetic fluctuations.

The fact that true coexistence (both properties carried by the same electrons) is only shown in rare cases can be explained theoretically: it is predicted that antiferromagnetic fluctuations are more favorable to superconductivity than ferromagnetic fluctuations [143, 144]. The number of candidates is reduced also by the fact that triplet equal spin pairing is induced only by longitudinal fluctuations, the transverse ones being pair-breaking [46], so isotropic 3D ferromagnet may be unfavorable.

Fulde-Ferrel-Larkin-Ovchinnikov State

Another way to obtain SC-FM, without ESP pairing and ferromagnetic fluctuations, is given by Fulde and Ferrel [58], and Larkin and Ovchinnikov [115] with the so-called FFLO state: in a situation where the size of the Fermi sea is different for the up and down spin directions (due to the polarization by a ferromagnetic instability and/or an externally applied magnetic field (Zeeman splitting)), beyond a certain degree polarization, it is favorable to build the Cooper pairs with a finite center of mass momentum, in order to partially compensate for the Fermi

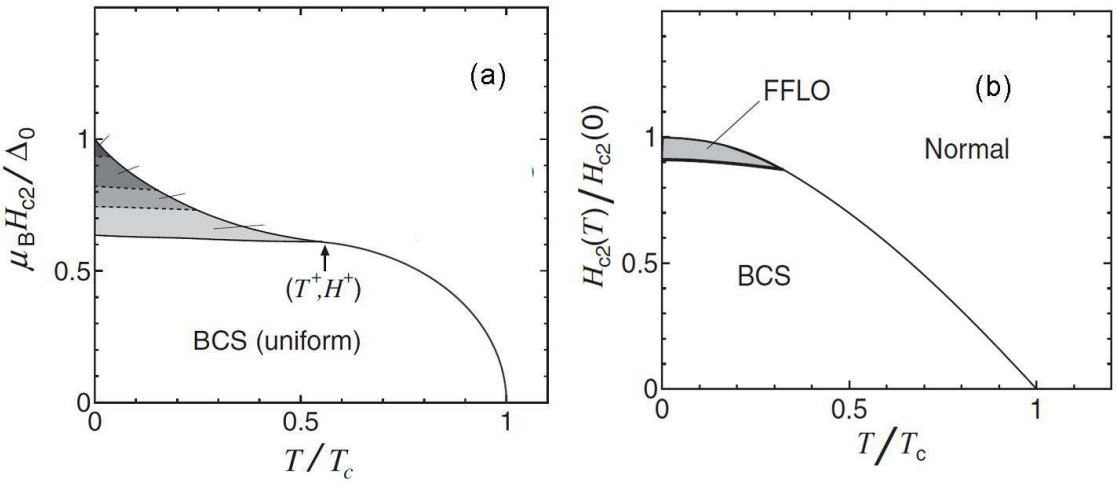


Figure 1.10 *Panel (a): (H-T) phase diagram of 2D superconductors. The point (T^+, H^+) represents the tricritical point where the FFLO state occurs. The different shaded areas show different states due to the increase of wave vectors $\vec{q}$ stabilizing the FFLO state [191]. Panel (b): (H-T) phase diagram in the presence of orbital effects. From [130].*

momentum mismatch[4] (see figure 1.9). Because of the finite center of mass momenta of the pairing state $(\vec{k}\uparrow, -\vec{k}+\vec{q}\downarrow)$, the superconducting order parameter has a spatial modulation in the real space. The FFLO state is stabilized with anisotropic Fermi surfaces, with weak orbital pair breaking [65] in very clean systems, as impurities destroy it [14, 211].

Under field, the FFLO state reduces the Pauli paramagnetic pair-breaking effect due to the Zeeman splitting of the Fermi surfaces, which means that the FFLO state enhances $H_{c_2}^P$, the Pauli limited critical field. For superconductivity limited only by the Pauli limitation, this induces an enhancement of the critical field below the temperature $T^+ = 0.56T_s$, as shown on panel (a) of figure 1.10: $H_{c_2}^{FFLO} \approx 1.07 H_{c_2}^P$ for 3D systems, $H_{c_2}^{FFLO} \approx 1.42 H_{c_2}^P$ for 2D systems and $H_{c_2}^{FFLO}$ diverges when $T \to 0$K for 1D systems (see [130] and references herein). The panel (b) of figure 1.10 shows the phase diagram in presence of the orbital effect.

In the ferromagnetic superconductors, at first sight, in the case of singlet pairing, one can expect the FFLO state to occur: the Fermi surfaces are naturally split by the ferromagnetism and are believed to be anisotropic. However, they are 3D systems with an internal exchange field possibly much larger than the possible enhancement of the paramagnetic limitation. Indeed, UCoGe is a low density carrier (small Fermi surfaces), thus even the small magnetization can lead to a large polarization. The finite wave vector $q = |\vec{q}|$ of the modulation of the FFLO state, which is typically limited to the inverse of the coherence length ξ ($q > 1/\xi$) will not be sufficient to compensate the Fermi wave vector mismatch. There is however a lack of theoretical considerations to conclude about the relevancy to describe that way the SC in the FM-SC, and a lack of experimental data to evaluate the internal exchange field or the Δk_f of the polarized Fermi sea.

[4] For a review of FFLO state in heavy fermion systems, see [130]

1.3.2 Heavy-Fermion Superconducting Ferromagnets

General Properties

Up to now, four superconducting ferromagnets have been discovered: UGe_2 in 2000 [182], URhGe in 2001 [10], UIr in 2004 [5] and UCoGe in 2007 [87]. All of them display a microscopic coexistence of superconductivity and (itinerant) ferromagnetism. The existence of the FM order in the SC state suggests p-wave superconductivity with triplet pairing [137].

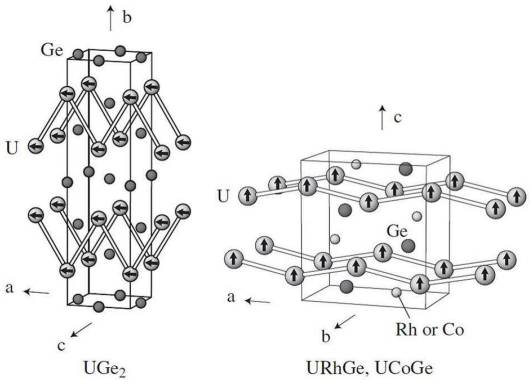


Figure 1.11 *Crystallographic structure of UGe_2, URhGe and UCoGe. The arrows represent the direction of the magnetic moments. From [8].*

The case of UIr is a bit different: it becomes superconducting under pressure at low temperature, between 2.6GPa and 2.8GPa with T_{sc}^{max}=0.14K. The very low critical field (H_{c_2}=25mT) and the fact that it is a non-centrosymmetric crystal suggest that the superconducting state is unfavorable [109]. Furthermore, the bulk existence of superconductivity has not been proved yet. Its properties are very different from the three others systems, thus, hereafter, the discussion will be only about UGe_2, URhGe and UCoGe.

These three systems have very similar properties, the following will review some of them[5]. They crystallize in an orthorhombic structure, with $ZrGa_2$ for the former and TiNiSi for the two latter. URhGe and UCoGe have the same crystallographic structure, Rh and Co atoms occupying the same site. The crystal structures are shown figure 1.11, the magnetic moments are carried by the U atoms and are along the **a**-axis for UGe_2, and along the **c**-axis for the two others. The ferromagnetic order occurs at T_{Curie}=52K, 9K and 2.5K in UGe_2, URhGe and UCoGe respectively (at ambient pressure) and appears to be Ising type [172, 88].

The superconductivity appears under pressure in UGe_2, between 1GPa and 1.5GPa, with the maximum of the superconducting temperature at 1.2GPa with T_{sc}=0.8K. The great advantage of URhGe and UCoGe is that they are superconductors at ambient pressure, at T_{sc}=0.25K and 0.7K respectively. The table 1.12 is an inventory of the main properties.

The small magnetic moment measured by magnetization, much lower than the one expected for free uranium ions or given by the Curie-Weiss law, suggests itinerant ferromagnetism. Bulk superconductivity has been proved by specific heat [216, 10, 87], and microscopic coexistence of FM and SC have been proved by NMR and μSR [112, 39, 152]. The large specific heat jump at the superconducting transition and neutron diffraction measurements have shown that f-electrons are responsible for both orders. The situation of cryptoferromagnetism discussed by Anderson [6] is not relevant here: the ferromagnetic domain size in UGe_2 is typically of the order of 4.4μm [179], far larger than the estimated superconducting coherence length ($\xi \approx$70nm). Moreover, superconductivity appears in the ferromagnetic state, not the opposite, as $ErRh_4B_4$ for example.

	UGe_2	URhGe	UCoGe
Structure	Ortho.	Ortho.	Ortho.
Space group	*Cmmm*	*Pnma*	*Pnma*
d_{U-U} (Å)	3.85	3.50	3.48
T_{Curie} (K)	52	9.5	~3
M_0 (μ_B)	1.48	0.4	~0.05
Mag. easy-axis	*a*	*c*	*c*
H_{int} (T)	0.28	0.08	0.01
γ (mJ/K^2 mol)	34	160	55
P_c (GPa)	1.5	<0	~1.2
T_{sc} (K)	0.8	0.26	0.7
$\Delta C/\gamma T_{sc}$	~0.3	0.6	0.7
H^a_{c2} (T)	1.4[a)]	2.5	>30
H^b_{c2} (T)	2.4[a)]	2	~18
H^c_{c2} (T)	4.8[a)]	0.7	0.6

a) The values of H_{c2} in UGe_2 are at ~1.2 GPa.

Figure 1.12 *Main properties of the three systems. d_{U-U} is the shortest distance between two U atoms. M_0 is the magnetization and H_{int} is the internal field due to the ferromagnetism. P_c is the critical pressure associated with the disappearance of ferromagnetism. $H_{c_2}^{a,b,c}$ is the critical field for **H//a,b,c**-axis (the values for H_{c_2} have been taken at 1.2GPa for UGe_2). From [8].*

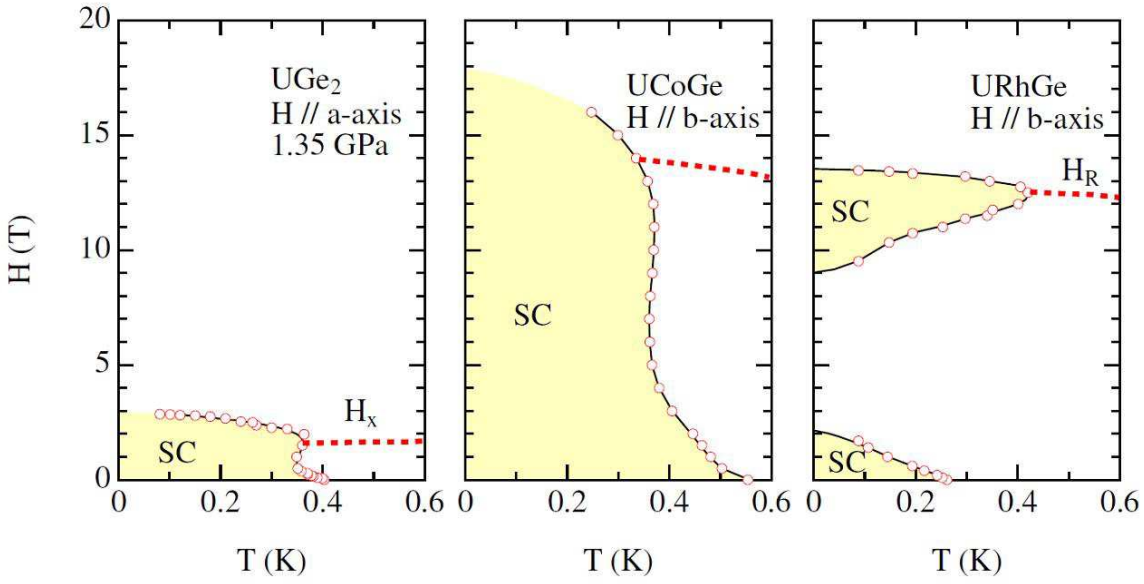


Figure 1.13 *Critical fields of UGe_2 [190], UCoGe [12] and URhGe [118] along one particular direction. From [11].*

Field Induced Superconducting Phases

A re-entrant phase or the reinforcement of superconductivity in the ferromagnetic state appears in the three systems, showing an unusual interplay between both orders (figure 1.13). In UGe_2, the enhancement is linked to the metamagnetic transition, from the small moment FM1 phase to the large moment FM2 phase, and in URhGe, it happens during the re-orientation of the magnetic moment along the **b**-axis, for a critical field $H_R \approx 12$T [118]. At H_R, a topological change of the Fermi surface via a Lifshitz transition could also occur [239], and a maximum of the effective mass m* is observed, which could explain the re-entrant phase [142]. In UCoGe, at the maximum of the reinforcement, a Lifshitz transition is suspected to occur [127] with the enhancement of the effective mass [12], but it is not associated to

[5]For a more complete review, the reader can look into Aoki's papers [8, 9]

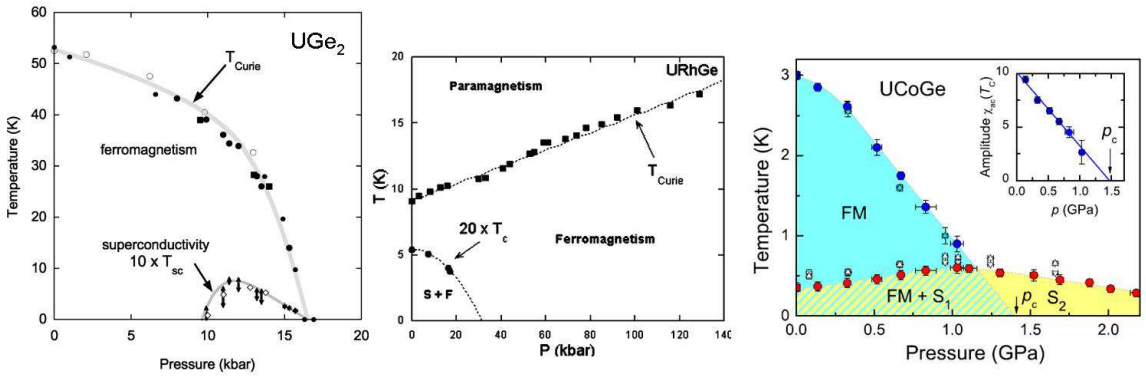


Figure 1.14 *(P-T) phase diagram of UGe_2 [84], URhGe [68] and UCoGe [193, 72].*

the re-orientation of the magnetization, which happens at much higher field (an anomaly is seen in magnetization at 45T) [106]. The high upper critical fields support triplet pairing [122, 84, 69, 12].

With the presence of the ferromagnetism in the superconducting state, it is natural to think that the systems could be multigapped: the coupling strength can be different on the Fermi sheets with opposite spin directions [140]. It is also possible that only one band becomes superconducting, like the A1 phase of the superfluid ^{3}He. Multigap superconductivity due to the band structure is also considered [180].

Pressure Phase Diagram

So far, the properties of the three compounds were similar. A big difference lies in the hydrostatic pressure dependence of the superconductivity, shown figure 1.14. In UGe_2 and UCoGe, the ferromagnetism is suppressed by the pressure, whereas the Curie temperature increases in URhGe (the fact to go away from the magnetic instability leads to the suppression of superconductivity). In UGe_2 and URhGe, the superconducting state is observed only in the ferromagnetic region, whereas in UCoGe, it extends in the paramagnetic region and the almost pressure-independent T_{sc} suggests that the superconductivity is mediated by the longitudinal ferromagnetic spin fluctuations [143, 233].

Case of UCoGe

Contrary to UGe_2 and URhGe, where the superconductivity occurs deep inside the ferromagnetic state ($T_{sc} \ll T_{Curie}$), the superconductivity in UCoGe appears close to the ferromagnetic transition ($T_{sc} \approx T_{Curie}/3$). This last transition could be weakly first order [75, 152, 60], as expected as the proximity of a ferromagnetic QCP [139, 212]. The fact that it is close to ferromagnetic instabilities (known for a long time [220, 26, 28]), by applying pressure (figure 1.14) or by chemical substitution [85, 83] enables the study of the role of the QCP for the superconductivity. UCoGe is suspected to be a metal with small Fermi sheets [87, 180, 13, 127] with a strong hybridization between the f and the d-electrons [57, 149]. The interatomic distance between the two nearest U atoms is d_{U-U}=0.348nm [220, 180], at the border of the localized/itinerant character of the f-electrons in term of Hill limit (d_{U-U}=0.35nm) [80]. Photoelectron spectroscopy suggests the duality character from room temperature measurements

[180], and the f-electrons become essentially itinerant at 20K [57]. At the Curie temperature, the Fermi surface is expected to change drastically, going from an almost semi-metallic behavior in the PM state to a metallic one in the FM state [180].

Magnetic fluctuations are present in this system far above T_{Curie} and have been found to be anisotropic [153, 88, 205]. In addition to the coexistence with the ferromagnetism, the large upper critical field [12], Co-NQR [153] and Co-NMR [73] measurements strongly suggest spin-triplet pairing, mediated through these longitudinal ferromagnetic fluctuations [74].

1.4 Goal of the Thesis

In this thesis, two systems have been studied by thermal conductivity: the superconducting ferromagnet UCoGe and the weak antiferromagnet $YbRh_2Si_2$.

The initial goal of my thesis was to use thermal conductivity measurements to try answering to the following open questions in UCoGe:

- as the physical properties are very sensitive to the sample preparation, it is worthy to wonder if the exotic behavior of the critical field seen by resistivity is intrinsic or if it is an artifact (a wrong conclusion about superconductivity can be done with only resistivity measurements), and to compare quantitatively the shape of the H_{c_2} as determined by resistivity and bulk measurements.

- the form of superconducting gap is not known, and no experimental evidence has been given about possible multigap superconductivity.

Naturally, as these measurements were the first thermal conductivity measurements performed on UCoGe, some "complications" have appeared, requiring a deeper study of the temperature and field dependence in the normal state, leading to the new point of view on the magnetic excitations in UCoGe. To be able to distinguish the intrinsic properties from the extrinsic ones (caused from impurities or inhomogeneities in the sample for example), several samples of different qualities (in term of residual resistivity ratio) have been measured.

The good results obtained on UCoGe have been a motivation to study the magnetic quantum critical point in the other compound $YbRh_2Si_2$, which can be done "easily" as it does not display superconductivity. Contrary to UCoGe, thermal conductivity measurements have already been done, and our goal was to verify the deviation of the Wiedemann-Franz law close to the quantum critical point. Thermal conductivity of $YbRh_2Si_2$, easier to measure than in UCoGe due to the better geometry of the sample, has been performed at very low temperatures and under fields.

Chapter 2

Experimental Methods

This chapter is dedicated to the description of the experimental techniques I used during my thesis, as well as the experimental probes. The goal to this chapter is not to explain and describe precisely the functioning of every tools, but to give the basic information necessary for the understanding by a non specialist.

As almost all my experiments were done at very low temperatures, I first describe the dilution fridges I used, with the special features and the work I have done to refurbish a second fridge. Then I explain how to measure the resistivity and the thermal conductivity. The second probe is explained more in details as it is experimentally difficult to perform this experiment, because lots of sources of error are present. The last part of this chapter concerns the XMCD experiments, performed in ESRF in Grenoble.

2.1 Dilution Fridges

Due to their low temperature transitions (T_c ~1K), heavy fermions have often to be studied in a dilution fridge. Two different ones were used during my thesis, equipped with superconducting magnets.

The first dilution fridge is a home made dilution fridge and has been used for more than 30 years ago. It can reach a temperature as low as 7mK in a magnetic field of 8.5T. The great advantages of this cryostat are its very low temperatures, its low sensitivity to mechanical noises (acoustic, vibrations...) and the good thermometry. This latter point is crucial for thermal conductivity experiments. Another advantage is the fact that the superconducting magnet is warmed up at each run (it is fixed on the vacuum chamber of the dilution fridge). The first cooling occurs at strictly zero field, in the sense that no residual field is present in the magnet. This enables to perform very low magnetic field measurements, further controlled by a Hall probe for a precise determination of the magnetic field when it is small (H<0.1T). The drawback is a rather long cooling or warm up time, of order of three days, however negligible when the low temperature thermal conductivity measurements are performed under magnetic field (usually some months).

Thermometry on this fridge relies on three thermometers, used for different temperature ranges:

- a high temperature germanium thermometer (Ge22007) from 20K to 2K
- a low temperature germanium thermometer (Ge1) from 2K to 0.1K

- a carbon Matsushita thermometer (CMrouge) below 0.1K

These thermometers are in a zero field region, and are used as a reference to re-calibrate the sample thermometers under field. They have been calibrated with fixed points, 768 and 747 from the NBS ranging from 15mK up to 7K. The two germanium thermometers are highly stable and reproducible. The carbon thermometer has to be re-calibrated at each run, using a paramagnetic salt (CMN). The CMN has a well-known susceptibility behavior with temperature (a Curie-Weiss law):

$$\chi = \chi_0 + \frac{C}{T-\theta}$$

θ is of the ordering temperature of the CMN, $\theta \simeq$0.75mK (constant between thermal cycles). The susceptibility is measured with a mutual inductance bridge and the two parameters χ_0 and C have to be determined each time. In order to do so, the CMN susceptibility is measured between 0.1K and 1K, with as reference the germanium thermometer. This allows to re-calibrate the carbon thermometer. The CMN is an accurate way to measure the temperature, but it is very sensitive to the magnetic field. The use of this method is possible only at zero magnetic field and the CMN needs to be demagnetized at room temperature between each experiment. Under field, only the above three thermometers are used as references.

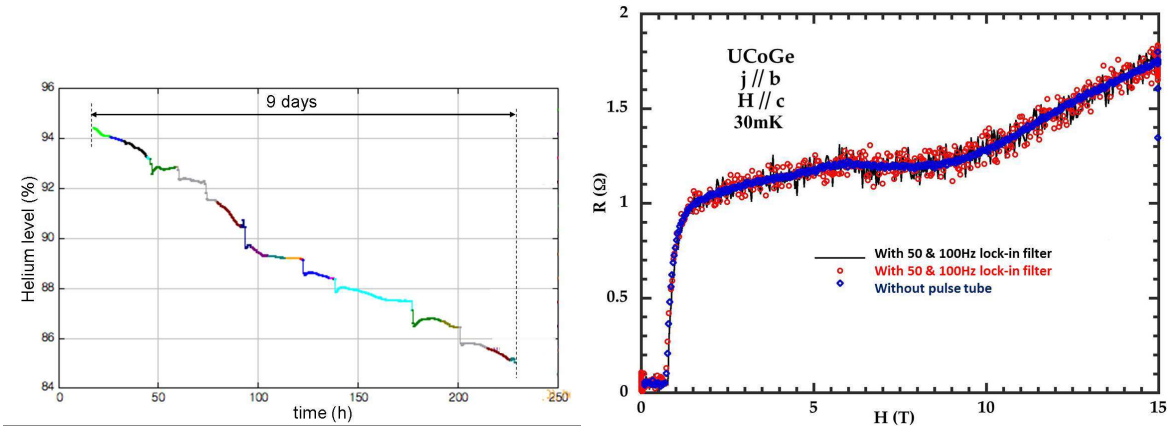


Figure 2.1 *Helium consumption of the 15T dilution (on the left) and the effect of the vibrations due to the pulse-tube on a magnetoresistivity measurement at 30mK (on the right).*

The second dilution fridge is also a homemade cryostat, but with a flow rate of "only" 30μmoles/sec (instead of 100μmoles/sec for the previous one), and no discrete silver powder heat exchangers. The initial performance was a temperature of 50mK with an 8T magnet. During my thesis, a 15T magnet with a large diameter (ϕ=64mm) and a field cancellation region has been installed. As the wiring of the dilution fridge was old and slightly damaged, it was decided to redo it. The first step was to remove the old wires and to install proper thermalisation on the 1K pot, the still and the mixing chamber. Seven Jaeger plugs were installed, each one with 12 wires. The used wires are copper wires (ϕ=80μm) and superconducting NbTi wires (ϕ=50μm), with CuNi sheath:

- copper wires between the room temperature plugs and the 1K pot ($\sim$1.5m and $\sim$ 3Ω per wire)

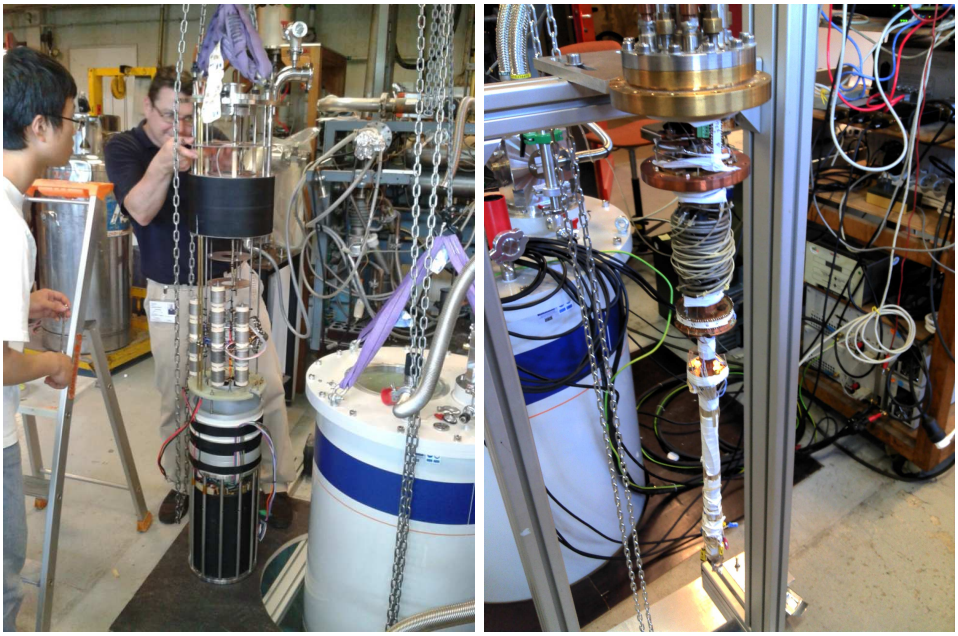


Figure 2.2 *The 15T magnet (on the left) during the preparation and the dilution fridge after the wiring (on the right).*

- superconducting NbTi wires between the 1K pot and the still (∼10cm and ∼ 20Ω per wire at room temperature)
- superconducting NbTi wires between the still and the mixing chamber (∼60cm and ∼ 100Ω per wire at room temperature)
- copper wires from the mixing chamber to the sample holder (∼50cm)

At the mixing chamber, 4x12 wires are available for the measurements, and 6 supplementary copper wires for the measurement of the thermo-electric power (Seebeck and Nernst effects). The dilution fridge had previously only 20 wires available (and not very reliable ones!), and it is now possible to measure more samples at the same times, which has also been eased by the larger diameter of the new superconducting magnet (more place available).

To increase the cooling power, a turbo-molecular pump has been added on the dilution circuit. With all this changes, the dilution fridge is now able to reach temperature as low as 20mK and the cooling power at 100mK is 10μW. The low temperature, the high field, the large diameter and the number of wires available make this dilution a very interesting fridge. The temperature is measured with a CarbonGlass thermometer from room temperature to 5K and a large temperature range germanium thermometer below 5K to the lowest temperature. Due to the high field magnet, the rod from the mixing chamber to the sample holder is not made from massive copper or silver (to avoid long relaxation time due to the increase of the specific heat hyperfine contribution and excessive heating by Eddy currents), and we have used a fiberglass rod covered with silver sheets. The good thermalisation between the mixing chamber and the sample holder has been verified at 30mK by putting here a thermometer: both thermometers (from the mixing chamber and the sample holder) have the same time response at zero field.

In addition to the superconducting magnet, a helium recondensing system, based on a pulse-tube, is installed directly in the cryostat. This system reduces the helium loss of the experiment by recondensing the helium evaporating from the bath. The typical helium consumption is displayed figure 2.1 on the left. The loss of helium was 10% (∼12l) in 9 days, each step corresponding to a change of the magnetic field, giving an autonomy of about one month.

The biggest problem with this recondensing system is the mechanical vibrations of the pulse-tube, leading to an additional electric noise. The effect on resistivity measurements at 30mK is shown on figure 2.1 on the right: a magnetoresistance measurement has been performed on UCoGe at 30mK from 0T to 15T. The blue curve corresponds to the measurement without pulse-tube and the red and the black are with the pulse-tube on (the black is with a 50Hz notch filter on the lock-in detection). The pulse-tube increases the noise, but it is constant with the magnetic field. In this case, it means that the additional noise is not vibration noises that we have also detected on the thermal conductivity set-up. It has been seen that the pulse-tube has negligible effects for temperatures above 100mK.

A picture of the 15T magnet before the installation (on the left) and the dilution after the wiring are shown on figure 2.2.

2.2 Resistivity Measurements

The resistivity (ρ) measurement is a basic characterization of metallic systems. It is easy to prepare and it is very rapid to have a complete curve (typically less than half a day to have a resistivity curve from room temperature to 0.3K). It is a transport property, sensitive to the electron density, the Fermi velocity and the mean free path. Additional measurements are always needed to identify the transition (specific heat, susceptibility, magnetization, neutrons...).

Resistivity measurement is also used to detect Fermi liquid behavior. Theoretically, the finite lifetime of charged quasiparticles, which behave as $(\epsilon - \epsilon_F)^{-2}$ close to the Fermi level, translates into a resistivity law $\rho = \rho_0 + A.T^2$, with ρ_0 the residual resistivity at zero temperature and A a coefficient proportional to the square of the effective mass of the quasiparticles. In the case of a Fermi liquid, the measurement of the A coefficient with the variation of an external parameter (magnetic field, pressure, chemical doping...) is a simple way to monitor the evolution of the effective mass ($A \propto (m^*)^2$), which is indicative of correlation strength in heavy fermion. In the same way, a strong deviation from a T^2 law at low temperature is the signature of a non Fermi liquid behavior, so of some kind of instability of the Fermi sea. At high temperature, other mechanisms can be responsible for the deviation (phonons, Kondo effect...).

The resistivity is a directional measurement, which means that anisotropic effects may be studied this way. It is a good probe to detect superconductivity, but it should be confirmed by other measurements. Indeed, the resistivity measurement may be affected by surface effects, and the superconducting transition (the fall to zero resistance) may be due to defaults on the surface (inhomogeneities, constraint...) and if a path is becoming superconducting in the compound, it will short-circuit the resistivity [134]. This effect has already induced some famous mistakes: superconductivity has been claimed in $ZrZn_2$ (which is theoretically predicted for very pure samples) in 2001 [166], but it appeared that the superconductivity was induced by cutting the sample by spark erosion, leading to a large density of zirconium

at the surface [240].

Practically, the resistivity is measured with the standard four wires method: the AC current is applied at each extrema of the sample and the voltage is measured with two other contacts at the same frequency. The signal is increased with a room temperature low noise preamplifier (gain of 10^4). In some cases, a low temperature transformer can be added for additional noise reduction. This technique avoids measuring the resistances of the wires and of the contacts. Good contacts are necessary to measure at low temperature, as it is possible to heat the sample via the contacts due to Joule effect. In order to do that, $15\mu m$ diameter gold wires are used and are spot-welded to the samples. The easy set-up for resistivity enables to measure several samples at the same time during one experiment. The usual resistances measured are in the order of magnitude of $R \approx 1m\Omega$, with contact resistances inferior to $1m\Omega$. The electrical current used for the measurements is approximately 0.1mA (lower at low temperature), which means a measured voltage in the order of magnitude of 1mV (with the pre-amplifier).

2.3 Thermal Conductivity Measurements

2.3.1 Theory

Principle

If electrical conductivity measures the efficiency of a compound to transport charge (only with the electrons), thermal conductivity (κ) is the equivalent with the heat. As heat is energy, thermal conductivity measures the efficiency of a material to transport an excess of energy from a part to another. κ is sensitive to any excitations of the order of magnitude of k_BT. This is the most sensitive probe at low temperature to low energy excitations ($\sim 1\mu$eV for thermal conductivity at 10mK, to be compared to ~ 0.1meV for neutronic diffraction). Thus, in the most general case, κ is directly linked with the spectrum of phonons and the density of states of the electrons. In some systems, other excitations can be present: magnetic fluctuations or magnons for magnetic material, excitons... Thermal conductivity can be viewed as realizing a spectroscopy of the thermal excitations in the material, but with a resolution which is also of the order of k_BT.

Another closely related probe is the specific heat. It measures the capability of a material to heat and it is a true thermodynamic quantity. However, at low temperature (typically below 100mK in heavy fermions), the nuclei specific heat (the hyperfine contribution) is becoming predominant and corrections are necessary. As the nuclei cannot carry heat, there is no correction at low temperature to obtain κ. This makes it very useful for materials with small critical temperatures (like the heavy fermions systems). Another advantage of thermal conductivity compared to specific heat is that it is a directional probe, sensitive to the anisotropy of the crystal.

Different Contributions and Wiedemann-Franz Law

All excitations will mix together in the total signal, so it is important to know the different contributions to κ to be able to remove the unwanted signal to the interesting one. One hypothesis done from now (and in this whole thesis) is we assume the addition of the different contributions: each heat channel is in parallel, i.e. $\kappa_{tot} = \kappa_{el} + \kappa_{ph} + \kappa_{mag} + \ldots$, with κ_{el} the electronic contribution, κ_{ph} the contribution due to phonons, κ_{mag} the magnetic contribution.

The electronic thermal conductivity is classically deduced from the resistivity through the Wiedemann-Franz law (WFL) [54]: it has been shown that the ratio $L = \frac{\kappa\rho}{T}$ does not depend on the metal at low temperature and tends to the Lorenz number $L \underset{T\to 0K}{\longrightarrow} L_0$=2.44 10^{-8}W.K^{-2}.m^{-1} (see e.g. [1]). In the following, the quantity $\frac{L}{L_0} = \frac{\kappa\rho}{L_0 T}$ is called the Lorenz ratio. The physical interpretation of this law is that the electrons carry heat and charges with the same efficiency. The WFL is usually valid at low (when $T \to$0K) and high temperatures ($T \approx$200-300K). At intermediate temperatures, the deviation is due to the electronic inelastic scattering and the contribution of the phonons. The phonons contribution (and any extra contribution in general) will cause a positive deviation ($L/L_0 > 1$) as it adds supplementary contributions to the heat transport, but not to the charge transport. The electronic inelastic scattering acts the opposite way, the electrons are "less efficient" to carry heat than charge. Indeed, a charge current is only suppressed by scattering processes with large wave vector transfer. A heat current is affected by the same processes but also by scattering events reducing the excess heat of the carriers. Therefore, calculations of charge and thermal resistivities distinguish "horizontal" processes, affecting similarly both quantities and thus inducing no deviation of the WFL, and "vertical" processes (only change of energy), affecting only thermal conductivity. A schematic representation of both processes is shown figure 2.3, panel **2)**. At low temperature, the WFL is obeyed again as the thermal conductivity is dominated by elastic scattering on the impurities. In the case of an ideal metal, the Lorenz ratio could decrease to 0 at zero temperature. The effect of the impurities on the WFL is displayed figure 2.3, panel **1)**.

The WFL is a robust law in the sense that it is difficult for a normal system to break it down at zero temperature, except in the case of a superconductor. The violation is due to the decoupling of charge carriers and heat carriers. Strong violation has also been found in systems with spin-charge separation (spin excitations and charges propagate independently) [232]. The proximity of a quantum critical point can also induce the violation, with the divergence of the effective mass [101], but this point is still under debate.

The lattice thermal conductivity is more complex to determine in a large temperature range, as the mechanisms which carry heat via phonons change with the temperature. At high temperature, the lattice thermal conductivity is limited by Umklapp processes. At low temperatures, the phonons are limited by phonon-phonon scattering on the crystal boundaries in insulators, or by electron-phonon scattering in metals ($\kappa_{ph} \sim T^2$).

In our case, we will assume that the lattice thermal conductivity is limited only by electron-phonon scattering, leading to $\kappa_{ph} = P.T^2$, with P a field independent parameter. In principle, for high enough purity samples ($l > 1/q_{pg}$), the parameter P should be almost independent of ρ_0, the residual resistivity (but not to the crystallographic direction).

No general law exists for the magnetic contributions to the thermal conductivity, and it changes from a system to another. A phenomenological model has been established for our measurements that reproduces quite well the data. But due to the lack of theoretical background and its large sensitivity of the choice of the parameters (difficult to estimate precisely), it will be explained in details in the Appendix .1.

In a Superconductor

Concerning superconductivity, a naive consideration would be that if the electrical resistivity goes to zero, as the ratio $\frac{\kappa\rho}{T}$ should stay constant (through the WFL), κ/T will also diverge. The actual case is almost the opposite: κ/T decreases more rapidly to zero in general (for

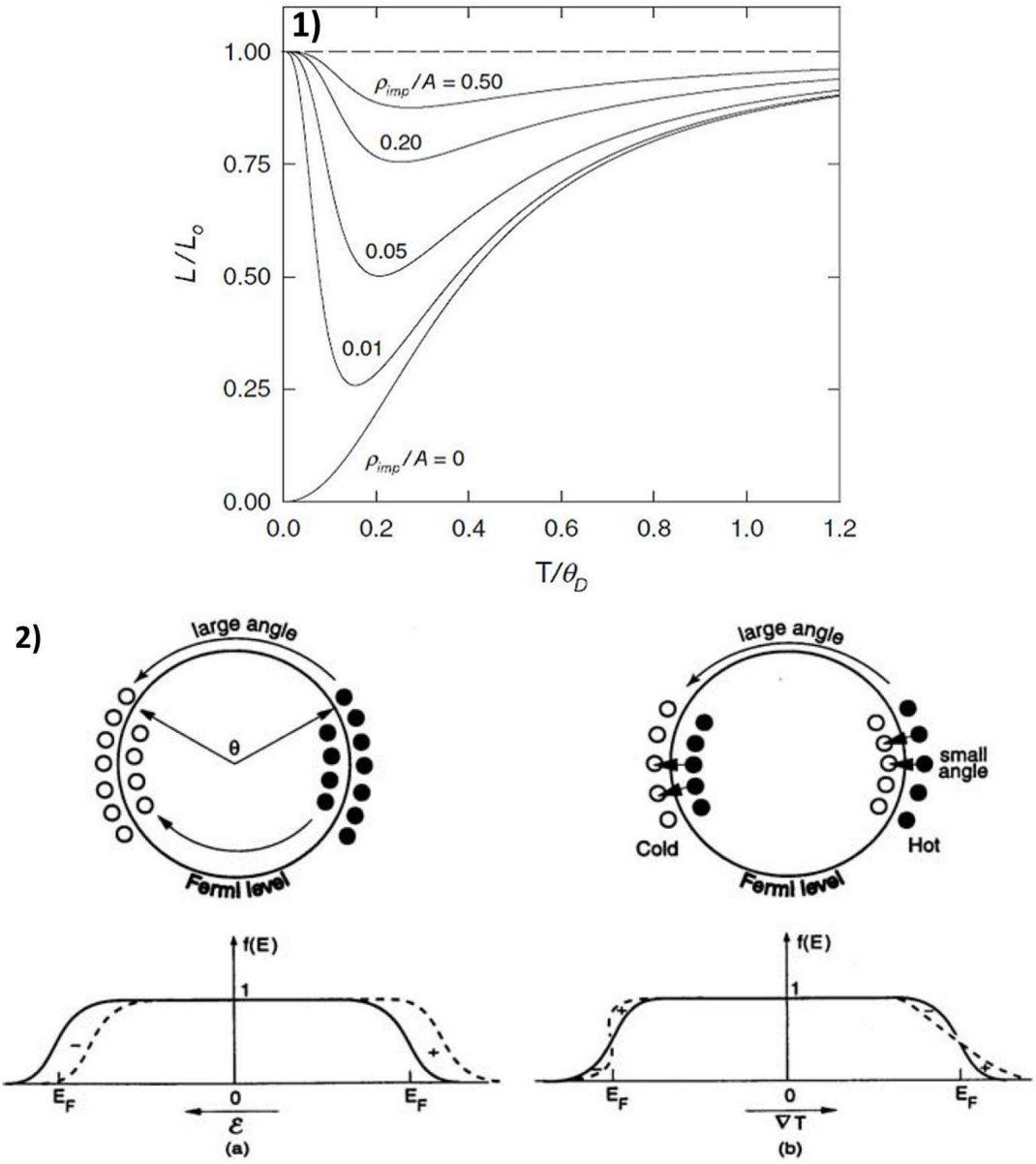


Figure 2.3 *Panel **1)** Evolution of the Lorenz ratio with the number of impurities. The ratio ρ_{imp}/A represents the number of impurities in the system ($\rho_{imp}/A = 0$ is for an ideal system), θ_D is the Debye temperature. Panel **2)** Representation of the horizontal (Panel **2 a)**) and vertical (Panel **2 b)**) processes of the electronic quasipaticle thermal conductivity. The solid and the dashed lines represent the undisturbed and disturbed Fermi distribution respectively, by an electric field (Panel **2 a)**) and a thermal gradient (Panel **2 b)**). An electric field shifts the entire distribution, whereas a temperature gradient creates asymmetry in the distribution function. The large-angle scattering are the horizontal processes and small-angle scattering are the vertical processes, with a change in the energy of the electrons. Large angle processes can also induce a change of the energy of the electrons (like scattering with phonons at high temperature), but affect the same way electronic and thermal conductivities, and thus do not cause deviations of the WFL. From [219].*

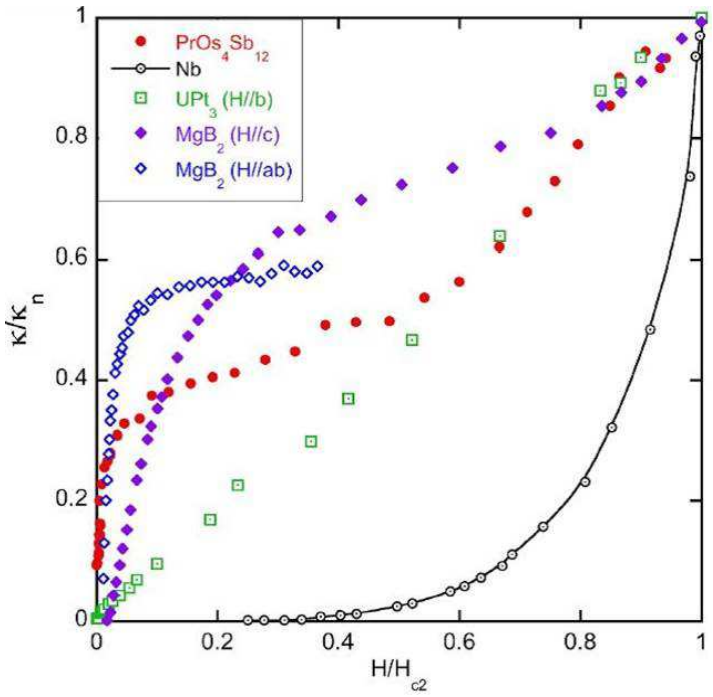


Figure 2.4 *Magnetic field dependence of the normalized residual thermal conductivity of some compounds. Nb shows an exponential behavior whereas UPt_3 is almost linear. MgB_2 and $PrOs_4Sb_{12}$ are multigap superconductors. From [188].*

BCS superconductor for example), and superconductors behave like an insulator as regards heat transport at low temperatures compared to T_{sc}. This happens because, in the superconducting state, heat and charges are carried by two different channels. The condensate of Cooper pairs has no entropy, and so carries no heat, whereas it is responsible for the infinite electrical conductivity. Only the electronic excitations carry heat, but they do not participate to the electrical current. So this strong violation of the WFL by superconductors can be simply understood in the framework of the "two fluid model", which implies different heat (excitations) and charge (Cooper pairs) carriers.

Besides, thermal conductivity is a very interesting probe for superconductivity because it makes a spectroscopy of the thermal excitations. κ is sensitive to the electronic density of states (DOS) in the superconducting state and so to the superconducting gap. For example, for a fully gapped superconductor (like the BCS superconductors), the electronic DOS decreases exponentially with the temperature, so κ is expected to act the same way. In the case of nodes of the superconducting gap, "more" excitations are available at low temperature and κ will decrease more slowly. The table 2.1 gives the expected behavior of κ in the superconducting state depending on the topology of the superconducting gap. As a consequence, the interesting quantity is not the total thermal conductivity, but the contribution due to the quasiparticles (the only one linked to the electronic DOS). This is the reason why a big effort is made to try to separate the different contributions (electrons, phonons...).

As the thermal conductivity is a directional probe, the temperature dependence of κ depends on the direction of the heat current with respect to the nodes of the gap. Moreover, in the case of line of nodes, the residual thermal conductivity ($\frac{\kappa}{T}|_{T\to 0K}$, named $\frac{\kappa_0}{T}$ hereafter), when measured in the direction of the nodes, in the superconducting state should obey to a

Gap shape	Theoretical description of κ
Full gap	$e^{-1/T}$
Point nodes	T^5
Line nodes	T^3

Table 2.1 *Theoretical laws for κ (when measured in the direction of the nodes) in the superconducting state depending on the shape of the gap.*

universal law, which does not depend on the purity of the crystal, in the clean limit [189]:

$$\frac{\kappa_0}{T} = \frac{\pi^2 k_B^2}{3} N_F v_F^2 \frac{a\hbar}{2\mu\Delta_0} \tag{2.1}$$

N_F is the DOS at the Fermi energy, v_F the Fermi velocity at the nodes, $\mu\Delta_0$ the slope of the gap at the nodes and a a parameter close to unity. This universal limit is not valid for point nodes, of course not for inhomogeneous samples (if some part of the compound remains normal) or in case of multigap superconductors.

The magnetic field dependence of κ can also give information about the gap symmetry (s-wave, p-wave...) or the presence of additional small gaps (multigap superconductors). In the case of gap nodes, the magnetic field creates a Doppler shift of the excitation spectrum, resulting in a fast increase of $\kappa(H)$ at low field for $T \to 0$K (see [229] and [3] for d-wave superconductors). For multigap superconductors, the field dependence of the thermal conductivity at low temperature reveals the presence of field scales below H_{c_2}, due to the effective critical field where the small gap is closed. Some examples are shown figure 2.4, which displays the normalized residual thermal conductivity of Nb (BCS superconductor), UPt_3 (believed to have line nodes), MgB_2 and $PrOs_4Sb_{12}$ (multigap superconductors). The angular dependence of the thermal conductivity under field is a way to probe the gap symmetry [126, 230] (see e.g. the case of UPt_3 [123]).

2.3.2 In Practice

Principle

The principle of the measurements is very simple: a thermal gradient is applied in a material and the difference of the temperature at each extremity is related to the thermal conductivity.

The story starts with the Fourier law, the heat flux density ($\vec{j_Q}$) is proportional to the temperature gradient, the constant of proportionality is the thermal conductivity:

$$\vec{j_Q} = -\kappa.\vec{\nabla}T \tag{2.2}$$

Experimentally, the samples are bar shaped and the heat flux propagates only in one direction (say, $\vec{x}$). So, $\vec{j_Q}$=j$_Q\vec{x}$ and $\vec{\nabla}T = \frac{dT}{dx}\vec{x}$. The thermal gradient is small (few percents of the absolute temperature), the linear regime is a good approximation, which means that it is possible to simplify : $\frac{dT}{dx} = \frac{\Delta T}{l}$, with $\Delta T = T_{hot} - T_{cold}$ the gradient in the sample and l the distance between which the gradient is measured. To create the gradient, a constant power is applied through the sample, so $j_Q = \frac{P}{S}$, with P the power applying through the sample and S its surface.

The thermal conductivity is so:

$$\kappa = \frac{l}{S}.\frac{P}{T_{hot} - T_{cold}} \tag{2.3}$$

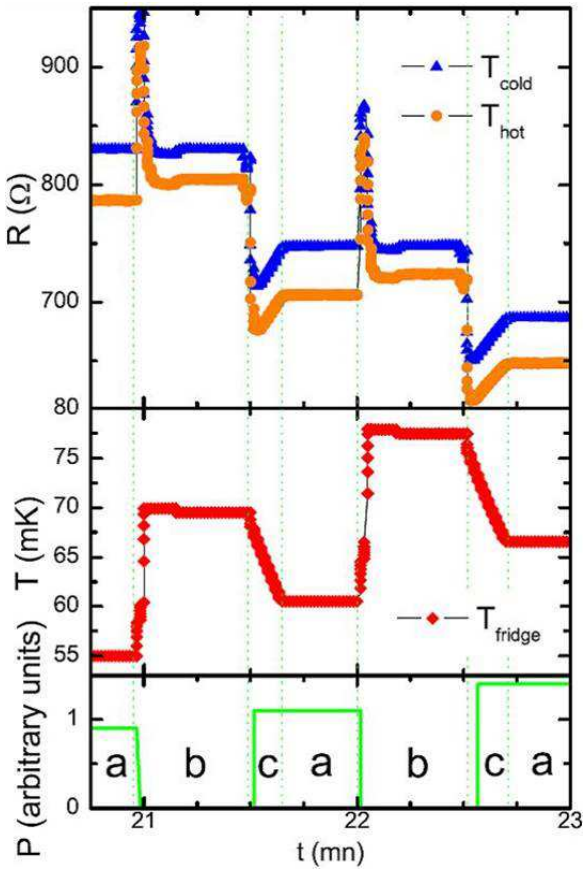


Figure 2.5 *Typical measurements of thermal conductivity with each step. The upper graph is the value (in* Ω*) of the cold and hot thermometers, in the middle the regulation temperature of the fridge and at the bottom, the power of the heater. The step (a) corresponds to the measurement of the thermal gradient (with the heater on,* $P \neq 0$*). Then, the heater is stopped (*$P = 0$*) and the fridge regulates the temperature on the temperature of the cold thermometer with power (step (b)). The thermometers are measured the second time here. The step (c) is the next point and the cycle starts again for the new point (*$P \neq 0$*).*

$\frac{l}{S}$ is called the geometric factor. In practice, the heat power is produced with a resistance via the Joule effect: $P = R.i^2$, with R the resistance and i the current applied. It is necessary to measure the thermal gradient without applying any power ($\Delta T_0 = T_{hot}^{P=0} - T_{cold}^{P=0}$) to avoid errors from the calibration of the thermometers. The actual measured quantity is thus:

$$\kappa = \frac{l}{S}.\frac{R.i^2}{(T_{hot} - T_{cold}) - (T_{hot}^{P=0} - T_{cold}^{P=0})} \tag{2.4}$$

The resistance used to apply the gradient (called the heater) is a $10k\Omega$ metallic film resistance. The resistance has a very weak temperature dependence at low temperature (variations lower than 0.5%) and its large value ensure that the power is dissipated mainly through the resistance. To have a maximum of precision for the power, the voltage of the resistance is measured during the application of the gradient. Practically, the power is $P_{heater} = V_{heater}.i_{heater}$. Because the measurements are done under vacuum and below 10K, radiation and convection losses can be completely neglected, and the most important is to avoid conduction losses on the set-up (see below).

The resistivity can be measured on the same setup with the same contacts on the sample, which enables to calculate directly the WFL without errors on the geometrical factor. The current is sent through the contacts of the heater and the fridge (the ground) and the voltage is measured through the contacts of the thermometers. It is also possible to measure the thermo-electric power (Seebeck effect) with the same contacts.

The measurement is made in two steps. The fridge is regulated at a fixed temperature

(T_{fridge}) and a constant power is applied in the heater. When the steady state is obtained, the temperatures at the cold part and at the hot part are measured. As the thermal contact between the sample and the fridge is not perfect, a gradient is present, and T_{fridge} and T_{cold} do not have the same value. The second step is the measurement of ΔT_0, to correct the calibration of the thermometers. No power is applied and the temperature of the fridge is regulated on the cold temperature when the gradient was applied ($T_{fridge}^{P=0} = T_{cold}^{P\neq 0}$). The cold and hot temperatures are measured, as well as the voltage of the heater (to verify that there is no offset voltage) and the thermal conductivity is calculated using formula 2.4. All steps are summarized figure 2.5. The resistivity is measured after the step (b) and before the step (c).

For thermal conductivity, a high precision is required on the measurements of the thermometers. Indeed, the important quantity is the gradient of the temperature, which is usually $\frac{\Delta T}{T} \in [0.1, 10]\%$ of the absolute temperature. A small error in the absolute temperature will be much more important in the gradient: if, e.g. we take a gradient $\frac{\Delta T}{T} = 1\%$ and we have an uncertainty of 0.1% of the absolute temperature, the precision of the gradient will be 10%. And as two thermometers are needed to measure the gradient, the actual precision is 20%! Thermal conductivity is directly linked to this error. This is the reason why a special effort was done to calibrate precisely the thermometers of the fridge and the gradient was measured during a long time with average and control of the drift (the average lasts approximately 5min at high temperature, 30min at the lowest temperature at zero field and up to 2h at low temperature at 8T!). To minimize the thermometry errors, the measurements are done with the larger possible gradient (as high as 10% below 30mK) and several measurements are done with different values of the gradient to confirm that the thermal conductivity does not depend on it.

Thermal Conductivity Setup

To measure κ, a regular two-thermometer one-heater setup is used with a four wires geometry: one end of the sample is glued (with silver paint) on the fridge (the cold finger) and on the other end is fixed the heater. The gradient is measured with two thermometers thermalized with two gold wires on the sample: a picture and a sketch of the setup are shown on figure 2.6. The thermometers used to measure the gradient are carbon Matsushita thermometers. We used these thermometers for their high sensitivity and their fast response at very low temperature, instead of the usual RuO_2, which have the advantage of higher reproducibility and weaker magnetoresistance. So, calibration needs to be done at each magnetic field, which is done with the measurement without power in the heater (step (b)). Down to the lowest temperature ($T_{min} \approx$10mK), no saturation is visible on the resistance of the thermometers, which ensures that the sample is well thermalized. To reduce the equilibrium time at low temperature, the size the thermometers has been reduced to decrease their specific heat. To measure the resistance of the thermometers, Au/In layers have been deposited on each end and the solders are made with indium. The thermometers and the heater are glued on silver sheets with GE varnish (to avoid electrical contact), the thermal contact between the thermometers and the sample is made through these sheets and superconducting wires are soldered to these sheets to measure the resistivity. To ensure that the thermometers measure only the temperature of the sample, and that the heat power of the heater goes only through it, they are suspended on the sample holder with Kevlar wires. This choice is made as Kevlar wires, in addition to be a good thermal insulators, have good mechanical properties (easy to

manipulate and relatively solid).

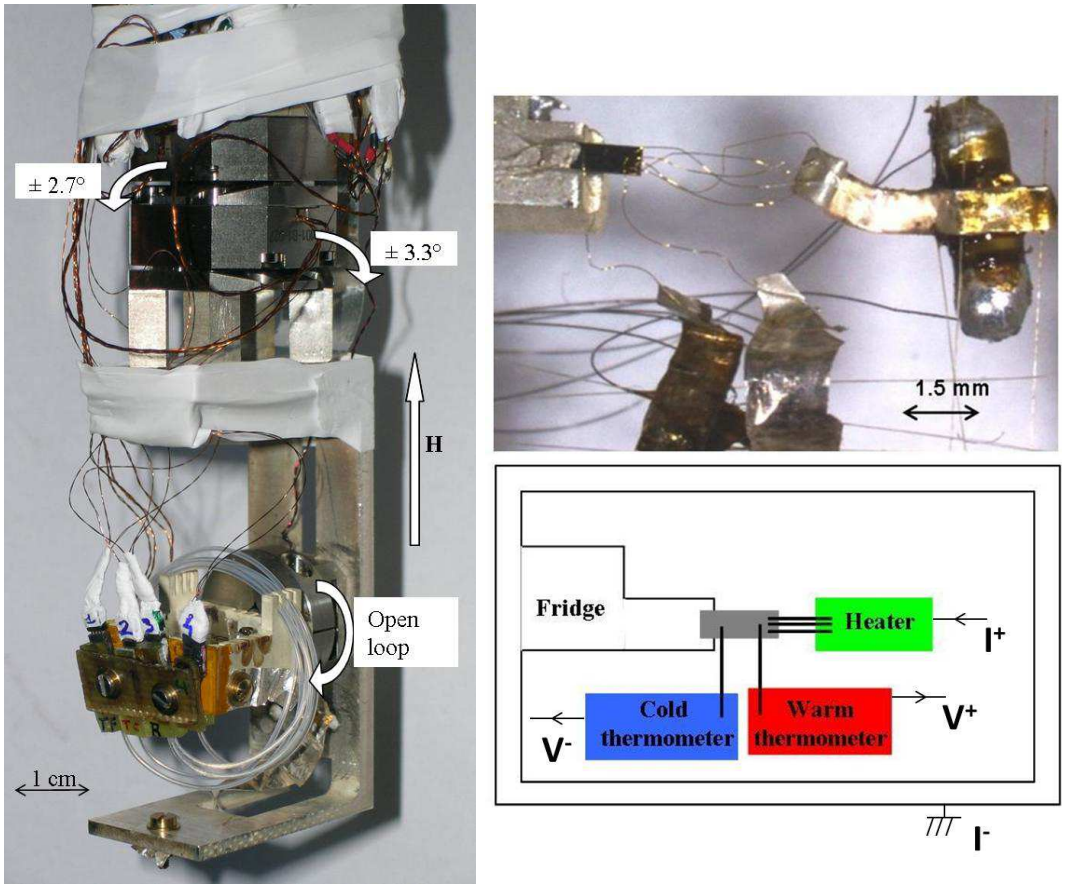


Figure 2.6 *On the left: the whole stage with the two goniometers, the rotator and the sample holder. On the right, a zoom of the thermal conductivity setup: regular two-thermometer one-heater setup for the thermal conductivity measurements (photo on the top and sketch on the bottom).*

To ensure a good thermalisation between the mixing chamber and the sample holder, the sample holder is made out of massive silver, which has a small hyperfine specific heat (compared to copper). This is an advantage at low temperatures under field, when the hyperfine contributions to the specific heat become dominant, and the equilibrium state is taking longer and longer time. The fact that we used massive silver (instead of a rod recovered with silver sheets) may be a problem for the field sweep measurements. During field sweep, Eddy currents will heat the metal. However, for these experiments, we need to work at fixed field, so the only constraint is a rather low field sweep rate (2-4 T/hour) during the field changes.

The thermal conductivity frame has been installed on a piezo-rotator, which itself suspended on two piezo goniometers. They enable to rotate the sample in-situ and to align precisely one crystallographic direction with the magnetic field. They are visible on the left picture of the figure 2.6. The rotator is used to rotate the sample of 90° and the goniometers are used to align precisely the sample with the magnetic field, with an angle of ±3° in two orthogonal directions. The goniometers and the rotator are working with piezo-actuator positioners to enable very small angle steps at low temperature ($0.02m°$ for the goniometers

and $0.5m^\circ$ for the rotator). They are also equipped with positioning resistances to determine directly their relative angles.

A similar frame is used for the 15T dilution, except that the sample holder is not in massive silver but in high performance polymer PEEK (polyether ether katone) covered with silver sheets, due to the higher available field. The first tests in a dilution fridge were difficult, but concluding. Some problems appear at low temperature because of the pulse-tube, but it has been shown that it has only small effects above 100mK (and it is always possible to stop the pulse-tube, notably for the lowest temperature measurements).

Errors Sources

The principle of the measurement is quite simple, but, experimentally, many sources of error have to be taken into account. Three effects can carry heat: conduction (through a material or several materials in contact), convection (through a fluid) and radiation (electromagnetic heat transfer when there is a difference of temperature between two bodies).

The thermal radiation power is very small in our case. With the shield on the still, the radiation power is between 0.7K (the still) and 10mK (the minimum temperature of the sample), and, with the Stefan's law, is estimated to be p=14nW.m^{-2}. With a surface of the sample of $\sim$1mm^2, the total radiation power of roughly $P=14\cdot10^{-15}$W, negligible compared to the power used to create the gradient (P_{heater} $\approx$0.1nW at the lowest temperature).

Similarly, the losses through convection are negligible: charcoals have been installed inside the vacuum chamber. Charcoals act as a cryogenic pump at low temperature and prevent the presence of exchange gas up to 10K, avoiding convection losses.

The last (but not the least!) practical source of error concerns the thermal insulation of the sample, the thermometers and the heater from the rest of the world. Indeed, they have to be in thermal contact only with the sample, and not directly with the fridge. As far below the superconducting temperature, conventional superconductors are very good thermal insulators (in addition to be perfect electrical conductors), bare superconducting wires have been used (NbTi (T_{sc} $\approx$9K), ϕ=25μm, without CuNi matrix) to measure the resistance of the thermometers and to apply a current in the heater. The thermometers and the heater are suspended to the fridge with Kevlar wires, which guarantees at the same time a good thermal insulation and a good mechanical resistance. 15μm diameter gold wires are used to connect the sample to the thermometers, the heater and the fridge.

2.4 X-ray Magnetic Circular Dichroism

The principle of X-ray Magnetic Circular Dichroism (XMCD) mesurements is to probe the magnetic state of an element of the crystal through electronic excitations reached with polarized X-rays. The X-rays will be absorbed at a specific energy, corresponding to a well-known transition between two electronic shells. This gives the X-ray Absorption Near Edge Structure (XANES) signal. The excited state depends on the polarization of the X-rays (+ or -), and the difference of the XANES signal measured with each polarization gives the XMCD signal. A detailed explanation of the principle is given in the section 3.3.1. In the following, only the experimental set-up is described.

The measurements have been done at the ESRF in Grenoble on the ID12 beamline. The sample can be cooled down to 2K, with a pumped ^{4}He fridge, and a magnetic field up to 17T can be applied. The probe and the fridge used are displayed figure 2.7. The energy



Figure 2.7 *Probe (left) and the fridge with the X-rays line (right) used at the ID12 line at ESRF.*

U				**Co**			**Ge**
$4d_{3/2,5/2} \rightarrow 5f$		$3d_{3/2,5/2} \rightarrow 5f$		$2p_{1/2,3/2} \rightarrow 3d$		$1s \rightarrow 4p$	$1s \rightarrow 4p$
N_5	N_4	M_5	M_4	L_3	L_2	K	K
736.2	778.3	3552	3728	778.1	793.2	7709	11103

Table 2.2 *Energy of the different edges, in eV, of the Uranium, the Cobalt and the Germanium.*

range available of the X-rays is from 2keV to 15keV. The electronic transitions in UCoGe are detailed table 2.2. With this energy range, only some electronic shells can be probed: the Co L-edge ($2p \rightarrow 3d$ transition) and the U N-edges ($4d_{3/2,5/2} \rightarrow 5f$) cannot be measured, as it lies at approximately 0.8keV. This is not such a problem, as the energy of the U N_4-edge and of the Co L_3-edge are very close to each other, which means that the signals will overlap, and thus be very difficult to interpret quantitatively. Only the K-edge of the cobalt is available (the $1s \rightarrow 4p$ transition), but the signal is smaller, and is more difficult to interpret. The figure 2.8 shows the measurable absorption edges on the ID12 line.

The experimental set-up of ID12 is shown figure 2.9. The XANES signal is measured in a backscattering geometry with a grazing angle of about 15°. The X-rays pass first through a hybrid electromagnet/permanent magnet helical undulator (HELIOS II), which is also used to flip the helicity of the beam (positive and negative circular polarization). The absorption spectra was measured in the fluorescence yield mode, using Si photodiodes. The energy initial beam is first roughly selected with the undulator (in one of the three of the ranges: 2-4.5keV, 5-9keV and 9-15keV), and then more precisely by the monochromator (in Si(111)). The signal harmonics are removed with the vertical focusing mirror (VFM). The first step of the experiment is to "find" the sample with the beam, and then to find the best spot on its surface (the signal with the maximum intensity). To avoid experimental artefacts, the measurements were done at both positive and negative fields, and then averaged.

Because of optical effects, the circular polarization rate is reduced to 35% and 45% for the U M_5-edge and the U M_4-edge respectively. This reduction of the signal is due to the

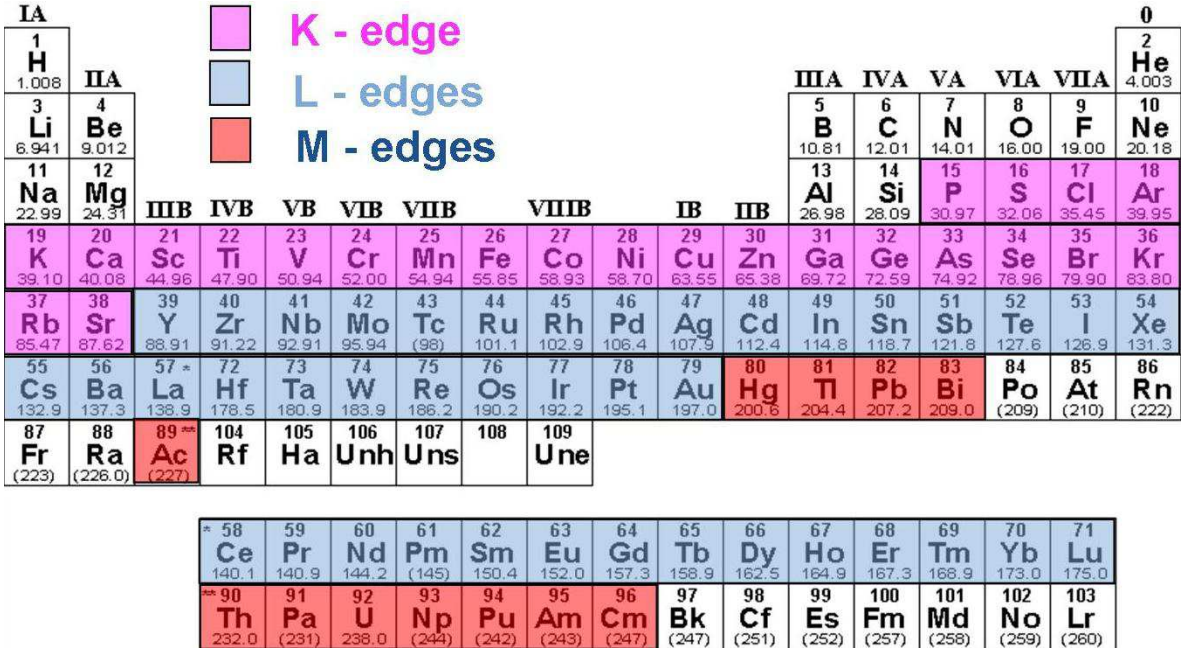


Figure 2.8 *Measurable absorption edges by XMCD at ID12 line.*

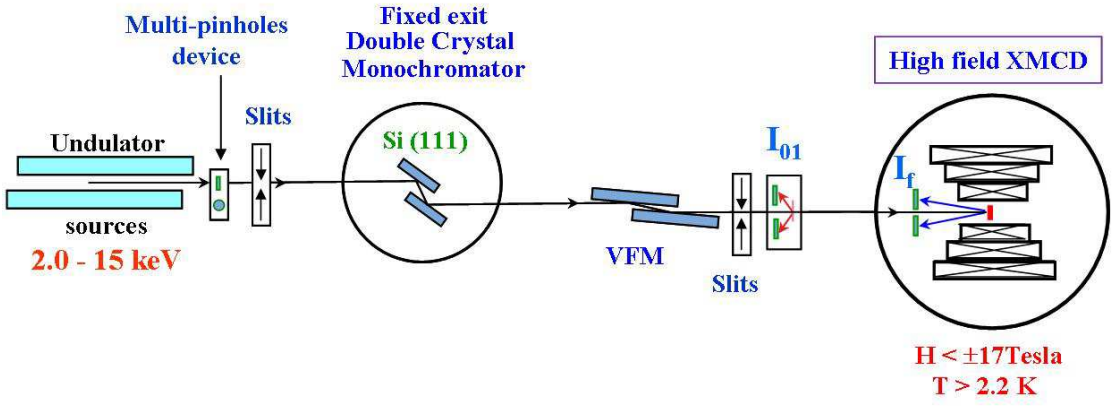


Figure 2.9 *ESRF beamline ID12.*

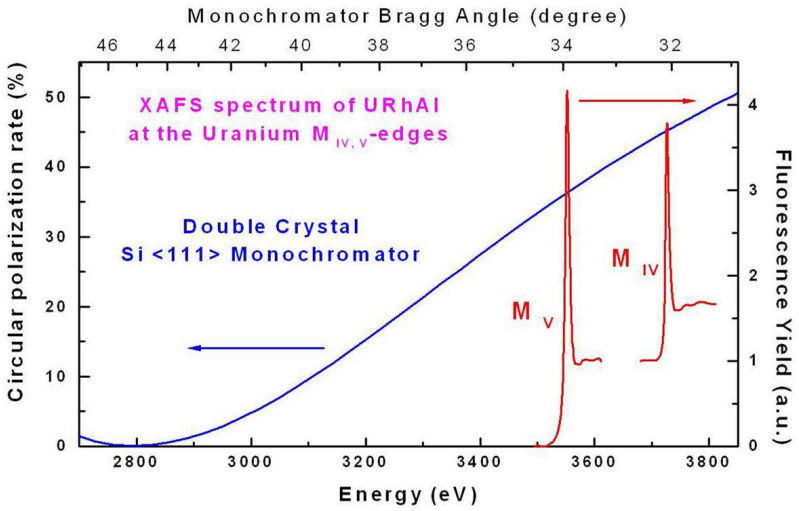


Figure 2.10 *Polarization transfer by the monochromator at the U M-edges.*

fact that at the energy of the U M-edges ($\approx$ 3.6keV), the Bragg angle of the Si(111) crystal monochromator is above the Brewster angle (see figure 2.10). For higher energies (the K-edges of the cobalt and of the germanium), the circular polarization rate is about 90%. Corrections are done to restore the full signal.

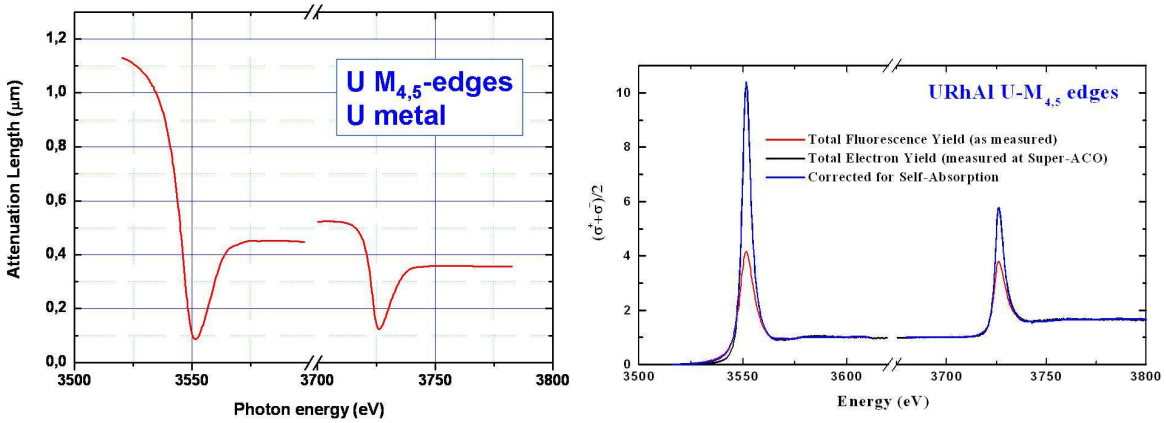


Figure 2.11 *On the left: Penetration length of the X-rays in fonction of the energy, close to the U M-edges. The penetretion length is strongly decreased at the M-edges. On the right: the effect of the the self-absorption corrections of the signal.*

The X-ray absorption spectra has been done assuming semi-infinite sample (no boarder effects), the beam diameter needs to be much smaller than the size of the sample. For our measurements, the diameter of the beam was $\approx$0.1mm, and the samples had square surface with $\sim$1mm length, thus the last hypothesis was experimentally fulfilled. Hard X-rays have a penetration length $\approx 1\mu$m, thus it can be considered as a bulk probe. However, the penetration length depends on the X-ray energy (see the left part of figure 2.11 for the U M-edges), a strong decrease is present at the energy corresponding to the M-edges (called "self-absorption"). Thus, corrections of the measured signal need to be done to take this effect

into account, the difference of the signal without and with the self-absorption correction is shown figure 2.11 on the right. Other corrections are done, which take into account the fluorescence of the subshell, the angle incidence of the X-ray beam and the solid angle of the detector.

Special care need to be taken during the sample preparation, in particular with the surface contamination: samples have been cleaved at the last moment, before the measurements. It has also been seen that the signal is reduced if we use polished surfaces instead of cleaved surfaces, with in addition a change of the signal, which may be due the change of magnetic properties resulting from the damages induced by the polishing. The size of the beam is quite small ($\sim$100μm), this enables to "choose" a good spot on the sample.

Chapter 3

First results on UCoGe

This chapter is about the results, other than thermal conductivity, on the superconducting ferromagnet UCoGe. During my thesis, several samples of different qualities have been measured, which are described in the first part. The results are divided into several parts: the first will be the determination of the critical field H_{c_2} of the superconductivity with the thermal conductivity as a probe, followed by the XMCD measurements.

The thermal conductivity measurements are presented in the next chapter.

3.1 Measured Samples

Five samples of UCoGe have been measured by thermal conductivity during my thesis. All of them have been grown by Czochralski technique[1] in our laboratory. One difficulty in the study of UCoGe is that its properties are very sensitive on the starting composition and growth conditions [8, 168]: superconductivity without ferromagnetism has been observed in bad quality samples. To ensure they are single crystals, Laue diffraction, resistivity and specific heat at low temperature are measured on each sample. Laue diffraction gives information on the crystallinity of the sample. The Residual Resistivity Ratio (RRR), corresponding to the ratio between the resistivity at room temperature and the resistivity extrapolated at zero temperature (RRR=ρ_{300K}/ρ_{0K}), is related to the number of impurities and defaults in the compound. The higher it is, the better the sample. Resistive and the specific heat transitions reflect different aspects of the sample homogeneity: a homogeneous sample will have a sharp resistive transition, which can be blurred by filamentary regions of higher superconducting temperatures. Specific heat is a bulk property, and its width is controlled by the bulk homogeneity (a superconducting filament with higher superconducting temperature would have no weight in the specific heat curve). A typical specific heat measurement in UCoGe is shown on the left of the figure 3.1. The increase at low temperature corresponds to the hyperfine nuclear contribution.

As seen in the introduction, UCoGe has strongly anisotropic and quality dependent properties. All samples measured are bar-shaped along one crystallographic direction. Hereafter, the samples are named S_x^i, with the superscript i the crystallographic direction of the bar, which corresponds to the (electric and heat) current direction, and the subscript x is the RRR. The table 3.1 shows the different details of samples : the name, the direction of the

[1] As I did not at all perform crystal growth during my thesis, no detail is given here, but the reader can look in any materials book for information.

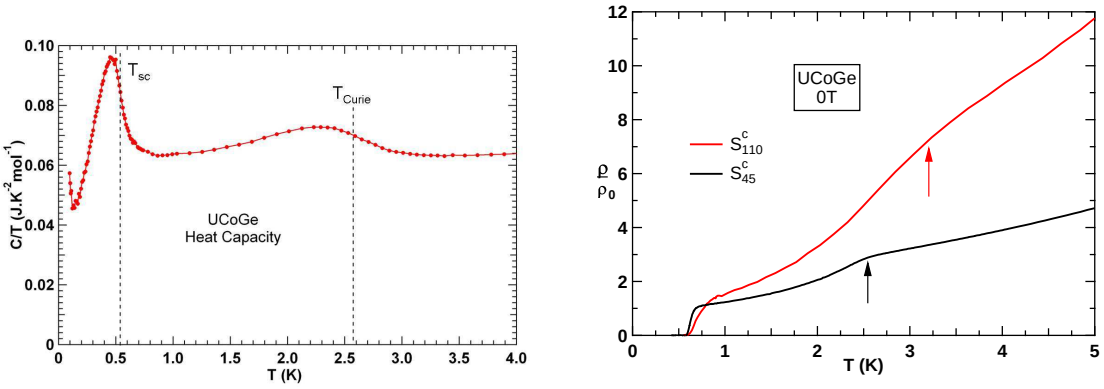


Figure 3.1 *On the left: a typical specific heat measurement of UCoGe, with the ferromagnetic transition at 2.5K (the same as measured by resistivity) and the superconducting transition at 0.55K (smaller than the one measured by resistivity). On the right: comparison at zero field of the normalized resistivity ρ/ρ_0 of samples S^c_{47} and S^c_{110}. The anomaly at the ferromagnetic transition is clearer and the superconducting transition is sharper in the sample S^c_{47} despite its lower RRR. The arrows show the Curie temperature.*

Samples	$\mathbf{j}_Q$	RRR	Size $a \times b \times c$ (mm^3)	$T_{sc}^{\rho=0}$ [ΔT_{sc}]	T_{sc}^{κ}
S^c_{16}	**c**	16	$0.34 \times 0.43 \times 1.7$	0.53K [0.22K]	0.49K
S^c_{47}	**c**	47	$0.2 \times 0.5 \times 1.74$	0.58K [0.14K]	0.5K
S^a_{65}	**a**	65	$2 \times 0.3 \times 0.3$	0.61K [0.27K]	0.48K
S^c_{110}	**c**	110	$0.32 \times 0.56 \times 0.56$	0.6K [0.26K]	0.45K
S^b_{150}	**b**	150	$0.36 \times 0.58 \times 0.36$	0.65K [0.26K]	0.5K

Table 3.1 *Properties of the studied samples with the direction of the current $\mathbf{j}_Q$, the RRR, the size, the superconducting transition temperature (T_{sc}) at zero field measured by resistivity, the width of the transition in brackets and T_{sc} as measured by thermal conductivity.*

heat current, the RRR, the size, the superconducting transition temperature at zero field measured by resistivity (T_{sc}^{ρ}), the width of the transition in brackets and the superconducting transition temperature as measured by thermal conductivity (T_{sc}^{κ}).

All samples have been annealed, but sample S^c_{47} has been annealed at higher temperature to improve its homogeneity [86, 221]. The effect of this high temperature annealing is visible with the sharp resistive superconducting transition, and with the clear anomaly corresponding to the Curie temperature and the superconducting transition by thermal conductivity. This is an evidence that the RRR is not enough to described the quality of the crystal, and that a big RRR does not necessary mean a high homogeneity sample. To illustrate this, the right graph of figure 3.1 shows the normalized resistivity (ρ/ρ_0) of samples S^c_{47} and S^c_{110} at zero field. The ferromagnetic transition is clearer and the superconducting transition sharper in the sample S_c^{47}, despite its lower RRR.

However, probably due to the high temperature annealing, sample S^c_{47} showed some problems: it was not possible to recover the S-shape of the critical field by thermal conductivity, even with the help of the rotator. It appeared that the sample was intrinsically misaligned: the figure 3.2 on the left shows the angular dependence at 1T and 2.5K of the Curie anomaly by resistivity. Indeed, the figure on the right shows the resistivity at 1T with the field along

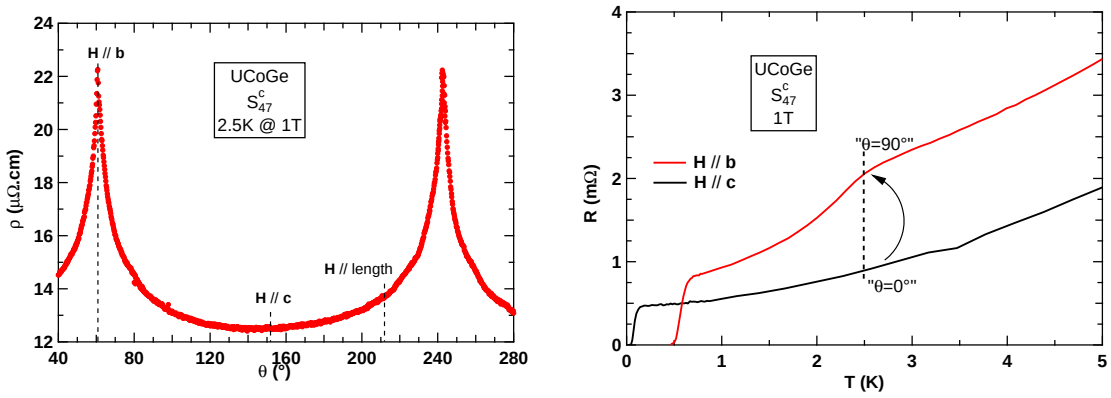


Figure 3.2 *Angular dependence (from* ***c*** *to* ***b****-axis) of the Curie temperature at 2.5K and 1T by resistivity on the left and the resistivity measurements at 1T for* ***H//b*** *and* ***H//c*** *(on the right). The angular dependence has been performed along the dotted line.*

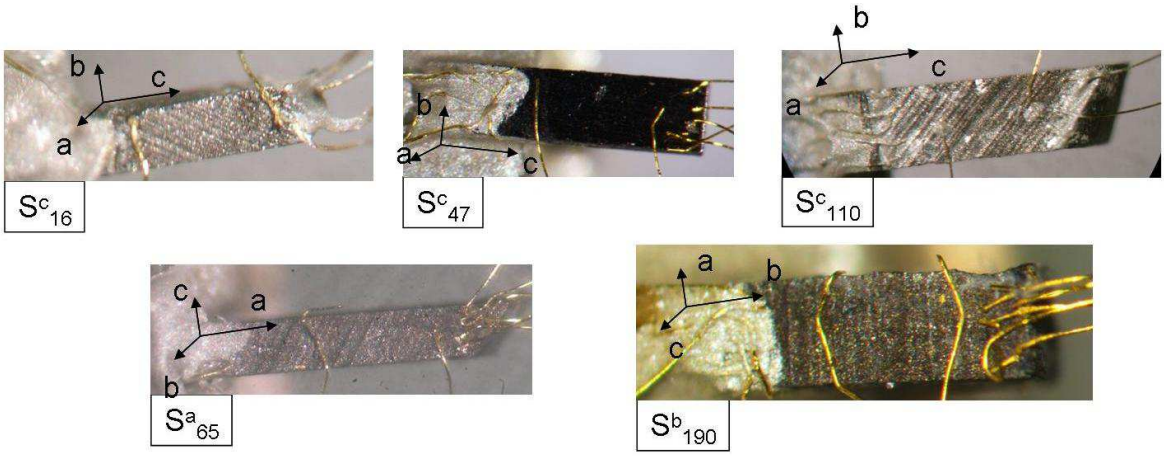


Figure 3.3 *Pictures of the samples, the length of each sample is roughly 1mm.*

the **c**-axis (in black) and along the **b**-axis (in red). The Curie anomaly is visible only when the magnetic field is well aligned along the **b**-axis, which is marked by the increase of the resistivity in the angular dependence. This measurement shows that the main axis (supposed to be the **c**-axis) is misaligned by 70° from this axis. Such a misalignment cannot be explained with the X-ray photographs, which show a well-aligned single crystal. Neutron diffraction reveals that this sample contains several grains with two big parts, one of which is misaligned. We guess that the high temperature annealing induced this effect. So measurements performed on this sample have to be taken in a qualitative view, no quantitative conclusion will be done.

The picture of the samples is seen figure 3.3. The gold wires for electrical and thermal contacts are visible and the left side was glued to the fridge (with the silver paint), in addition to spot-welded gold wires (masked by the silver paint).

3.2 Critical Fields

The goal of this part is to confirm the S-shape and the upward curvature of the upper critical fields seen by resistivity measurements, as displayed on figure 3.4.

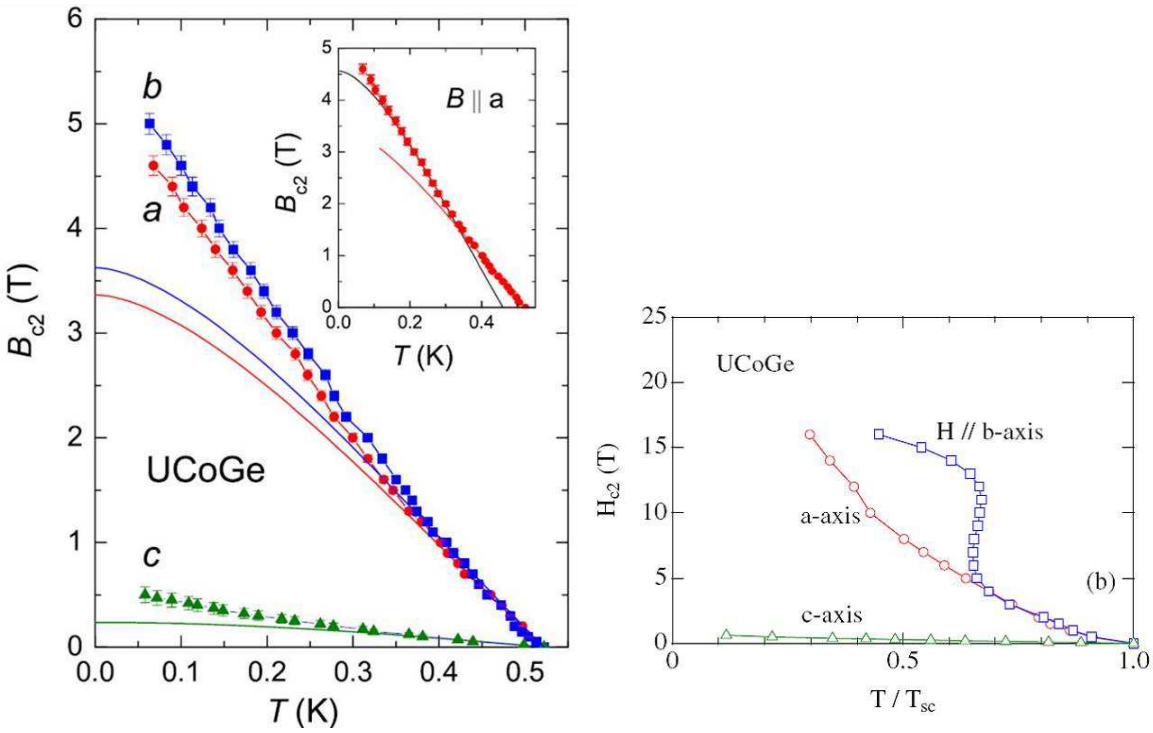


Figure 3.4 *Critical field of UCoGe along the three crystallographic directions [86, 12].*

3.2.1 How to determine the critical temperature?

In this section, thermal conductivity is used as a bulk probe of the superconducting transition, the only difficulty being the way to determine a sound criterion to define the critical temperature. In samples S^c_{16} and S^c_{47}, the superconducting temperature was easy to find as there was a clear anomaly in the measurements. For the others, the transition takes place in the low temperature raise of κ/T, due to the suppression of inelastic scattering and it does not necessary correspond to the maximum of κ/T. Naively, it is possible to think that at the superconducting transition, as the electrons are condensing, less heat carriers are available and thus the thermal conductivity should decrease. In practice, opposite behaviors can be observed for κ/T at T_{sc}, depending on the temperature range, or on the sample quality. In some superconductors, the transition is not visible (in UPt_3 [20] and MgB_2 [196] for example), and if the quality of the sample is good enough, the thermal conductivity can even increase first at T_{sc}: the inelastic electronic scattering is reduced, which leads to an increased electron or phonon mean free path in the superconducting state. In $CeCoIn_5$, κ/T increases at T_{sc} and the value of κ/T at the lowest measured temperature ($T/T_{sc} < 100$) is larger than the value at T_{sc} [214]!

To determine precisely the critical temperature, the next procedure has been followed:

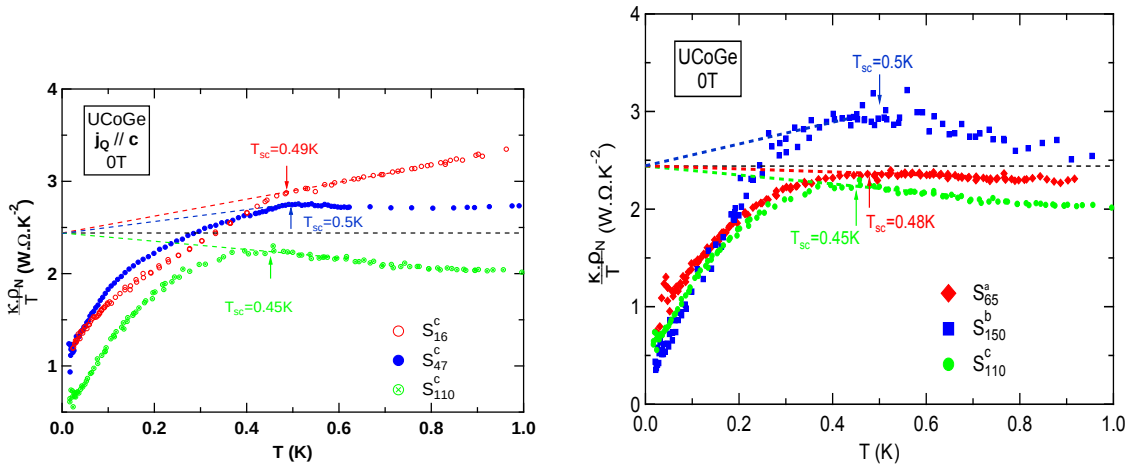


Figure 3.5 *The Lorenz number of each sample at zero field. The arrows corresponds to the superconducting transition. T_{sc} is quite easy to determine, except for sample S^b_{150} where a complete analysis is needed.*

- the resistivity has been extrapolated to 0K with the help of a power law: $\rho_N = \rho_0 + AT^n$, with ρ_0, A and n determined in the normal phase.
- the Lorenz number is plotted with the extrapolated resistivity: $L = \kappa.\rho_N/T$
- in most cases, the Lorenz number in the normal phase can be extrapolated linearly to L_0, so T_{sc} is determined by the onset of the deviation from the extrapolated linear behavior. For sample S^b_{150}, the Lorenz number cannot be extrapolated to L_0 below T_{sc}. To determine the superconducting temperature in this case, a complete analysis of the normal phase is needed to estimate the thermal conductivity in the superconducting phase, and the superconducting temperature corresponds to the deviation to L_0 of the quantity κ/κ_N, κ_N being the estimated thermal conductivity without superconductivity. The details of the calculation of κ_N are given in the Appendix .1.

An example is shown figure 3.5, the Lorenz number $L = \kappa.\rho_N/T$ is plotted for all samples at 0T.

The critical field has been measured with **H**//**b** and **H**//**c** by thermal conductivity in samples S^c_{16} and S^b_{150}, and only by resistivity in sample S^c_{47}. I will first study the critical field when the magnetic field is applied along the **b**-crystallographic axis (H^b_{c2}), then with the field along the **c**-crystallographic axis (H^c_{c2}). The fourth part is the critical field measured by resistivity in sample S^c_{47}.

3.2.2 H//b

As it was explained, the physical properties of UCoGe in the superconducting state along the **b**-axis are strongly anisotropic with the magnetic field, so the use of piezo-rotator and goniometers to align the sample *in-situ* with the field is necessary. The first step of the measurements is the alignment. To do so, as the superconducting temperature in the S-shape decreases rapidly with the misalignment along the other crystallographic axes, the resistivity is measured in the superconducting transition. After rotation, if the resistivity decreases, it

means that the superconducting temperature increases: we are going in the right way. The procedure is repeated in the two directions until the resistivity reaches a minimum: the **b**-axis of the sample is parallel to the magnetic field.

The figure 3.6 displays the thermal conductivity measurements of samples S^c_{16} (on the left) and S^b_{150} (on the right) at low temperatures with **H**//**b**. In inset are the corresponding resistivity measurements.

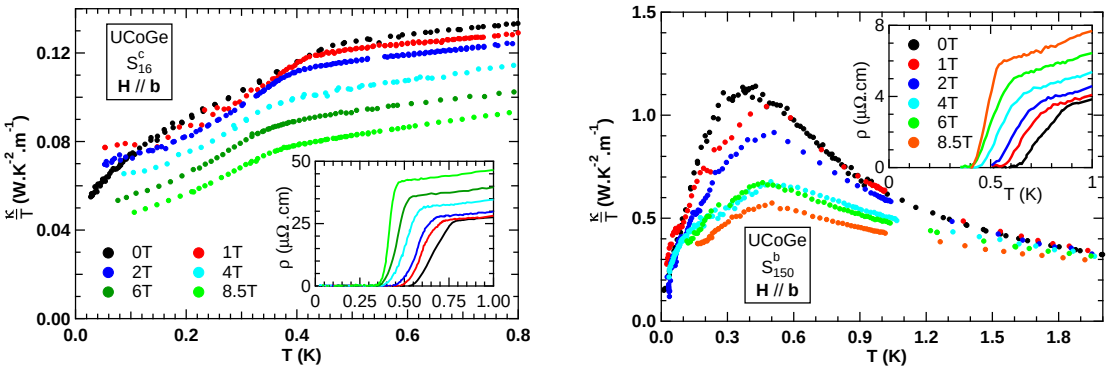


Figure 3.6 *Thermal conductivity and resistivity measurements (in inset) at low temperatures of samples S^c_{16} (on the left) and S^b_{150} (on the right).*

The bare data of thermal conductivity show that T^κ_{sc} varies only little with the field in both samples compared to T^ρ_{sc}. The critical field up to 8.5T is shown figure 3.7. T^ρ_{sc} has been taken as the middle point of the transition ($\rho = 0.5\rho_N$). The hatched area corresponds to the width of the transition, i.e. when at 90% and 10% of the resistivity without superconductivity ($\rho = 0.9\rho_N$ and $\rho = 0.1\rho_N$). Even if the S-shape seen by Aoki *et al.* [12] is not seen by resistivity (the magnetic field may be not high enough), the slope of the critical field measured by thermal conductivity is almost vertical and the beginning of the increase of the superconducting temperature is visible in both samples. We confirm here that the S-shape is a bulk property of UCoGe.

Concerning T^ρ_{sc}, several observations can be done: its width decreases with increasing field. This is evidences that the superconductivity is not very homogeneous and that the magnetic field suppresses "weak" superconducting parts due to defaults or inhomogeneities for example. The same conclusion can be done with T^κ_{sc}: the superconducting transition becomes sharper by thermal conductivity under field. However, other mechanisms (like Andreev scattering on vortices) enhance the thermal conductivity anomaly under field, even in ideal superconductors. Furthermore, in sample S^c_{16}, T^ρ_{sc} is getting closer to T^κ_{sc} with the field. At zero field, the difference of both critical temperatures is large ($T^\rho_{sc} - T^\kappa_{sc} \approx 0.25$K) whereas it is less than 50mK at 8.5T! For sample S^b_{150}, T^κ_{sc} appears at the level of the tail of the resistive transition: roughly speaking, the resistive transition is more and more dominated by the bulk superconductivity.

There is no robust explanation of this difference between bulk and resistive transitions: this is not a simple effect of the quality, as T^ρ_{sc} increases faster with the RRR than T^κ_{sc} (see table 3.1). This behavior is not only seen on UCoGe: the first example is $CeIrIn_5$, the superconducting transition is at 1.2K by resistivity and at 0.4K by specific heat [162]. Another example is the compound $CeRhIn_5$: the antiferromagnetism (present at ambient pressure) is

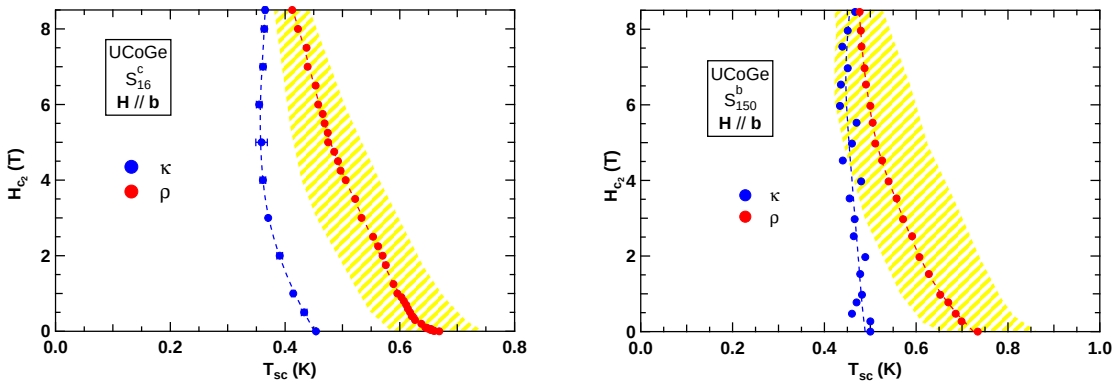


Figure 3.7 *Critical field of samples S^c_{16} (on the left) and S^b_{150} (on the right) with* $\mathbf{H}//\mathbf{b}$. *In blue is the critical field measured by thermal conductivity and in red by resistivity (taken in the middle of the transition). The yellow hatched area corresponds to the width of the resistive transition (see text). The dotted lines are guides to the eyes.*

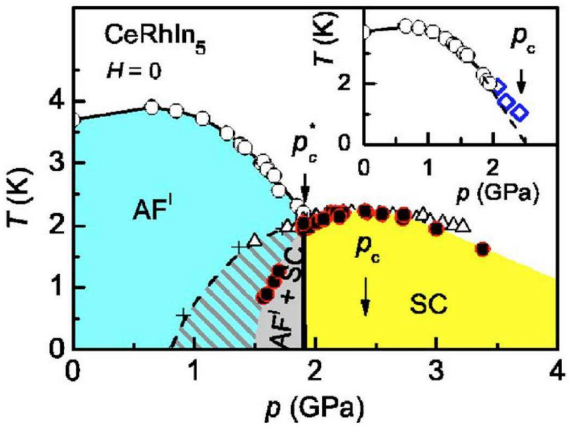


Figure 3.8 *Phase diagram of $CeRhIn_5$ under pressure [108]. The round points (•) are the transition measured by specific heat, the triangles (△) by susceptibility and the crosses (+) by resistivity. In the magnetic phase, the superconducting temperature differs according to the probe, whereas it is similar in the non magnetic phase.*

suppressed by applying pressure with coexistence of superconductivity in a pressure range [76] (see figure 3.8). In the state where antiferromagnetism and superconductivity coexist, there is a large difference between the resistive and the bulk transition [108]. This difference decreases when the pressure increases and is almost zero in the paramagnetic state. As it is observed in very high quality single crystals (RRR≈ 1000), structural defaults and inhomogeneities are believed not to be responsible for this difference. This effect is believed to be due to intrinsic inhomogeneities of the superconducting state [159] in the antiferromagnetic state, only visible by resistivity and not by thermodynamic measurements. These intrinsic inhomogeneities no longer exist in the paramagnetic phase, leading to the same critical temperature for both probes.

As a Lifshitz transition is claimed to happen at 11T [127] in UCoGe when $\mathbf{H}//\mathbf{b}$, a similar effect may be possible to explain the difference between T^{ρ}_{sc} and T^{κ}_{sc}. To verify this hypothesis, it is necessary to perform the experiment at higher fields. This is planned to be done in the 15T dilution fridge.

An interesting point is the difference of the slope of the critical field measured by thermal conductivity and by resistivity. The initial slope of the critical field is proportional to the critical temperature divided by the square of the Fermi velocity of the quasiparticles:

$$\frac{dH_{c_2}}{dT}\Big|_{T=T_{sc}} \propto \frac{T_{sc}}{v_F^2} \tag{3.1}$$

If this relation is correct in the case of UCoGe, the Fermi velocity is overestimated with the resistivity measurements. UCoGe has small amount of charge carriers, so it was expected to have a small Fermi velocity, which explains the very large slope (almost vertical for the bulk transition) of the critical field close to T_{sc}.

The very high value of $H_{c_2}(0K)$ points out that in this field direction, **H//b**, as well as when **H//a**, the critical field is dominated by the orbital limitation ($H_{c_2}^{orb} \propto 1/v_F^2$), as the Pauli limitation is estimated at $H_P \approx$1T. This is consistent with the triplet pairing of the Cooper pairs. The small Fermi velocity v_F can explain the huge $H_{c_2}^b(0)$ (compared to the small T_{sc}), but not the S-shape.

This feature seems very similar to the re-entrant phase in the other ferromagnetic superconductor URhGe [118]: the alignment of the spins with the magnetic field (**H//b**) leads to a field induced superconducting phase. Shubnikov-de Haas oscillations reveal that a topological transition may happen at the re-entrant field $H_c \approx$10T [239]. Thermopower measurements (Seebeck effect) showed that a topological transition could happen in UCoGe at the critical field $H_c \approx$11T at the maximum of T_{sc} in the S-shape [127], but without the reorientation of the spins with the field, which seems to happen only at very high fields ($H \approx$50T) [106].

The critical field along the **a**-axis has not been measured by thermal conductivity, but it will be very interesting to do it. By resistivity, the slope of the critical field is the same near T_{sc} with **H//a** and **H//b** [12]. An open question is to know if the bulk critical field has the same slope, and if so, the critical field along the **a**-axis would show a very exotic behavior at higher fields.

3.2.3 H//c

The much lower critical field ($H_{c_2}^c(0) \approx$1T) and the insensitivity of the physical properties to a slight misalignment of the field with the crystallographic axis make it was easier to measure H_{c_2} along **c** than along the **b**-axis. This means that it was not necessary to use the piezo-rotator and the goniometers, the alignment at room temperature by eyes is enough. The goal here was to probe the upward curvature of the critical field seen by resistivity [86].

The figure 3.9 displays the thermal conductivity measurements of samples S_{16}^c (on the left) and S_{150}^b (on the right) at low temperature with **H//c**. The arrows show the superconducting temperatures. In inset is the corresponding resistivity measurements. With the increase of the magnetic field, the superconducting transition becomes more difficult to determine as it happens at low temperature, especially for sample S_{150}^b.

The critical field is shown figure 3.10. The blue lines are the superconducting temperatures measured by thermal conductivity and the red lines by resistivity. The yellow hatched area is the width of the resistive transition, determined the same way as for **H//b**. The first observation that can be done is the difference of $H_{c_2}^c(0)$ for both sample: by resistivity and by thermal conductivity, the critical field is higher in sample S_{150}^b. This is maybe an effect of the quality. Such a change in the critical field has already been seen in URhGe: the critical field and the superconducting temperature increase with the RRR [69]. But a striking difference

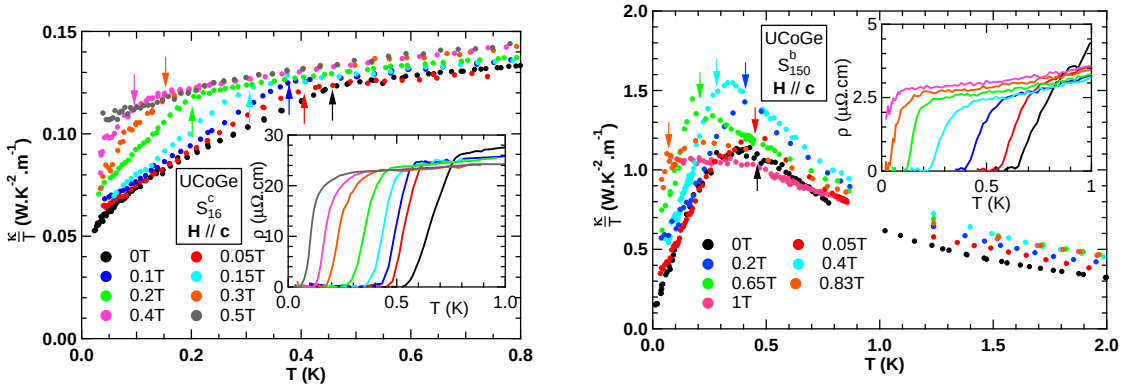


Figure 3.9 *Thermal conductivity and resistivity measurements (in inset) at low temperature of samples S^c_{16} (on the left) and S^b_{150} (on the right) with **H//c**. The arrows show to the superconducting temperature.*

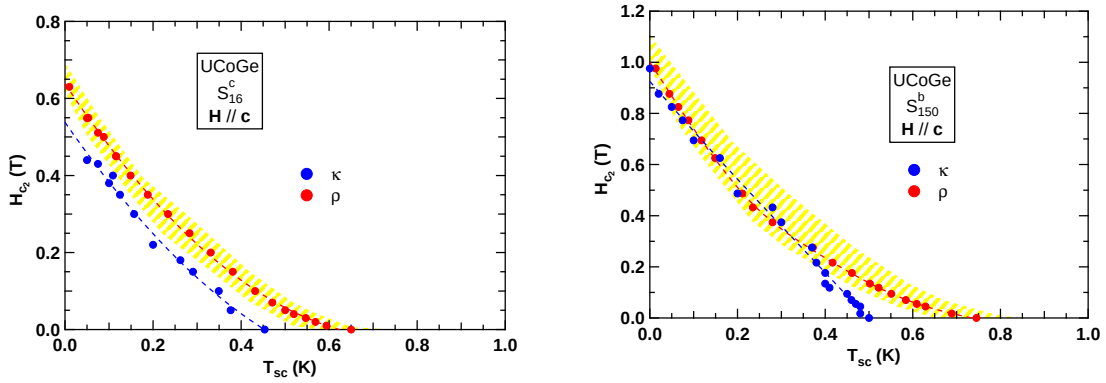


Figure 3.10 *Critical field of samples S^c_{16} (on the left) and S^b_{150} (on the right) with **H//c**. In blue is the critical field measured by thermal conductivity and in red by resistivity (taken in the middle of the transition). The yellow hatched area corresponds to the width of the resistive transition (see text). The dotted lines are guides to the eyes.*

in UCoGe is that $H^{c,\kappa}_{c2}(0)$ changes with the RRR, but not T^{κ}_{sc} (observed at least at zero field in the five samples)! In my measurements, only sample S^c_{16} has this low critical field, the others having similar ones ($H^{c,\rho}_{c2}(0) \approx$1T).

The critical field has an upward curvature with both probes. The measurement of $H^{c,\kappa}_{c2}$ of sample S^b_{150} is not precise enough to determine if it has an upward curvature or a linear behavior. These measurements show that this second exotic feature of the critical field is an intrinsic property. At low field, the difference between T^{ρ}_{sc} and T^{κ}_{sc} is large but it decreases with the field. For fields above $H^{c,\kappa}_{c2}/5$, the difference does not change anymore: this is the signature of filamentary superconductivity which is easily suppressed under magnetic field. This may have the same origin as for the configuration **H//b**, the effects of spread defaults which can change locally the system (homogeneity, hydrostatic pressure...). The upward curvature down to the lowest temperature is unusual: the critical field should saturate at low temperature.

Contrary to URhGe, where completely "broken symmetry" *p*-wave polar state could de-

scribe, on early (dirty) samples, the critical field in the three crystallographic directions (except the re-entrant phase) [184, 69], the critical field of UCoGe cannot be reproduced by the same theory, as it does not predict an upward curvature down to 0K, nor the S-shape. Different theories calculate the critical field along the **a** and the **b**-axis [138, 105], but always fail to give a good description of $H^c_{c_2}$. The upward curvature of $H^a_{c_2}$ and $H^b_{c_2}$ at low field may be described by a crossover between two phases in a multiband superconductor [140, 105].

Here is now an attempt to explain the upward curvature with the compromise between pair-breaking effects due to the magnetic fluctuations and the regular Pauli and/or orbital limitations. As it has been seen in UCoGe, anisotropic magnetic fluctuations, first revealed by NMR [153, 152] then by neutron scattering [205], are present, predominantly along the easy magnetization axis (**c**-axis), and appear below 80K, far above the Curie temperature. The study of the thermal conductivity in the normal phase (section 4.2) has also shown that the thermal conductivity is dominated by these fluctuations. The NMR studies have shown that the fluctuations seem to be responsible for superconductivity [74], but some magnetic fluctuations (by their wave vectors or their frequencies) can also be a mechanism for pair-breaking effects in the superconducting state [135].

In UCoGe, the Ising character of the magnetic fluctuations has been proved, and it was shown that when the magnetic field is applied along the **c**-axis, the intensity of magnetic fluctuations is decreasing, while they are almost field independent when the field is applied along the **a** or **b** direction [74]. It will be shown in section 4.2 that the intensity of the magnetic fluctuations decreases with the field up to 4T before saturating, which means that at $H = H^c_{c_2}(0)$, pair-breaking effects are still decreasing. As a result, the increase of the magnetic field reduces pair-breaking effects, so to an effective increase of T_{sc}. This effect, in combination with the orbital limitation, can be responsible for the upward curvature. A schematic sketch is shown figure 3.11: the upper critical field without pair-breaking effects is represented by the black straight line. If pair-breaking effects are added, and if they are not sensitive to the magnetic field, the upper critical field shifts to lower critical temperature and field (black dashed line). If now, the pair-breaking effects are reduced with the increase of the magnetic field, the upper critical field will get closer to the situation without pair-breaking effects, and can thus lead to an upward critical field (red straight line).

However, this explanation does not take into account the fact that the magnetic field, when $\mathbf{H}//\mathbf{c}$, seems to decrease the coupling constant of the Cooper pair [210]. This may be responsible for the large difference between the slope of $H^a_{c_2}$ and of $H^c_{c_2}$ close to T_{sc}, but not the upward curvature.

3.2.4 Critical Field of Sample S^c_{47}

This last subsection of this part concerns the measurements done on sample S^c_{47}. This sample shows clear and sharp transitions (the ferromagnetic and the superconducting ones), and it has been decided to perform accurate resistivity measurements in order to obtain a precise critical field, and special efforts have been done at very low magnetic fields. The measurements have been done with a zero field cooled magnet to avoid parasite residual field, and the value of the field has been determined precisely with a Hall sensor.

The measurements with $\mathbf{H}//\mathbf{c}$ are shown figure 3.12, with on the right, the measurements at very low fields. T_{Curie} increases with the field and the anomaly on the resistivity disappears rapidly with the field (it becomes invisible above 0.2T). In inset is shown the superconducting

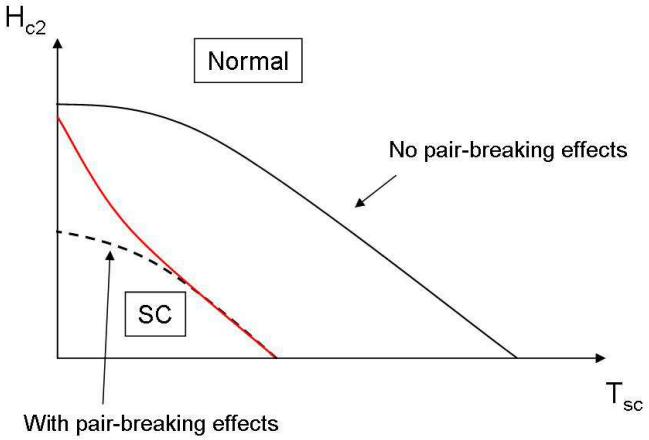


Figure 3.11 *Schematic sketch of the effect of the field dependent pair-breaking effects on the upper critical field. The upper critical field without and with (constant) pair-breaking effects is represented by the black straight line and the black dashed line respectively. The situation where the pair-breaking effects are reduced with the field is shown through the red straight line.*

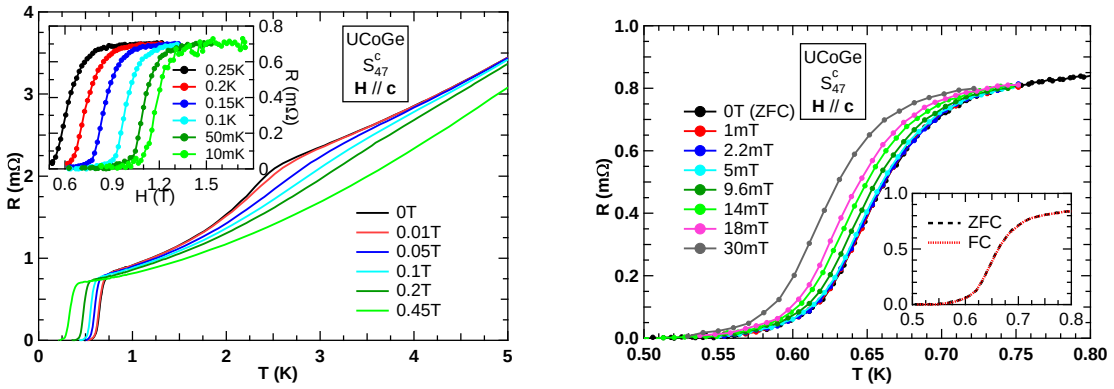


Figure 3.12 *Resitivity measurements of sample S^c_{47} with **H//c**. On the left, the measurements at high fields. In inset: the field dependence at low temperature. The right figure shows the measurements at very low fields. In inset, the superconducting transition at zero field with zero field cooled (ZFC) magnet, i.e. the sample is not polarized and ferromagnetic domains are still present, and with a polarized sample (field cooled (FC) magnet).*

transition by field sweep at low temperature. The figure on the right shows the very low magnetic field dependence of the resistivity. Up to 5mT, there is almost no change in the superconducting temperature, and then, T_{sc} decreases faster with the field. This effect is believed to be the alignment of the ferromagnetic domains with the magnetic field. At zero field, the resistive transition has been measured twice: the first time with the zero field cooled magnet, that is to say at strictly zero field with a non polarized sample, and at zero field with a polarized sample. In this case, a sufficiently large magnetic field was applied to have only one ferromagnetic domain, and the field of 0T has been obtained again with the help of the Hall sensor (called field cooled (FC) measurements). The difference of the resistivity between these two measurements at zero field is shown in the inset of figure 3.12: the resistive

transition at zero field is independent of the polarization of the sample as both transitions (the ZFC and FC measurements) match exactly.

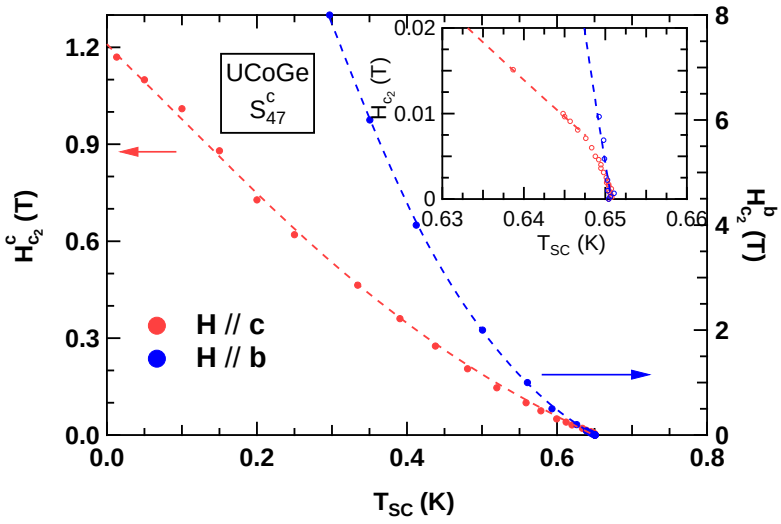


Figure 3.13 *Critical field of sample S^c_{47} measured by resistivity with **H//c** and **H//b**. In inset: zoom of the very low field part. A small step is visible in the critical field at low field when **H//c** whereas it is strictly linear when **H//b**. The dashed lines are guides to the eyes.*

The figure 3.13 displays the critical field with **H//c** and **H//b**. The S-shape of $H^b_{c_2}$ is not visible here, but $H^c_{c_2}$ exhibits the upward curvature. The new point here is the very low field part, shown in the inset of the figure 3.13: $H^c_{c_2}$ is first little sensitive to the magnetic field up to 10mT. The slope close to T_{sc} is similar in $H^c_{c_2}$ and in $H^b_{c_2}$. This very low field effect is due to the re-orientation of the ferromagnetic domains with the magnetic field: first, the magnetic field in the material is screened by the rearrangement of the domains. The Cooper pairs do not see the magnetic field. Once the material becomes single domain, the electrons see the magnetic field normally and the critical field decreases faster. This particular field corresponds to the magnetic field induced by the spontaneous magnetization, which is found to be approximately 8mT. This value is very close to 9.5mT, the value found by magnetization measurements [40, 161]. The magnetic field penetrates through the sample at very low field as it is suspected that UCoGe is in spontaneous vortex state at zero field (absence of Meissner state) [40, 152, 161], or with very small H_{c_1} [161]. The vertical slope of H_{c_2} at very low fields has already been seen in URhGe [69], where $H^c_{c_2}$ has a vertical slope close to T_{sc} up to 50mT, the higher field is due to its higher magnetization.

Some works have already been done on the very low fields part of $H^c_{c_2}$ [227], which have claimed that T_{sc} first increases with the magnetic field up to 2mT. They claimed that the zero field state in UCoGe is governed by spin fluctuations and the ferromagnetism appears at 2mT. In bad quality samples of UCoGe, it is easier to have superconductivity than ferromagnetism, and the effect seen is certainly an artifact due to the fact that there is no clear signature of ferromagnetism in their measurements.

3.2.5 Conclusion

The measurement of the upper critical field by thermal conductivity has confirmed the intrinsic character of the S-shape when the field is applied along the **b**-axis, and the upward curvature when **H**//**c**. Indeed, the thermal conductivity is a bulk probe, and both effects have been seen in two different samples with very different qualities (in term of RRR).

A large difference between the superconducting temperature measured by resistivity and thermal conductivity has been observed in both field configurations, and is reduced with the increase of the applied magnetic field. This indicates that the superconductivity seen by resistivity is partly induced by inhomogeneities and defaults, which is therefore "weak", and is easily suppressed by a magnetic field. This leads to a large difference in the slope of the upper critical field close to T_{sc}, particularly when **H**//**b**. The slope of $H^b_{c_2}(T \to T_{sc})$ measured by thermal conductivity is almost vertical, indicating that the possible triplet-pairing of the Cooper pairs, with $H^b_{c_2}(T \to T_{sc})$ dominated by orbital limitations. Due to this almost vertical slope when **H**//**b**, the measurements of H_{c_2} in the configuration **H**//**a** are important, as $H^a_{c_2}(T \to T_{sc}) \approx H^b_{c_2}(T \to T_{sc})$ when measured by resistivity.

At very low field (H<10mT), the upper critical field (measured by resistivity) displays an almost vertical slope when **H**//**c**, and is believed to correspond to the alignment of the ferromagnetic domains with the field, as it has already been observed in URhGe.

3.3 XMCD

X-ray Magnetic Circular Dichroism (XMCD) experiments have been performed in UCoGe with the field along the **b** and the **c**-axis, at 3K and up to 17T. We have studied extensively the configuration **H**//**c** compared to the other configuration. The reason is that it is the simplest configuration for the first study, and the easiest one to extract information on the ordered moment by extrapolation to zero field. We also wanted to check the existence of a ferrimagnetic transition, claimed to occur at 9T [170, 202]. XMCD experiment is the perfect tool to detect this kind of transition.

The first part of this section describes the principle of the measurements, with the definition of the sum rules to enable to obtain the spin and orbital moments. The next part shows the results, first in the case **H**//**c** then **H**//**b**.

3.3.1 Principle

XMCD technique enables to do a microscopic study of the magnetism of a material by using X-rays. The principle has been approached for the first time in 1926 by W. Kartschagin and E. Tschetwerikowa [100] and the first calculations came in 1975 [45]. The first experimental evidence was given in 1987 by G. Schutz *et al.* [187].

The principle of XMCD measurements is to excite the magnetic states of a compound by the absorption of circularly polarized X-rays. The states do not have the same absorption rate according to the helicity (parallel or antiparallel) of the X-rays compared to the sample magnetization. The measured quantity is so:

$$\Delta\mu = \mu^+ - \mu^- \tag{3.2}$$

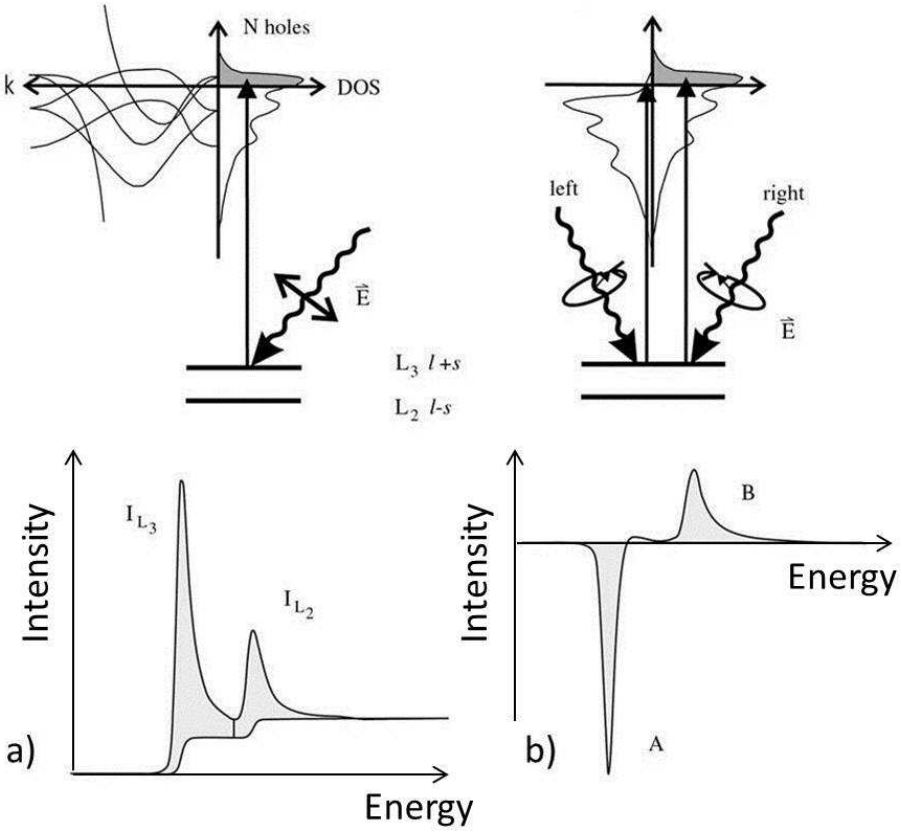


Figure 3.14 *Sketch of the principle of XMCD measurements for the L-edge (corresponding to the d-electrons). (a) The excitation of the level (top) gives the X-ray absorption near edge structure (XANES) (on the bottom). (b) With the use of circularly polarized X-rays, two XANES are obtained, depending on the unoccupied states of each spin (up/down) and the difference of the spectrum is the XMCD signal (on the bottom). Sum rules with the areas A and B give the spin moment and the orbital moment (see text). From [203].*

with $\mu^{+/-}$ the absorption cross-sections for the circularly polarized X-rays with helicity parallel (+) and antiparallel (-) to the sample magnetization. As a result, it probes the empty states with spin up/down and if the energy of the X-rays is tunable, it is possible to selectively probe the state of each atom and each shell in the material by choosing the energy corresponding to an absorption edge of this element. The great advantage of this technique is the possibility to measure the spin moment and the orbital moment on a precise element of the crystal. A sketch of the principle and the expected signals for L-edge absorption (corresponding to the transition between the $2p$ state to $3d$ state) are shown figure 3.14. Each polarization gives the X-ray absorption near edge structure (XANES) signal of the unoccupied state, and the difference between the two spectra is the XMCD signal.

To calculate the spin moment and the orbital moment of each atomic shell, sum rules have been established [217, 30]. The areas of XANES and XMCD signals are needed, $I_{L_{2,3}}$ is the area of the XANES signal corresponding to the $L_{2,3}$ edges. The L_2-edge corresponds to the transition $2p_{1/2} \rightarrow 3d_{3/2}$, the L_3-edge to $2p_{3/2} \rightarrow 3d_{5/2}$. We define $\Delta I_{L_{2,3}} = I^+_{L_{2,3}} - I^-_{L_{2,3}}$ ($\Delta I_{L_3} \equiv A$ and $\Delta I_{L_3} \equiv B$, A and B the areas shown figure 3.14). The angular moment

($\mu_L = - < L_z > \mu_B$) and the spin moment ($\mu_s = -2 < S_z > \mu_B$) are given by:

$$< L_z >= \frac{4}{3} n_h \frac{(\Delta I_{L_3} + \Delta I_{L_2})}{I_{L_3} + I_{L_2}} \tag{3.3}$$

$$2 < S_z > +7 < T_z >= 2n_h \frac{(\Delta I_{L_3} - 2\Delta I_{L_2})}{I_{L_3} + I_{L_2}} \tag{3.4}$$

n_h is the number of holes in the $3d$ shell and $< T_z >$ is the intra-atomic magnetic dipole moment, which measures the anisotropy of the spin distribution due to crystal field interaction or/and spin-orbit coupling. Its value cannot be determined directly, but for L-edge absorption in the $3d$ transition metals, it is commonly admitted that $< T_z > \ll < S_z >$.

The M_4 (M_5) edge corresponds to a transition from $3d_{3/2}$ ($3d_{5/2}$) states to $5f$-states. The M_4 absorption signal is proportional to the number of the $5f_{5/2}$ holes whereas the M_5 one depends mainly on the number of the $5f_{7/2}$ holes. Thus, a change in the ratio between the M_4 and the M_5 signal (characterized with the branching ratio, see below) indicates a change of the population within the $5f$-states, and can be interpreted as a shift of the Fermi energy.

As for L-edge, the areas of the XANES and XMCD of the M-edges are needed to extract the orbital and spin moments and are defined the same way. For M-edge absorption, the sum rules are:

$$< L_z >= 2n_h \frac{\Delta I_{M_5} + \Delta I_{M_4}}{I_{M_5} + I_{M_4}} \tag{3.5}$$

$$2 < S_z^{eff} >= 2 < S_z > +6 < T_z >= n_h \frac{2\Delta I_{M_5} - 3\Delta I_{M_4}}{I_{M_5} + I_{M_4}} \tag{3.6}$$

n_h is the number of holes in the $5f$ shell, $I_{M_{4,5}}$ is the integral of the XANES signal and $\Delta I_{M_{4,5}}$ the integral of the XMCD signal at the $M_{4,5}$-edge. Contrary to the L-edge, the $< T_z >$ term is not negligible compared to $< S_z >$. It is however possible to estimate $< T_z >$ with the combination of several experiments, but it is usually estimated from theoretical considerations. For free U^{3+} and U^{4+} ions, calculations of the $< L_z >$, $< S_z >$ and $< T_z >$ terms are given in table 3.2 [226] for different coupling schemes (CS) (LS coupling, Intermediate Coupling (IC) or jj coupling).

The coupling schemes are theoretical treatment of atomic spectroscopy, depending on the strength of the spin-orbit coupling compared to the electronic Coulomb repulsion: in the case of a weak spin-orbit interactions (compared to the Coulomb repulsion), the L-S coupling (or Russell-Saunders coupling, the easiest case) is valid. In this case, the sum of the electronic spin s gives the total spin S. Similarly, the total orbital momentum L comes from the sum of the orbital momentum l of the electrons, and the angular momentum is J=L+S. For a strong spin-orbit interaction (jj coupling), the angular momentum is j=l+s and the total angular momentum J is the sum of the electronic angular momentum j. The Intermediate Coupling is between these two limit cases (see e.g. [67]).

The orbital moment is given by $\mu_L = - < L_z > \mu_B$, the spin moment by $\mu_S = -2 < S_z > \mu_B$ and the magnetic dipole moment by $\mu_{md} = -6 < T_z > \mu_B$.

The branching ratio corresponds to the relative intensity of the M_5-edge, and is experimentally determined as:

$$B = \frac{I_{M_5}}{I_{M_5} + I_{M_4}} \tag{3.7}$$

CS	n_e^{5f}	$< L_z >$	$< S_z >$	$< T_z >$	μ_{md}/μ_S
LS	2 (U^{4+})	-4.8	0.8	0.462	1.73
	3 (U^{3+})	-5.72	1.227	0.172	0.42
IC	2 (U^{4+})	-4.698	0.698	0.809	3.48
	3 (U^{3+})	-5.571	1.070	0.659	1.85
jj	2 (U^{4+})	-4.53	0.5714	0.9143	4.80
	3 (U^{3+})	-5.16	0.6428	1.0286	4.80

Table 3.2 *Calculations of $< L_z >$, $< S_z >$ and $< T_z >$ for free uranium ion, depending on the coupling schemes, from [226].*

CS	n_e^{5f}	$< W^{110} >$	$\frac{<W^{110}>}{n_h}$	B
LS	2 (U^{4+})	-2	-1/6	0.667
	3 (U^{3+})	-7/3	-0.2121	0.685
IC	2 (U^{4+})	-2.588	-0.2157	0.686
	3 (U^{3+})	-3.562	-0.3238	0.729
jj	2 (U^{4+})	-8/3	-0.2222	0.689
	3 (U^{3+})	-4	-0.3636	0.745

Table 3.3 *Calculations of the spin-orbit expectation value $< W^{110} >$, $< W^{110} > /n_h$ and the branching ration B depending on the number of f-electrons and the coupling scheme.*

It measures the spin-orbit coupling, through the relative occupation of the $f_{5/2}$ and $f_{7/2}$ states. As there is a connection between the spin-orbit expectation value and the degree of localization of the $5f$-electrons, its comparison with the theoretical values gives information about the range of $5f$ occupation number, in case this number is not precisely known.

The expection value of the angular part of the spin-orbit interaction is given by [225]:

$$< l.s >= \frac{3}{2} < W^{110} > \tag{3.8}$$

$$\frac{2 < l.s >}{3n_h} = -\frac{5}{2}(B - \frac{3}{5}) - \Delta \tag{3.9}$$

with $< W^{110} >$ the expectation value for the angular part of the $5f$ spin-orbit electron operator, n_h the number of holes in the $5f$ shell and Δ a quantity depending on the electron configuration (expected to be small for $M_{4,5}$-edges [237]). Calculations in the intermediate coupling (IC) scheme gives the theoretical values of $\Delta = -0.014$ and $\Delta = -0.010$ for the $5f^3(U^{3+})$ and $5f^2(U^{4+})$ configurations respectively [225].

The spin-orbit expectation value can be expressed in the number of electrons of the $5f_{5/2}$ level ($n_{5/2}$) and of the $5f_{7/2}$ level ($n_{7/2}$):

$$< W^{110} >= n_{7/2} - \frac{4}{3}n_{5/2} \tag{3.10}$$

with $n = n_{5/2} + n_{7/2}$ the number of $5f$ electrons.

The values of $< W^{110} >$ and of the branching ratio B have been calculated for different coupling schemes for the $5f^3(U^{3+})$ and $5f^2(U^{4+})$ configurations and are shown table 3.3.

3.3.2 Results

H//c

XMCD measurements have been performed on the U M-edges (transition from the $3d \rightarrow 5f$ states) and on the K-edges (transition from the $1s \rightarrow 4p$ states) of the cobalt and the germanium. The most interesting edge for the cobalt would have been the L-edges ($2p \rightarrow 3d$), but not accessible as it is outside the energy range available at ID12. To avoid artifacts, each signal is measured at positive and negative fields.

XANES and XMCD signals corresponding to the U M_4- and M_5-edges of UCoGe in the field configuration **H//c** at 3K are shown figure 3.15. As a reminder, the XANES signal corresponds to the measured signal and the XMCD is the difference of the XANES signal with the two different polarizations of the X-ray. The shape of the XMCD signal is without apparent structure. The M_5 signal is known to be sensitive to subtle change in the electronic structure and therefore hybridization effects, crystal field, exchange interaction and/or on-site Coulomb interactions can result in change of the M_5 dichroic shape. The M_5-edge has a positive as well as a negative lobe and the M_4-edge is a negative peak.

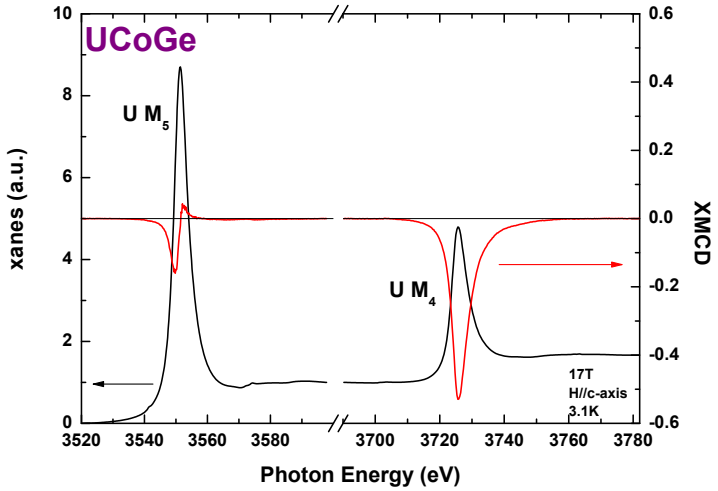


Figure 3.15 *XANES and XMCD of the U M_4- and M_5-edges at 3K and 17T with* ***H//c****.*

The XANES and XMCD signals of the K-edge of the cobalt and the germanium at 3K, 17T are shown figure 3.16. The XMCD signal is very difficult to interpret quantitavely for two reasons. The first is that a large part of the signal is caused by the large spin-orbit coupling with the uranium atom (the large positive and negative peaks at 7710eV for the cobalt and the negative peak at 11110eV for the germanium). Note that the positive peak is absent in hcp Co. This indicates that the spin-orbit interaction of uranium plays a significant role in the shape of the dichroic signal at the Co K-edge. The other reason is that above approximately 7720eV for the Co and 11140eV for the Ge, the signal is not anymore XMCD but magnetic EXAFS (Extended X-ray Absorption Fine Structure, related to the local surrounding of the Co/Ge atoms), which explains why the XMCD signal is not flat above the maximum peak. Furthermore, the XMCD signal of the K-edge measures only the orbital moment of the $4p$

electrons.

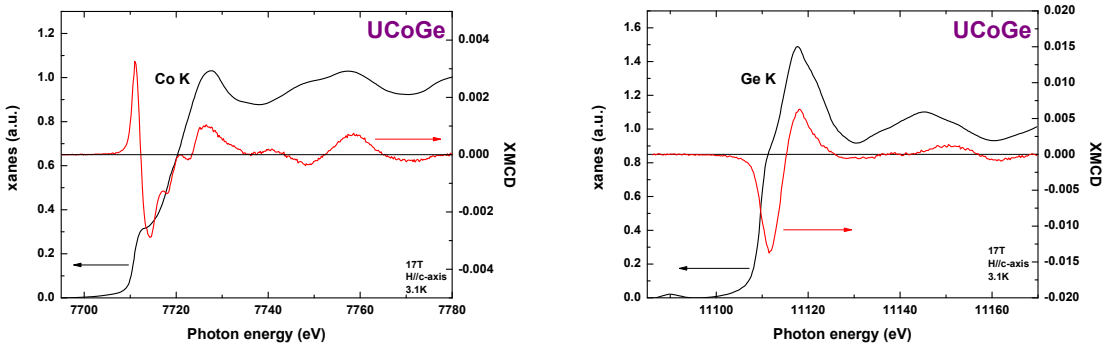


Figure 3.16 *XANES and XMCD of the K-edges of the cobalt (left panel) and of the germanium (right panel) at 3K and 17T with* ***H//c****.*

With XMCD measurements, the magnetization of each edge is available, by measuring the amplitude of the maximum of the signal as function of the applied field. The figure 3.17 shows the XMCD intensity of the U M_4-edge as a function of the magnetic field. The macroscopic magnetization, from [106], is also plotted (right axis). The zoom at low field is shown in inset. The comparison with the macroscopic magnetization enables to determine the temperature of the sample, which is estimated to be around 3K. The similar shape with the macroscopic measurements indicates that the macroscopic magnetization and the $5f$ uranium moment have the same field dependence.

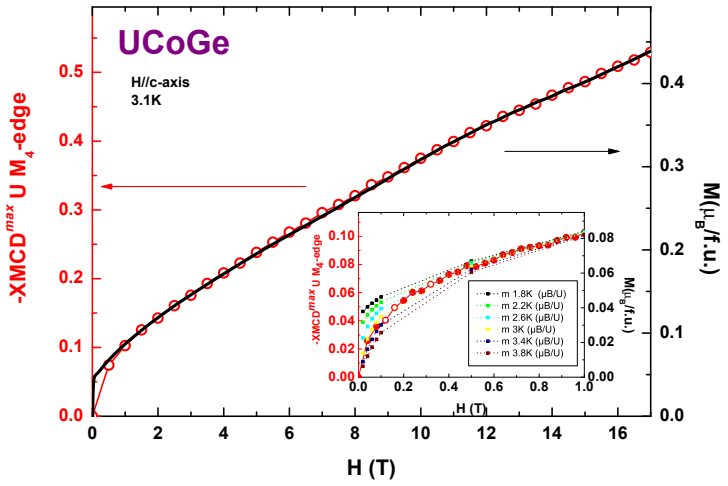


Figure 3.17 *XMCD of the U M_4-edge at 3K between 0T and 17T,* ***H//c****, with the comparison with the macroscopic magnetization (right axis). In inset is shown the low field measurements, which enables to determine the temperature of the sample.*

The magnetization of the cobalt and of the germanium are seen figure 3.18, where it is compared with the magnetization of the U M_4-edge.

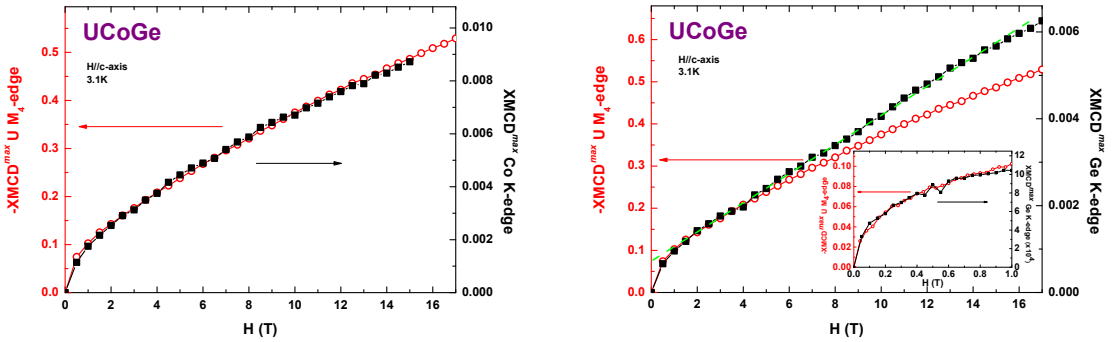


Figure 3.18 *Magnetization of the K-edge of the cobalt (left panel) and the germanium (right panel) at 3K between 0T and 17T,* ***H//c****, with the comparison with the U M_4 magnetization (right axis). In inset is shown the low field magnetization of the cobalt.*

Whereas the moment on the cobalt seems induced by the moment of the uranium, and is part of the total magnetization (due to the similar shape), the magnetization of the germanium is different. At low field, the magnetization on the germanium site is the same as on the uranium site, but at higher field, it is linear. This indicates that the induced moment on the germanium site is not due to the magnetization of the uranium above 2T, but only to the regular Zeeman effect, leading to a linear polarization. The coupling between germanium and uranium atoms may be responsible only for the low field part, and is weak at higher fields, and the anomalous mechanism responsible for the curvature of the magnetization does not affect the germanium magnetization. The fact that this effect is seen on the Ge magnetization, but not on the Co one may come from the stronger hybridization between U $5f$ and Co $3d$ electrons than between U $5f$ and Ge $4p$ electrons.

The comparison of the XMCD measurements measured at 1T and at 17T are shown figure 3.19. For both edges, the XMCD signal at 17T has been increased by a factor 5.2 (see insets), which is just an effect of the increase of the magnetization with the field.

The XANES signal is the same at 1T and 17T for the U M_4-edge and the U M_5-edge. The little mismatch in the U M_5-edge between 1T and 17T is due the fact that the position of the beam changes a little bit with the magnetic field, which means that we are not looking exactly at the same spot on the sample when the field is changing. This has been confirmed by further experiments having the opposite effect.

H//b

The XANES and XMCD signals of the U M_4- and M_5-edges in the configuration **H//b** are shown on the left panel of figure 3.20. The signal has a similar shape as the one measured with the configuration **H//c**.

The maximum of the XMCD signal of the U M_4-edge is shown in the right side of the figure 3.20. In that case too, the moment carried by the uranium can explain, at least partly, the macroscopic magnetization (from [106]). Contrary to the configuration **H//c**, the magnetization has the regular linear behavior with the field, only polarization effect occurs due to the anisotropy of the magnetization axis in UCoGe (the **b**-axis is a hard axis).

The XMCD signal increases regularly with the magnetic field, without any anomalies. At

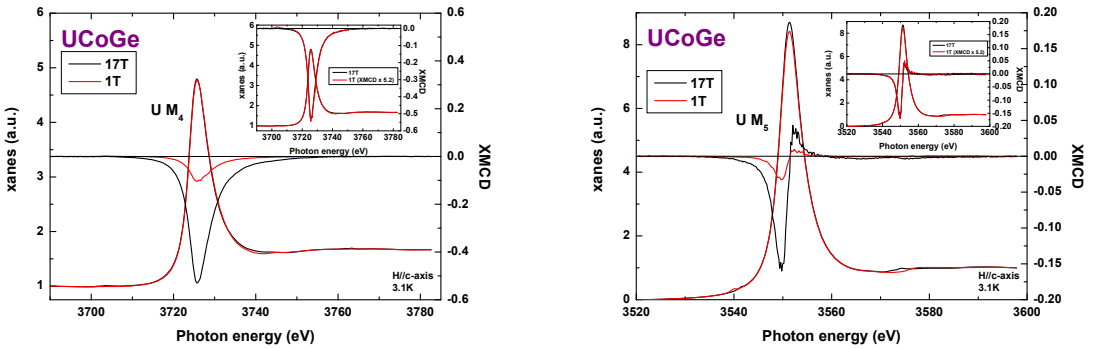


Figure 3.19 *Comparison of XANES and XMCD of the uranium between 1T and 17T for the M_4-edge (left panel) and the M_5-edge (right panel) with **H**//**c**. By multiplying the XMCD at 1T by a factor 5.2, the signal matches completely the signal at 17T (in inset).*

11T, the superconducting temperature displays a maximum in the critical field [12], with a possible Lifshitz transition [127]. The absence of any anomalies may be caused by the high temperature measurements, or a small misalignment between the field and the **b**-axis (it is not possible to align precisely the **b**-axis to the magnetic field).

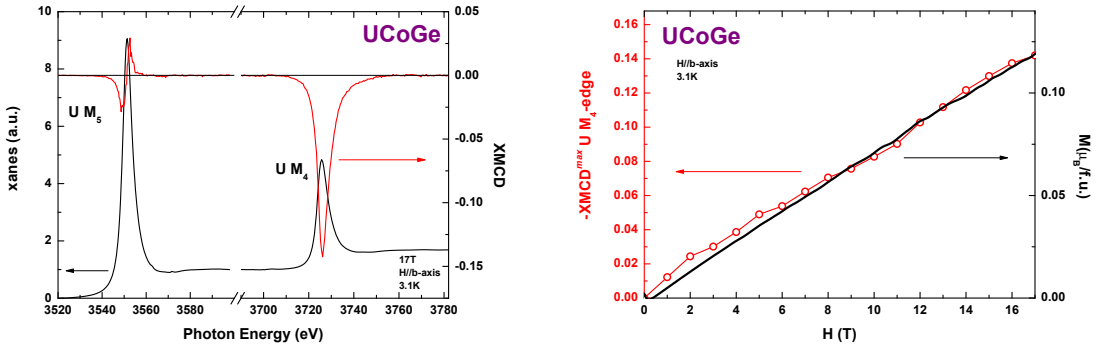


Figure 3.20 *Left panel: the XANES and XMCD measurements of the U M-edges at 3K, 17T, with **H**//**b**. Right panel: magnetization of the U M_4-edge at 3K between 0T and 17T, with the comparison with the macroscopic magnetization (right axis).*

3.3.3 Discussion

Comparison Between the 1T and 17T Measurements, H//c

The table 3.4 shows the branching ratio (parameter B) with the population of the 7/2 and the 5/2 levels depending on the the uranium configuration (U^{4+} or U^{3+}). Its value, $B = 0.700 \pm 0.002$ at 17T //**c**, is in-between those calculated for U^{4+} and U^{3+} in the IC scheme (respectively 0.686 and 0.729, see table 3.3). XMCD measurements confirm that U atoms are rather in U^{3+} configuration than in U^{4+} configuration, as the latter leads to a negative value of $n_{7/2}$, which is not physical. This is in agreement with core-level photoemission spectroscopy

B ±0.002	$\frac{2}{3}\frac{<l.s>}{n_h^{5f}} - \Delta$	n_e^{5f}	Δ	$n_{5/2}$	$n_{7/2}$
0.700	-0.25	2 (U^{4+})	-0.014	2.21	-0.21
		3 (U^{3+})	-0.010	2.51	0.49

Table 3.4 *Number of electrons in the 5/2 and 7/2 levels depending on the configuration of the uranium (U^{4+} or U^{3+}) with the branching ratio and other parameters.*

CS	n_e^{5f}	$\mu_L^U(5f)$ $(\mu_B/atom)$	$\mu_S^U(5f)$ $(\mu_B/atom)$	$\mu_{tot}^U(5f)$ $(\mu_B/atom)$	$\frac{\mu_L^U(5f)}{\mu_S^U(5f)}$
LS	2 (U^{4+})	0.749	-0.334	0.415	-2.24
	3 (U^{3+})	0.685	-0.588	0.097	-1.16
IC	2 (U^{4+})	0.749	-0.203	0.545	-3.68
	3 (U^{3+})	0.685	-0.293	0.392	-2.34
jj	2 (U^{4+})	0.749	-0.157	0.592	-4.77
	3 (U^{3+})	0.685	-0.144	0.541	-4.76

Table 3.5 *Values of the orbital and spin moments depending on the coupling schemes (CS) and the number of f-electrons at 17T with **H**//**c**. The yellow line shows the configuration choosen. Note that $\mu_L^U(5f)$ does not depend on the CS, and is better estimated than $\mu_S^U(5f)$.*

measurements [57], which suggest that n_e^{5f} is close but lower than 3, and by band structure calculations ($n_e^{5f} = 2.84$) [180].

To evaluate the spin component $< S_z >$, the term $< T_z >$ is needed. As this is not possible to measure directly this term, calculations are needed to estimate it. The different values of the ratio $R_T = \mu_{md}/\mu_S$ are shown in table 3.2.

The value of the orbital moment and the spin moment calculated at 17T with **H**//**c**, depending on the coupling schemes and the number of f-electrons is shown table 3.5. In yellow is shown the chosen configuration. The IC scheme gives the best agreement with the macroscopic measurements[2]. The total moment calculated with XMCD, $\mu_{tot}^U = 0.392\mu_B$, is lower to the one measured by magnetization, $m_{tot} = 0.44\mu_B$ [106]. The missing moment comes from the fact that the paramagnetism of the cobalt and the conduction electrons are not included. The paramagnetism of the cobalt is not taken into account (it is expected that the magnetization of the germanium is very small), and, as the measurements are done in the K-edge, it is difficult to extract the magnetization on this site. Concerning the conduction electrons, the main contribution should come from the 6d-band of uranium, and they have been measured to be approximated by 10% of the total magnetization[3], and opposite to it ($m_{cond} \approx -0.1 m_{tot}$), and can thus only "increase" the missing moment.

The ratio $\mu_L^U/\mu_S^U = -2.34$ is slightly below that for the free U^{3+} ions value ($\mu_L^U/\mu_S^U = -2.6$), but deviates strongly from U^{4+} ions value ($\mu_L^U/\mu_S^U = -3.36$). The smaller value is caused by the reduction of the orbital moment due to the hybridization with the other atoms.

The values at 1T are given in the table 3.6, with the IC coupling and in the U^{3+} configuration. As for the 17T measurements, the total moment, $\mu_{5f}^U = 0.075\mu_B$, is a bit lower than the macroscopic one, $m_{tot} = 0.08\mu_B$ [106]. The ratio $\mu_L^U/\mu_S^U = -2.29$ is very close to

[2] This is consistent with the fact that, usually, the IC scheme describes the best actinide-based systems.

[3] Experimental estimation, coming from the comparison between the macroscopic moment and the moment measured by neutronic diffraction or by combination between Compton effect and XMCD measurements.

CS	n_e^{5f}	$\mu_L^U(5f)$ $(\mu_B/atom)$	$\mu_S^U(5f)$ $(\mu_B/atom)$	$\mu_{tot}^U(5f)$ $(\mu_B/atom)$	$\frac{\mu_L^U(5f)}{\mu_S^U(5f)}$
IC	3 (U^{3+})	0.133	-0.058	0.075	-2.29

Table 3.6 *Value of the orbital and spin moments at 1T with* ***H//c****.*

the value at 17T, indicating the magnetic field acts proportionally on both orbital and spin moments in the configuration **H//c**.

The values of μ_L^U/μ_S^U are in disagreement with the neutron experiments [170], where the ratio μ_L^U/μ_S^U is -3.6 at 3T and -2.88 at 12T. However, in their calculations, even by taking into account the magnetization of the cobalt (only the spin part), a large part of the magnetization is missing to reproduce the macroscopic one. They have $\mu_{int} = \mu_{tot} - \mu_{tot}^U - \mu_S^{Co} = 0.08\mu_B$ at 3T and $\mu_{int} = 0.30\mu_B$ at 12T. From a theoretical point of view, the different band calculations done [38, 42, 180] predict an almost cancellation of the spin and orbital moment of the U site and large moment on the cobalt site. However, their calculations cannot reproduce the small moment in UCoGe, thus it is not possible to make any comparisons with our results.

Comparison with Resistivity Measurements

The results obtained by XMCD can be compared with the resistivity measurements performed up to 15T and in the temperature range $T \in [50mK; 5K]$.

The first point to check is that no anomaly is seen in the XMCD curve of the cobalt, indicating that no magnetic transitions are detected in the whole field range. This is in contradiction with resistivity experiments, where the ferro-to-ferrimagnetic transition is claimed to occur at 9T, **H//c** (figure 3.21) [202]. To avoid the possibility that the absence of transition is due to the "high" temperature XMCD measurements (3K) compared to the "low" temperature resistive measurements (40mK), magnetoresistivity measurements have been performed up to 5K, 15T.

In the literature, magnetoresistivity measurements have already been done and have reported several anomalies in the configuration **H//c**, as shown figure 3.21. The first goal of the measurements is to study the temperature dependence of the 9T anomaly. If this anomaly emerges from a ferro-to-ferrimagnetic transition (thus a magnetic transition) and is still detectable by resistivity at 3K, it means that it should be detectable by XMCD.

The magnetoresistance have been performed on a sample with $\mathbf{j}_Q$**//a** and RRR=37, and is shown figure 3.22.

The magnetoresistivity is positive at low temperature and becomes negative by increasing temperature. Several regimes are present. At low fields, low temperatures, there is the superconductivity, and there is a first anomaly at 6T (called T_1), where the magnetoresistivity goes from positive to slightly negative (almost flat). At 9T, a second anomaly is visible (called T_2), where the magnetoresistivity becomes positive. The low field anomaly goes to smaller fields with the increase of the temperature and becomes more a more difficult to detect whereas the high field anomaly is visible in the whole temperature range. With a zoom on the resistivity measurements, shown on the right panel of figure 3.23, another anomaly is visible just below T_1, and there is a deep minimum at low field (the anomalies are shown by the black arrows). The number of anomalies and regimes in the range 0T-15T and 0K-5K is an evidence to the very complicated physics that takes place in UCoGe, and measurements

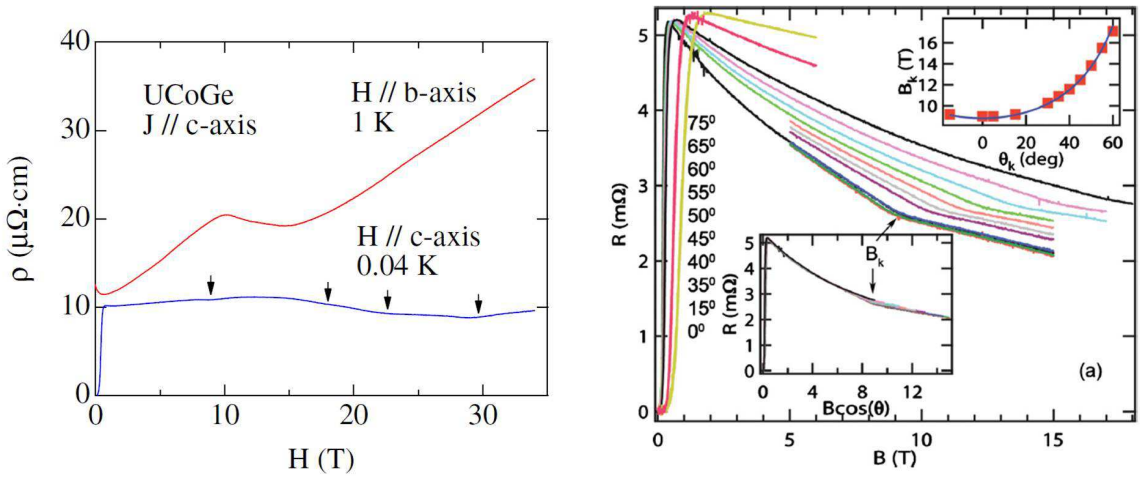


Figure 3.21 *Magnetorestivity of UCoGe measured by Aoki et al. [13] (left panel) and by Steven et al. [202] (right panel) at 40mK with* $\boldsymbol{j}_Q//\boldsymbol{c}$*,* $\theta = 0°$ *corresponds to* $\boldsymbol{H}//\boldsymbol{c}$ *and* $\theta = 90°$ *corresponds to* $\boldsymbol{H}$ *in the* $(\boldsymbol{a}, \boldsymbol{b})$ *plane. Several anomalies are visible below 35T, and the left panel is the angular study of the one at 9T.*

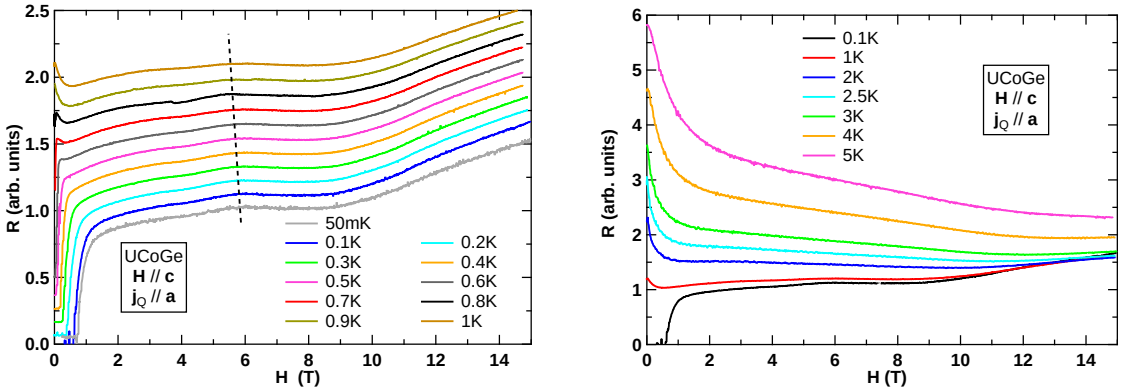


Figure 3.22 *Magnetorestivity of UCoGe below 1K (left panel) and above (right panel) in the configuration* $\boldsymbol{H}//\boldsymbol{c}$ *and* $\boldsymbol{j}_Q//\boldsymbol{a}$*.*

with other probes are needed to determine the nature of the anomalies.

The left panel of figure 3.23 shows the temperature and field dependence of both anomalies, with the superconducting transition as a reference. At low temperature, T_1 is almost field independent below 1K and then goes rapidly to 0. T_2 increases slightly with the magnetic field and seems to decrease above 4K.

If the anomaly detected at 9T (T_2) has the same origin that the one measured by Steven *et al.* [202], it is possible to detect it up to 5K. The absence of anomaly on the magnetization curve of the cobalt measured by XMCD indicates that the anomaly seen by resistivity cannot be a ferro-to-ferrimagnetic transition.

The magnetoresistivity of UCoGe is very complex, with several anomalies and regimes between 0T and 15T. This can be explained by the unusual big change of the number of $5f$-electrons with the magnetic field, which could induce Fermi surface change: this seems to

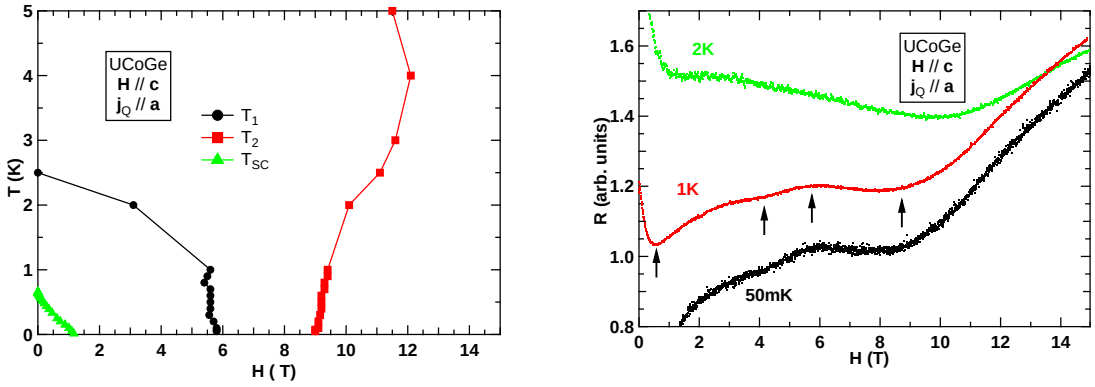


Figure 3.23 *Left panel: temperature and field dependence of the resistive anomalies. The superconducting temperature has also been plotted (green triangles). Right panel: zoom on the magnetoresistivity at 50mK (in black), 1K (in red) and 2K (in green). The arrows show the different anomales visible.*

CS	n_e^{5f}	$\mu_L^U(5f)$ $(\mu_B/atom)$	$\mu_S^U(5f)$ $(\mu_B/atom)$	$\mu_{tot}^U(5f)$ $(\mu_B/atom)$	$\frac{\mu_L^U(5f)}{\mu_S^U(5f)}$
IC	3 (U^{3+})	0.163	-0.079	0.084	-2.06

Table 3.7 *Value of the orbital and spin moments at 17T with **H//b**.*

be observed by Shubnikov-de-Haas measurements, where the frequencies of the oscillations (corresponding to one Fermi sheet) change with the magnetic fields [17].

Comparison Between the Configurations H//b and H//c

The moment at 17T with the field applied along the **b**-axis is shown table 3.7. The total moment measured on the uranium site, $\mu_{tot}^U = 0.084\mu_B$ is smaller than the macroscopic moment, $m_{tot} = 0.13\mu_B$. The ratio $\mu_L^U/\mu_S^U = -2.06$ is significantly smaller than in the other configuration. The field does not affect the same way the orbital and the spin moments as for **H**//**c**, the spin moment is more sensitive to the field than the orbital moment. This is an effect of the anisotropy of the magnetization.

The comparison of the XMCD signal of the uranium (M_4- and M_5-edges) between the configurations **H**//**b** and **H**//**c** is shown figure 3.24. The XMCD signal when **H**//**b** is smaller than in the other configuration, as the XMCD signal measures the magnetization. When **H**//**b**, the magnetization increases more slowly than in the configuration **H**//**c**, when it is applied along the easy axis. With a multiplicative factor, the XMCD signal of the M_4-edge with **H**//**b** matches perfectly with the signal with **H**//**c**. However, for the M_5-edge, the signals **H**//**b** and **H**//**c** are proportional, but the shapes are different. The consequence is a large change in the ratio μ_L^U/μ_S^U.

Comparison with XMCD on the Co L-edges

Recently, XMCD measurements in UCoGe have been done by another group at lower energy [27] to measure the $L_{2,3}$-edges of the cobalt. The data, shown figure 3.25 at 1.5K, are difficult to interpret because the U N_4-edge ($4d_{3/2} \rightarrow 5f$ transition, at 778.1eV) is very close to the Co

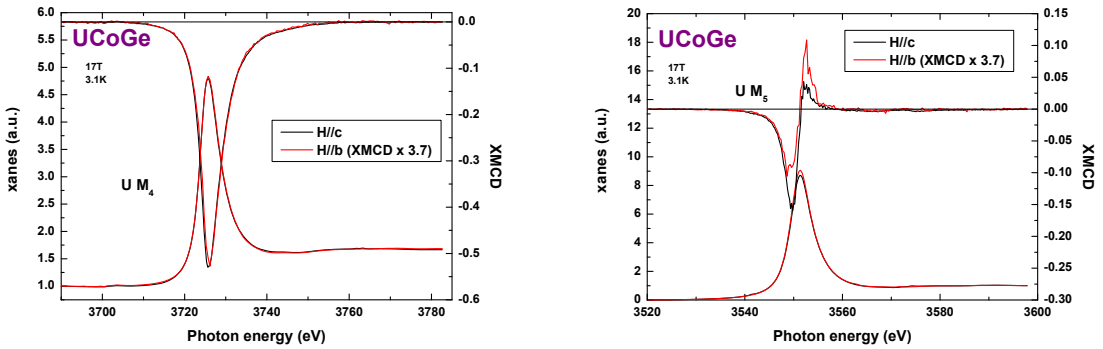


Figure 3.24 *Comparison of XANES and XMCD of the uranium at 3K, 17T between the configurations* ***H//b*** *and* ***H//c*** *for the M_4-edge (left panel) and the M_5-edge (right panel). A multiplying factor has been applied on the XMCD signal when* ***H//b****.*

L_3-edge (778.3eV). Another difficulty is that the soft X-rays have a smaller penetration depth ($\approx 10nm$), and, as a the result, are more sensitive to the surface state than hard X-rays.

It is nevertheless possible to get qualitative information. The XMCD of the L_3-edge is negative whereas it is positive for the L_2-edge, but much smaller. As a consequence, from the first sum rule for the L-edge, we deduce that the $< L_z >$ term is negative. Thus, the orbital moment of the cobalt is parallel to the applied magnetic field ($\mu_L = - < L_z > \mu_B$). If we assume that the $< T_z >$ term is negligible, from the second sum rule it is possible to deduce that the $< S_z >$ term of the cobalt is negative, leading again to the conclusion that the spin moment is parallel to the applied field ($\mu_S = -2 < S_z > \mu_B$). The small XMCD signal (multiplied by 20 figure 3.25) at 1.5K and 6T indicates that the magnetization carried by the Co is small.

Let us try to estimate the cobalt moment anyway. The figure 3.19 shows that the XMCD intensity at 17T with $\mathbf{H}//\mathbf{c}$ at 5.2 times larger than the XMCD intensity at 1T. This factor is partly due to the increase of the magnetization with the field. The macroscopic moment increases by a factor 5.5 between 1T and 17T ($0.08\mu_B$ and $0.44\mu_B$ respectively).

The total moment is: $\mu_{total} = \mu^U + \mu^{Co} + \mu^{Ge}$, with $\mu^U = \mu^U_{5f} + \mu_{cond}$, where μ_{cond} is the moment carried by the conduction electrons, usually estimated as 10% of the total moment. This contribution is caused by the polarization with the spin moment of the uranium, and has thus a negative value. In the following, it is assumed that the germanium moment is negligible ($\mu^{Ge} \ll 0.01\mu_B$).

At 3K and 17T, with $\mathbf{H}//\mathbf{c}$, $\mu_{total} = 0.44\mu_B$ (measured by magnetization measurements [106]), so $\mu_{cond} = -0.044\mu_B$, and the XMCD measurements have given $\mu^U_{5f} = 0.392\mu_B$, giving $\mu^{Co} = 0.09\mu_B$. Similarly, at 1T, $\mathbf{H}//\mathbf{c}$, $\mu_{total} = 0.08\mu_B$ [106] and $\mu^U_{5f} = 0.075\mu_B$ (by XMCD), leading to $\mu_{cond} = -0.008\mu_B$ and, as a result $\mu^{Co} = 0.013\mu_B$.

These calculations give $|\mu^{Co}/\mu^U_{5f}| \approx 0.17$ at 1T and $|\mu^{Co}/\mu^U_{5f}| \approx 0.22$ at 17T. The ratio, which should stay constant with the field when $\mathbf{H}//\mathbf{c}$, has the same order of magnitude in our measurements, which means that the cobalt moment calculated has the good order of magnitude. The small difference can come from the error on the estimation of the $< T_z >$ term, leading to an error on μ^{5f}_S.

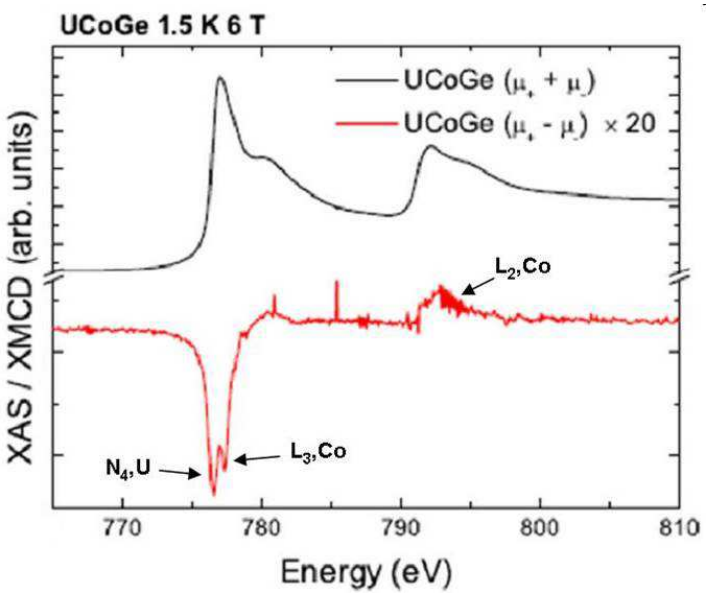


Figure 3.25 *XMCD measurements at low energy. The L_3-edge and the L_2-edge of the cobalt has been measured, but the proximity of the N_4-edge of the uranium to the L_3 edge makes the results difficult to interpret.*

As expected, the cobalt moment is positive (parallel to the field), which is in disagreement with the polarized neutron results [170]. Another point at variance with the neutron experiments is that they showed that the ratio $|\mu^{Co}/\mu^{U}_{5f}|$ varies from 0.3 to 0.84 (or from 0 to 0.38, depending on the model) between 3T and 12T, whereas the field dependence of the XMCD intensities at the U M_4- and at the Co K-edges is similar and is proportional to to macroscopic magnetization (left panel of figure 3.18). This means that the magnetic moments of both sites have the same magnetic dependence, and this leads to a constant ratio $|\mu^{Co}/\mu^{U}_{5f}|$ with the field. The same behavior has been found in the compound UCoAl in the paramagnetic state [213], confirming the induced nature of the cobalt moment.

3.3.4 Conclusion

As a conclusion, in UCoGe, similarly to UCoAl measured recently [213], the orbital moment of the uranium, as well as the spin and orbital moments of the cobalt are aligned in parallel to the magnetic field, whereas the spin moment of the uranium is antiparallel. This is in disagreement with the neutron scattering experiments, with an antiparallel induced moment on the cobalt [170]. A sketch is shown figure 3.26.

A Lifshitz transition has been proposed to occur at 11T, **H**//**b** [127], at the maximum of the enhancement of the superconducting temperature [12]. No anomaly on the XMCD intensity of the U M_4-edge has been detected between 0T up to 17T, in agreement with the macroscopic magnetization measurements [106]. This

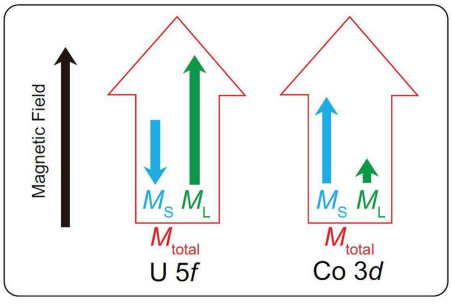


Figure 3.26 *Schematic sketch of the direction of the Co and U moments in UCoGe, similar to UCoAl [213]. The arrows are not in scale.*

absence of anomaly may be caused by a small misalignment between the **b**-axis and the magnetic field, as it has been seen that some properties are anisotropic with a strong angular dependence (very peaked along the **b**-axis) [12]. It could also be that magnetization is not the most sensitive quantity to detect such an anomaly.

Chapter 4

Thermal Conductivity Measurements

This chapter gets to the heart of the matter: the thermal conductivity measurements. The first section is a study of the effect of the quality of the samples in the thermal conductivity, to be able to distinguish "extrinsic" from "intrinsic" effects. Then comes a large section on the study of the thermal conductivity in the normal phase of UCoGe, as it appears more complicated than initially believed. The last part is the study of the thermal conductivity in the superconducting phase.

4.1 Effect of the Quality (H=0T)

The comparison between different samples is done, among which three are with the heat current along the **c**-axis. They have first been measured to be able to compare them and to determine how the quality affects the thermal conductivity measurements. Once it has been done, two different samples with the current along the two other crystallographic directions have been measured. It will be seen that the main difference in the normal phase can be explained by the difference of the RRR.

The figure 4.1 shows the thermal conductivity divided by the temperature at zero field of the five samples up to 7K. At the Curie temperature, the thermal conductivity shows a kink more or less pronounced depending on the sample homogeneity. At the superconducting transition, there is another kink for sample S^c_{16}, but it is much more difficult to distinguish on the other samples because it happens in the strong raise of κ/T due to the increased electronic contribution on cooling (suppression of inelastic scattering). In section 4.3, it will be shown that this (bulk) superconducting transition happens approximately at the same temperature ($T_{sc} \approx 0.5K$) whereas the Curie temperature of sample S^c_{110} ($T_{Curie} \approx 3K$) is higher than in the other ones ($T_{Curie} \approx 2.5K$). We observed that for samples of high RRR, the onset of the resistive transition could be as high as 0.9K, but with a very large width (between 0.2 and 0.3K). For example, the highest Curie temperature of the sample S^c_{110} is associated with a resistive superconducting transition 0.3K wide, and is certainly due to inhomogeneities in this sample, despite its high purity in term of RRR.

For each sample, the thermal conductivity in the paramagnetic (PM) state (above 3K) varies very little and it increases strongly in the ferromagnetic (FM) state (except for sample S^c_{16}). This observation is consistent with the resistivity measurements which shows that the

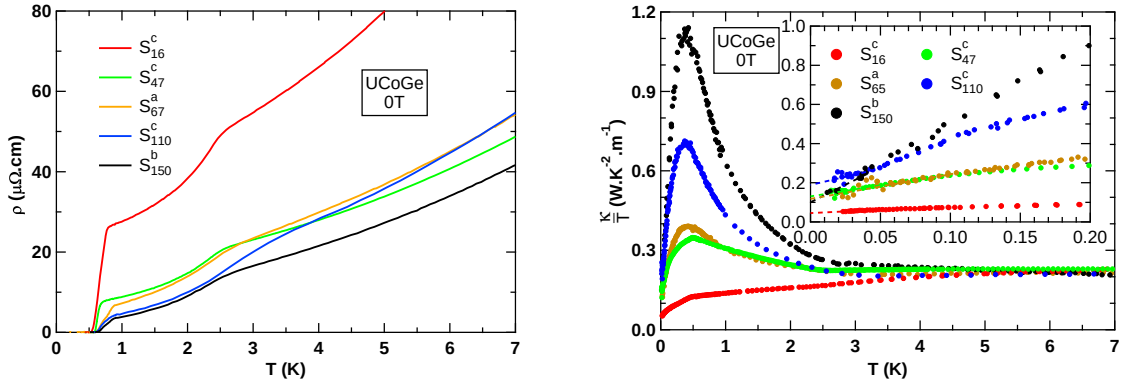


Figure 4.1 *Resitivity (on the left) and thermal conductivity divided by the temperature (on the right) at zero field. Despite the difference of the resistivity in the paramagnetic state between each sample, the thermal conductivity is very similar. In the ferromagnetic state, κ/T increases (except for sample S^c_{16}) and the higher the RRR, the stronger the increase. In inset : Zoom of the low temperature part. The extrapolation at 0K (dashed lines) leads to different values depending on the sample, i.e. the quality. Three different values with $\boldsymbol{j}_Q//\boldsymbol{c}$ mean the regime of the universal limit is not reached.*

mean free path of the electrons is increased in the FM state and on cooling. The large increase of the thermal conductivity has already been seen in classic systems, as in silver for example [235]: a maximum of κ appears at $\approx 15K$ and is only due to the increase of the electronic contribution. Even if the origin is different in UCoGe, the consequence is similar. Contrary to the thermal conductivity, the electrical resistivity is strongly suppressed in the PM state with the increase of the RRR. This indicates that the thermal conductivity is not dominated by electronic contribution but by others, less sensitive to the quality (like phonons).

With thermal conductivity has been measured the resistivity, to be able to verify the Wiedemann-Franz law. The figure 4.2 displayed the Lorenz ratio ($L/L_0 = \kappa\rho/(L_0 T)$) for each sample at 0T. The Lorenz ratio is much larger in sample S^c_{16} at high temperature than in the other samples, confirming the thermal conductivity is not dominated only by the electronic contribution, but also by other contributions. High temperature thermal conductivity in a sample similar to S^c_{16} (in terms of RRR) shows also high value of the Lorenz number, with a maximum at 25K [221]. Due to the SC transition, the Lorenz ratio is not known at low temperature, but can be extrapolated more or less linearly to 1 at 0K, except for sample S^b_{150} where superconductivity happens during the increase of the Lorenz ratio. To confirm the validity of the measurements, one has performed measurements at 2T, $\mathbf{H}//\mathbf{c}$ (above $H_{c_2}(0)$). The Lorenz ratio can be extrapolated to 1, corroborating our measurements.

For samples S^c_{110} and S^a_{65}, the Lorenz ratio falls below 1, indicating the importance of inelastic electronic scattering. At 1K, except for the sample S^b_{150}, the Lorenz ratio decreases with improved RRR. As it will be seen in the next section, an extra heat channel appears below 2K, and its contribution to the total thermal conductivity is quite small, except in the sample S^b_{150}, where it contributes to approximately 25% of the total signal at 0.5K ($\leq 10\%$ in the other samples) and is responsible for the increase of the Lorenz ratio. For the analysis of the thermal conductivity, it will be important to take into account inelastic scattering to estimate the electronic quasiparticle thermal conductivity.

Concerning the superconducting state, it is important to notice that, for a given current direction ($\mathbf{j}_Q//\mathbf{c}$), κ/T (linearly) extrapolated at zero temperature of each sample is different

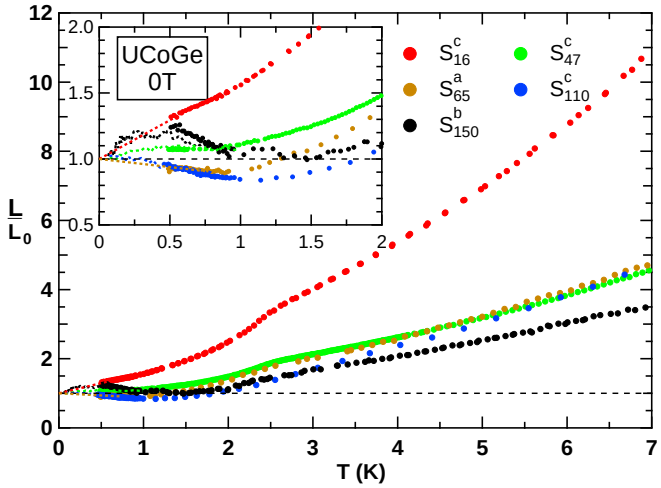


Figure 4.2 *The Lorenz ratio calculated for each sample with a zoom of the low temperature in inset. The dotted lines are the extrapolation at zero temperature, either linearly (for samples S^c_{16} and S^a_{65}), or with the measurements at 2T with **H**//**c** (no superconducting phase).*

(see the inset of the figure 4.1): the experiments give $\frac{\kappa}{T}|_{T\to 0K} = 0.147,\ 0.123$ and 0.048 $\mathrm{WK^{-2}m^{-1}}$ for samples S^c_{110}, S^c_{47} and S^c_{16} respectively, no universal limit is observed in the superconducting state in the measured samples. This may be due either to the fact that the samples are not homogeneous enough, or to the fact that the universal limit does not exist in UCoGe, which is possible if there are no line nodes in the superconducting gap in the **c**-direction or if it is a multigap superconductor [189].

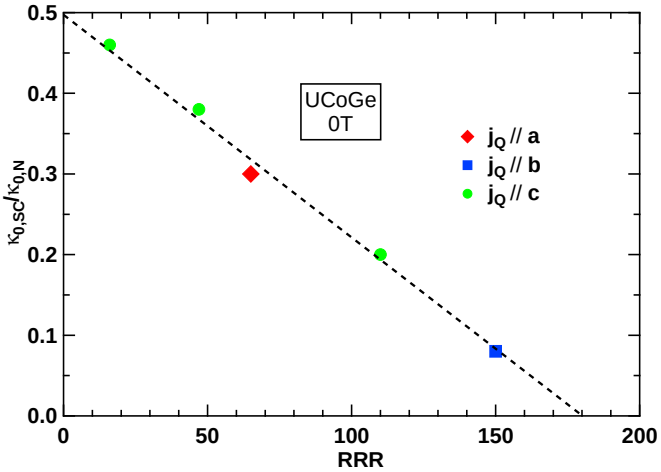


Figure 4.3 *Normalized residual thermal conductivity versus the RRR. The ratio $\frac{\kappa_{0,sc}}{\kappa_{0,N}}$ decreases roughly linearly with the RRR without saturation yet.*

If we look at the normalized residual thermal conductivity in the superconducting state ($\frac{\kappa_{0,N}}{T} = \frac{L_0}{\rho_0}$), the ratio $\frac{\kappa_{0,sc}}{\kappa_{0,N}}$ is roughly linear with the RRR, as shown figure 4.3. This shows that no "intrinsic" residual term is observed up to now, as would have been expected for an

analog of the A1 phase of superfluid ^{3}He, where only part of the Fermi surface is gapped. It shows also that slightly higher RRR are needed to be able to conclude with certainty about the superconducting gap: the residual term is small in sample S^b_{150}, but probably still too large. Indeed, "small" residual terms can lead to a wrong conclusion for the superconducting gap. In UPt_3, the first thermal conductivity measurements gave an isotropic and linear thermal conductivity (κ/T) in the superconducting state [20] and much better quality samples were required to observed the "intrinsic" T^2-behavior [121]. For UCoGe, we can hope that we are not far from reaching this intrinsic regime, but not yet there.

4.2 Analysis of the Normal Phase

This section will only focus on the normal phase of UCoGe, and is split into three subsections: first I will describe the bare measurements, without further analysis. Then, assuming the additivity of the different mechanisms to κ, I will decompose the total thermal conductivity into two contributions: the regular electronic quasiparticle thermal conductivity on the basis of the WFL, and "other" contributions (composed of phonons, magnetic fluctuations...). In the next part, the results are compared with existing theories. In the Appendix .1, a phenomenological model is given to try to decompose these other contributions to the thermal conductivity, based on a kinetic model, to get a more quantitative point of view.

A number of figures will be shown. On each one, there is a label with the name of the sample studied (S^i_x), keeping in mind that the exponent is the current direction ($\mathbf{j}_Q//\mathbf{i}$), and x the RRR. For clarity reasons, only the measurements at 0T, 2T and 6T will be shown. The sample S^a_{65} has been measured only at zero field and 2T ($\mathbf{H}//\mathbf{c}$), the others having a complete study with $\mathbf{H}//\mathbf{c}$. Only samples S^c_{16} and S^b_{150} have been studied with $\mathbf{H}//\mathbf{b}$.

4.2.1 Bare Results

In this subsection, I will just do some observations of the results obtained under magnetic field, when applied along the **b** and the **c**-axis. This section starts with the case $\mathbf{H}//\mathbf{c}$, followed by the case $\mathbf{H}//\mathbf{b}$. The electronic quasiparticle thermal conductivity is named κ_{qp}, and the other contributions to the thermal conductivity (due to phonons, magnons...) is called κ_{other}.

H//c

The left figure 4.4 shows the thermal conductivity and the resistivity (in inset) on the sample S^c_{16} in the configuration $\mathbf{H}//\mathbf{c}$. The arrows highlight the behavior with the magnetic field. At zero field, an anomaly is visible at $T_{Curie} \approx$2.5K on both thermal conductivity and electrical resistivity. The superconductivity is marked by a clear kink in the thermal conductivity at T^κ_{sc}=0.5K. As $H^c_{c_2}$<1T, the other curves do not exhibit superconductivity. Contrary to the resistivity, the thermal conductivity has a non monotonic behavior with the temperature and the field: at low field, κ/T increases with the increase of the temperature in the whole temperature range, and for fields above 6T, a maximum appears at low temperature. This is the first indication that the electronic quasiparticle contribution cannot explain alone the thermal conductivity behavior. This is seen quantitatively on figure 4.4, right panel, which shows that the Lorenz ratio reaches values above 10 at 7K at zero field: the electronic quasiparticle contribution is then at most 10% of the total. Concerning the field behavior, κ/T increases

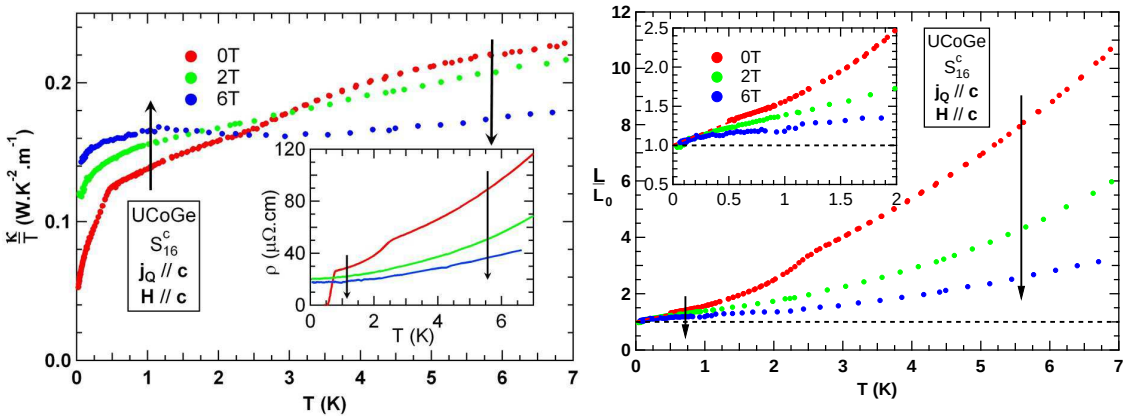


Figure 4.4 *On the left, the thermal conductivity and the resistivity (in inset) of sample S^c_{16} with the field along the* ***c****-axis. On the right is displayed the WFL with a zoom of the low temperature part in inset. The arrows highlight the behavior of the corresponding quantity with the magnetic field.*

with the field at low temperature (T$\lesssim$2K) whereas it decreases with field at high temperature (T>2K). This is in contradiction with the negative magnetoresistivity (the resistivity decreases with the magnetic field) observed in the whole temperature range (0<T$\leqslant$7K). But it shows again the importance of the other contributions above 2K. Below this temperature, the other contributions may still be present, but the thermal conductivity appears governed by the electronic thermal conductivity, and recovers a "normal" behavior with the magnetic field. The Lorenz ratio decreases strongly with the magnetic field in this whole temperature range. This decrease of L/L_0 with field arises partly from the negative magnetoresistance, which implies an increased quasiparticle contribution to the thermal conductivity under field. However, above 2K, the left panel of figure 4.4 shows that κ/T decreases with field instead! Therefore, simultaneously, it is expected that the other contributions are strongly suppressed by the field, so as to overcompensate the increased electronic quasiparticle contribution. As regards the Lorenz ratio, if the direct additivity of the contributions is assumed to be correct[1], i.e. $\kappa = \kappa_{qp} + \kappa_{other}$, the Lorenz ratio can be written as:

$$\frac{L}{L_0} = \frac{\kappa.\rho}{L_0 T} = \frac{\kappa_{qp}.\rho}{L_0 T} + \frac{\kappa_{other}.\rho}{L_0 T} \tag{4.1}$$

$$= \frac{L_{qp}}{L_0} + \frac{L_{other}}{L_0} \tag{4.2}$$

The first term corresponds to the electronic quasiparticle contribution and tends to 1 when T$\rightarrow$0K. This term is equal to 1 in the absence of inelastic electronic scattering, otherwise is inferior to 1 (see figure 2.3 in the chapter 2), but cannot be superior to 1. The positive deviation of the Lorenz ratio comes from the second term, named L_{other}/L_0. It contributes positively and goes to 0 at zero temperature. So the decrease of the Lorenz ratio with the field corresponds to the reduction of this term, due both to a decreasing ρ and κ_{other} with field. Still with the additivity of the mechanisms, the other contributions can be decomposed into a (regular) phononic part and extra contributions (which can be magnetic, excitonic...): $\kappa_{other} = \kappa_{ph} + \kappa_{extra}$. The lattice contribution to the thermal conductivity is usually very

[1]This is not necessary the case, as it has been shown for the additivity of electron-electron and electron-impurity scattering in the electronic term [22].

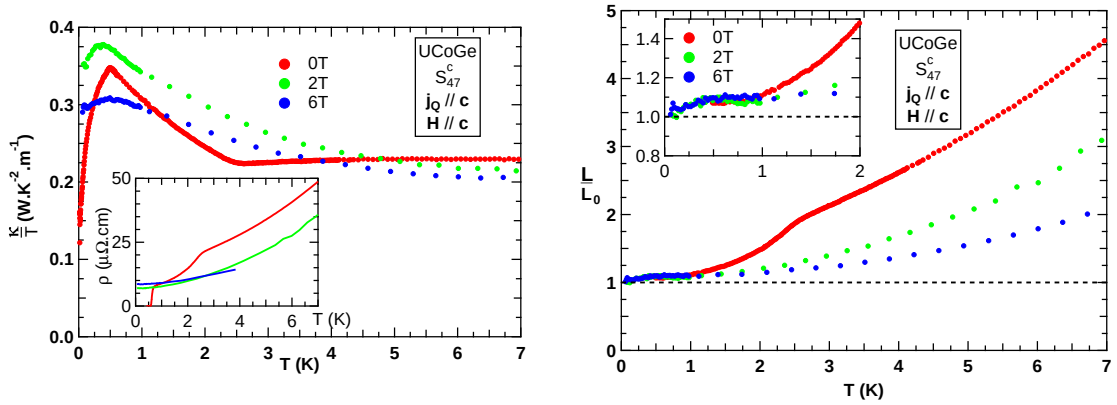


Figure 4.5 *On the left, the thermal conductivity and the resistivity (in inset) of sample S^c_{47} with the field along the* **c***-axis. On the right is displayed the Lorenz number with a zoom of the low temperature part in inset.*

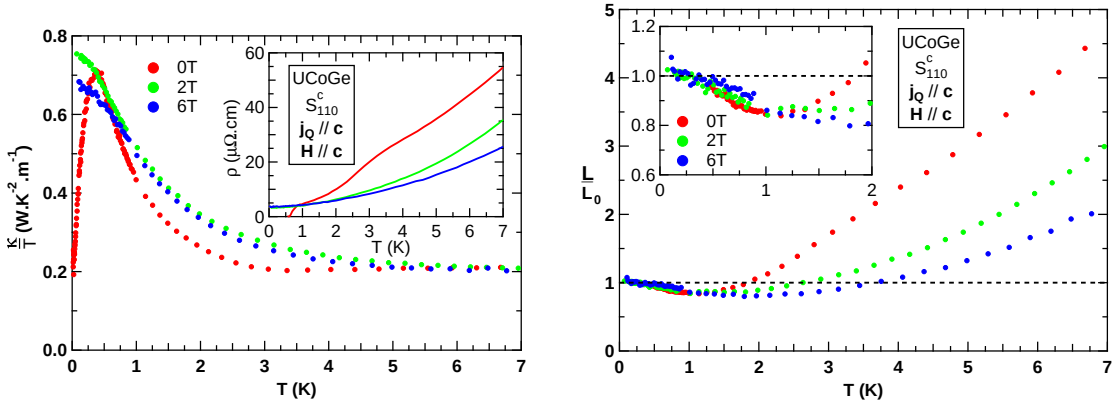


Figure 4.6 *On the left, the thermal conductivity and the resistivity (in inset) of sample S^c_{110} with the field along the* **c***-axis. On the right is displayed the Lorenz ratio with a zoom of the low temperature part in inset.*

little dependent to the magnetic field, which means that the field dependence of the Lorenz ratio mainly comes from the third term κ_{extra}, and from ρ.

All these observations lead to the conclusion that some non-negligible extra contributions (besides the electronic one) to the thermal conductivity are present at low temperatures and that they are at least partly due to magnetic excitations in order to explain its field suppression (for **H**//**c**).

This study has been done with the other samples, and the same conclusions can be obtained. They are less striking in the other samples as their better qualities diminish the weight of the extra contribution with respect to the larger electronic quasiparticle contribution. Indeed, it is reasonable to assume that these other contributions have the same order of magnitude in all samples, but not the electronic quasiparticle contribution (directly linked to the resistivity).

The figure 4.5 shows (on the left) the thermal conductivity and the resistivity (in inset) of sample S^c_{47} with **H**//**c**. The Lorenz ratio is plotted on the right side. At 0T, the thermal

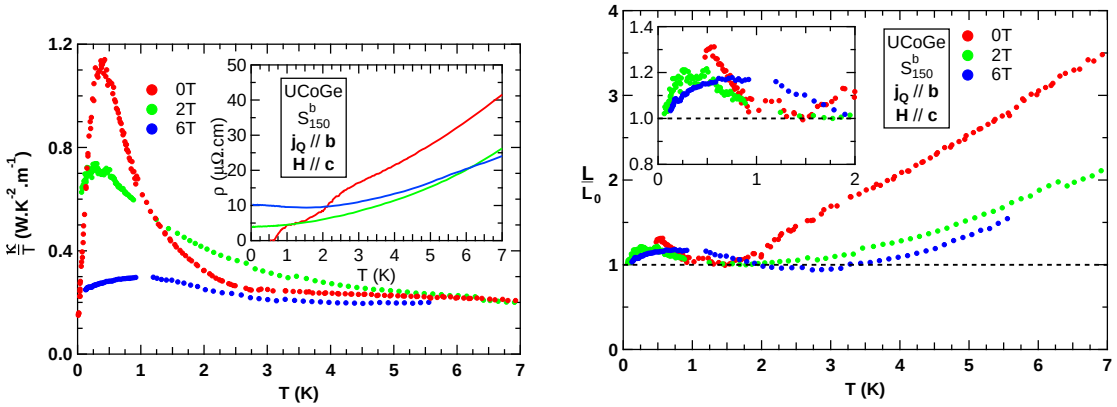


Figure 4.7 *On the left, the thermal conductivity and the resistivity (in inset) of sample S^b_{150} with the field along the* ***c****-axis. On the right is displayed the WFL with a zoom of the low temperature part in inset.*

conductivity has well defined ferromagnetic and superconducting transitions at 2.5K and 0.5K respectively, highlighting the high homogeneity of the sample. The magnetoresistivity is negative at high temperature and becomes positive at low temperature. In that case again, the thermal conductivity is in agreement with the magnetoresistance at low temperature, but not at high temperature (both thermal conductivity and resistivity decrease with the field), and the Lorenz ratio is suppressed with the magnetic field. The maximum of κ/T at low temperature is visible at 2T, contrasting with the behavior of ρ. It points to a small field dependent extra contribution even at this low temperatures. This may explain also why L/L_0 remains always above 1 in this sample down to low temperature (see the inset of the right part of the figure 4.5): by decreasing the temperature, the Lorenz ratio decreases but seems to saturates at 1K with a slight bump before decreasing again below 0.5K.

The results of sample S^c_{110} with $\mathbf{H}//\mathbf{c}$ are displayed figure 4.6. The thermal conductivity (on the left) and the resistivity (in the inset) are quite similar to those of the sample S^c_{47}: the thermal conductivity increases in the ferromagnetic phase and the magnetoresistance is positive at low temperature and negative at high temperature. In that case, the disagreement between the behavior of κ and ρ under field is not so obvious, the electronic thermal conductivity is dominant in this sample. This is confirmed by the Lorenz ratio (on the right of the figure 4.6): the Lorenz ratio falls under 1 due to the inelastic electronic scattering. Once more, at high temperature, the Lorenz ratio decreases with the field whereas it is almost field independent at low temperature.

The figure 4.7 displays the results of sample S^b_{150} with $\mathbf{H}//\mathbf{c}$. At first sight, the thermal conductivity (on the left side) looks like the one of sample S^c_{47}: a strong increase in the ferromagnetic state, a maximum at low temperature under field, a non monotonic magnetoresistance with the temperature and the disagreement with the resistivity under field at high temperature. One big difference is that the thermal conductivity seems a lot more sensitive to the field in that case at low temperature: the thermal conductivity has decreased by more than a factor 3 between 0T and 6T at 0.5K, against a decrease of 15% in sample S^c_{47}! The behavior of the Lorenz ratio is also very interesting: as before, the Lorenz ratio decreases under field at high temperature, and, as the RRR is the highest, a strong drop below 1 was expected at low temperature. But the opposite happens: by decreasing the temperature, the

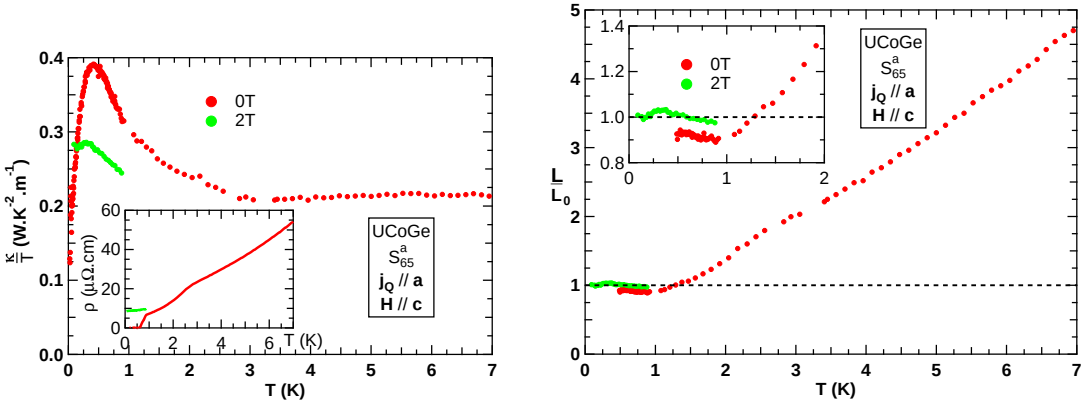


Figure 4.8 *On the left, the thermal conductivity and the resistivity (in inset) of sample S^a_{65} with the field along the* **c***-axis. On the right is displayed the Lorenz ratio with a zoom of the low temperature part in inset.*

Lorenz ratio shows a minimum between 1K and 1.5K but remains above 1, before increasing again with a maximum at 0.5K to extrapolate to 1 when T→0K. The low temperature part is shown in the inset and is field dependent. This feature confirms the idea of a low temperature contribution mentioned in the previous paragraph: this increase could be caused by the appearance of a new thermal excitation or by a change of its dispersion, much more intense along the **b**-axis than in the **c**-direction. As it is field dependent, it is believed to have also a magnetic origin.

The sample S^a_{65} has been studied only at zero field and at 2T below 1K ($\mathbf{H}//\mathbf{c}$). The results are shown figure 4.8. It is not possible to make extensive conclusions on this sample, but we can give some basic arguments: the thermal conductivity seems to behave like that of the sample S^b_{150}: it decreases rapidly with the field. Concerning the Lorenz ratio, it goes below 1 at zero field and it seems that there is a small bump at 2T, which put this sample between the sample S^c_{47} and S^c_{110}. This seems normal, as its RRR (65) is between the RRR of these two samples. An extra contribution to the thermal conductivity may be present at low temperature, but, in that case, its intensity is very small.

Before going to the case $\mathbf{H}//\mathbf{b}$, here is a summary of the observations done during this analysis:

- κ/T cannot be explained by the magnetoresistivity in the whole temperature range (T∈[10mK, 7K])
- L/L_0 decreases rapidly with the field at high temperature
- an extra contribution to κ appears at low temperature and is very intense when $\mathbf{j}_Q//\mathbf{b}$

This leads to the following preliminary conclusions:

- κ is dominated at high temperature by non-electronic contributions, partly magnetic
- these contributions are strongly field sensitive when $\mathbf{H}//\mathbf{c}$
- another extra contribution appears at low temperature and seems also to be magnetic

- this low temperature contribution is highly anisotropic, as it is barely visible when $\mathbf{j}_Q//\mathbf{a}$ and $\mathbf{j}_Q//\mathbf{c}$ and is very intense when $\mathbf{j}_Q//\mathbf{b}$

H//b

It is time now to study the case $\mathbf{H}//\mathbf{b}$, measured only on samples S^b_{150} and S^c_{16}. Here again, I will start with the observations of sample S^c_{16} before going to the other one.

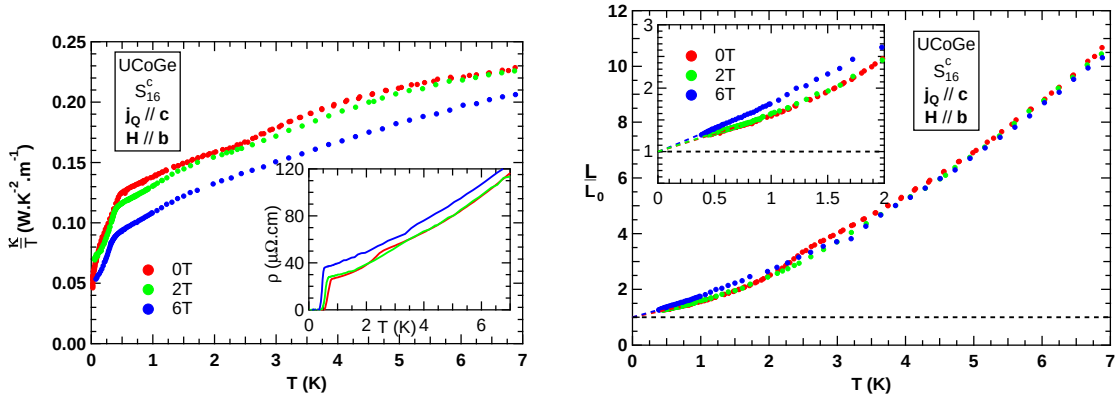


Figure 4.9 *On the left, the thermal conductivity and the resistivity (in inset) of sample S^c_{16} with the field along the* ***b****-axis. On the right is displayed the Lorenz ratio with a zoom of the low temperature part in inset.*

The figure 4.9 shows the results obtained in sample S^c_{16} with $\mathbf{H}//\mathbf{b}$. These measurements have been made during two different cooling: first at low temperatures (T<1K) with a well aligned sample with the field (the superconducting transition is still here at 8T and the beginning of the S-shape is visible) and then another experiment has been performed to measure the high temperature part (above 1K). During this experiment, the alignment of the sample with the field was not very good, which explains why the Curie temperature is not visible at high field (by thermal conductivity and resistivity). Nevertheless, in that case, the behavior of the thermal conductivity (on the left) can be explained by the magnetoresistance in the whole temperature range: κ/T decreases with the field and the resistivity (in inset) increases. The positive magnetoresistivity is only due to the transverse configuration ($\mathbf{j}_Q \perp \mathbf{H}$). The consequence of the magnetic field is far less dramatic on κ/T compared to the previous field direction ($\mathbf{H}//\mathbf{c}$): κ/T is only shifted to lower values. Another impressive difference with the previous case is the Lorenz ratio under field: in this configuration, the Lorenz ratio is field independent in the paramagnetic state and L/L_0 increases little in the ferromagnetic state. This feature proves that the magnetic field has little effects on the electronic inelastic scattering (see resistivity) and on the extra contributions.

The thermal conductivity and the resistivity of sample S^b_{150} with $\mathbf{H}//\mathbf{b}$ are shown figure 4.10 on the left. κ/T and ρ are almost field independent in the paramagnetic state, and the ferromagnetic state is described by a positive magnetoresitivity, accordingly a decreasing thermal conductivity with field. The anomaly at 2.5K at high fields ensures the good alignment of the **b**-axis with the field. As in the previous case, the Lorenz ratio (on the right) is field independent in the paramagnetic phase. In this sample, L/L_0 increases again below 1.5K in zero field. This increase of L/L_0 below 1.5K is present at all fields, but it becomes

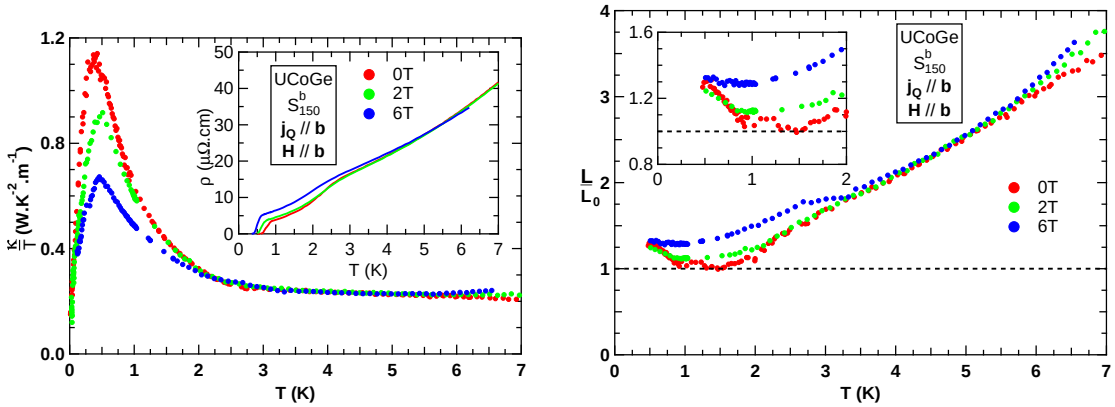


Figure 4.10 *On the left, the thermal conductivity and the resistivity (in inset) of sample S^b_{150} with the field along the* **b***-axis. On the right is displayed the Lorenz ratio with a zoom of the low temperature part in inset.*

less and less pronounced: the low temperature extra contribution seems to spread out with the field in this configuration.

The study with the field along the **a**-axis is missing to conclude unambiguously, but the following preliminary conclusion can be done: κ/T in UCoGe is dominated by low temperature extra contributions, which are believed to be partly magnetic. It appears that two different excitations are present: one above 1K, which spread up to high temperature and one at low temperature (below 2K), and this one shows a strong anisotropy between the **b**-axis (very intense) and the **a**- and **c**-axis (barely detectable). Furthermore, the high temperature extra contribution shows a strong sensitivity to the direction of the magnetic field: the configuration **H**//**c** suppresses it rapidly, whereas it is field insensitive when **H**//**b**. This feature is less obvious for the low temperature contribution.

It is known that the magnetic fluctuations have a great importance in the properties of UCoGe, as they are believed to be responsible for the superconductivity [74]. They have been observed at high temperature by NMR [88] (from 80K, approximately the coherence temperature of the Kondo lattice [221]) and neutron scattering [205], and they are strongly suppressed when **H**//**c** and field insensitive when **H**$\perp$**c**. They may be responsible for the high temperature extra contribution. The low temperature contribution may be a consequence of the ferromagnetism, and thus could be a new excitation, or just a result of the modification of the excitation spectrum below T_{Curie}, due to the predicted drastic change of the Fermi surface at the ferromagnetic transition [180].

Now that the interpretation of the bare data has given several preliminary conclusions, the next section will present a more quantitative analysis with the decomposition of κ into the electronic quasiparticle part and the other contributions.

4.2.2 Analysis of the Normal Phase

The first hypothesis done, and mentioned before, is that the heat channels are supposed to be in parallel and it is thus possible to add them: $\kappa_{tot} = \kappa_{qp} + \kappa_{phonon} + \kappa_{extra}$.

To deduce the electronic quasiparticle thermal conductivity, we take the WFL as a basis:

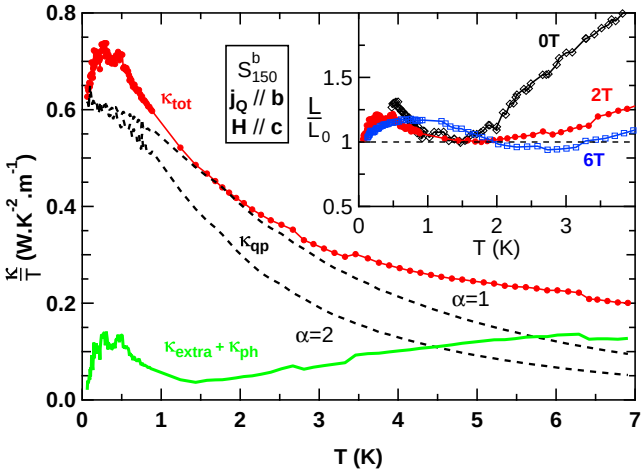


Figure 4.11 *Thermal conductivity of sample S^b_{150} at 2T with **H**//**c**. The red line is the total thermal conductivity, the black dashed lines are $\frac{\kappa_{qp}}{T}$ with α=1 and α=2 respectively. The straight green line is the other contribution $\frac{\kappa_{other}}{T} = \frac{\kappa_{tot}}{T} - \frac{\kappa_{qp}}{T}$. In inset is shown the Lorenz ratio at 0T, 2T and 6T in the configuration **H**//**c**.*

$\frac{\kappa_{qp}}{T} = \frac{L_0}{\rho}$. As in some samples, the quantity L/L_0 falls below 1, the effect of the electronic inelastic scattering needs to be taken into account. Indeed, the direct use of the WFL would give $\kappa_{qp} > \kappa_{tot}$. In order to do that, we use what we call a modified Wiedemann-Franz law (named mWFL thereafter) [231]:

$$\frac{\kappa_{qp}}{T} = \frac{L_0}{\rho_0 + \alpha(\rho - \rho_0)} \tag{4.3}$$

ρ_0 is the residual resistivity and $\alpha = 1 + W_{vert}/W_{hor}$, where W_{vert} and W_{hor} are respectively the scattering rates due to inelastic vertical and horizontal processes, assuming that Mathiessen's rule holds. α is a sample dependent coefficient, larger than 1, and this model has been used in the study of the heavy fermions UPt_3 [121] or $CeRhIn_5$ [156]. This formula is a phenomenological, but convenient, estimation of the electronic thermal conductivity. This α term is supposed to be temperature and field independent. This crude simplification can be valid for temperatures much smaller than the typical energy of the fluctuations responsible for the inelastic scattering (for temperature smaller than the minimum of the expected Lorenz ratio, see figure 2.3 in the section 2.3.1). The use of this simple model is motivated by the lack of theories on thermal conductivity on Ising ferromagnets. For each field, the resistivity has been extrapolated to the lowest temperature (in the superconducting state) by using the formula:

$$\rho = \rho_0 + A.T^n \tag{4.4}$$

The coefficients ρ_0, A and n are found by fitting the normal part. Thereafter, κ_{qp}/T is calculated using the previous formula in the superconducting state, so it is plotted in the whole temperature range.

The figure 4.11 shows the thermal conductivity of sample S^b_{150} at 2T with **H**//**c**. The black dashed lines correspond to κ_{qp}/T with $\alpha = 1$ and $\alpha = 2$. The green straight line is the the extra contribution $\frac{\kappa_{other}}{T} = \frac{\kappa_{tot}}{T} - \frac{\kappa_{qp}}{T}$, with $\alpha = 1.36$, which can be considered as a lower bound of this contribution: larger values of α would enhance κ_{other}. This figure shows that

the low temperature maximum of κ/T is little dependent on the value of α, whereas the high temperature part is much more.

In order to find the α coefficient, two assumptions have been done: the first one is that the Curie anomaly is purely electronic and that the extra contribution should have no anomaly at T_{Curie}. This assumption is not very restrictive as it happens that in UCoGe, large value of α (superior to 3) is necessary to see the anomaly at T_{Curie} on κ_{other}. The second limitation comes from the fact that α is assumed to be field independent (i.e. the same when $\mathbf{H}//\mathbf{b}$ and $\mathbf{H}//\mathbf{c}$). κ_{other} should also stay positive for every fields measured, which would mean otherwise that the electronic quasiparticle contribution is overestimated.

As this convenient way to determine κ_{qp} is phenomenological, it works only for "classical" behavior of the resistivity. The lack of theoretical background prevents to use the mWFL to estimate κ_{qp} in sample S^b_{150} when H>4T, $\mathbf{H}//\mathbf{c}$, due to the orbital effects (see inset of figure 4.7). The electronic quasiparticle thermal conductivity in sample S^b_{150} at 6T and 8T, $\mathbf{H}//\mathbf{c}$, will not be determined precisely and thus κ_{other} will be just a rough guess.

The figure 4.12 shows the decomposition of κ_{tot}/T of each sample at H=0T. The low temperature part of κ_{other}/T is missing due to the superconductivity. If the assumptions are correct, κ/T is dominated at high temperature by κ_{other}/T, which corresponds to approximately 90% of the total signal!

The figure 4.13 shows the extra contribution at zero field for each sample (the phonon thermal conductivity has been removed), with the value of the α coefficient. The value of the phonon contribution is calculated in the Appendix .1. An interesting feature is that κ_{extra}/T is very similar for each sample in the paramagnetic state. It decreases to zero at low temperature when $\mathbf{j}_Q//\mathbf{a}$ and $\mathbf{j}_Q//\mathbf{c}$ and the increase is obvious below 1.5K in sample S^b_{150}.

The evolution of this extra contribution of samples S^c_{16} and S^b_{150} under magnetic field, in both field configurations, is displayed on figure 4.14. This confirms one of the preliminary conclusions of the previous section: the decrease of the Lorenz ratio with H at high temperature is for the most part due to the reduction of κ_{other}/T. The low temperature part is also field sensitive, especially in sample S^b_{150}, the low temperature contribution strongly decreases with the field and seems also to spread out.

When $\mathbf{H}//\mathbf{b}$, there is almost no change in the paramagnetic state (the small effect in sample S^c_{16} may be due to a small misalignment). In the ferromagnetic state, there is here only small changes, the low temperature extra contribution seems to be reduced and spread, even if this is difficult to conclude precisely because of superconductivity.

The evolution of the extra contribution, $\mathbf{H}//\mathbf{c}$, of samples S^c_{47} and S^c_{110} is shown 4.15. The same qualitative conclusion as for sample S^c_{16} can be done: the Lorenz ratio decreases with the field in the whole temperature range, even if it is less obvious below 1K.

An attempt to decompose the non electronic thermal conductivity is given in the Appendix .1, which takes into account the contribution of the phonons, and both magnetic contributions seen on the bare data. This model confirms the conclusions done before. The table 4.1 shows the amplitude of the low temperature contribution (M_{LT}) and the gap of this contribution (the initial increase, ϵ^{LT}_{min}), which shows that the amplitude is large when $\mathbf{j}_Q//\mathbf{b}$ and small when $\mathbf{j}_Q//\mathbf{a}$. The gap of the fluctuations does not vary a lot between each sample. These coefficients are deduced from the formula 14 given in the Appendix .1.

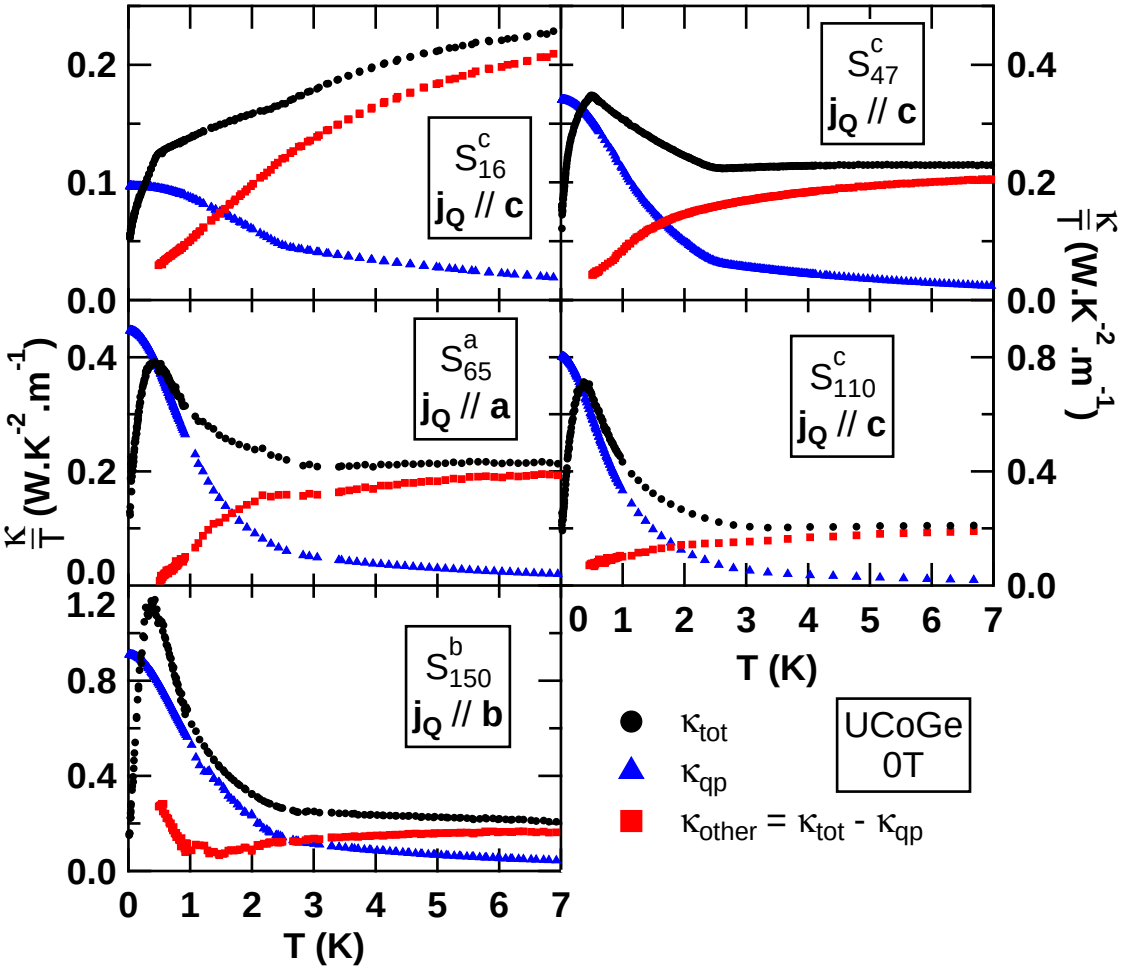


Figure 4.12 *Decomposition of κ_{tot}/T with the electronic (κ_{qp}/T) and the other (κ_{other}/T) contributions of each sample at 0T. The low temperature part is missing due to the superconductivity.*

Sample	α	P ($W.K^{-3}.m^{-1}$)	M_{LT} ($W.K^{-2}.m^{-1}$)	ϵ_{min}^{LT} (K)
S_{16}^{c}	1.14	0.017	0.018	1.24
S_{47}^{c}	2.29	0.009	0.022	0.5
S_{65}^{a}	2.4	0.006	0.003	0.5
S_{110}^{c}	2.5	0.01	0.054	1
S_{150}^{b}	1.36	0.01	**0.45**	0.5

Table 4.1 *α term, amplitudes of the phonon contribution P, of the low temperature contribution M_{LT} and of its gap ϵ_{min}^{LT}. The coefficients are deduced from the formula 14, given in the Appendix .1*

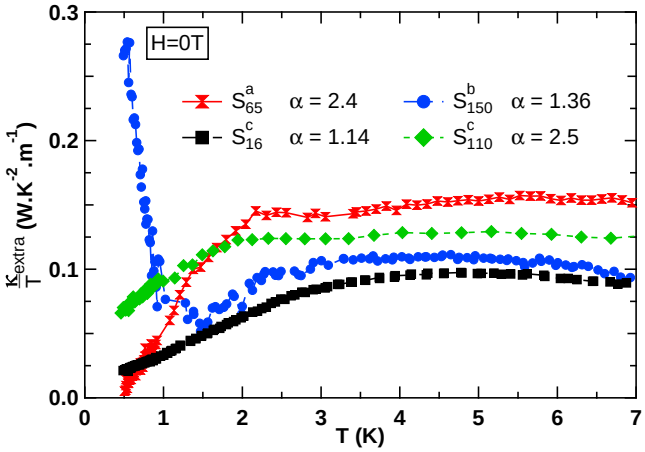


Figure 4.13 *The deduced extra contribution from the mWFL at 0T of all samples. The contributions of the phonons have been removed.*

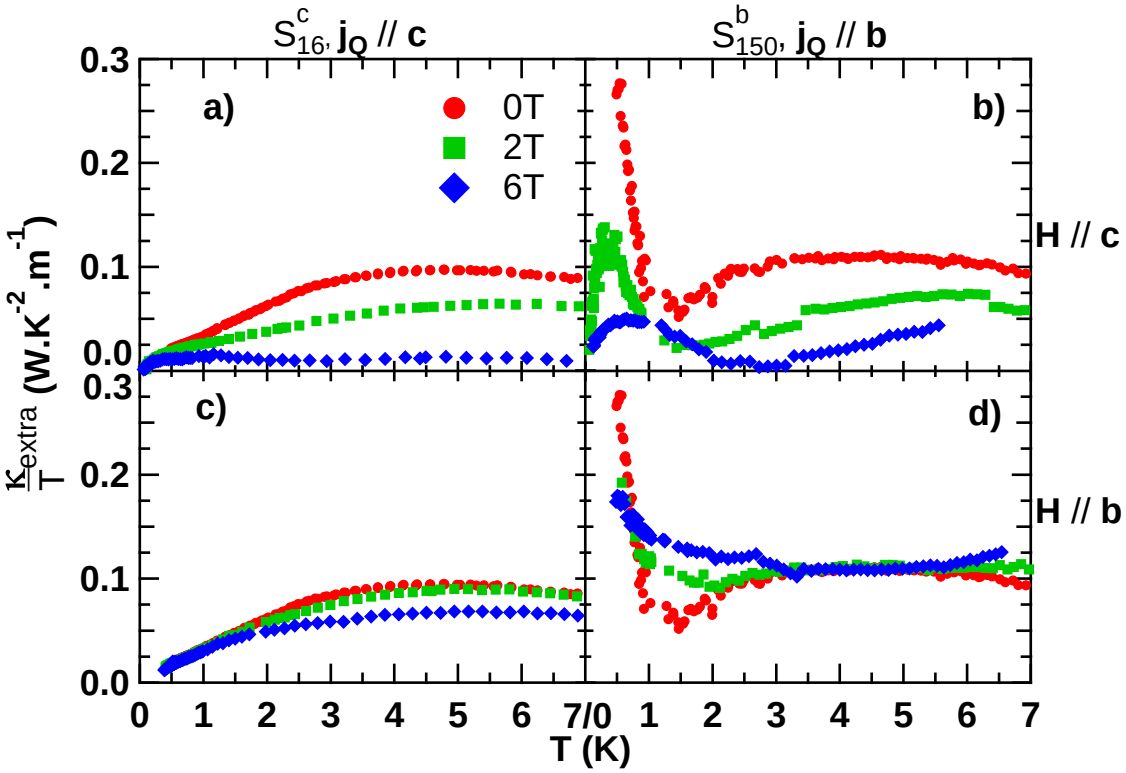


Figure 4.14 *Evolution of κ_{extra} of the thermal conductivity for samples S^b_{150} (panels **a)** and **c)**) and S^c_{16} (panels **b)** and **d)**) at 0T, 2T and 6T. The panels **a)** and **b)** are for **H//c**, with strong suppression of this contribution, and the panels **c)** and **d)** for **H//b**, showing far less field dependence, and a broadening of the low temperature contribution of sample S^b_{150}.*

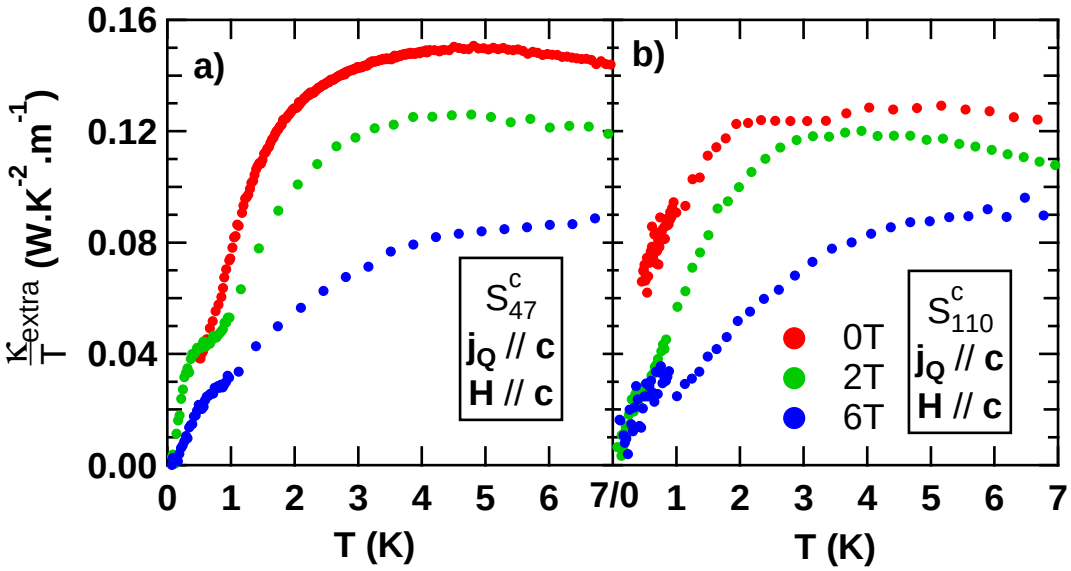


Figure 4.15 *Evolution of the extra contribution with the magnetic field when applied along the* **c***-axis for samples* S^c_{47} *(panel* ***a****)) and* S^c_{110} *(panel* ***b****)).*

4.2.3 Discussion

The preliminary conclusions have been confirmed by the previous study: the existence of an anisotropic extra contribution in UCoGe at low temperature. This extra contribution shows a highly anisotropic magnetic field dependence, the field applied parallel to the magnetization suppresses strongly these excitations, whereas perpendicular to the moments, it has almost no effect (we can guess it is true when **H**//**a**).

These features of κ_{extra}/T are very close to what has been observed by NMR [88, 74]: the magnetic fluctuations are detected at high temperature, from 80K (far above T_{Curie}), and are sensitive to the magnetic field only when applied along the **c**-axis, as shown figure 4.16. By measuring $1/T_1$ and the Knight shift for the three directions of the field, it was also proved that the magnetic fluctuations are purely longitudinal, which is coherent with the strong Ising anisotropy. So it seems reasonable to identify the extra contribution detected by heat transport, to the longitudinal magnetic fluctuations detected by NMR. The new information is that these modes can carry heat, so are not just incoherent local moment fluctuations but propagating modes. Moreover, we find that between 3K and 7K, this contribution depends little of the crystallographic orientation, contrary to the additional low temperature contribution dominant below 1K, which is much stronger along the **b**-axis than along the **c** or **a**-axis. Therefore, the nature of these magnetic fluctuations seems to change when the ferromagnetic order develops.

A most striking feature of our results is the strong anisotropy of the extra contribution appearing below T_{Curie}. Such a strong anisotropy has been also seen on the thermal expansion measurements [60]: at T_{Curie}, there is a large change along the **b**-axis, a smaller along the **c**-axis and almost no change along the **a**-axis, similarly to our measurements. Both effects could be due to the predicted strong change of the Fermi surface below T_{Curie} [180], and its expected feedback on the magnetic excitation spectrum in an itinerant ferromagnet.

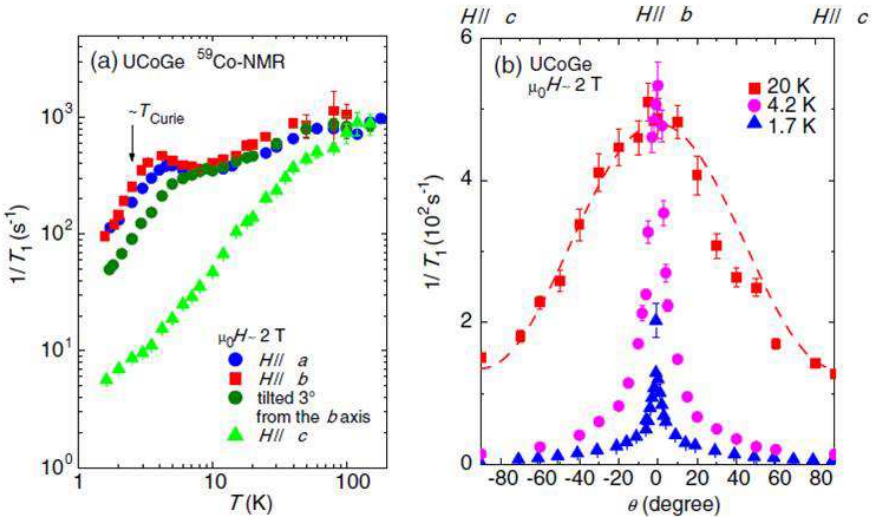


Figure 4.16 *Panel* ***(a)****: Evolution of* $1/T_1$ *by NMR measurements. At 2T, the ratio* $1/T_1$ *does not depend on the field direction when applied along the* ***a*** *and the* ***b****-axis, but is strongly suppressed when applied along the* ***c****-axis, indicating the longitudinal character of the magnetic fluctuations. The suppression starts has high temperatures, approximately 80K. Panel* ***(b)****: Angle dependence of the relaxation rate of the magnetic fluctuations at several temperatures. At 20K (in red), the angle evolution is regular, as seen by the expected sinusoidal behavior (dashed line). At lower temperatures, a sharp maximum lies when* ***H*** *is close to the* ***b****-axis, indicating that the fluctuations are suppressed by the component along the* ***c****-axis of the magnetic field. From [74].*

To go further in the study of the extra contribution, theoretical help is needed. The effect of the spin fluctuations in the thermal conductivity of a nearly ferromagnet or a weak ferromagnet has already been calculated [98, 224, 97], but the calculations take only into account the effect on the scattering rate of the conduction electrons (leading to a negative deviation of the WFL), and not a new heat channel as measured here (positive deviation of the WFL). These effects on κ/T are certainly present in UCoGe, but the large resistivity of our samples makes these spin fluctuation contributions masked by the extra contributions. In other weak (or nearly) magnetic systems, better quality samples are available and the opposite happens: the possible extra contributions are hidden by the large value of κ_{qp}/T. A nice example is $ZrZn_2$ [194], a weak ferromagnet (T_{Curie}=28K, $m = 0.17\mu_B$): the electrical resistivity is $10\mu\Omega$.cm at 50K, for $40\mu\Omega$.cm at 7K in our best sample. This allows to neglect completely the non-electronic contributions and to observe the $T^{5/3}$-law by electrical resistivity and the additional linear term by thermal resistivity predicted by Ueda and Moriya [224]. This kind of scattering rate on the conduction electrons has also be measured in the heavy fermion antiferromagnet $CeRhIn_5$ [156]. A maximum in the thermal conductivity is foreseen in weak itinerant ferromagnet, close to a ferromagnetic instability, with the presence of spin-fluctuations and disorders [157]. However, this effect goes with a minimum in resistivity and is an electronic feature (as it leads to the reduction of the Lorenz ratio, with $L/L_0 < 1$), and so cannot explain our observations. In all the cited theories before, the ferromagnetism comes from the partly filled d-bands, which are responsible for the spin fluctuations, and the conduction electrons from the s-band. The conduction electrons are scattered due to the spin fluctuations via the s-d exchange interaction. Moreover, theory is developped for isotropic 3D systems. In UCoGe, the ferromagnetism arises from the $5f$-electrons, which are characterized

by their duality localized-itinerant. In the case of hybridization between the f-band and others bands, Moriya and Takimoto [145] have calculated that the effects of the spin fluctuations are similar as for d-electron systems. In the case of delocalized f-electrons, a naive picture is that these electrons will only add a new electronic channel, which is included in the WFL. Due to the duality itinerant/localized of the f-electrons in UCoGe, both features can happen at the same time. However, the Ising anisotropy is not treated yet by theories.

In magnetic insulators, it is common that a new heat channel appears at the ordering temperature, or that magnetic fluctuations contribute to the heat transport (see e.g. [195, 78, 119]): the local moment can have a long-range coherence length above the transition temperature. In UCoGe, despite the itinerant character of the ferromagnetism, the same scenario seems to happen. As the previous systems are insulators, the study of the magnetic contribution in the thermal conductivity is easier than in a metal. To our knowledge, it is the first time that spin fluctuations are seen to contribute to thermal conductivity via a new heat channel in a metallic system above T_{Curie}.

In the ordered state, the extra contribution can come from magnons instead of magnetic fluctuations. In Yttrium Iron Garnet systems [158], a ferrimagnetic insulator, it is believed that the phonons and ferromagnetic magnons contributes to the thermal conductivity ($\kappa = \kappa_{ph}+\kappa_m$). A theoretical difficulty with the thermal conductivity of the ferromagnetic magnons that their dispersion relations ($\hbar\omega_k = Dk^2$) can change at low temperature [155]. In metals, the magnons can also be responsible for another heat channel. These have been seen in the permalloys Fe-Ni [241], in the rare-earth antiferromagnet dodecaborides [141] and in the ferromagnetic gadolinium [94]. Note that in that former case, the magnetic contribution represents 3% of the total contribution at 4K. In the latter case, the magnetic contribution appears below T_{Curie} and slowly increases before reaching the maximum in the temperature range 100K-200K (depending on the model for the lattice contribution), and is approximately 10% of the total contribution. The low temperature extra contribution in UCoGe seems similar to this one, with a magnitude of $10-25\%$ at T_{sc} and 0T, according to the sample and the current direction (see figure 4.12). It is clear under field (figure 4.14) that the maximum of this contribution is at around 0.5T at 2T, far below T_{Curie}. If the magnetic contribution has the same shape as the one found in Ga [94], the slow increase from T_{Curie} can explain why no anomaly is detected on UCoGe in κ_{extra}/T. More recently, some extra contributions have been observed in the weak antiferromagnet $YbRh_2Si_2$ [164] in the antiferromagnetic state (T_{Neel}=70mK) at very low temperature (T<30mK) and are assumed to be magnons. Even if the authors do not point out this fact, this contribution seems to survive at fields higher than the critical field. This feature has been confirmed by our measurements (see chapter 5).

Some statistical calculations have been done to determine the thermal conductivity of magnetic systems. Bayrakci *et al.* [19] have calculated the magnetic contribution with four magnons scattering processes without adjusting parameters in the Heisenberg antiferromagnet Rb_2MnF_4. The magnetic contribution increases slowly in the antiferromagnetic state and the maximum is at $T_{max} = T_N/4$. The calculations for 2-D Ising ferromagnet have also been performed [70, 4] with a second-order phase transition. It appears that the thermal conductivity due to the ferromagnetism is maximum at T_{Curie}, which cannot explain our results. The reasons for this discrepancy may come from the fact that the calculations are done for a second-order transition, in a two-dimension system with localized spins.

4.2.4 Conclusion

In conclusion, thermal transport in UCoGe reveals the presence of magnetic fluctuations, identified to the longitudinal fluctuations seen by NMR, with isotropic spectrum above T_{Curie}, and propagation mainly along the **b**-axis at lower temperatures. It supports an itinerant limit for the magnetism of this compound, despite the strong Ising anisotropy of its magnetic properties, a key feature for the understanding of its superconducting properties. The strong anisotropy of the contributions of these fluctuations to thermal transport below T_{Curie} may emerge from the possible dramatic change of the Fermi surface across the ferromagnetic transition [180]. It seems to be the first time that such a contribution is identified in metallic systems, and urges for theoretical investigations of direct heat transport by spin fluctuations in metallic weak ferro- or antiferromagnets.

4.3 Analysis of the Superconducting Phase

4.3.1 Introduction

With the study of the normal state, it is now possible to focus on the superconductivity. The interesting quantity to probe the superconducting state is the electronic quasiparticle thermal conductivity, as the temperature dependence of κ_{qp} can give an idea of the order parameter.

The electronic quasiparticle thermal conductivity in the normal state, $\kappa_{qp,N}$, below 1K is deduced by extrapolating the resistivity at zero temperature, supposing a Fermi liquid behavior ($\rho = \rho_0 + AT^2$) with the previous model (expression 4.3). In the superconducting state (below 0.5K), $\kappa_{qp,N}$ deduced this way depends only little of the value of the α coefficient, even for sample S^b_{150}, which has the largest extra contribution.

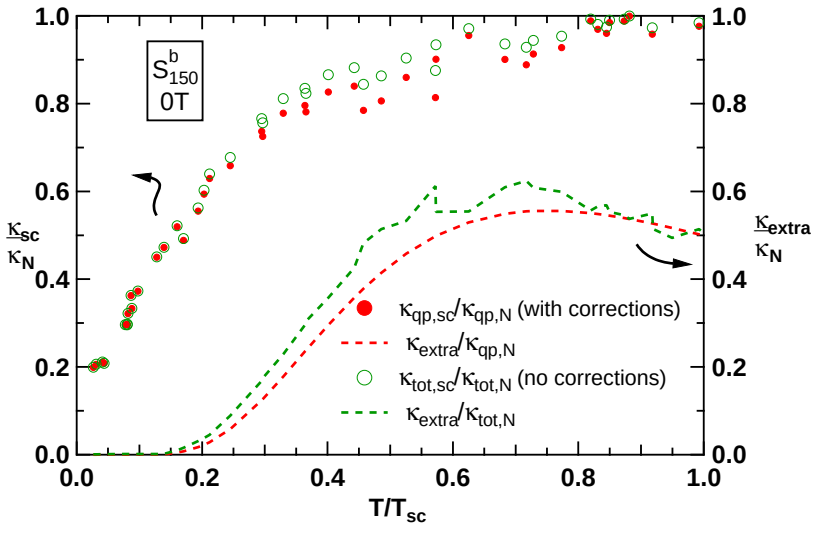


Figure 4.17 *Normalized electronic thermal conductivity of sample S^b_{150}, $\kappa_{qp,sc}/\kappa_{qp,N}$, with the corrections done: $\kappa_{qp,sc} = \kappa_{tot,sc} - \kappa_{extra}$ and $\kappa_{qp,N} = \kappa_{tot,N} - \kappa_{extra}$, κ_{extra} is the estimation of the extra contribution (see text). In the same graph is shown the quantity $\kappa_{tot,sc}/\kappa_{tot,N}$, without any corrections ($\kappa_{tot,N} = \kappa_{qp,N} + \kappa_{extra}$). The dashed lines show the quantities $\kappa_{extra}/\kappa_{qp,N}$ (with the corrections) and $\kappa_{extra}/\kappa_{tot,N}$ (without the corrections).*

In the previous section, it has be seen that the thermal conductivity in UCoGe is composed of an extra contribution in addition to the electronic one, which is supposed not to be electronic. The phenomenological model showed in the Appendix .1 should allow to extrapolate what should be this extra contribution in the superconducting state. However, the extrapolation of the extra contribution in the superconducting state is not very accurate, as it can change in the superconducting state while reproducing the normal state thermal conductivity. Therefore, the electronic quasiparticle thermal conductivity in the superconducting state is approximated as $\kappa_{qp,sc} \equiv \kappa_{tot,sc}$. As it will be seen in the next paragraph, this assumption can be considered to be valid in all samples, except for sample S^b_{150}. In this sample, this assumption is true "by chance" only for the study of the normalized thermal conductivity, as it is seen figure 4.17. The quantity $\kappa_{qp,sc}/\kappa_{qp,N}$, the interesting one, has been corrected with the removal of the extra contribution in the superconducting state using the model used in the Appendix .1, supposing that the extra contribution does not change in the superconducting state, i.e. $\kappa_{qp,sc} = \kappa_{tot,sc} - \kappa_{extra}$. The other quantity, $\kappa_{tot,sc}/\kappa_{tot,N}$, the estimated one, has not been corrected.

Both ratios are very similar, which means that the corrections do not affect drastically the normalized ratio in the superconducting state. The fact that they are similar is explained by the fact that the quantities $\kappa_{extra}/\kappa_{qp,N}$ and $\kappa_{extra}/\kappa_{tot,N}$ are very close. Furthermore, the extra contribution is maximum at zero field and decreases rapidly under field, which means that the corrections in the normalized thermal conductivity are even smaller in the measurements under fields.

As a consequence the approximation $\kappa_{qp,sc}/\kappa_{qp,N} \approx \kappa_{tot,sc}/\kappa_{tot,N}$ is supposed to be valid, even for sample S^b_{150}. In the following of this section, the next notation will be used: $\kappa_{qp,sc} \equiv \kappa_{sc}$ and $\kappa_{qp,N} \equiv \kappa_N$.

In this section, I will first compare the samples at zero field to see the effect of the quality and the anisotropy of the superconducting gap. I will then discuss the results when the field is applied along the **c**-axis and, at the end, the results when $\mathbf{H}//\mathbf{b}$.

4.3.2 Anisotropy at 0T

Figure 4.18 on the left shows the normalized electronic thermal conductivity versus normalized temperature at zero field for the three samples with $\mathbf{j}_Q//\mathbf{c}$. The behavior of the normalized thermal conductivity is similar in the three cases: a small decrease below T_{sc} followed by a faster decrease a lower temperature. The normalized residual term decreases with the increase of the RRR.

Figure 4.18 also shows, as a comparison, the normalized non-electronic thermal conductivity, i.e. $\kappa_{extra}/\kappa_{qp,N}$. Except for sample S^c_{16}, the non-electronic thermal conductivity represents less than 15% of the total signal at the superconducting temperature and is rapidly decreasing when the temperature is lowered. This means that the estimation of the electronic thermal conductivity in the superconducting state is sensitive to the previous model only close to the superconducting transition, the corrections being negligible at lower temperature when $\mathbf{j}_Q//\mathbf{c}$.

Figure 4.18 on the right shows $\kappa_{qp,sc}/\kappa_{qp,N}$ for the current applied in the three directions. It also shows the normalized non-electronic thermal conductivity. As before, the correction is small for samples S^a_{65} and S^c_{110}.

Two regimes are present: a slow decrease below T_{sc} then a faster decrease. As seen previously, the normalized residual thermal conductivity is lower when the RRR is higher. It

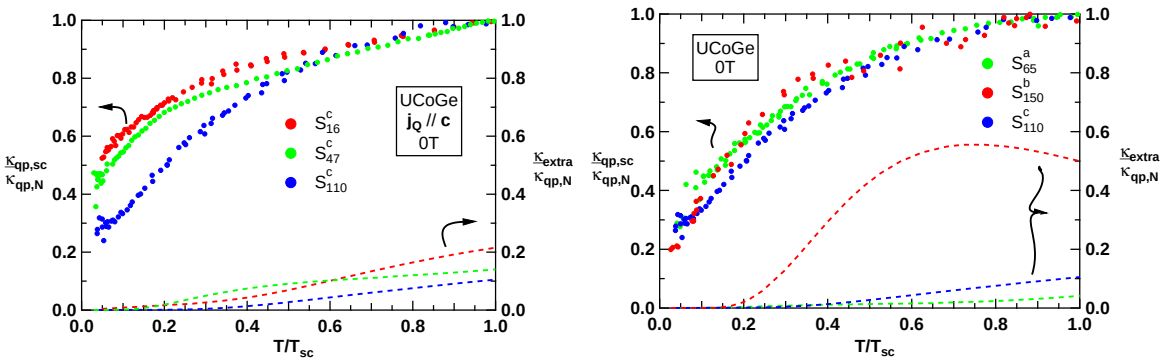


Figure 4.18 *Normalized electronic thermal conductivity ($\kappa_{qp,sc}/\kappa_{qp,N}$) versus normalized temperature at zero field for the three samples with $\boldsymbol{j_Q}$ // $\boldsymbol{c}$ (on the left) and the comparison with the three different directions for $\boldsymbol{j_Q}$. The dashed lines are the normalized non-electronic thermal conductivity ($\kappa_{extra}/\kappa_{qp,N}$).*

is thus not possible to conclude if this is due to gap anisotropy or just the effect of the RRR.

Astonishingly, the figure 4.18 shows also that the normalized thermal conductivity in the superconducting state is rather isotropic, which was not predicted in UCoGe. There may be three explanations: the just mentioned influence of the impurities and defects which dominate the thermal conductivity at low temperature, a hybrid gap, as UPt_3 [71] or multigap effects. Further studies on better samples are needed to discriminate between these scenarios.

4.3.3 H//c

In this field direction, three samples have been measured at low fields: S^c_{16}, S^c_{47} and S^b_{150}. Samples S^c_{47} and S^b_{150} have been measured at very low field to explore multigap superconductivity. The low critical field in this crystallographic direction (H_{c_2} ≈1T) allows the complete study of the superconducting state.

Temperature Dependence

The figure 4.19 displays the temperature dependence of κ/T of samples S^c_{16} (on the left) and S^c_{47} (on the right) with $\mathbf{H}//\mathbf{c}$. The normal phase is fully recovered at 0.5T for sample S^c_{16} and at 1T in the other sample. In the superconducting state, the zero field curve seems to show two regimes: between T_{sc} and 0.15K, κ/T decreases slowly with the decrease of the temperature, and below 0.15K, the decrease is more pronounced and is linear. This change of regime disappears very fast for small applied field: for fields higher than 0.2T, the thermal conductivity decreases linearly from T_{sc} down to the lowest measured temperature. The linear dependence of the thermal conductivity is confirmed in the bottom line of the figure 4.19: at finite field, κ_{sc}/κ_N versus T/T_{sc} shows more or less the same slope for each measured field for sample S^c_{16}.

Field Dependence

The figure 4.20 shows the field dependence of κ/T. In sample S^c_{16}, in the normal phase, κ/T is almost constant and displays a quadratic behavior in the superconducting state (see inset

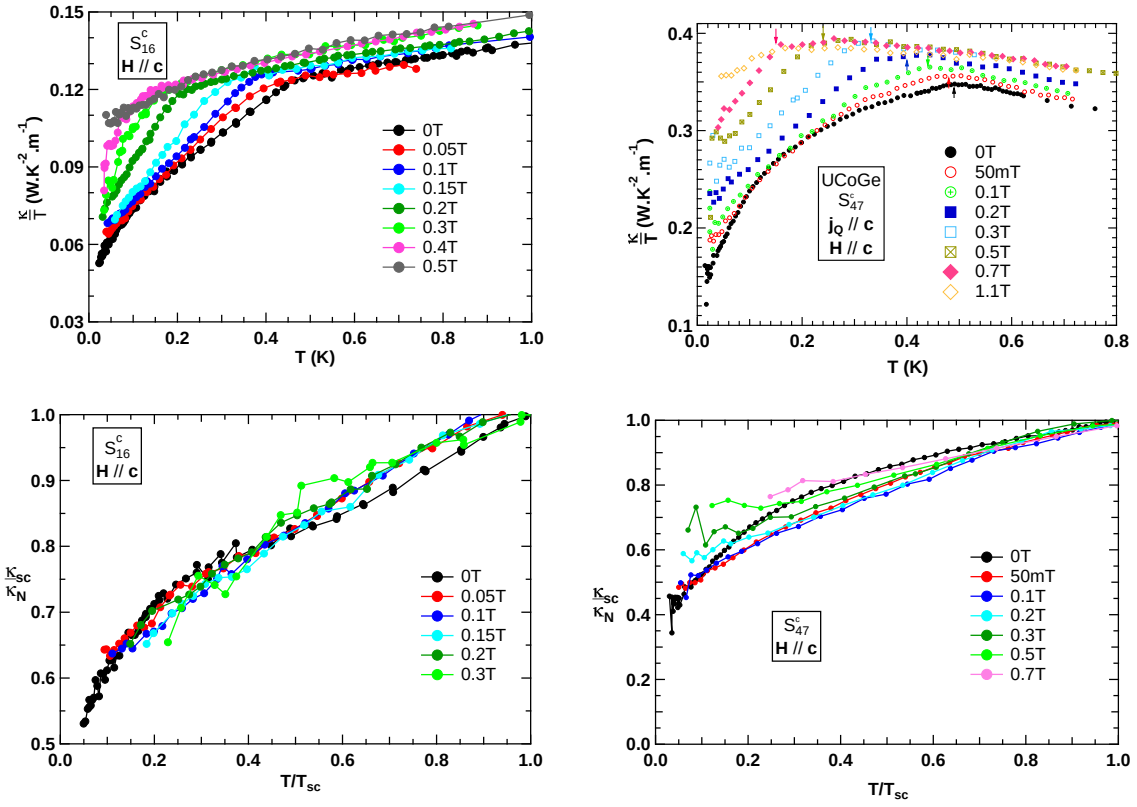


Figure 4.19 *On the top, the temperature dependence of κ/T of samples S^c_{16} (on the left) and S^c_{47} (on the left) with **H//c**. On the bottom, κ_{sc}/κ_N in function of the normalized temperature T/T_{sc}.*

with κ/T vs. H^2). In the two other samples, κ/T has a maximum in the normal phase (measurement at 0.6K and 0.5K respectively). In sample S^c_{47}, except at low fields, κ/T is linear with the field up to the critical field. In samples S^c_{47} and S^b_{150}, the low field regime evolves rapidly with the temperature at low temperatures: κ/T raises rapidly when the field increases below 0.1T, evoking the Doppler shift effect, or the closure of a small gap. The effect of the Doppler shift have been calculated in the case of lines of nodes in the superconducting gap for a *d*-wave superconductor: at zero field or very low temperatures (with respect to T_{sc}), κ is governed by excitations close to the gap nodes and the Doppler shift leads to an increased density of state, so to an increase ($\sim \sqrt{H}$) of κ. At finite temperature, diffusion on the vortices or the energy dependence of the scattering time lead to a decrease of κ with field [228, 113].

At higher temperature, this feature disappears, and the field dependence of κ/T in sample S^b_{150} displays even a minimum at 0.1T. At low temperature, κ/T is almost constant with H in the latter sample.

The evolution of κ_{sc}/κ_N with the normalized field H/H_{c_2} (figure 4.21) displays two different behaviors between zero temperature and finite temperatures: except for sample S^c_{47}, κ_{sc}/κ_N extrapolated at 0T exhibits a plateau from H$\approx 0.1H_{c_2}$ to H$\approx 0.6H_{c_2}$=0.3T, at 60% and 40% of the value in the normal state in samples S^c_{16} and S^b_{150} respectively. The difference of behavior in sample S^c_{47} may be due to the intrinsic misalignment of the sample discussed in the first part of the previous chapter (section 3.1). The three samples show the rapid increase

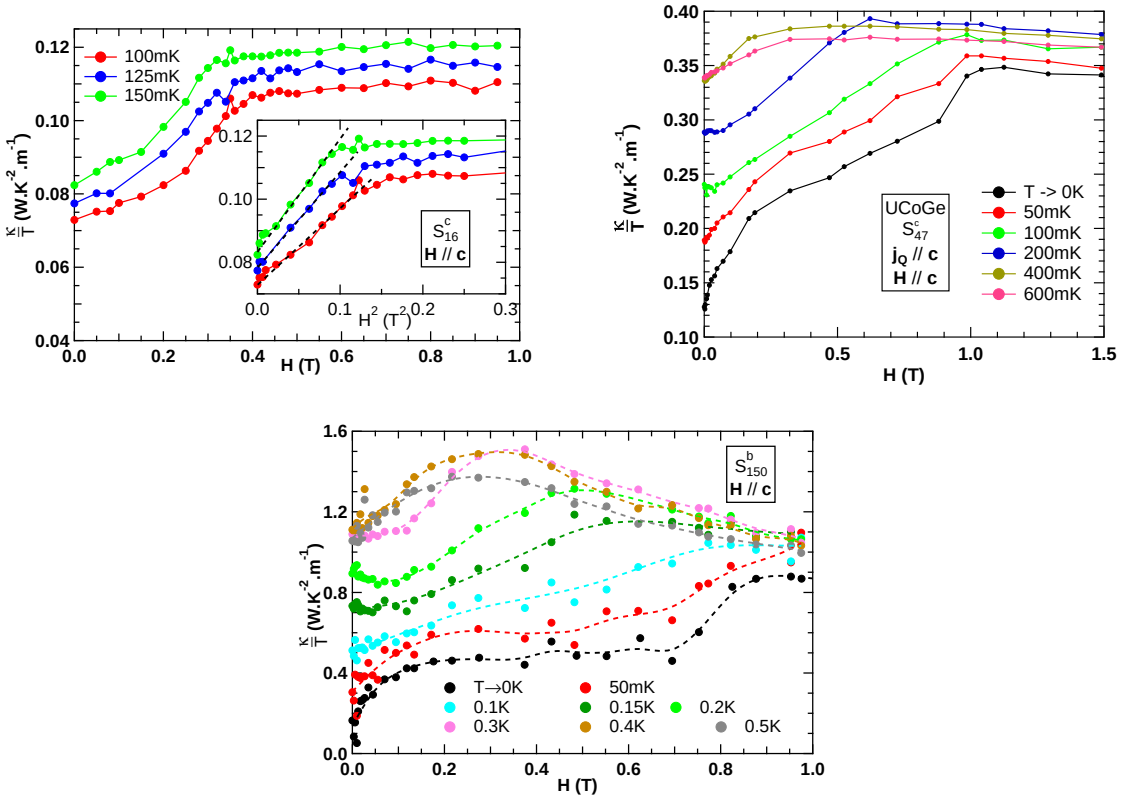


Figure 4.20 *Field dependence of κ/T of samples S^c_{16} (on the left) and S^c_{47} (on the right) and S^b_{150} (on the bottom) with **H**//**c**. In inset is shown the H^2 dependence of κ/T in the superconducting state of sample S^c_{16}.*

at low field when T→0K, and at finite temperature, κ_{sc}/κ_N first decreases with the field then increases again. This behavior is seen also in conventional superconductors, like niobium [120], vanadium [31], or in the heavy fermion UPt_3 [20]. It is attributed to the scattering of the heat carrier by vortices. At low field, vortices have small interactions due to their large distance and provide an additional scattering mechanism. At higher field, the lattice is formed, and, as a result, the vortices do not contribute anymore to the scattering.

4.3.4 H//b

Temperature Dependence

The figure 4.22 shows the temperature dependence of the thermal conductivity of samples S^c_{16} (on the left) and S^b_{150} (on the right) with the field along the **b**-axis. In the first sample, the superconducting transition is clear at all magnetic fields. Except at low field, κ/T seems to shift to lower value with the field, even in the superconducting state. At low field, with the increase of the field, κ/T goes from negative curvature (at 0T) to positive one (from 0.1T): this is may be the effect of the Doppler shift [229] or the closure of a small gap.

The figure 4.23 shows κ_{sc}/κ_N versus T/T_{sc} of sample S^b_{150}. In the superconducting state, there is no clear change of the behavior with the field.

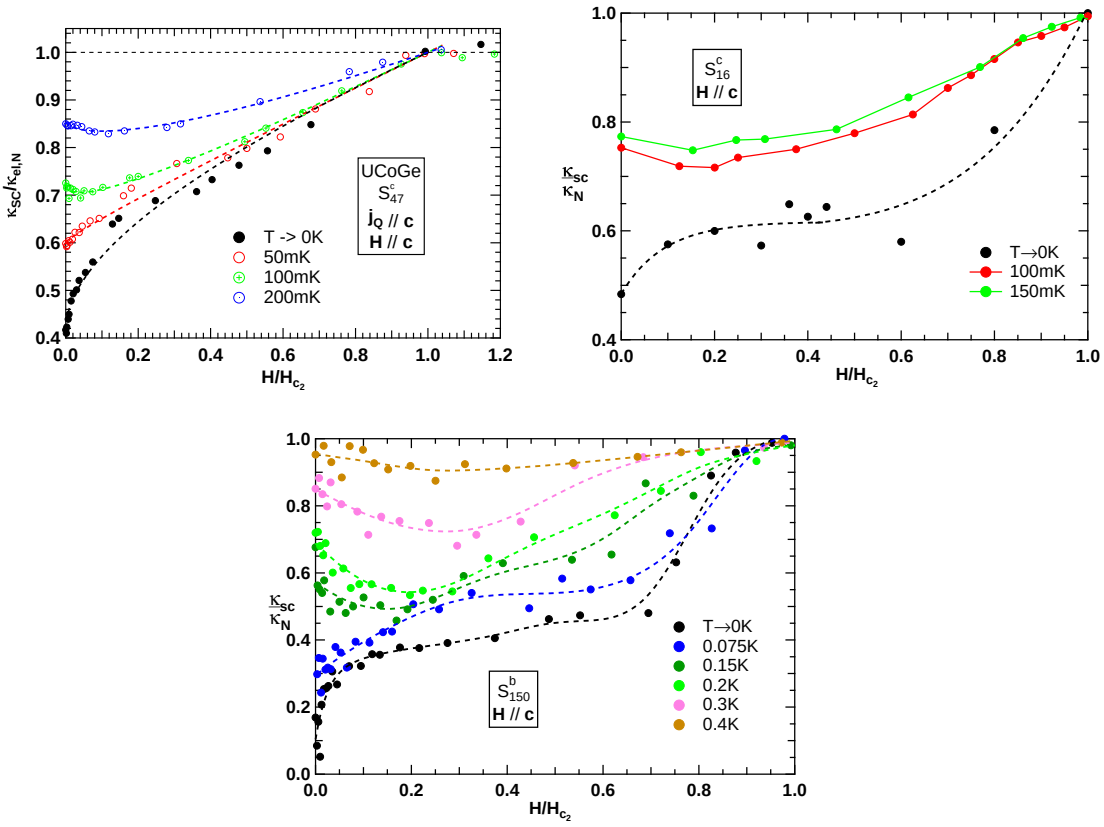


Figure 4.21 *κ_{sc}/κ_N plotted against H/H_{c_2} (on the right) of samples S^c_{16} (on the left), S^c_{47} (on the left) and S^b_{150} (on the bottom) with **H//c**. The dashed lines are guides to the eyes.*

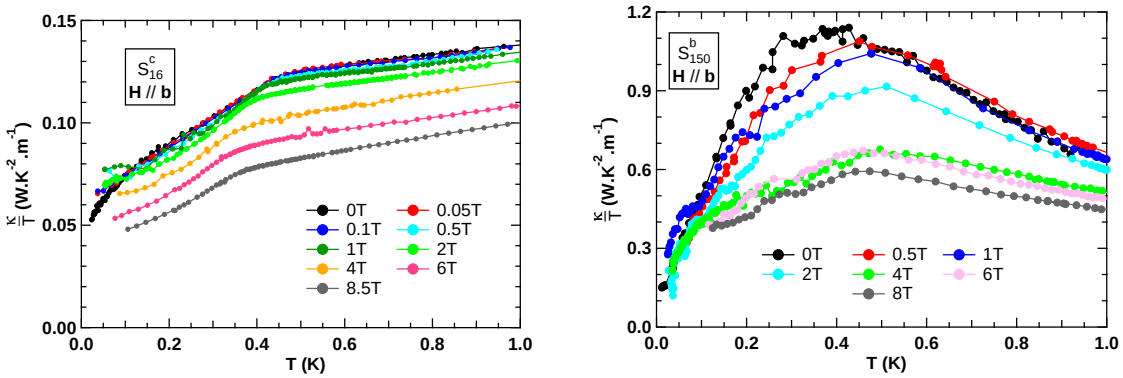


Figure 4.22 *Thermal conductivity in the superconducting state of samples S^c_{16} (on the left) and S^b_{150} (on the right) when **H//b**.*

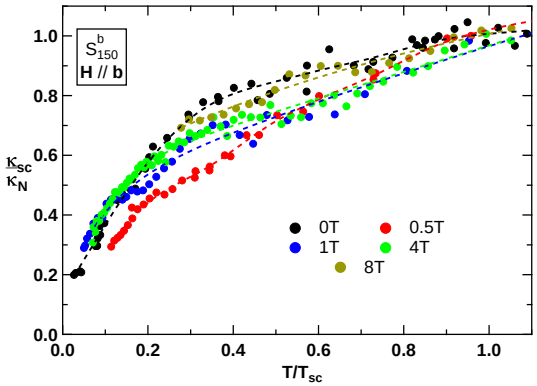


Figure 4.23 *κ_{sc}/κ_N versus T/T_{sc} of sample S^b_{150} when **H//b**.*

The figure 4.24 shows κ_{sc}/κ_N versus T/T_{sc} (on the left) and versus $(T/T_{sc})^2$ (on the right). Below 0.5T, κ_{sc}/κ_N seems linear whereas it is more quadratic above 1T, indicating a possible change of the superconducting gap under field, as the closing of a small gap.

Field Dependence

The figure 4.25 shows the field dependence of the thermal conductivity of sample S^b_{150}. The bare thermal conductivity (on the left) shows that at low temperatures, κ/T is almost constant for H>1T and decreases with the field at higher temperatures. Below 1T, another regime seems to occur. This is more obvious with the normalized thermal conductivity (on the right): κ_{sc}/κ_N shows a slight linear increase above 1T at every temperatures but decreases when the field decreases below 1T. Between 0K and 0.1K, a minimum at around 0.2T appears. This is the same feature as seen when **H//c** (figure 4.21, heat channel created by the vortices).

The increase of κ_{sc}/κ_N at low field when T→0K may be due to the closure of a small gap (in case of multigap superconductivity) or to the Doppler shift. The residual normalized thermal conductivity (figure 4.24) shows the same behavior as the other sample: a first rapid increase up to 1T followed by a saturation up to 8.5T. The same feature, seen on two samples

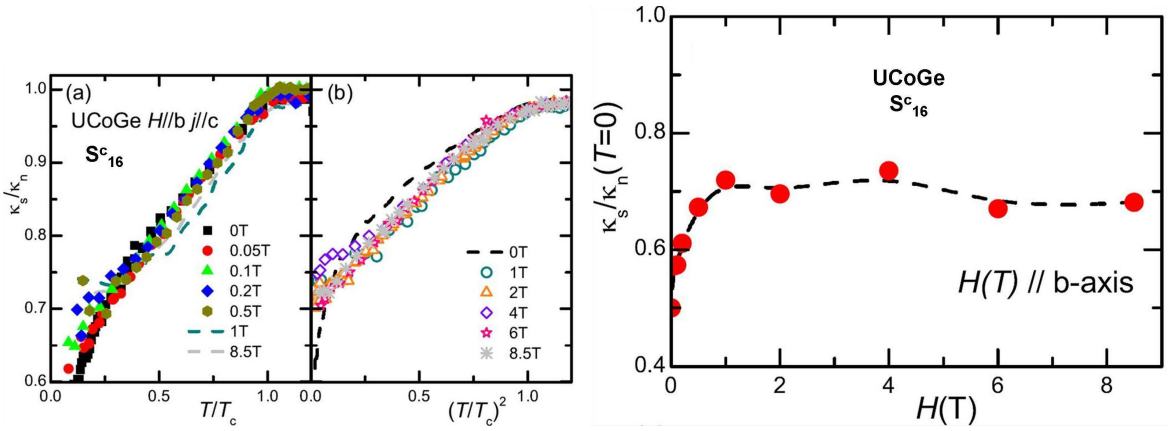


Figure 4.24 *κ_{sc}/κ_N versus T/T_{sc} (on the left) and versus $(T/T_{sc})^2$ (in the middle) and versus H (on the right) of sample S^c_{16} when* ***H//b****.*

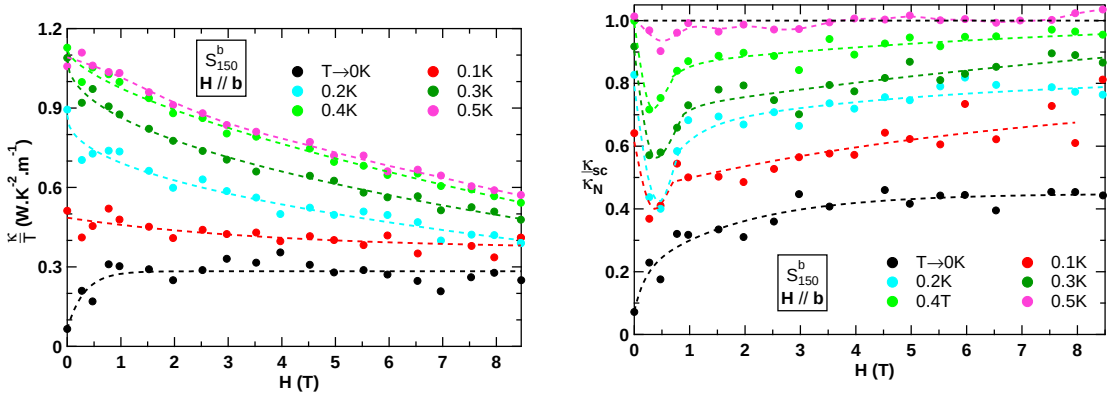


Figure 4.25 *Field dependence of κ/T (on the left) and of κ_{sc}/κ_N (on the right) of sample S^b_{150} when* ***H//b****.*

of very different qualities, confirms the intrinsic character of this increase and this plateau, and acts in favor of multigap superconductivity. The fact that the heat current was along two different axis suggests also an isotropic superconducting gap.

The next step is the measurement of the thermal conductivity above 8T to observe the anomaly (if there is one) at the maximum of the S-shape (H≈11T)

4.3.5 Discussion

The three samples, with different qualities and current directions, display the same properties in the superconducting state. This allows to conclude on their intrinsic characters. The comparison of the normalized residual thermal conductivity between UCoGe extrapolated and other compounds is shown figure 4.26. In this graph, the bulk critical field along the **b**-axis has been taken at $H^b_{c_2}$=50T (the extrapolation to 0K of the slope of the critical field close to T_{sc}). For both field directions, two regimes are visible: first a rapid increase at low field (up to H≈ $0.05H_{c_2}$) then a plateau. A second step is found at $H/H_{c2} \approx 0.8$ when **H//c**. An interesting point, in the case **H//b** is that the superconducting temperature varies barely with

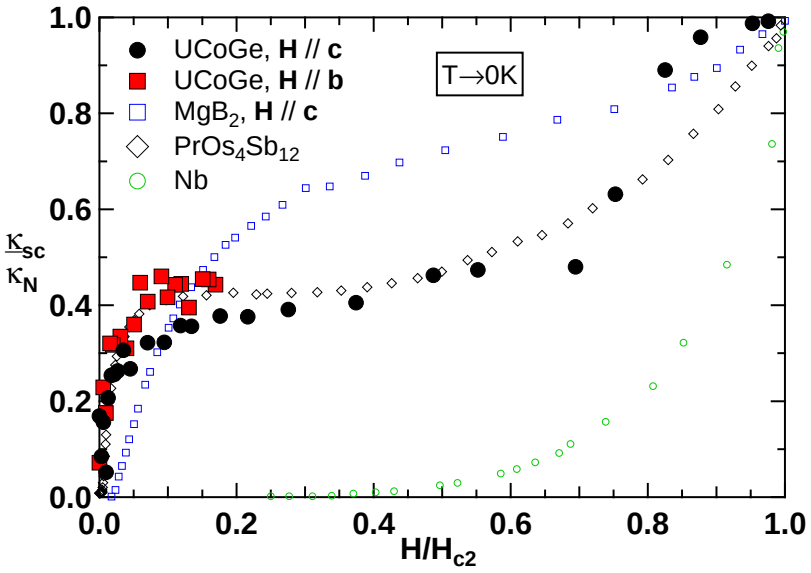


Figure 4.26 *The normalized thermal conductivity versus normalized field extrapolated at zero temperature, when the field is applied along the* ***b*** *and the* ***c****-axis of sample* S^b_{150}*. The critical field is along the* ***c****-axis is* $H^c_{c2} = 1T$ *and, along the* ***b****-axis, has been estimated at* H^b_{c2}*=50T. The figure displays also the thermal conductivity of Nb,* $PrOs_4Sb_{12}$ *and* MgB_2*, with* ***H//c****.*

the field whereas the thermal conductivity increases very rapidly at low fields. This two step behavior is typical of multigap superconductors. By comparison, the thermal conductivity of a one band superconductor Nb [120] and two band superconductors MgB_2 [196] and $PrOs_4Sb_{12}$ [188] is also reported on figure 4.26. This strong resemblance supports that superconductivity is not dominated by the Doppler shift, and tends to confirm the multigap behavior in UCoGe.

4.3.6 Conclusion

Thermal conductivity measurements is the superconducting phase on several samples of different qualities have shown that the regime of universal limit is not reached in UCoGe, which is consistent with multigap superconductivity, as indicated by the measurements. Similarly, the residual normalized thermal conductivity decreases with the increase of the RRR, meaning that there are no intrinsic "unpaired" Fermi sheets, corresponding of the minority and majority spins.

Astonishingly, the first transport measurements act in favor of an isotropic superconducting gap. But the residual term is still large, and we know that this feature could be completely change once pure enough samples will be probed. Multigap superconductivity is also confirmed in UCoGe, in the configurations **H**//**c** and **H**//**b**. The theoretical question is now to determine if the gaps come from the polarized Fermi sheets (due to ferromagnetism), or are caused by band effects (bands with $5f$ character having stronger coupling and so larger gaps than those with little $5f$ character). The next step is to probe the re-entrant superconducting phase at higher fields, and with the field along the hard magnetization axis, the **a**-axis.

Chapter 5

$YbRh_2Si_2$

This last chapter concerns the measurements on the compound $YbRh_2Si_2$, where the ground state lies close to a quantum critical point (QCP), and the absence of superconductivity facilates its study. Contrary to UCoGe, this compound has been intensively studied by very different techniques, and the purpose of ours was first to check the claim, by Steglich's groups, that the Wiedemann-Franz law (WFL) would be violated at the field driving the compound to the QCP [164]. To do so, very low temperature measurements have been done in a large range of fields to compare its effect in the antiferromagnetic phase, close to the QCP, and in the paramagnetic phase, and compare the effects in both phases.

In this chapter, the first section gives general information about $YbRh_2Si_2$, followed by the debate about the violation (or not) of the Wiedemann-Franz law at the quantum critical point. This debate was the motivation to study this system by thermal conductivity at very low temperatures. The third section is the technical description of the measurements. The fourth part is directly the results about the very low temperature measurements, with the discussion about the validity of the WFL, and the last parts are about the results in the whole temperature range, with the estimation of each different contribution to the thermal conductivity.

5.1 Scientific Background

Presentation of the System

$YbRh_2Si_2$, crystallizing in a tetragonal $ThCr_2Si_2$-structure has been first synthesized and studied down to very low temperatures as a candidate for a system very close to a QCP in 1999 [201, 222] (panel **a)** of figure 5.1). It becomes antiferromagnetic (AF) at low temperature, $T_N \approx$70mK (T_N is the Néel temperature) [223], with strong deviations from the Fermi liquid behaviors: non-Fermi liquid behavior (NFL) has been seen by transport ($\rho \sim T$) and thermodynamic measurements. At very low temperature (typically below 30mK), in the AF state, Fermi liquid behavior is recovered. A field of $H_c^{//c}$=0.6T (**H**//**c**) or $H_c^{\perp c}$=60mT (**H**$\perp$**c**) is enough to drive the system back to the paramagnetic phase, leading to a field induced QCP [61]. By applying pressure [108] or by chemical doping [36, 49, 116], a complex phase diagram appears, where paramagnetism, antiferromagnetism and ferromagnetism can be found, indicating a complex competition between the different orders. Below T_N, $YbRh_2Si_2$ exhibits weak antiferromagnetism with small moment $\mu_{ord} \approx 2 \cdot 10^{-3}\mu_B$ (compared to $\mu_{eff} \approx 1.4\mu_B$

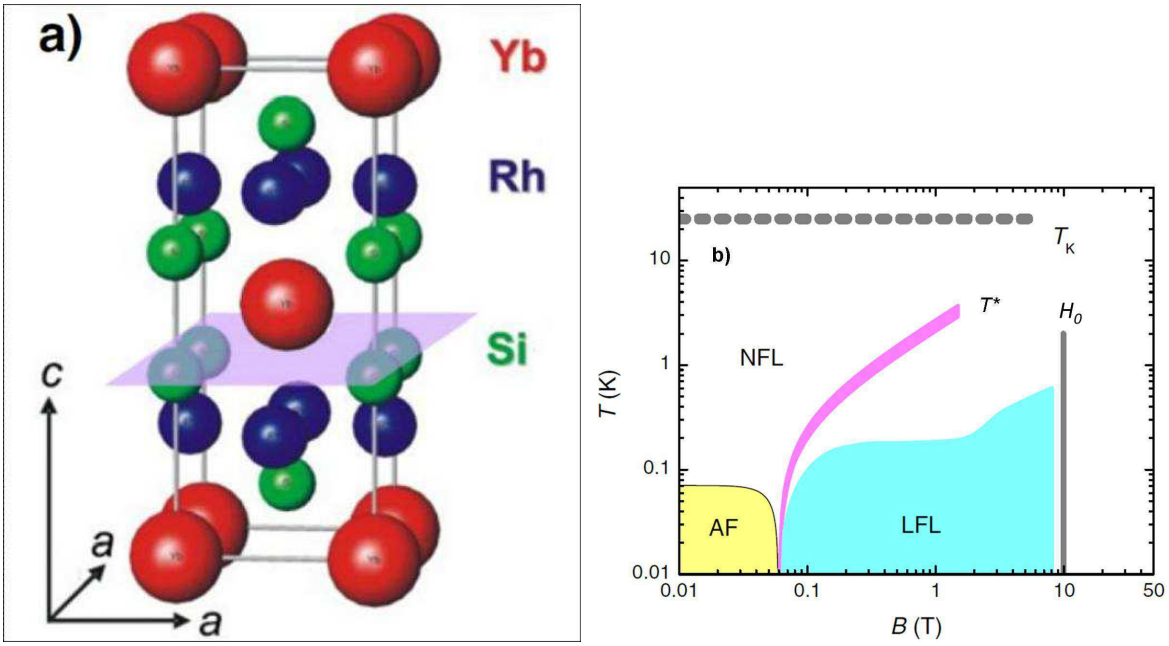


Figure 5.1 *Panel* ***a)*** *the tetragonal structure of $YbRh_2Si_2$ (from [238]). Panel* ***b)*** *the low field phase diagram of $YbRh_2Si_2$, with $\boldsymbol{H}\perp\boldsymbol{c}$. AF is the antiferromagnetic phase and LFL the paramagnetic phase with a Fermi liquid behavior. T^* is a crossover between the two regimes corresponding to the nature of the QCP (Kondo breakdown or Lifshitz transition), T_K is the coherence temperature and a topological transition is suspected to occur at H_0 [169]. Note that in the configuration $\boldsymbol{H}//\boldsymbol{c}$, a similar phase diagram is found. From [63].*

found via the Curie-Weiss law) [89, 37, 90].

In addition to the confirmation of the NFL behavior, Hall effect and thermodynamic measurements have shown the existence of a characteristic temperature T^* from the QCP, independent of the Fermi liquid regime [151] and is attributed to the crossover between the low field ($H < H_c$) and high field ($H > H_c$) regime [56]. The phase diagram is displayed on panel **b)** of figure 5.1. T_K represents the coherence temperature, and a Fermi surface reconstruction is suspected to occur at H_0 [169, 163].

One open question in $YbRh_2Si_2$ is the nature of the QCP: several mechanisms can be responsible for a QCP, as magnetic fluctuations, Kondo breakdown or valence fluctuations (see e.g. [62]). NMR measurements have shown the existence of large ferromagnetic fluctuations in competition with antiferromagnetic fluctuations [91], which are easily suppressed with the magnetic field. At the QCP, the compound shows NFL behavior with an increase of the effective mass, due to critical magnetic fluctuations [90]. It coincides with a change of the Fermi surface (seen with Hall effect). At least two scenarios can explain this: a Kondo breakdown QCP, leading to a change of the Fermi surface volume [160], or a simultaneous antiferromagnetic and topological transition [234]. Numbers of experimental observations can be interpreted with either scenarios, so that the debate about the nature of the QCP remains open [55, 66]. Theoretically, the calculation of the Lorenz ratio should discriminate between these two scenarios, with the violation (or not) of the WFL at the QCP [102].

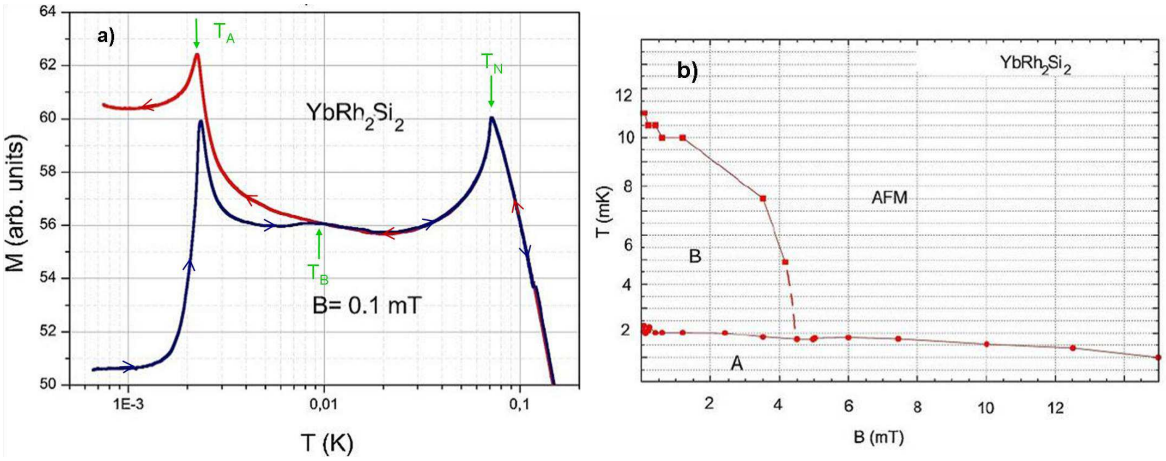


Figure 5.2 *Panel* ***a)*** *magnetization measurements at very low temperature of* $YbRh_2Si_2$ *with* $\boldsymbol{H \perp c}$*, highlighting the additional transitions. The transition to the A phase (*$T_A \approx 2mK$*) is marked by a clear peak (as the AF order at* T_N*) and the B phase by the onset of the hysteresis (the blue line was the measurements with an increase temperature and the red line with its decrease). Panel* ***b)*** *low temperature phase diagram. The B-phase is certainly antiferromagnetic and the A-phase is not determined yet [186].*

Wiedemann-Franz law and Quantum Critical Point

However, there is here another debate, more general, to know if, at a quantum critical point, the WFL will be violated in bulk systems: indeed, some "extreme" scenarios predict that at a QCP, quasiparticles should "desintegrate". This leads to a finite lifetime of these quasiparticles down to T=0K, and so to a possible violation of the WFL at T→0K, due to the decreased thermal transport compared to the electrical transport. Despite its simple assumptions, the WFL is very robust and it is very difficult to violate at zero temperature. Several QCP have been probed by thermal conductivity, and the validity of the WFL has been observed in $CeNi_2Ge_2$, which is close to a QCP [99], and through the QCP of the strontium ruthenate $Sr_3Ru_2O_7$ [175]. On the other hand, some violations have already been reported experimentally. To my knowledge, the first case reported was in the copper-oxides $(Pr,Ce)_2CuO_4$ [81], and later in $(Bi,Sr)_2CuO_6$, close to a metal/insulator transition [21, 171]. In $CeCoIn_5$, anisotropic violation of the WFL has been claimed (depending on the direction of the heat current) near the QCP [215], which points to an anisotropic destruction of the Fermi surface. Recently, the violation of the WFL has been reported in YbAgGe [43], but the very complex phase diagram and the not-so-low measurement temperatures (T>40mK) can give the erroneous conclusions. Note that none of these claims have been checked by independent measurements. A strong violation is possible when a spin-charge separation occurs [232], but this situation is closer to violation due to superconductivity (separation of charge and heat carriers) than to QCP.

Furthermore, erroneous violations have been reported due to extrinsic effects (like bad contacts on the sample): the first measurements of the thermal conductivity in MgB_2 reported strong deviation of the WFL at low temperature [196], and other measurements on different samples validated the law [197]. These examples show that only few compounds exhibit violation of the WFL, confirming its robustness. An experimental limitation, responsible for the lack of experimental data on the violation (or not) of the WFL at the QCP, is that

it often lies inside a superconducting dome (the extrapolation at zero temperature may be thus not enough accurate to conclude on its violation), and the number of systems without superconductivity at the QCP is rather limited. In $YbRh_2Si_2$, the validity of the WFL is not clear, and measurements by other groups have opposite conclusions about its violation [164] or not [124, 173]. An additional difficulty in this system is the presence of very low temperature phase transitions below T_N detected by magnetization measurements (see panel **a)** of figure 5.2) [185, 186]: a transition occurs at 12mK, which seems to be also an antiferromagnetic order, and disappears for H>5mT. Another one lies at 2mK (not determined yet), which is less sensitive to the field (see panel **b)** of figure 5.2). These transitions can produce additional magnetic fluctuations, and influence the inelastic scattering of the thermal conductivity at unusually low temperatures. With this in mind, measurements on $YbRh_2Si_2$ at very low temperature have been done at several fields, below the critical field and at several fields above.

Note also that new physics happens at higher field in $YbRh_2Si_2$: at 9.5T, the system seems to lose its heavy fermion character [218] with a strong decrease of the effective mass, and with another possible Lifshitz transition [169, 163], with a strong increase of the magnetization. Our measurements, however, were confined to fields below 4T.

5.2 Description of the Debate

Before arguing on the violation or the validity of the WFL at the QCP, let us first review where the debate comes from.

The figure 5.3 shows the thermal and electrical resistivity ($w_{th} = L_0T/\kappa$), measured by Pfau *et al.* [164], for $H < H_c$ at 0T (panel **a**), close to the QCP at 60mT (panel **b**) and above the critical field (0.3T (panel **c**) and 1T (panel **d**)). At 0T, a kink is visible at 70mK, corresponding to the Néel temperature. The Lorenz ratios at 0T and 60mT are displayed panel **e**, and at 0.3T and 1T panel **f**. At 0T and 60mT, the Lorenz ratios are very similar, indicating that the magnetic field has an effect mainly on the elastic electronic scattering (same effect on the electrical and thermal resistivities). However, below 30mK, the Lorenz ratios increase to become superior to 1, indicating the existence of an extra heat channel. This is very unusual at such low temperatures, where only the electrons usually contribute to the thermal resistivity. The appearance of this new channel can be attributed to magnons due to the low Néel temperature, or due to fluctuations caused by the lower temperature transitions (see figure 5.2), or maybe both. Anyway, in Pfau's paper, it is supposed that the WFL is expected to be verified at zero field when T→0K, and the thermal resistivity should increase again at lower temperature, and reach the value of the electrical resistivity.

The measurements at 60mT, very close to the QCP, show the same behavior at low temperature. In that case, deviations is attributed to the overdamped magnons. At 0.3T and 1T, such deviations are not seen, maybe due to the not low enough temperature measurements (T>60mK at 0.3T and 1T).

This low temperature feature is the reason why the violation of the WFL (or not) in $YbRh_2Si_2$ is still under debate: it appears at very low temperature (below 30mK), and the measurements done in the literature do not go at such low temperature at every fields measured [164, 124, 173]. The whole point is to know how one should subtract the extra contribution, in order to extrapolate the electronic quasiparticle thermal conductivity κ_{el}/T down

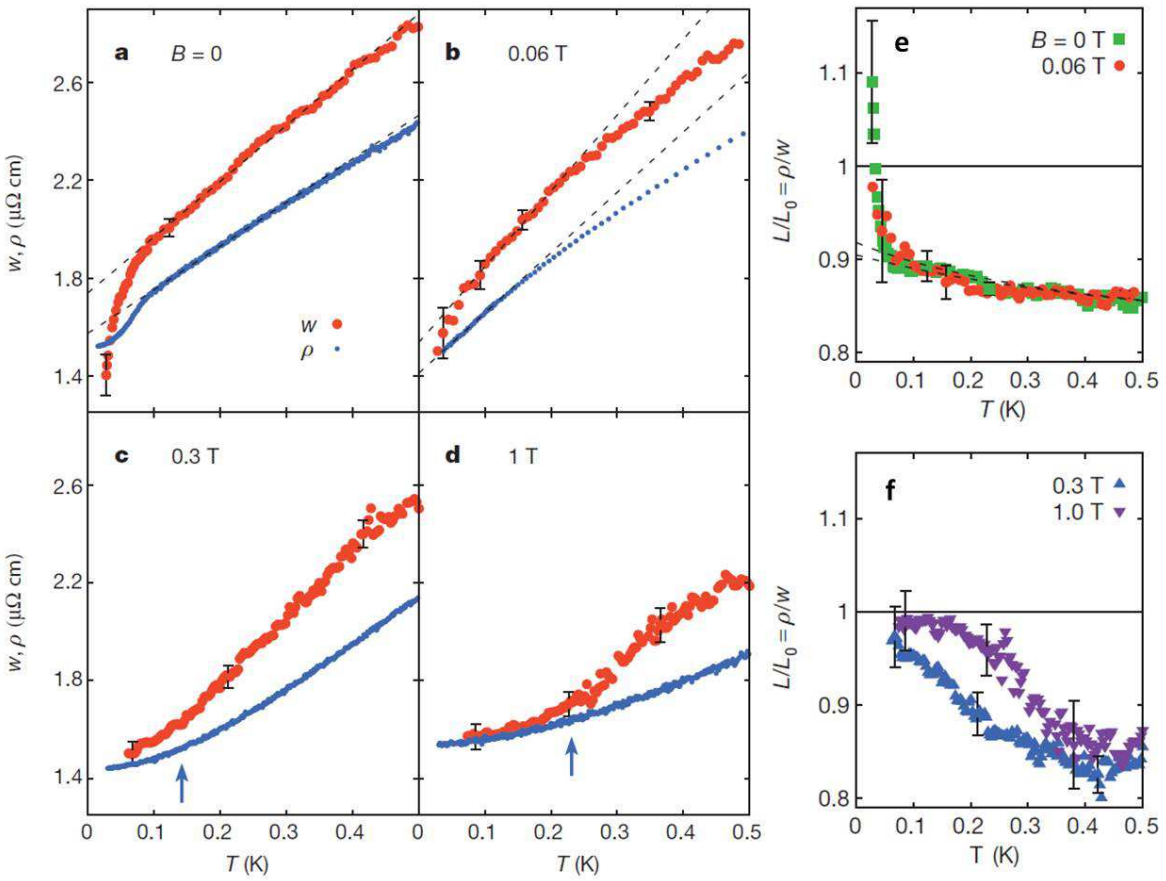


Figure 5.3 *Thermal (w_{th}) and electrical (ρ) resistivities, measured by Pfau et al. [164], below H_c at 0T (panel **a**), close to the QCP at 60mT (panel **b**) and above H_c (0.3T (panel **c**) and 1T (panel **d**)). The Lorenz ratios at 0T and 60mT are displayed panel **e**, and at 0.3T and 1T panel **f**.*

to 0K, and compare it to charge transport.

In our study, we endeavored to extend the measurements to temperatures as low as possible, and, by making analysis similar to those made in UCoGe, we intended to check of the measurements were compatible or not with the WFL.

5.3 Technical Description

The measured sample was grown by indium flux, the good quality single crystal is confirmed by the high RRR, RRR≈ 65. It is bared shape along the [110] direction (perpendicular to the **c**-axis) and its large length, 1.5*0.14*0.14 mm^3, give the opportunity to have a large geometrical factor (l/S≈555cm^{-1}), facilitating the measurements. The magnetic field was applied parallel to the current (longitudinal configuration: $\mathbf{H}//\mathbf{j}_Q//[110]$), up to 4T. The low field regimes were measured with a Hall sensor, to know precisely the value of the magnetic field applied. The experimental setup was the one used for UCoGe. Thermal conductivity was checked to be independent of the heat gradient applied, which was in the range $\Delta T/T \in [0.5, 20\%]$. Pictures of the sample on the thermal conductivity stage are shown figure 5.4.

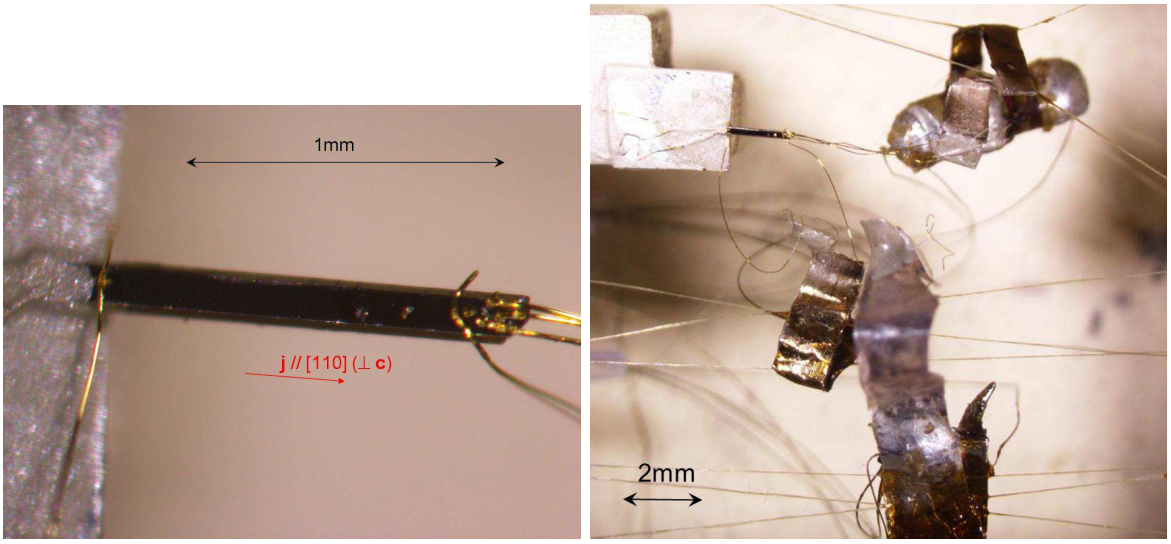


Figure 5.4 *Sample of $YbRh_2Si_2$ on the thermal conductivity set-up.*

A special effort has been done to perform the measurements at the lowest temperatures. Except at 3T and 4T, the thermal conductivity (with the electrical resistivity) has been measured down to 10mK, and the resistivity at 0T down to 7mK. To be able to distinguish the non electronic contribution, κ has been measured up to 7K at each field.

5.4 Results of the Very Low Temperature Measurements

Before showing the complete analysis of $YbRh_2Si_2$ under field, this subsection will only focus on the very low temperature measurements.

Comparison between H=0T and H=H_c

The figure 5.5 shows the thermal and electrical resistivities ($w_{th} = L_0T/\kappa$) at 0T (in red) and close to the QCP at 70mT (in blue), with a zoom in the low temperature part (upper inset) and the Lorenz ratio (lower inset). At 0T, a nice kink is visible at 70mK by electrical and thermal resistivity, corresponding to the Néel temperature. The results of our measurements are similar to those obtained by Pfau *et al.*. Thermal and electrical resistivities are very similar at 0T and 70mT above 1K. However, the Lorenz ratios are identical down to 70mK. Below 3K, the thermal resistivity is higher than electrical resistivity (so with a Lorenz ratio inferior to 1), indicating the electrical quasiparticle thermal conductivity is dominated by inelastic scattering. However, below 25mK, the Lorenz ratios increase to become superior to 1, in agreement with previous results [164].

Below 0.1K, the magnetic field affects the thermal resistivity only in the neighborhood of T_N=70mK, whereas the influence of the field is more prononced on the electrical resistivity. Furthermore, between 0T and 70mT, the Lorenz ratio is almost field independent, despite strong critical fluctuations around T_N, leading to marked anomalies on ρ and w_{th} in zero field. This may indicate that these critical fluctuations are mainly horizontal processes (dominated by large q_0), and therefore affect similarly ρ and w_{th}, or that the excess of vertical processes at T_N is compensated by the additional channel of the spin fluctuations. Below 50mK, the

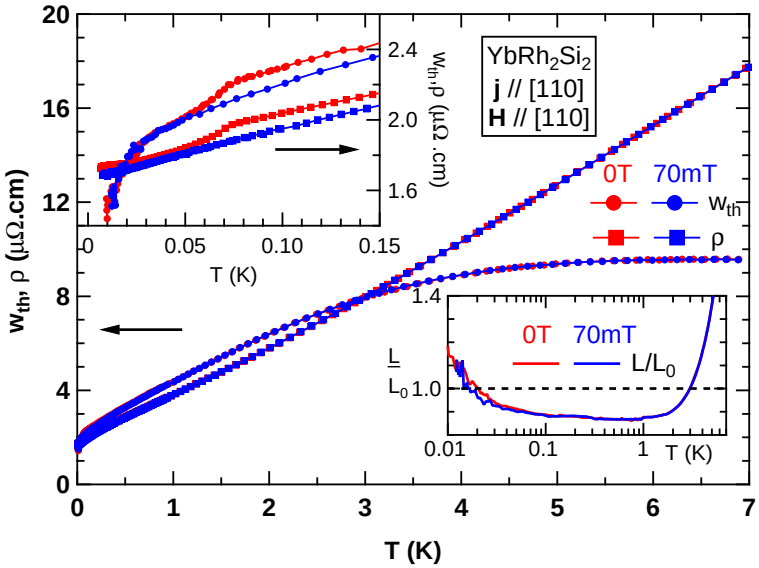


Figure 5.5 *Thermal (w_{th}) and electrical (ρ) resistivities at zero field (in red) and 70mT (in blue). The upper inset shows the zoom in the low temperature part. The lower inset displays the Lorenz ratio.*

thermal resistivities are identical, but not the electrical resistivities: a simple explanation is that the thermal resistivity is no longer dominated by the electronic quasiparticle contribution but by another one, almost field independent below 70mT. The fact that this effect appears below the Néel temperature reveals the possible magnetic nature of this new contribution. In any case, no phonon contribution is expected in this temperature range. Furthermore, the insensitivity to the field between 0T (in the antiferromagnetic state) and 70mT (in the paramagnetic state) seems to indicate that the contribution is not induced by magnons (which should be absent at 70mT), but more likely by magnetic fluctuations, and that they have the same nature at 0T and 70mT.

Field Dependence

The field dependence of the thermal conductivity of this very low temperature feature is shown figure 5.6, up to 0.1T. In inset is shown the corresponding electrical resistivity. With the increase of the field, (and the decrease of the Néel temperature), κ/T increases, except at very low temperatures (below 25mK), whereas the electrical resistivity is field dependent in the whole temperature range (except at low temperature in the AF state). This result is the same as the one displayed figure 5.5: the thermal conductivity is barely affected by the magnetic field at low temperature, even in the paramagnetic state.

The stronger increase of κ/T by decreasing the temperature below 20mK is better seen of the Lorenz ratio, figure 5.7 up to 0.5T, with the thermal conductivity in inset. Note that the Lorenz ratio does not extrapolate to 1, but to 0.97 ($L(\mathrm{T}\rightarrow 0\mathrm{K})\approx 0.97L_0$), the extrapolated value for fields higher than 0.5T (see also figures 5.12). This feature is robust as it happens at each field, this may be intrinsic or due to a small experimental error. Nevertheless, the fact that this value does not change with the field means that it cannot be seen as a violation of the WFL at the QCP. In the following, particularly to deduce the electronic contribution, the

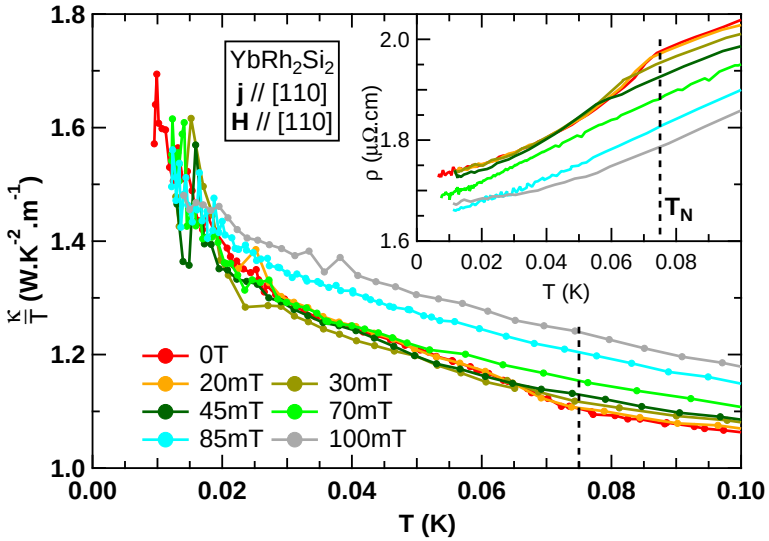


Figure 5.6 *Thermal conductivity and electrical resistivity (in inset) of $YbRh_2Si_2$ below 0.1K and below 0.1T. The vertical dashed lines represent the Néel temperature at zero field.*

Lorenz number taken is the value found for T→0K, and is called $\overline{L_0} = 0.97L_0$. Back in figure 5.7, the horizontal dashed line represents $L = \overline{L_0} = 0.97L_0$. The deviation of the Lorenz ratio at very low temperatures occurs at least up to 0.5T, much higher than the critical field H_c=0.06T.

The fact that the deviations occur for fields much higher than H_c (up to 1T in our measurements) confirms that magnons cannot be responsible for the extra contribution, as it occurs in the paramagnetic state. By increasing the magnetic field, the deviation of the WFL is getting smaller, which means that the effect responsible for this disappears.

Study of the Low Temperature Extra Contribution

This situation is similar to what has been observed in UCoGe: an extra contribution, maybe due to magnetic fluctuations, appears at low temperatures. To be able to estimate the low temperature extra contribution, a study similar to UCoGe is performed: the thermal conductivity at very low temperatures was supposed being composed of only the electronic quasiparticle contribution and this extra contribution, i.e. $\kappa = \kappa_{el} + \kappa_{extra}^{LT}$. To estimate κ_{el}, we used the same formula used to study UCoGe (expression 4.3 of the section 4.2.2):

$$\frac{\kappa_{el}}{T} = \frac{\overline{L_0}}{\rho_0 + \alpha(\rho - \rho_0)} \tag{5.1}$$

The α term (superior to 1) represents the effect of the inelastic scattering on κ. At these very low temperatures (below 0.1K), it is reasonable to suppose that this hypothesis is correct.

The figure 5.8 shows the thermal conductivity at very low temperatures (T<0.1K) at zero field, at 70mT (close to H_c) and at 0.27T (far above H_c). For the three fields, the best value of α is the same, with $\alpha = 2.2$. The determination of κ_{el} this way seems correct only at very low temperature at 0T and 70mT, and in a larger temperature range at 0.27T.

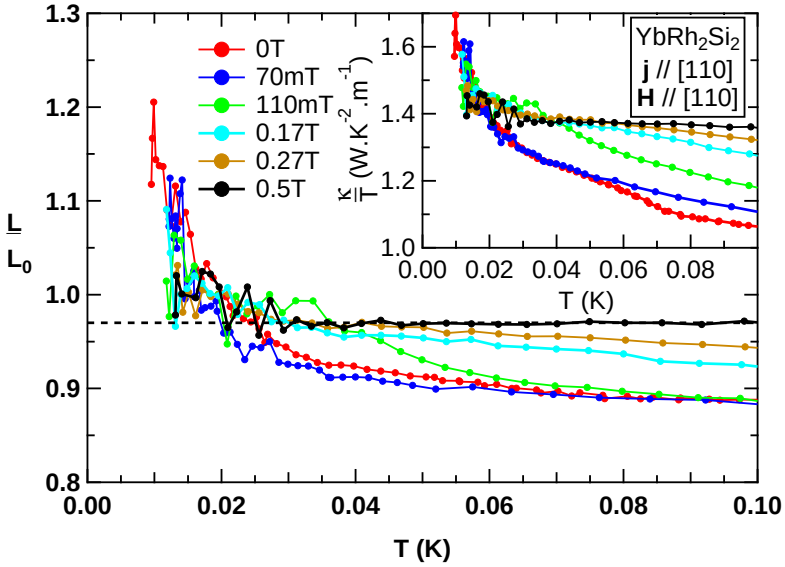


Figure 5.7 *Lorenz ratio at very low temperature (below 0.1K) and below 0.5T. In inset is shown the thermal conductivity. The deviation at very low temperature occurs at field much higher than the critical field (0.5T≫ H_c=0.06T). The horizontal dashed line represents $L = \overline{L_0} = 0.97L_0$.*

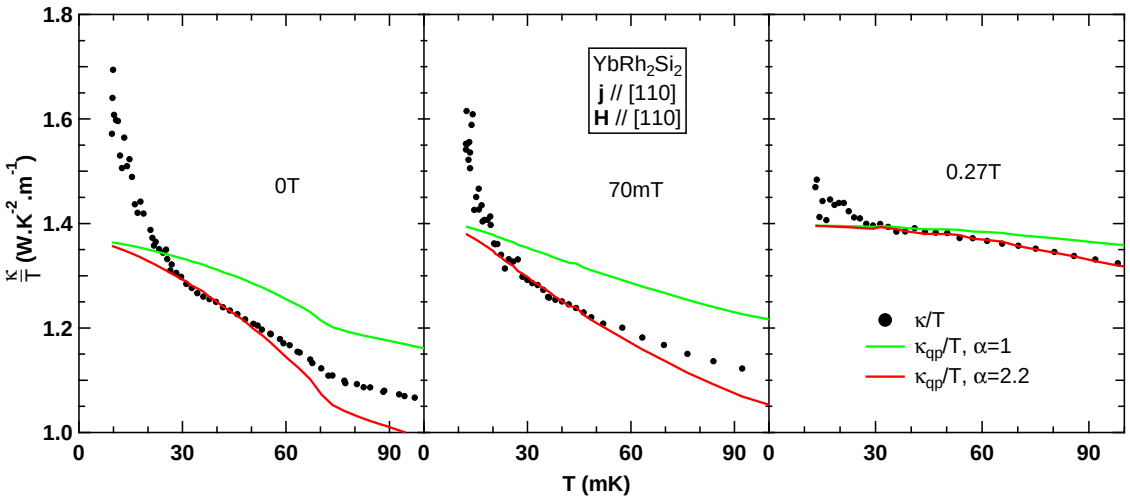


Figure 5.8 *Comparison of the electronic quasiparticle thermal conductivity using the expression 4.3 of the section 4.2.2 (used for UCoGe) with $\alpha = 1$ and $\alpha = 2.2$. The α term was determined to reproduce the low temperature thermal conductivity.*

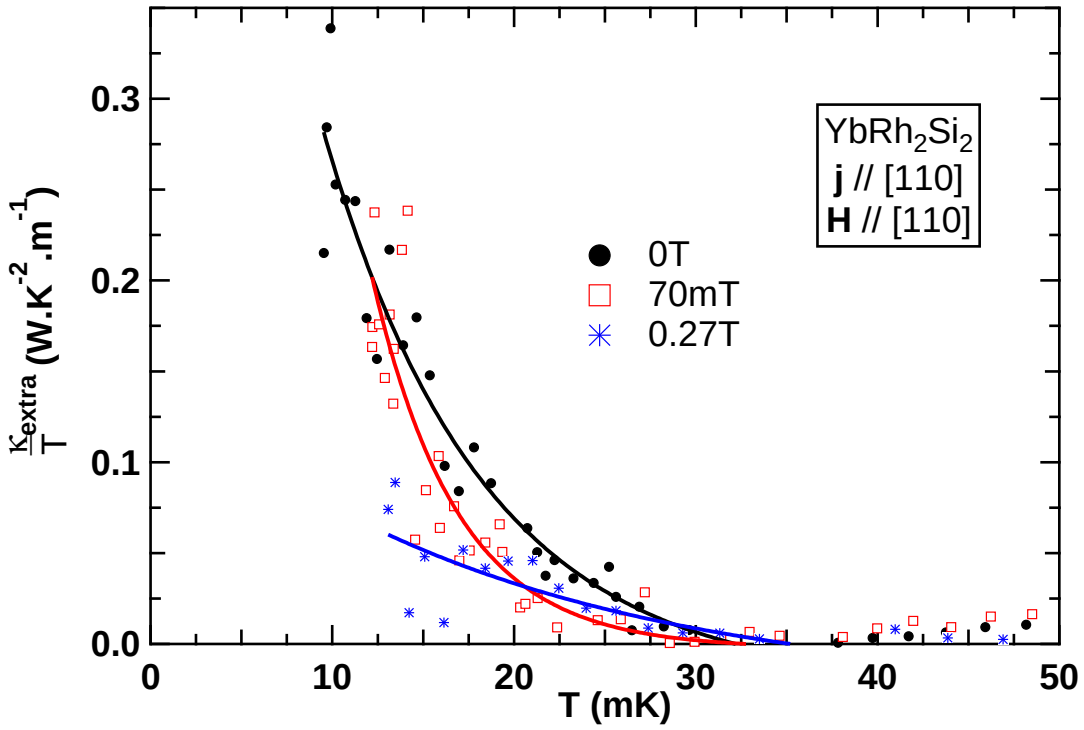


Figure 5.9 *Estimation of the very low temperature extra contribution to the thermal conductivity at 0T, 70mT and 0.27T. No significant changes are seen between 0T and 70mT, indicating that* κ^{LT}_{extra} *has certainly the same origin at both fields.* κ^{LT}_{extra} *exists for field higher than* H_c*, but the signal is smaller.*

With this approximation, it is possible to estimate the extra contribution at very low temperatures, $\kappa^{LT}_{extra} = \kappa - \kappa_{el}$. The comparison of κ^{LT}_{extra}/T at 0T, 70T and 0.27T is shown figure 5.9. No significant change of κ^{LT}_{extra}/T is visible between 0T and 70mT, indicating the possible same origin at both fields. For fields higher than H_c, the extra contribution is still detectable, but with a smaller signal. This conclusion does not depend on the way to determine κ_{el}, a different model gives the same results (see the next section for the description of the model from the measurements for T>40mK, the results obtained on the determination of κ^{LT}_{extra}/T are shown in the Appendix .3).

As a conclusion of this part, the extra contribution is seen at fields below and above the critical field H_c with no peculiar evolution except for a gradual decrease with the applied magnetic field. This has been deduced with an hypothesis for electronic quasiparticle contribution which also has no peculiar evolution accross H_c (α=2.2=constant).

Concerning the WFL, it is not possible to conclude by direct measurements its violation or not: measurements should be extended at lower temperatures, down to the mK temperature range (see figure 5.2). Note however that our data, which are perfectly compatible with those by Pfau *et al.*, can be analysed supposing a valid WFL.

5.5 General Results

The previous paragraph was dedicated only to the very low temperature measurements under fields. Nevertheless, the measurements were performed up to 7K and 4T. The following is the description and the discussion of these results at higher temperatures.

5.5.1 Description

For visibility reasons, the results below 1T and above 1T are shown in separated figures.

The measurements are displayed on figures 5.10 (the resistivity) and 5.11 (the thermal conductivity). At low temperatures (below 1K), the magnetic field drives the system toward a Fermi liquid behavior (the resistivity goes from a linear to a quadratic temperature dependence). Above 0.1T, the upward curvature of ρ is more and more pronounced in the whole temperature range with the increase of the field: the inelastic term of the resistivity decreases strongly with the increase of the magnetic field (decrease of the A coefficient of the resistivity law, in the case of a Fermi liquid behavior: $\rho = \rho_0 + AT^2$). The temperature at which the Fermi liquid behavior is recovered increases with the magnetic field, as the system is driven away from the magnetic instability.

At the same time of the appearance of the Fermi liquid behavior, the thermal conductivity stops "diverging" at low temperature but saturates instead. From 2T, a maximum appears in κ/T at low temperatures (≈0.2K), and the value of the maximum and the temperature where it appears seem to increase with the magnetic field.

In insets are shown the measurements up to 7K. Above 1K, the resistivity decreases with the magnetic field (inset of figure 5.10), but the thermal conductivity has a much less pronounced field dependence (inset of figure 5.11). This seems to indicate that the thermal conductivity is dominated at high temperature (above 1K) by extra contributions in addition to the electronic quasiparticle one.

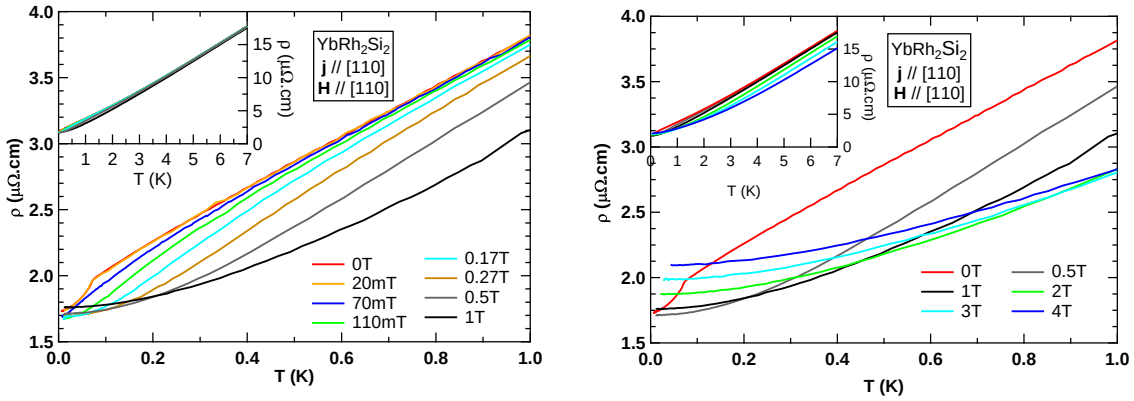


Figure 5.10 *Electrical resistivity of $YbRh_2Si_2$ below 1K and 1T (left panel) and above 1T (right panel). In insets are shown the same quantities in the whole temperature range.*

The Lorenz ratio is displayed figure 5.12, with the low field measurements (H<1T) on the left and the high field one (up to 4T) on the right.

At low field (up to 0.1T), between 0.1K and 0.5K, the Lorenz ratio is below 1, and almost constant down to 0.1K, with $L/L_0 \approx 0.87$. Below 0.1K, L/L_0 increases rapidly when

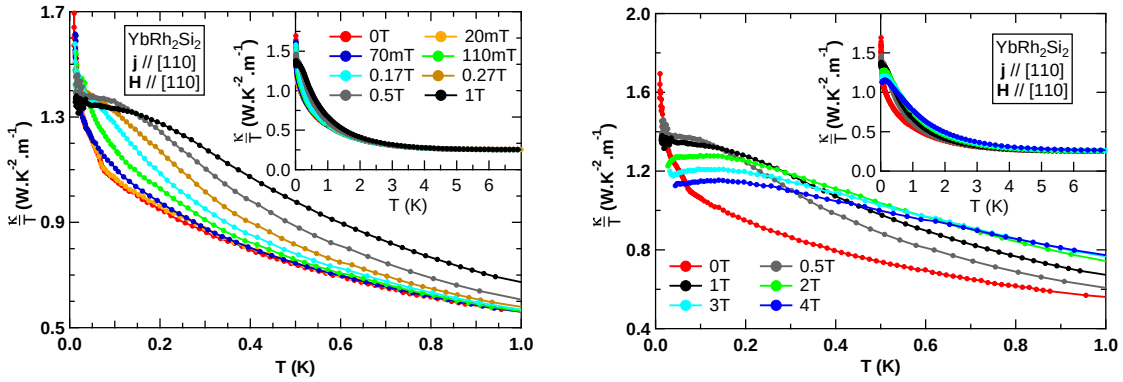


Figure 5.11 *Thermal conductivity of $YbRh_2Si_2$ below 1K ant 1T (left panel) and above 1T (right panel). In insets are shown the same quantities in the whole temperature range.*

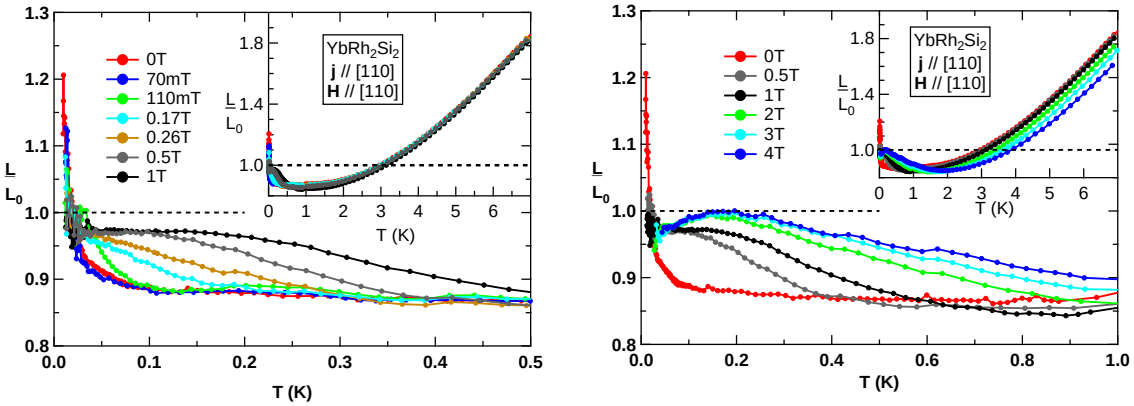


Figure 5.12 *Lorenz ratio below 1T (left panel) and up to 4T (right panel) below 1K. In insets are displayed the Lorenz ratios in the whole temperature range.*

the temperature decreases and goes above 1. The field range were the Lorenz ratio shows the plateau is approximately the same where the Seebeck coefficient (S/T) measured by thermoelectric power is constant [125] (by rescaling with the critical field, as the measurements have been performed in the configuration $\mathbf{H}//\mathbf{c}$). With the increase of the field, the Lorenz ratio increases at low temperature. Below 1T, the very low temperature violation of the WFL is visible at each field.

Above 1T, similarly to thermal conductivity, the Lorenz ratio displays a maximum at low temperature before reaching its zero temperature value $\overline{L_0}$. This unusual behavior may be the signature of the appearance of a new heat channel at low temperature under field or a change of the electronic quasiparticle contribution, and will be discussed in the next section. Above 2K, the Lorenz ratio decreases with the magnetic field (see the inset of the right panel of figure 5.12). This cannot be the effect of the reduction of a magnetic contribution to the thermal conductivity (as in UCoGe), indeed κ/T is almost field insensitive above 2K, whatever the magnetic field (see insets of figures 5.11).

Field sweep measurements have been performed up to 4T, below the Néel temperature (45mK), just above (0.1K) and far above (0.5K). The magnetic field dependence of the thermal conductivity and the resistivity of $YbRh_2Si_2$ are displayed figure 5.13. In insets are shown the low field part (below 0.5T). The dashed lines are guides to the eyes to distinguish the different behaviors, the vertical dotted line represents the critical field at 0K, H_c=60mT. κ/T and ρ have almost the same behavior, as respect from the WFL, I will thus only discuss the thermal conductivity results. At 45mK, κ/T is almost constant below 50mT, and then increases rapidly before reaching a maximum at 0.2T. Above this field, the thermal conductivity decreases linearly with the field. A similar behavior is seen at 100mK, with a maximum at 0.5T, and at 0.5K with a much broader maximum at 2T. The field at which the step-like increase begins is raising up with the temperature, and this increase becomes broader at higher temperatures.

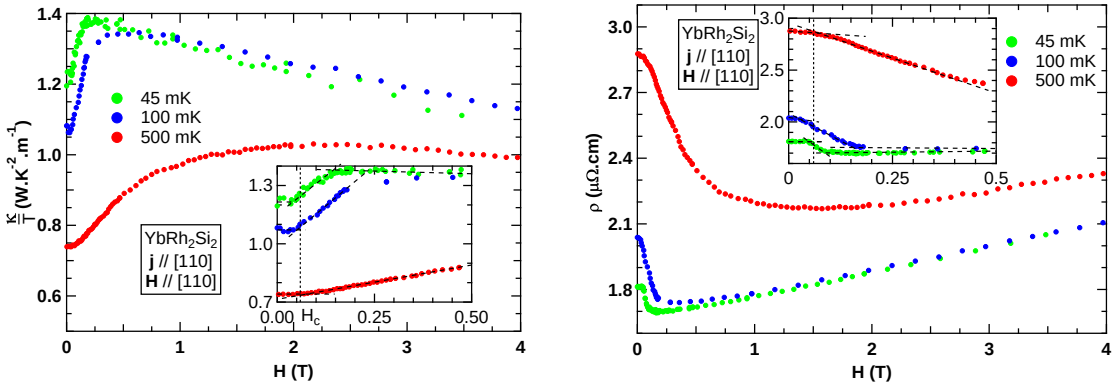


Figure 5.13 *Left panel: thermal conductivity in function of the field below the Néel temperature (45mK), just above (0.1K) and far above (0.5K). Right panel: corresponding resistivity. In insets are shown the low field part (below 0.5T). The dashed lines are guides to the eyes to highlight the changes of regimes, and the vertical dotted line represents the critical field at zero temperature (H_c=60mT) as a reference.*

The Lorenz ratio is shown figure 5.14 in the whole temperature range (left panel) and below 1T (right panel). As for the thermal conductivity and the resistivity, dashed lines have been added as guides to the eyes to distinguish different regimes. At 45mK and 0.1K, two regimes are visible: below approximately 0.2T, the Lorenz ratio varies rapidly, and then much less above this field. Above 0.2T, at 45mK, the Lorenz ratio decreases slowly with the field, and at 0.1K, it is almost constant up to 4T, with $L/L_0 \approx 0.97$. At 0.5K, a minimum appears at 0.45T, as reported in previous studies [164, 163, 124], which is believed to be related to T^*, the crossover between the low field and high field regime (see the phase diagram figure 5.1). By looking at the low field part at 45mK and 0.1K, the Lorenz ratio is almost constant below 60mT and 0.12T respectively, followed by a step-like increase. At 45mK, the step-like increase seems to start at 60mT, the critical field, but the noise in the measurements prevents to determine precisely the onset. The constant Lorenz ratio at low field does not seem related to the Néel temperature, as it is visible at 0.1K up to 0.1T. This plateau is maybe also linked to the constant Seebeck coefficient measured at low field [125].

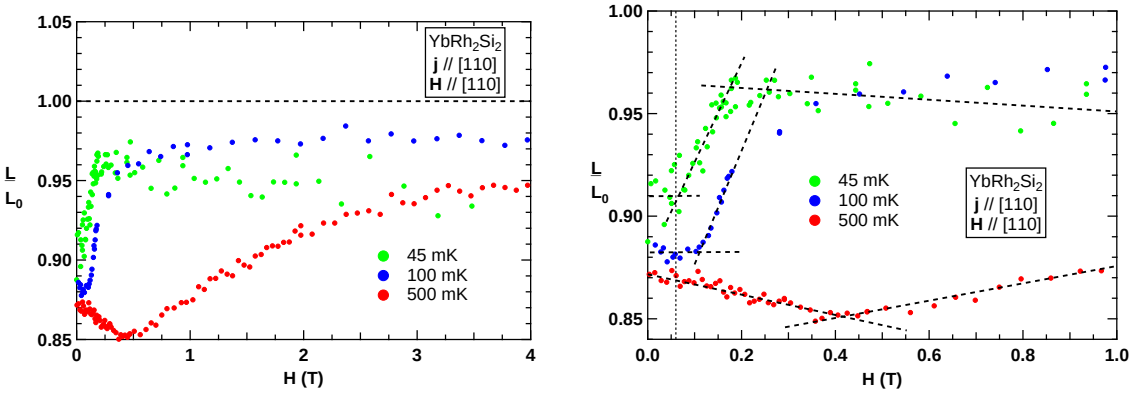


Figure 5.14 *Lorenz ratio in function of the field below the Néel temperature (45mK), just above (0.1K) and far above (0.5K), in the whole temperature range (left panel) and below 1T (right panel). The dashed lines are guides to the eyes to to highlight the changes of regimes, and the vertical dotted line represents the critical field at zero temperature (H_c=60mT) as a reference.*

5.5.2 Analysis

Resistivity

The study of the resistivity gives the A coefficient and the residual resistivity ρ_0, when the Fermi liquid behavior is expected: $\rho = \rho_0 + AT^2$. The values found, shown figure 5.15, are in agreement with the results reported in the literature: the A coefficient decreases strongly above the critical field, and the residual resistivity is constant in the antiferromagnetic state, decreases abruptly at the critical field and then increases linearly. The A coefficient is found to follow the law $A \sim H^{-1}$ close to H_c (but above), then $A \sim H^{-0.5}$ state above 0.4T, similar to what has found Knebel *et al.* [108], but in disagreement with the measurements of Gegenwart *et al.* [61]. Note that below 0.1T, the A coefficient is poorly defined: the fits are done below 40mK.

Study of κ at High Temperatures

The next step is an attempt to decompose the thermal conductivity into the different contributions. Like for UCoGe, the heat channels are assumed to be additive: $\kappa = \kappa_{el} + \kappa_{ph} + \kappa_{extra}$. Only the electron-phonon scattering is assumed to limit the phonon contribution, leading to $\kappa_{ph} = PT^2$, with P a temperature and field independent parameter.

The very low temperature part (below 30mK) has been discussed in the previous section and thus will not be discussed here. As $L/L_0 < 1$ in a large range of temperatures, and the deviation above 1 at high temperature (T>3K) is moderate (L/L_0 is always below 2 at 7K), we will first assume that only the electrons and the phonons contribute to the thermal conductivity, i.e. $\kappa_{extra} = 0$.

In $YbRh_2Si_2$, it has been seen by NMR and neutron scattering that magnetic fluctuations are present [91, 204]. At zero field, by lowering the temperature, the magnetic fluctuations go from commensurate (similar to a ferromagnet above the Curie temperature) to incommensurate fluctuations (in the (**a**,**b**) plane). By applying a magnetic field, ferromagnetic fluctuations are also detected [204]. These ferromagnetic fluctuations are even dominant in the paramagnetic state down to 0.2K. This is in line with the proximity of ferromagnetic order by applying

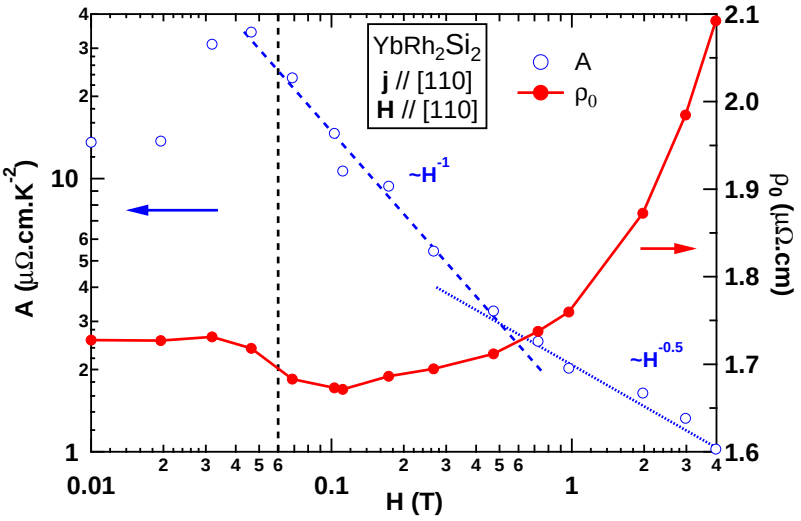


Figure 5.15 *A coefficient and the residual resistivity in function of the magnetic field. The vertical black dashed line shows the critical field H_c=60mT. Close to H_c, the A coefficient behaves as $A \sim H^{-1}$ (blue dashed line), then $A \sim H_c^{-0.5}$ (blue dotted line).*

pressure and chemical doping [108, 116]. That is why, except at low temperatures/low fields, $YbRh_2Si_2$ is seen as a ferromagnet above its Curie temperature.

The effect of ferromagnetic spin fluctuations on electrical and thermal resistivities (ρ and w_{th} respectively) have been predicted by Ueda and Moriya[1] [224]. When T$\gg T_{Curie}$:

$$\rho = \rho_0 + aT \tag{5.2}$$

$$w_{th} = w_1 + w_2 \tag{5.3}$$

$$= BT + \rho \tag{5.4}$$

In the case T$\gg T_{Curie}$, Ueda's theory predicts a linear behavior of the resistivity, which is true in a large range of temperature for each field measured here (see figure 5.10), but not at low temperature. As a consequence, the equation 5.4 is a justification of the model used to determined the electronic quasiparticle thermal conductivity in UCoGe, by taking into account the inelastic scattering with an α term (equation 4.3), with α independent of the temperature.

In the following, I will not try to decompose the electrical resistivity, and the next expression is used for the electronic thermal conductivity:

$$\frac{\kappa_{el}}{T} = \frac{\overline{L_0}}{w_{th}} = \frac{\overline{L_0}}{\rho + BT} \tag{5.5}$$

Such a type of electronic thermal conductivity has already been used in non-Fermi liquid regime, like in the weak ferromagnet $ZrZn_2$ [194].

[1]For the thermal resistivity, Ueda used the definition $w_{th}^{Ueda} = 1/\kappa$ in his paper, whereas I used here the same one as used previously, that is to say $w_{th} = \frac{\overline{L_0}T}{\kappa} = w_{th}^{Ueda} T.\overline{L_0}$.

By now, we have the formula for the thermal conductivity:

$$\frac{\kappa}{T} = \frac{\kappa_{el}}{T} + \frac{\kappa_{ph}}{T} \tag{5.6}$$

$$= \frac{\overline{L_0}}{\rho + BT} + PT \tag{5.7}$$

The expression 5.7 is very simple, as ρ is determined experimentally and the parameter P is field independent. Only the parameter B can vary with the field.

At low field, in the antiferromagnetic state and at the proximity of the QCP, the system is dominated by antiferromagnetic fluctuations, and thus the expression 5.7 is no longer valid. At high field (above 1T), the thermal conductivity shows a maximum at around 0.1-0.2K, certainly due to the appearance of a new heat channel, and is not incorporated in expression 5.7. Both features will be treated later on. As a consequence, the first analysis are done at high temperatures (basically above 1K), where the system is supposed to be dominated by ferromagnetic fluctuations.

The figure 5.16 shows the best fit of the thermal conductivity at high temperatures using formula 5.7. To see the deviation, the fit is extended to the lowest temperatures. At high temperatures, the expression 5.7 reproduces rather well the measurements. At low temperatures, two regimes are present: at low field, the fit (in black) overestimates the thermal conductivity (in red) whereas at higher field (above 0.5T), the fit underestimates the thermal conductivity.

At low field, the deviation might come from the appearance of the antiferromagnetic fluctuations [204]: $YbRh_2Si_2$ cannot be seen anymore as a ferromagnet above the Curie temperature at low temperatures. Above 0.2T, the estimated thermal conductivity does not overestimate anymore the total thermal conductivity: the antiferromagnetic fluctuations may have been totally suppressed by the magnetic field, and the simple model used could be valid in the whole temperature range. However, an additional deviation appears above 0.5T and keeps growing and spreading at higher temperatures with the magnetic field. This could be due either to an additional contribution, or to a change of the electronic thermal conductivity. As L/L_0 remains below 1, our measurements cannot discriminate between these two possibilities.

With this study, the parameter P describing the phonon thermal conductivity has been found to be equal to $P = 0.022$ W.K^{-3}.m^{-1}, close to 0.017 W.K^{-3}.m^{-1}, found by Pfau *et al.* [164]. The coefficient B increases linearly with the magnetic field, as shown figure 5.17. One suggestion to explain the increase is that in Ueda and Moriya's theory, the coefficient B is inversely proportional to the density of state of the electrons responsible for the ferromagnetic fluctuations (the d-electrons in their theory, the f ones in our case). Specific heat measurements have shown that the Sommerfeld coefficient decreases with the magnetic field [63], which is proportional to the electronic density of state. Thus, the decrease of the electronic density of state with the field might explain the increase of the B coefficient, which remains counter-intuitive: in UCoGe, ferromagnetic fluctuations were instead suppressed by an applied field, in which case, a decrease of B is expected, not the inverse.

Due to the good agreement between the fits and the measurements, the formula 5.7 is keeped for the following studies. This formula will be completed to reproduce the thermal conductivity in the whole temperature range.

Study of κ above 0.5T

Above 0.5T, the total thermal conductivity is inferior to our first estimation, with the maximum of deviation between 0.1K and 0.4K. I assume that this results from a new contribution

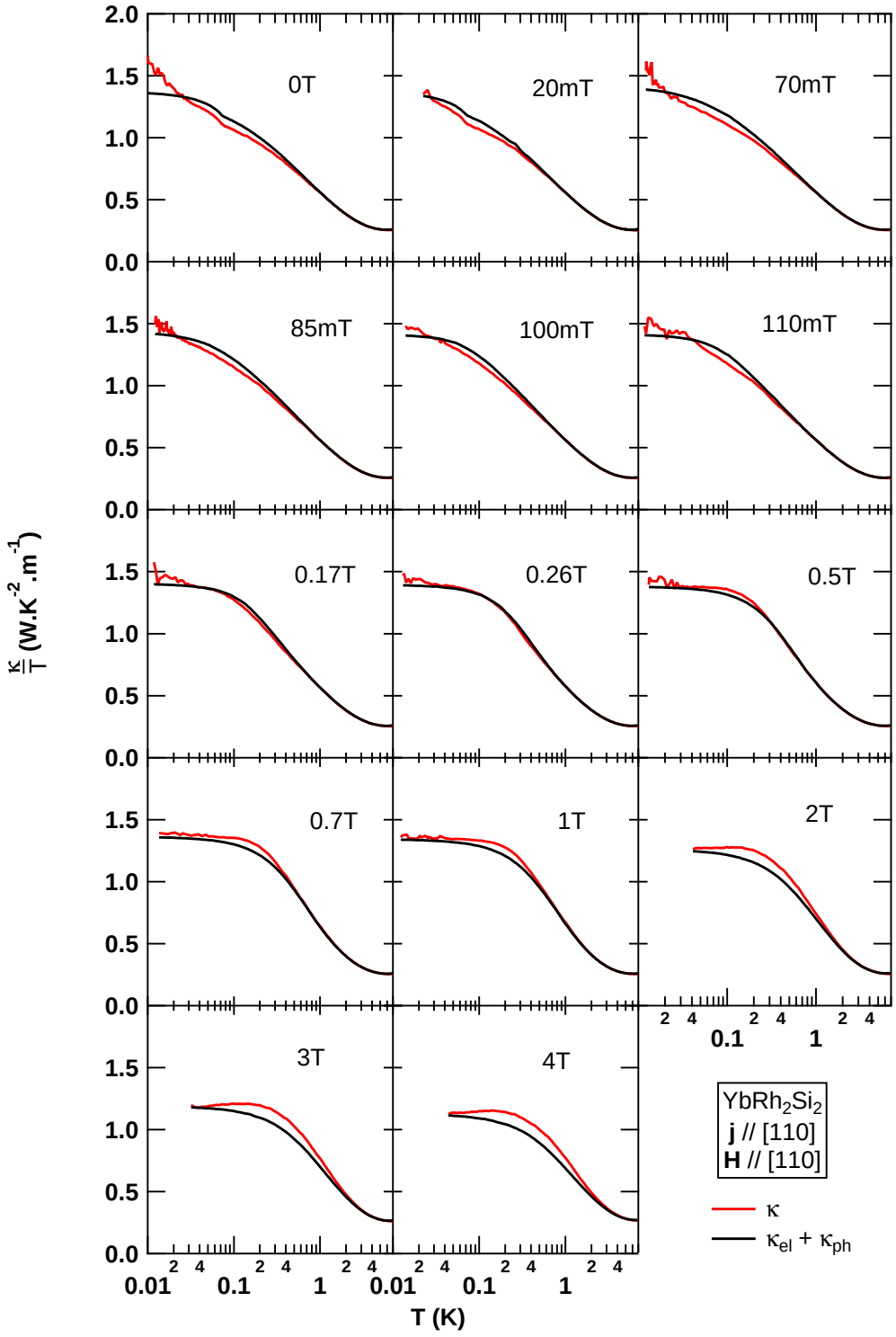


Figure 5.16 *Thermal conductivity (in red) and the fit using formula 5.7 (in black) at each field. At low fields, the thermal conductivity is overestimated whereas it is underestimated at high fields.*

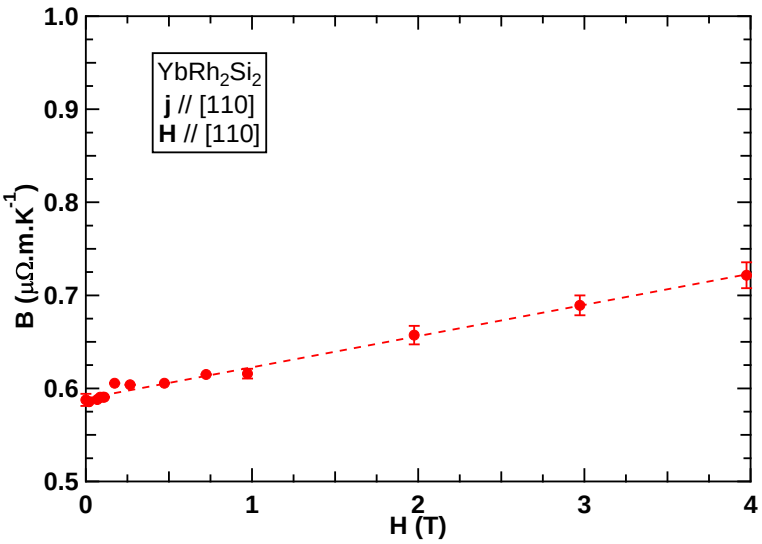


Figure 5.17 *Evolution of the B coefficient with the magnetic field. The dashed line is a linear fit.*

to the thermal conductivity, and which is not an electronic quasiparticle contribution, as the Lorenz ratio goes through a maximum. I will thus add a term κ_{extra} to the expression 5.7.

The figure 5.18 shows the quantity $\kappa_{extra} = \kappa - \kappa_{el} - \kappa_{ph}$. This extra contribution increases with the magnetic field, indicating most likely a magnetic origin, or that the magnetic field drives the system closer to the transition responsible for this extra contribution (or at the opposite, the system is getting further the transition which "blocks" the fluctuations). The slope at low temperature is the same for each field, but the maximum intensity increases with the magnetic field and the bandwidth spreads out. The straight lines are a fit using a model described in the Appendix .2.

The figure 5.19 shows the field dependence of the maximum of κ_{extra}/T and the temperature at which the maximum occurs, called T_{max}. Both quantities appears at around 0.2T, with first a strong increase with the field. The maximum seems to saturate above 2T whereas T_{max} increases linearly.

A more refined treatment of the study κ_{extra}/T is given in the Appendix .2, with a model with the initial increase, the maximum and the decrease as parameters, and similar behaviors has been observed. This model gives the straight lines of figure 5.18.

It seems that the extra contribution is linked to the QCP. One possible explanation is that with the magnetic field, antiferromagnetic fluctuations disappear in favor of ferromagnetic fluctuations. Their coherence length is very small, $\xi \approx 6$Å, but larger than $4f$-site [204]. This means that they are slightly delocalized and can thus be a medium to transport heat, the same way as UCoGe. If ferromagnetic fluctuations are strengthened with the field, this explains why the extra contribution is getting more and more important with the field.

Another possible origin is the presence of a transition at 3.5T and 9.5T [169, 163], attributed to band structure effects, which can induce additional fluctuations in the system. In this case, the origin of this extra contribution is not magnetic, and its increase in amplitude with H is due to the fact that the transition is getting closer by increasing the field, and thus the amplitude of the fluctuations increases.

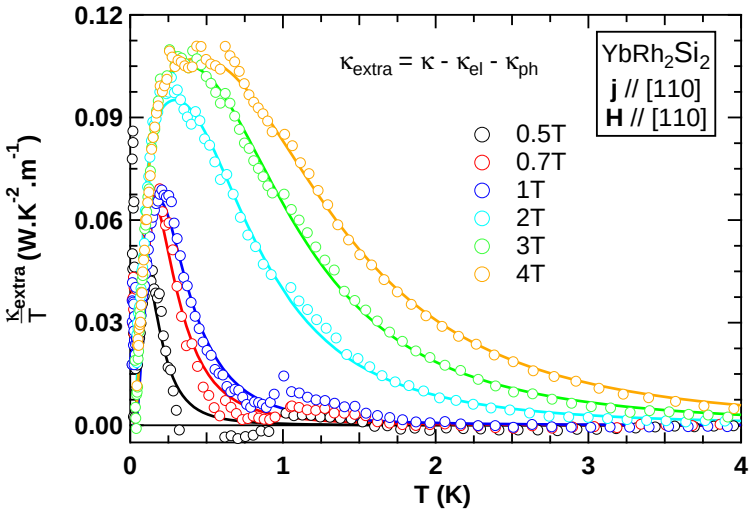


Figure 5.18 *Extra contribution to the thermal conductivity, defined as $\kappa_{extra} = \kappa - \kappa_{el} - \kappa_{ph}$, for fields above 0.5T. This extra contribution increases and spreads in temperature with the magnetic field. The straight lines are its estimations using formula 15 (see Appendix .2).*

To discriminate between these two hypothesis, measurements at higher field are necessary.

Study of κ below 0.5T

Below 0.3T, where the electronic specific heat shows a logarithmic dependence, $C/T \sim log(T)$, the simple formula 5.7 overestimates the thermal conductivity below 1K. The explanation given is that at low fields, low temperatures, the system is dominated by antiferromagnetic fluctuations instead of ferromagnetic ones.

As the thermal conductivity is smaller than the electronic one deduced simply with the Lorenz ratio, the mechanism responsible for this deviation is expected to be electronic (due to inelastic scattering, electron-phonon scattering...). In order to estimate the electronic contribution, an expression similar to the formula 5.5 is taken, but the additional term to the electronic thermal resistivity is supposed to be a power law, leading to:

$$\frac{\kappa_{el}}{T} = \frac{\overline{L_0}}{w_{th}} = \frac{\overline{L_0}}{\rho + B'T^m}$$

where the power law m is fixed for all fields. By fitting all the data altogether, the better fits have been found for $m = 0.5$. To my knowledge, there is no theory which predicts this exponent. Nevertheless, for temperatures and fields below 1K and 0.2T respectively, the following expression has been used for the thermal conductivity:

$$\frac{\kappa}{T} = \frac{\kappa_{el}}{T} + \frac{\kappa_{ph}}{T} \tag{5.8}$$

$$= \frac{\overline{L_0}}{\rho + B'\sqrt{T}} + PT \tag{5.9}$$

The P coefficient is the one found previously, P=0.022 W.K^{-3}.m^{-1}. The evolution of the B' parameter is shown figure 5.20. It slightly decreases with the magnetic field. The figure

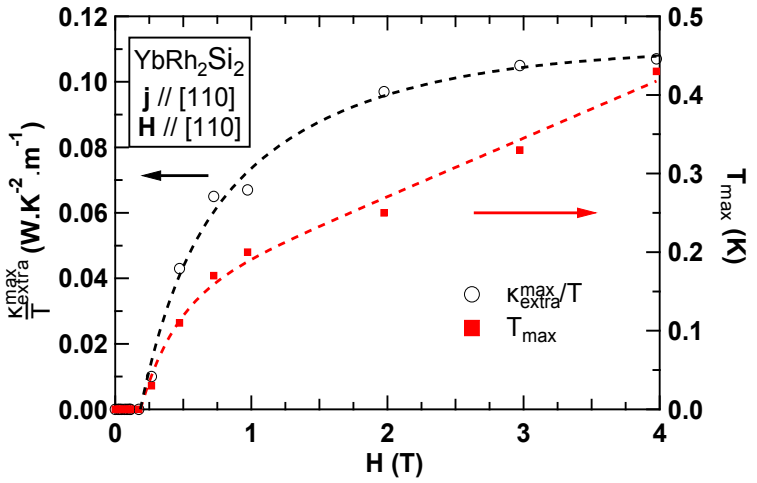


Figure 5.19 *Field dependence of the maximum of the extra contribution to the thermal conductivity, and the temperature at which it occurs. Dashed lines are guides to the eyes.*

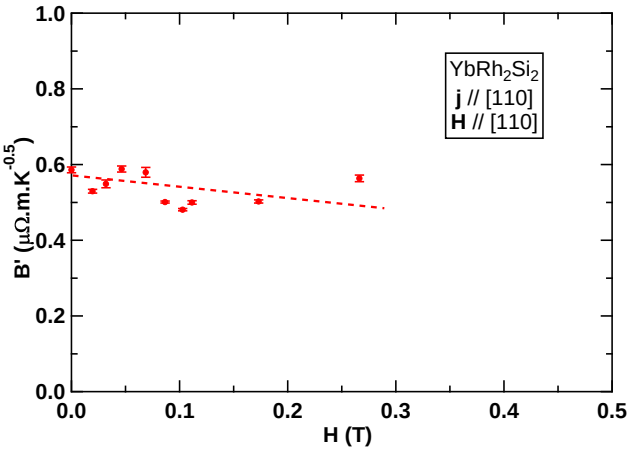


Figure 5.20 *Field evolution of the coefficient B'. The dashed line is a linear fit.*

5.21 shows the thermal conductivity and the estimated one using formula 5.9 at low field and below 1K. It has to be noted that the disappearance of the square root law does not coincide with the appearance of the new contribution studied in the previous paragraph: the square root law disappears above 0.26T, whereas the new contribution is visible from 0.17T.

The formula 5.9 reproduces again rather well the measurements between 30mK and 1K, as it is shown figure 5.21. In my model, the additional term to the electronic thermal resistivity goes suddenly from a linear behavior above 1K to a square root below 1K. The linear coefficient would rather decrease with the appearance of the incommensurate fluctuations and the square root one would increase on the opposite way.

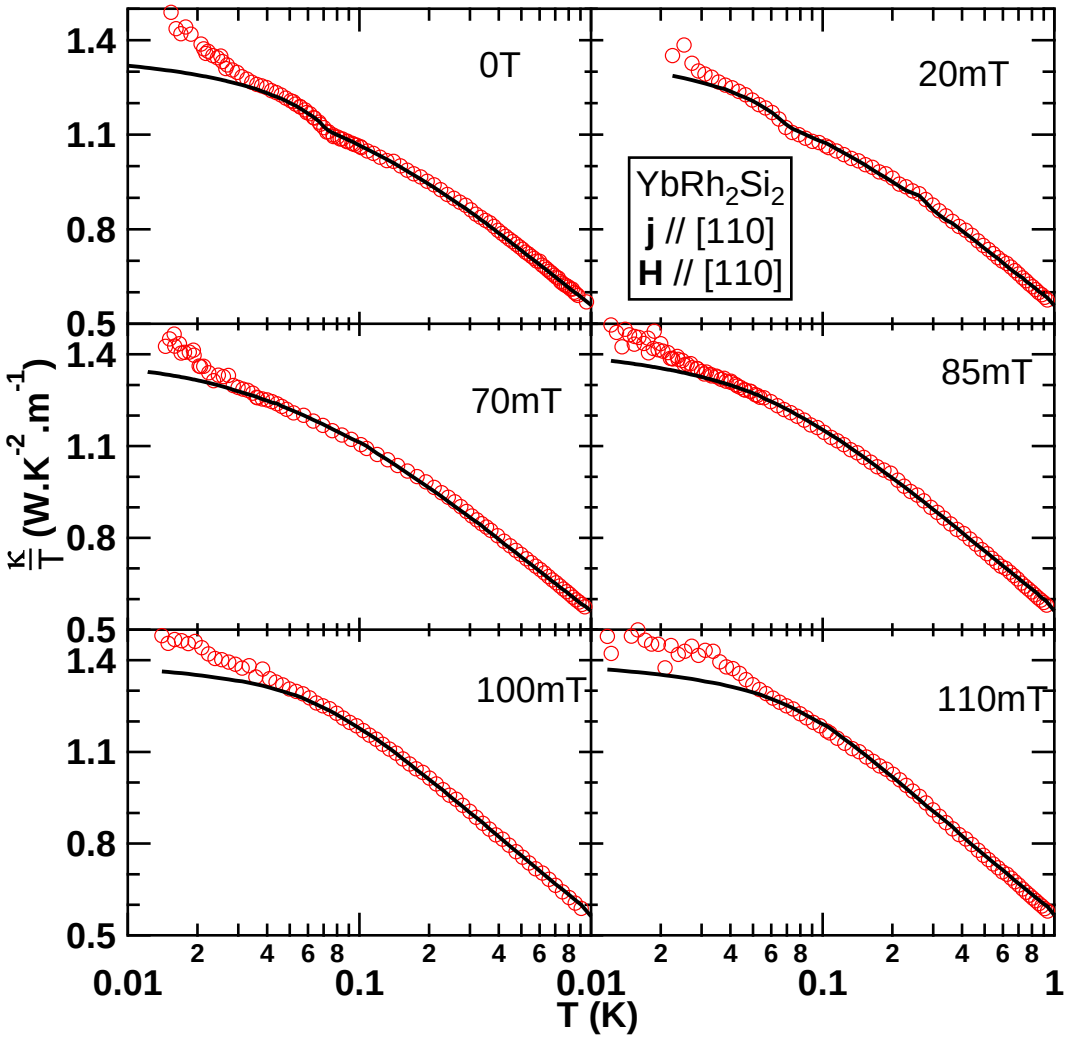


Figure 5.21 *Thermal conductivity (in red) and the estimate one using formula 5.9 (in black) at each field. This simple model reproduces very well the bare data except at very low temperature.*

5.6 Conclusion

The thermal conductivity measurements of $YbRh_2Si_2$ at very low temperatures cannot conclude convincingly for the violation (or the validity) of the WFL at the QCP. However, our results can be interpreted without its violation.

Interestingly, the thermal conductivity measurements agree with the neutron scattering measurements, that is to say $YbRh_2Si_2$ is dominated by ferromagnetic fluctuations at high temperature and under field, and it has been possible to use Ueda and Moriya's theory (effect of the spin fluctuations on the thermal resistivity in the weak ferromagnet) where the ferromagnetic fluctuations are expected.

From 0.3T, an additional deviation appears. Neutron scattering experiments have seen that the magnetic structure is complicated at high field, and have observed a resonance energy that grows with the magnetic field. The deviation seen by thermal conductivity may be related to this resonance, or from the transitions seen at 3.5T and 9.5T, which are believed to be topological transitions. Further experiments at higher fields are necessary to go further in the study of this deviation. Moreover, the measurements in a sample with a lower RRR would decrease the electronic quasiparticle thermal conductivity, and the study of this new regime would be easier if it comes from the appearance of an additional contribution.

Conclusion

Transport studies in the superconducting ferromagnet UCoGe have shown the importance of the magnetic fluctuations at low temperatures. Thermal conductivity decreases strongly with the magnetic field when it is applied along the easy magnetization axis (the **c**-axis), which cannot be explained only by the magnetoresistivity and so reveals an additional channel of heat transport due to spin fluctuations. The results are consistent with the NMR measurements, which have shown that the longitudinal magnetic fluctuations are strongly suppressed when $\mathbf{H}//\mathbf{c}$ and barely affected when $\mathbf{H}\perp\mathbf{c}$. This similarity suggests that the longitudinal magnetic fluctuations detected by NMR are responsible for a heat channel, which is measured by thermal conductivity. This extra contribution above the Curie temperature has the same order of magnitude in all the samples measured (RRR from 16 to 150) and its dispersion is rather isotropic (very similar for the heat current applied along the three crystallographic directions).

For temperatures below the Curie temperature ($T\lesssim 2.5K$), the extra contribution changes, and a strong anisotropy appears between the three crystallographic directions. The signal is very small (barely detectable) when the heat current $\mathbf{j}_Q$ is applied along the **a**-axis (the hard axis), small when $\mathbf{j}_Q//\mathbf{c}$ and strongly increases below 1K when $\mathbf{j}_Q//\mathbf{b}$. This strong anisotropy between the different axis at the Curie temperature has already been seen by thermal expansion. This "new" low-temperature contribution can emerge from two effects: the first is that it originates from ferromagnetic magnons (below T_{Curie}) instead of magnetic fluctuations. The other explanation is that a drastic change of the Fermi surface is predicted to occur at the ferromagnetic transition, which can induce a change in the excitation spectrum. This seems more likely, owing to the strong Ising anisotropy of UCoGe.

XMCD measurements have also been performed in the normal phase of UCoGe, at 3K, again in the configurations $\mathbf{H}//\mathbf{c}$ and $\mathbf{H}//\mathbf{b}$ up to 17T. When $\mathbf{H}//\mathbf{c}$, a ferro-to-ferrimagnetic transition is expected at 9T, and a Lifshitz transition at 11T when $\mathbf{H}//\mathbf{b}$. Both transitions have not been detected by XMCD measurements, maybe due to the too high measurement temperature. However, the presence of a ferrimagnetic state seems unlikely in UCoGe as we have found that the magnetic moment carried by the cobalt is parallel to the magnetic field and thus to the total moment of carried by the uranium.

Thermal conductivity has also been used to study the superconducting state, first at zero field to study the anisotropy and then under field in the configurations $\mathbf{H}//\mathbf{c}$ and $\mathbf{H}//\mathbf{b}$. The thermal conductivity measured with the heat current along the three directions ($\mathbf{j}_Q//\mathbf{a}$, $\mathbf{j}_Q//\mathbf{b}$ and $\mathbf{j}_Q//\mathbf{c}$) did not show strong anisotropy and the temperature dependence of κ/T is similar at 0T. However, the presence of inhomogeneities and defaults in the measured samples can prevent a definitive conclusion, and measurements in samples with better RRR are needed to conclude unambiguously.

A robust result is that multigap superconductivity has been detected in UCoGe, both by the temperature and the field dependence of κ/T, as it could be expected for ferromagnetic superconductors. An open question is to know if the multigap superconductivity comes from the polarization of the Fermi surfaces due to the ferromagnetism (superconductivity of majority and minority spins), or if it has the same origin as for the other multigap superconductors, that is to say the superconductivity of bands of different effective masses.

The other studied compound was $YbRh_2Si_2$, by transport measurements. Very low temperature thermal conductivity measurements (down to 9mK) have been performed under field, close to the magnetic quantum critical point. As reported in previous measurements, κ/T increases at very low temperatures. However, this increase of the thermal conductivity exists for fields above and below the critical field, which indicates that the effect responsible for this is not specific to the critical field. This prevents to conclude unambiguously on the validity of the Wiedemann-Franz law. However, our results can be interpreted entirely by supposing that the Wiedemann-Franz law is obeyed.

Perspectives

To complete the studies performed in this thesis, several additional experiments on UCoGe are needed. The easiest is to complete the upper critical field up to 15T, and with the field along the **a**-axis. At the view of the bulk $H^b_{c_2}$, it seems unlikely that slope of the bulk $H^a_{c_2}$ is the same, as measured by resistivity measurements.

The other important point to complete is the measurements the anisotropy of the extra contributions at low temperature. If, above 2K, the extra contributions have for origin the longitudinal ferromagnatic fluctuations detected by NMR, they should be almost field independent when $\mathbf{H}//\mathbf{a}$, similarly to the case $\mathbf{H}//\mathbf{b}$. This has to be verified.

Preliminary results seems to indicate that this extra contribution below 2K is almost zero when $\mathbf{j}_Q//\mathbf{a}$, but this has to be confirmed. Moreover, it could interesting to study the very low temperature extra contribution in the configuration $\mathbf{j}_Q//\mathbf{b}$ in a sample with a lower electronic contribution (lower RRR). This very low temperature extra contribution, in that case, should be easier to extract and thus to study.

Concerning $YbRh_2Si_2$, it is not possible, from my point of view, to go further in the study of the violation of the Wiedemann-Franz law, as it should imply measurements at too low temperatures, and the transition at 2mK could anyway prevent any unquestionable conclusion. What could be done however is the study of the very low temperature thermal conductivity on a different sample, to see the effects of the quality on this strong deviation.

The second interesting point in $YbRh_2Si_2$ is the study of the extra contribution that appears from 1T at around 0.5K. Its origin is not known, and measurements at higher fields or/and with the current in the other direction ($\mathbf{j}_Q//\mathbf{c}$), in samples with lower RRR, can help in its study and discriminate some scenarios.

Conclusion en Français

Les mesures de transport dans le supraconducteur ferromagnétique UCoGe ont montré l'importance des fluctuations magnétiques à basses températures. La conductivité thermique diminue fortement avec le champ magnétique lorsque celui-ci est appliqué selon l'axe de facile aimantation (l'axe **c**), ce qui ne peut pas s'expliquer en prenant uniquement en compte la magnétorésistivité. Cela révèle l'existence d'un cannal de chaleur additionnel causé par les fluctuations de spin. Les résultats sont cohérents avec les mesures de RMN, qui ont montré que les fluctuations magnétiques longitudinales sont fortement diminuées lorsque $\mathbf{H}//\mathbf{c}$ et faiblement affectuées lorsque $\mathbf{H}\perp\mathbf{c}$. Cette similarité suggère que les fluctuations magnétiques longitudinales détectées par RMN sont responsables du canal de chaleur vue par conductivité thermique. L'amplitude de cette contribution supplémentaire au dessus de la température de Curie a le même ordre de grandeur dans tous les échantillons mesurés (avec un RRR allant de 16 jusqu'à 150) avec une dispersion plutôt isotrope (très similaires pour le courant de chaleur appliqué selon les trois directions cristallographiques).

Pour des températures inférieures à la température de Curie ($T\lesssim 2.5K$), la contribution supplémentaire change, et une forte anisotropie apparaît entre les trois directions cristallographiques. Le signal est très faible (à peine détectable) lorsque le courant de chaleur $\mathbf{j}_Q$ est selon l'axe **a** (de difficile aimantation), petit lorsque $\mathbf{j}_Q//\mathbf{c}$ et augmente fortement sous 1K lorsque $\mathbf{j}_Q//\mathbf{b}$. Cette forte anisotropie entre les différents axes à la température de Curie a déjà été observée par expansion thermique. Cette "nouvelle" contribution "basse" température peut avoir deux causes: la première est qu'elle est causée par des magnons ferromagnétiques (sous T_{Curie}) au lieu des fluctuations magnétiques. La seconde explication est qu'un changement radical de la surface de Fermi est prédis lors de la transition ferromagnétique, ce qui peut induire un changement dans le spectre d'excitation. Cette explication semble plus vraisemblable, étant donné le caractère fortement Ising de UCoGe.

Des mesures de XMCD ont également été réalisé dans la phase normale de UCoGe, à 3K, toujours dans les configurations $\mathbf{H}//\mathbf{b}$ et $\mathbf{H}//\mathbf{c}$, jusqu'à 17T. Dans la configuration $\mathbf{H}//\mathbf{c}$, une transition de l'état ferromagnétique à un état ferrimagnétique est attendue à 9T, et une transition de Lifshitz à 11T lorsque $\mathbf{H}//\mathbf{b}$. Aucune des transitions n'a été observée par XMCD, peut-être à cause de la température de mesure trop élevée. Cependant, la présence d'état ferrimagnétique semble peu probable dans UCoGe, car nous avons trouvé que le moment porté par le cobalt est parallèle au champ magnétique et donc au moment total porté par l'uranium.

La conductivité thermique a également été utilisée pour étudier l'état supraconducteur, d'abord à champ nul pour étudier l'anisotropie, puis sous champ dans les configurations $\mathbf{H}//\mathbf{b}$ et $\mathbf{H}//\mathbf{c}$. La conductivité thermique mesurée avec le courant de chaleur dans les trois directions cristallographiques ($\mathbf{j}_Q//\mathbf{a}$, $\mathbf{j}_Q//\mathbf{b}$ and $\mathbf{j}_Q//\mathbf{c}$) n'a pas montré de forte anisotropie

et la dépendance de κ/T avec la température est similaire à 0T. Cependant, la présence de défauts et d'inhomogénéités dans les échantillons mesurés empêchent une conclusion définitive, et des mesures dans des échantillons avec des meilleurs RRR sont nécessaires pour conclure de manière certaine.

Un résultat robuste est le caractère multigap détecté dans UCoGe par les dépendences en température et en champ de la conductivité thermique, comme attendu pour un supraconducteur ferromagnétique. Une question ouverte est de savoir si la supraconductivité multigap est causée par la polarisation des surfaces de Fermi par le ferromagnétisme (supraconductivité des spins majoritaires et minoritaires), ou si elle a la même origine que les autres supraconducteurs multigaps, c'est-à-dire la supraconductivité des bandes de différentes masses effectives.

Le second composé étudié fut $YbRh_2Si_2$, par des mesures de transport. Des mesures de conductivité thermique à très basses températures (jusqu'à 9mK) ont été effectuées sous champ, proche du point critique quantique magnétique. Comme constaté par des mesures précédentes, κ/T augmente à très basses températures. Cependant, cette augmentation existe pour des champs magnétiques inférieures et supérieures au champ critique, indiquant que l'effet responsable de cette augmentation n'est pas spécifique au champ critique. Cela empêche de pouvoir conclure sans ambiguïté la validité de la loi de Wiedemann-Franz, bien que nos résultats puissent être complètement interprétés supposant cette loi vérifiée.

Appendix

.1 Phenomenological Model of the Normal State of UCoGe

Several models exist to describe the magnetic contributions of the thermal conductivity, but are often dedicated to a special system. In this section, I will develop a phenomenological model to describe more quantitatively the thermal conductivity of UCoGe.

The previous analysis of the normal phase shows the existence of at least two extra heat channels: one dominant above 1K and another below 1K. κ would be the sum of three contributions: the electronic quasiparticle thermal conductivity (κ_{qp}), a lattice contribution (κ_{ph}), and an extra contribution, with probably a "low"-temperature and a "high"-temperature contribution (κ_{extra}^{LT} and κ_{extra}^{HT} respectively). Only the other contributions ($\kappa_{other} = \kappa_{ph} + \kappa_{extra}$ and $\kappa_{extra} = \kappa_{extra}^{LT} + \kappa_{extra}^{HT}$) will be discussed here as κ_{qp} has been evaluated in the subsection 4.2.2.

The measurements are done at low temperature, the lattice contribution is assumed to be limited only by the phonon-electron scattering, which leads to $\kappa_{ph} = P.T^2$. At first approximation, the phonon spectra does not depend on the magnetic field, leading to the parameter P temperature and field independent. Furthermore, it should have the same order of magnitude between each sample.

For the extra contributions, we used a simple kinetic model[2], valid for 1D systems, but which reproduces well enough the data and allows to extract quantitatively the field dependence of the amplitude and temperature spread of these contributions :

$$\kappa_{extra} = \frac{d}{dT} \sum_k v_k \epsilon_k n_k l_k \tag{10}$$

with v_k, ϵ_k and l_k the velocity, the energy and the mean free path of the magnetic excitations. We took a momentum and T-independent mean free path, as well as a Fermi-Dirac distribution of the excitations[3]:

$$n_k = \frac{1}{1 + e^{\epsilon_k / k_B T}} \tag{11}$$

For a 1D case, expression 10 does not depend on any precise form of v_k (which we do not know anyway). The final form gives the following expression:

[2] inspired from Hess' work in the spin ladder system $Sr_{14}Cu_{24-x}Zn_xO_{41}$ [79]

[3] As little are known about these excitations, the simplest form is taken for the distribution. Anyway, the precise form of the distribution is not important as it gives basically the same results.

Sample	α	P $W.K^{-3}.m^{-1}$	M_{HT} $W.K^{-2}.m^{-1}$	ϵ_{max}^{HT} K	ϵ_{min}^{HT} K	M_{LT} $W.K^{-2}.m^{-1}$	ϵ_{max}^{LT} K	ϵ_{min}^{LT} K
S_{16}^{c}	1.14	0.017	0.06	50	5.75	0.018	5.2	1.24
S_{47}^{c}	2.29	0.009	0.09	50	3.62	0.022	3.46	0.5
S_{65}^{a}	2.4	0.006	0.096	50	3.68	0.003	3.5	0.5
S_{110}^{c}	2.5	0.01	0.079	50	3.85	0.054	3.59	1
S_{150}^{b}	1.36	0.01	0.072	50	5	**0.45**	1.4	0.6

Table 1 *Calculated coefficients of the analysis of the normal phase with the described model at 0T.*

$$\kappa_{extra} = \frac{M}{T^2}\int_{\epsilon_{min}}^{\epsilon_{max}} \frac{\exp(\epsilon/k_BT)}{(1+\exp(\epsilon/k_BT))^2}\epsilon^2 d\epsilon = M.f(T;\epsilon_{min};\epsilon_{max}) \tag{12}$$

This expression is similar to a Debye model for the phonon contribution. Here, M is a constant (proportional to the mean free path) and ϵ_{min} is an energy gap, ϵ_{max} a cut-off. This very simple model describes remarkably well our data, when two contributions are taken into account.

To summarize, we fitted this extra contribution by :

$$\kappa_{other} = \kappa_{ph} + \kappa_{extra,HT} + \kappa_{extra,LT} \tag{13}$$
$$= PT^2 + M_{HT}f(T;\epsilon_{min}^{HT};\epsilon_{max}^{HT}) + M_{LT}f(T;\epsilon_{min}^{LT};\epsilon_{max}^{LT}) \tag{14}$$

"HT" and "LT" mean "High Temperature" and "Low Temperature", P,M_{HT} and M_{LT} are the amplitudes of the phonon and the high and low temperature extra contributions respectively. As the high temperature contribution depends a lot of the value of α and the low temperature one is less dependent, in the following, the only consistent parameters are the energy gap of the low temperature contributions ϵ_{min}^{LT}, its amplitude M and its bandwidth ϵ_{max}^{LT}, but only for sample S_{150}^{b} (better determined due to the well defined maximum).

To determine the coefficients, the following procedure has been followed: as the phonon contribution is constant with the field, the extra contribution ($\kappa_{extra} = \kappa_{other} - \kappa_{ph}$) should remain positive at any field. The parameters of both extra contributions should have a smooth field dependence. Because of the superconductivity, the coefficients ϵ_{min}^{LT} and M_{LT} are not well defined. In the case $\mathbf{H}//\mathbf{c}$, these parameters are imposed from the extrapolation of the high field measurements (without superconductivity). When the field is along the **b**-axis, the superconductivity occurs in the whole field range, the low temperature gap ϵ_{min}^{LT} is thus taken constant with the field. The upper limit of the high temperature fluctuations ϵ_{max}^{HT} cannot be determined precisely as the measurements have been done up to 7K, the high value we find confirms that fluctuations start to appear at high temperature, far above the ordering temperature. In that sense they are compatible with the fluctuations observed by NMR [74].

The calculated coefficients of each sample at 0T are displayed table 1. The decomposition of κ_{other}/T with our model is displayed in the figure 22 for sample S_{16}^{c} and 23 for sample S_{150}^{b} with $\mathbf{H}//\mathbf{c}$ and $\mathbf{H}//\mathbf{b}$. The decomposition of samples S_{47}^{c} and S_{110}^{c} with $\mathbf{H}//\mathbf{c}$ are shown figures 24 and the decomposition at 0T of sample S_{65}^{a} is shown figure 25. Astonishingly, this simple model with two extra contributions reproduces rather well the thermal conductivity

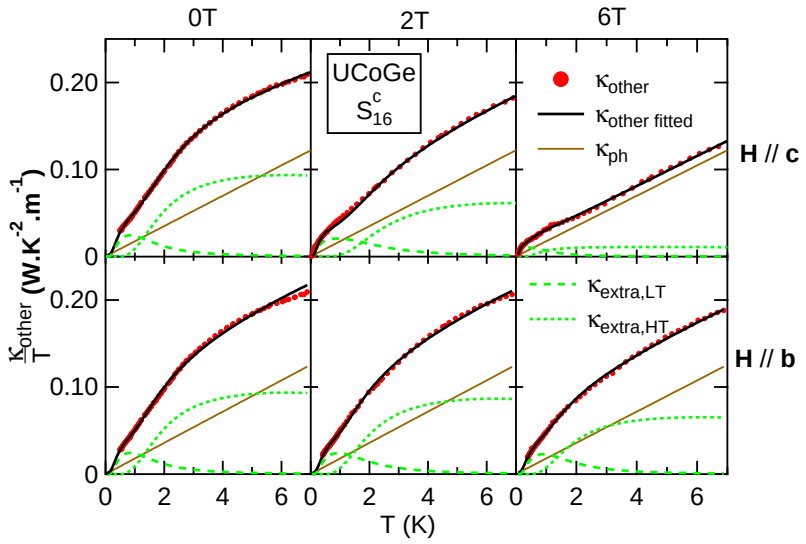


Figure 22 *Decomposition of the extra contribution in sample S^c_{16} at 0T, 2T and 6T. The top line is with **H//c** and the bottom line with **H//b**. Each contribution is represented with the estimated other contributions (black solid line).*

at all fields measured, except for sample S^b_{150} for H>4T, because of the orbital effects. It was not possible to take into account these effects in our model.

The extrapolation of $\kappa_{mag,LT}/T$ is tricky at low temperature in the superconducting state, as the maximum of this contribution is calculated to be at around 0.5K in each sample. This is particularly true in sample S^b_{150}, it is difficult to determine precisely the intensity of the maximum at zero field. Another difficulty is the determination of the coefficient ϵ^{HT}_{min} and ϵ^{LT}_{max} (corresponding to the decrease of $\kappa_{mag,HT}/T$ and the increase of $\kappa_{mag,LT}/T$) as they are hidden in the total extra contribution.

It is now possible to extract the different parameters to see the field dependence and to have a global view of how these contributions evolve with the magnetic field. For visibility reasons, only the evolution of the parameters of sample S^b_{150} will be shown, the other samples having qualitatively the same field dependence.

Figure 26 shows the normalized amplitude $M/M_{H=0T}$ of the low temperature magnetic contributions with the magnetic field applied along the **c**-axis and the **b**-axis. The amplitude decreases with the field in both configurations with a similar behavior: it is very sensitive to the magnetic field, it decreases faster up to 2T then seems to saturate at 10% (**H//c**) and 20% (**H//b**) of the initial value.

If we look now at the energy gap of the fluctuations, the magnetic field has only little influence on the gap of the low-temperature fluctuations (right panel of figure 26). Due to superconductivity, it was not possible to determine precisely the energy gap at low field when **H//c** and within the whole field range when **H//b**. For the last case, the energy gaps have been taken constant : ϵ^{LT}_{min}=0.5K. The almost constant gap with the field is surprising and indicates that it does not depend (or only little) on the magnetization of the sample.

The bandwidth of the low temperature excitation is shown on the same figure: the magnetic field has a similar effect on ϵ^{LT}_{max} in both configurations (**H//c** and **H//b**). ϵ^{LT}_{max} increases

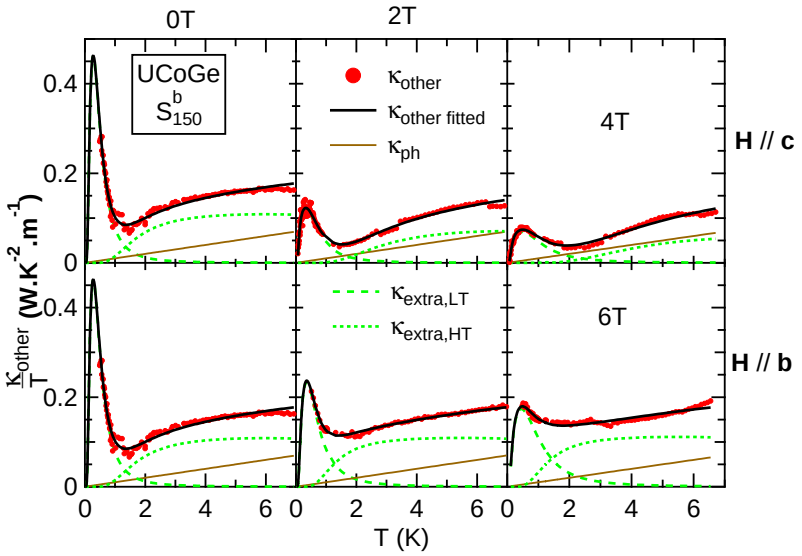


Figure 23 *Decomposition of the extra contribution in sample S^b_{150} at 0T, 2T and 4T (**H**//**c**) and 6T (**H**//**b**). The top line is with **H**//**c** and the bottom line with **H**//**b**. Note that due to the orbital effect, the model does not work for H>4T, **H**//**c**. Each contribution is represented with the estimated extra contribution (black solid line).*

with the magnetic field, confirming the spread to higher temperature of the low temperature contributions. The increase is slightly stronger when **H**//**c**.

These observations of the coefficients representing the low temperature contribution are surprising: whereas the high temperature contribution is almost field independent when **H**//**b**, and decreases strongly when **H**//**c**, the low temperature contribution has a similar field dependence in both field directions. This indicates that the anisotropy of the field direction seen in the high temperature contribution is absent in the low temperature extra contribution.

It is tricky to do more quantitative observations, as our model is phenomenological, but the variation of the parameters show a new feature: the low temperature extra contributions have a similar field dependence in the configurations **H**//**c** and **H**//**b**. An open question left for future studies is to determine if this low-temperature contribution appears indeed only below T_{Curie}, and if it corresponds to new modes (transverse, despite the Ising character?) related to the long range ferromagnetic order, or if it is the same origin as the high temperature one, but with another dispersion due to the predicted drastic change of the Fermi surface at the Curie temperature [180].

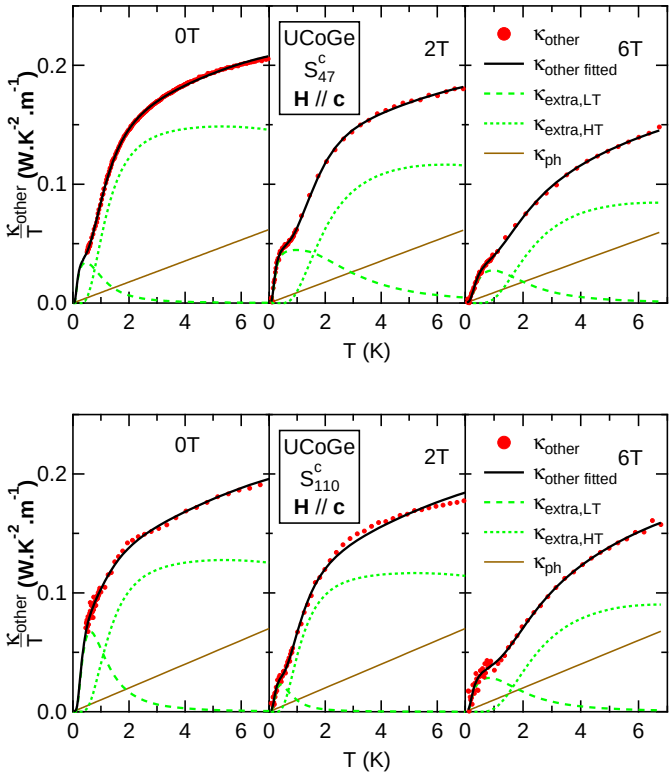


Figure 24 *Decomposition of the other contribution in sample S^c_{47} (upper line) and S^c_{110} (bottom line) at 0T, 2T and 6T. Each contribution is represented with the estimated other contribution (black solid line).*

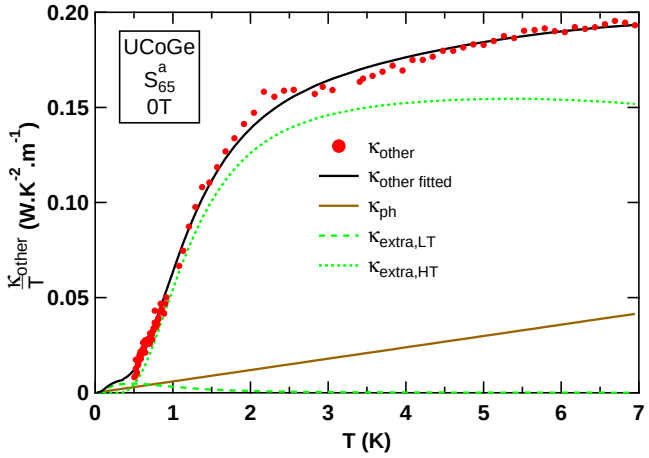


Figure 25 *Decomposition of the other contribution in sample S^a_{65} at 0T. Each contribution is represented with the estimated extra contribution (black solid line).*

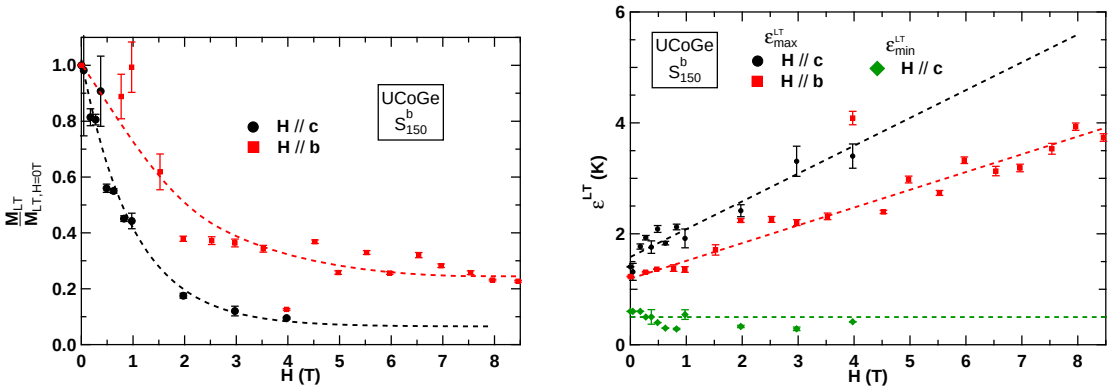


Figure 26 *Normalized amplitude of the low-temperature magnetic contributions (left panel), and the energy gap ϵ_{min}^{LT} and the bandwidth ϵ_{max}^{LT} of the low-temperature excitation (right panel) when **H//c** and **H//b** of sample S_{150}^{b}. The energy gaps for **H//b** have been taken constant (see text). Dashed lines are guide to the eyes.*

.2 Study of κ at High Fields in $YbRh_2Si_2$

This appendix gives an attempt to describe the extra contribution seen in $YbRh_2Si_2$ above 0.5T (see the right panel of figure 5.11 and 5.18), called κ_{extra}.

To do so, the extra contribution will be estimated with the same expression as the one used for UCoGe.

$$\kappa_{extra} = \frac{M}{T^2}\int_{\epsilon_{min}}^{\epsilon_{max}} \frac{\exp(\epsilon/k_BT)}{(1+\exp(\epsilon/k_BT))^2}\epsilon^2 d\epsilon = M.T.f(T;\epsilon_{min};\epsilon_{max}) \tag{15}$$

The M coefficient represents the amplitude of the extra contribution, ϵ_{min} is the low temperature increase and ϵ_{max} the bandwidth at high temperature. This gives the thermal conductivity at high field:

$$\frac{\kappa}{T} = \frac{\overline{L_0}}{\rho + BT} + PT + M.f(T;\epsilon_{min};\epsilon_{max}) \tag{16}$$

The parameters B and P have been estimated in the main section. Thus, only three parameters have to be estimated. This simple model reproduces very well the data, as shown figure 5.18, where the straight lines are the fits with the model, and figure 28 on the total thermal conductivity, except the very low temperature part (below 40mK). The good agreement between the fits and the data is an argument in favor of the validity of our model.

The figure 27 shows the field dependence of the parameters M (left panel), ϵ_{min} and ϵ_{max} (right panel). The parameters M and ϵ_{min} increase rapidly from 0.2T to become constant at 0.5T. The decrease below 0.5T can be simply explain by the fact that the signal is very weak at those fields, with thus a large uncertainty. The coefficient ϵ_{max} increases almost linearly with the field, with the relation $\epsilon_{max}(K) \approx H(T)$. The field at which the coefficients are zero is found to be 0.2T approximately, close to the QCP.

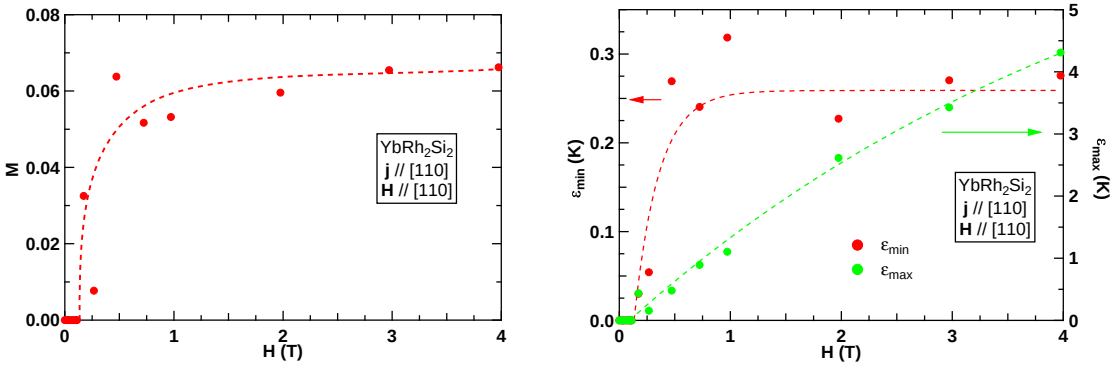


Figure 27 *Field evolution of the parameters M (left panel), ϵ_{min} and ϵ_{max} (right panel). The dashed lines are guides to the eyes.*

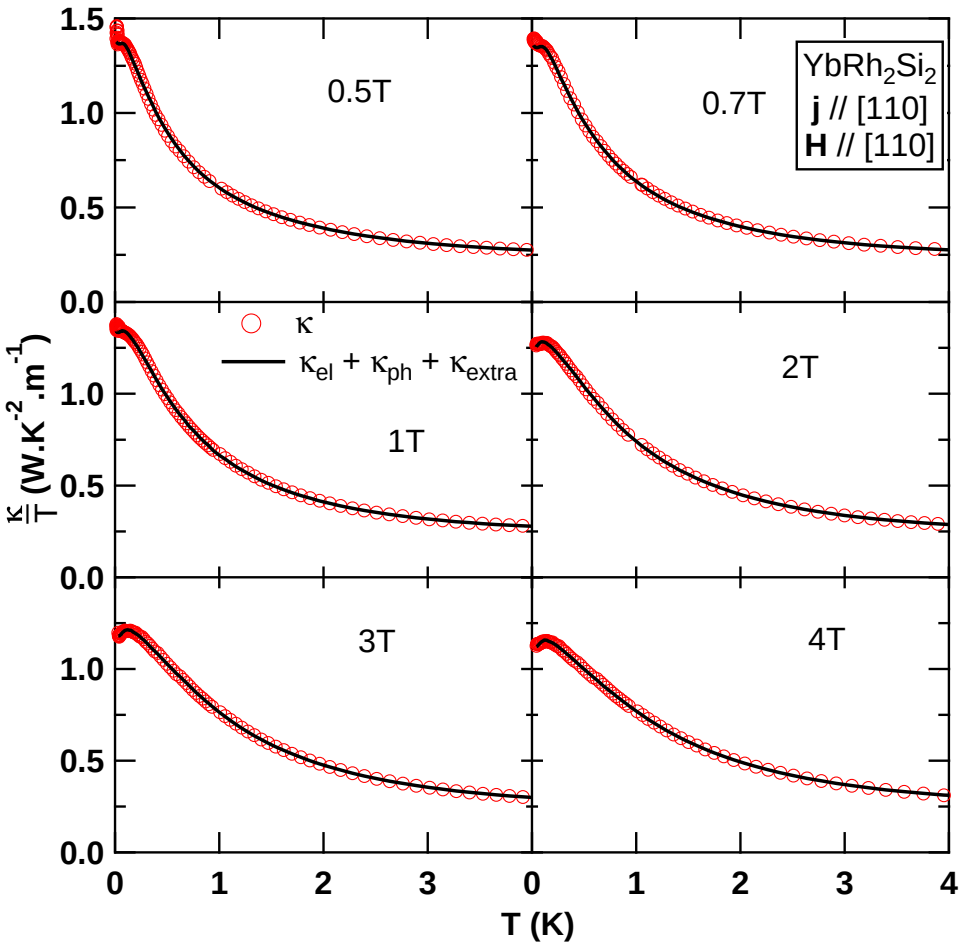


Figure 28 *Thermal conductivity (in red) and the estimate using formula 16 (in black) above 0.5T. This model reproduces well the bare data above 40mK.*

.3 Study of the Very Low Temperature Regime in $YbRh_2Si_2$

This second appendix on $YbRh_2Si_2$ is an alternative study of the very low temperature contribution, and another attempt to extract it from the total thermal conductivity.

The previous studies at low and high fields give good estimations of the thermal conductivity in the whole temperature range, except at very low temperature. As the deviation is always positive (increase of κ/T), it is assumed that another heat channel appears at low temperature, which can be simply added to the rest of the thermal conductivity. If the thermal conductivity estimated previously is called κ^{HT} and the very low temperature part κ^{LT}_{extra} (HT and LT for high and low temperature respectively), we have:

$$\kappa_{tot} = \kappa^{HT} + \kappa^{LT}_{extra}$$

The expression of κ^{HT} depends on the magnetic field (expression 5.9 at low field and expression 16 at higher field). The figure 30 shows $\kappa^{LT}_{extra}/T = \kappa_{tot}/T - \kappa^{HT}/T$ at each field. Above 2T, the measurements are done down to 40mK and no deviation is seen at low temperature.

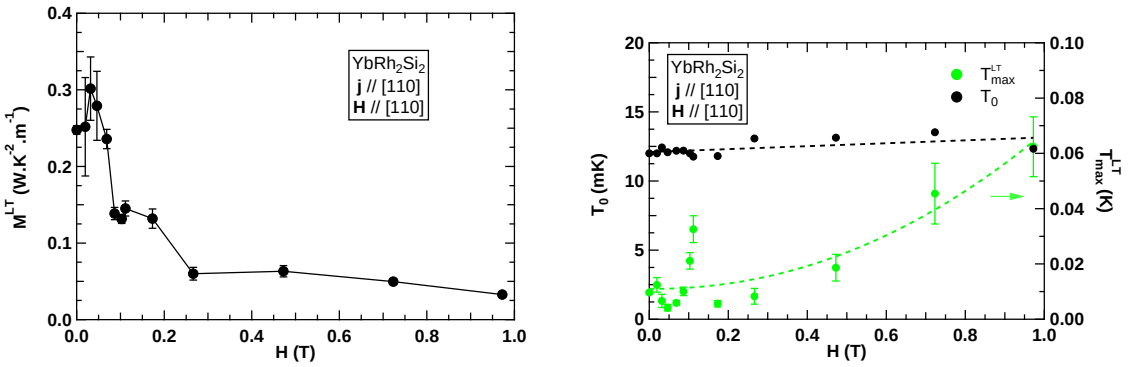


Figure 29 *Field evolution of the parameter M^{LT} (left panel) and of the parameters T_0 and T^{LT}_{max} (right panel). The dashed lines are guids to the eyes.*

The deviation at low temperature extends to fields much higher than 60mT, where the QCP is. As below, in the AF state, the deviation is still there, nothing indicates the different nature of this extra contribution in the ordered state and at the QCP. Its intensity decreases with the magnetic field.

At zero field, there is no reason why the WFL should be violated, this extra contribution should reach a maximum and then goes to zero when T→0K. Thus, the WFL should not be violated at the QCP if the nature of the κ^{LT}_{extra} leading to the deviation of the WFL is similar.

To go a bit further in the study of κ^{LT}_{extra}, they are fitted with an exponential law:

$$\frac{\kappa^{LT}_{extra}}{T} = M^{LT}.exp(-\frac{T - T_0}{T^{LT}_{max}}) \tag{17}$$

This expression is not physical, as it does not predict the decrease of κ^{LT}_{extra} at lower temperature, but can be seen as the approximation of expression 15 after the maximum. The black lines of figure 30 are the best fits of the very low temperature contribution.

An interesting feature, seen on figure 29, is that the coefficient M^{LT} varies little with the field below 0.1T and then decreases rapidly. The coefficient T_0 is almost constant in the whole field range ($T_0 \approx$12.5mK) and T^{LT}_{max} increases slightly above 0.4T.

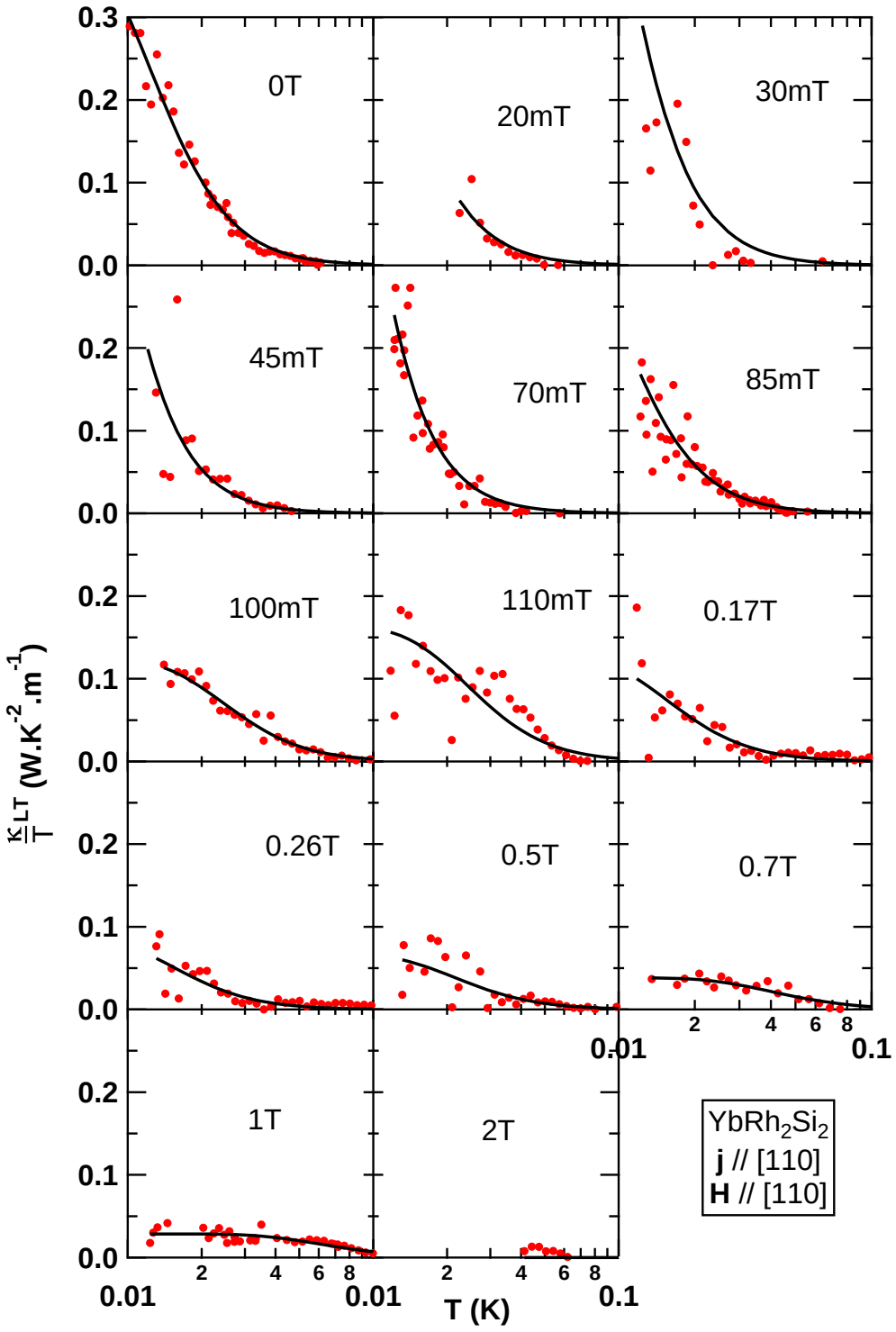


Figure 30 *Estimation of the very low part of the thermal conductivity by removing the higher temperature part. Above 2T, no deviation is seen at low temperature. The black lines are fits, using formula 17.*

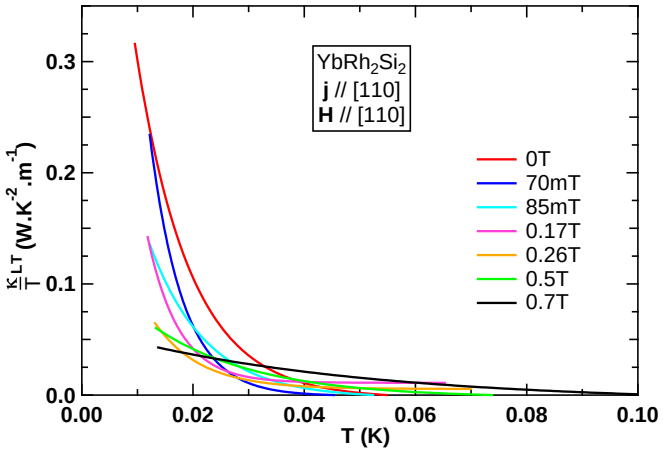


Figure 31 *Comparison of the estimations of the very low part of the thermal conductivity, using formula 17.*

The validity of expression is questionable, as it cannot predict the decrease of κ_{extra}^{LT} at lower temperature. It can nevertheless reproduce the extra contribution, and thus it makes an average of the noise of the measurements and makes easier a direct comparison between these contributions. The figure 31 shows the extra contribution deduced with the expression 17.

The first observation that can be done is that the intensity of κ_{extra}^{LT}/T seems to decrease with the magnetic field. Between 0T and 70mT, the increase starts at lower tempeature (approximately 50mK at 0T and 40mK at 70mT), and above 70mT spreads to higher temperature with the increase of the magnetic field. This feature indicates that the extra contribution seems to be linked to the QCP.

This more complex analysis gives the same conclusion as the one given with a simpler model.

Bibliography

[1] Abrikosov, A. *Introduction to the Theory of Normal Metals.* Academic Press Inc (December 1972), 1972.

[2] Abrikosov, A. A. Superconductivity due to Ferromagnetically Ordered Localized Spins. *Journal of Physics: Condensed Matter 13*, 48 (2001), L943.

[3] Adachi, H., Miranovic, P., Ichioka, M., and Machida, K. Electronic thermal conductivity in a superconducting vortex state. *Physica C: Superconductivity 463-465* (2007), 36 – 39.

[4] Agliari, E., Casartelli, M., and Vezzani, A. Energy transport in an ising disordered model. *Journal of Statistical Mechanics: Theory and Experiment 2009*, 07 (2009), P07041.

[5] Akazawa, T., Hidaka, H., Fujiwara, T., Kobayashi, T. C., Yamamoto, E., Haga, Y., Settai, R., and Onuki, Y. Pressure-induced superconductivity in ferromagnetic UIr without inversion symmetry. *Journal of Physics: Condensed Matter 16* (2004), L29.

[6] Anderson, P. W., and Suhl, H. Spin alignment in the superconducting state. *Phys. Rev. 116* (Nov 1959), 898–900.

[7] Andres, K., Graebner, J. E., and Ott, H. R. $4f$-Virtual-Bound-State Formation in $CeAl_3$ at Low Temperatures. *Phys. Rev. Lett. 35* (Dec 1975), 1779–1782.

[8] Aoki, D., and Flouquet, J. Ferromagnetism and superconductivity in uranium compounds. *Journal of the Physical Society of Japan 81*, 1 (2011), 011003.

[9] Aoki, D., Hardy, F., Miyake, A., Taufour, V., Matsuda, T. D., and Flouquet, J. Properties of ferromagnetic superconductors. *Comptes Rendus Physique 12* (2011), 573 – 583.

[10] Aoki, D., Huxley, A., Ressouche, E., Braithwaite, D., Flouquet, J., Brison, J., Lhotel, E., and Paulsen, C. Coexistence of superconductivity and ferromagnetism in URhGe. *Nature 413*, 6856 (OCT 11 2001), 613–616.

[11] Aoki, D., Matsuda, T. D., Hardy, F., Meingast, C., Taufour, V., Hassinger, E., Sheikin, I., Paulsen, C., Knebel, G., Kotegawa, H., and Flouquet, J. Superconductivity reinforced by magnetic field and the magnetic instability in uranium ferromagnets. *Journal of the Physical Society of Japan 80SA*, Supplement A (2011), SA008.

[12] Aoki, D., Matsuda, T. D., Taufour, V., Hassinger, E., Knebel, G., and Flouquet, J. Extremely Large and Anisotropic Upper Critical Field and the Ferromagnetic Instability in UCoGe. *Journal of the Physical Society of Japan 78*, 11 (2009), 113709.

[13] Aoki, D., Sheikin, I., Matsuda, T. D., Taufour, V., Knebel, G., and Flouquet, J. First Observation of Quantum Oscillations in the Ferromagnetic Superconductor UCoGe. *Journal of the Physical Society of Japan 80*, 1 (2011), 013705.

[14] Aslamazov, L. Influence of Impurities on Existence of an Inhomogeneous State In a Ferromagnetic Superconductor. *JETP 28*, 4 (1969), 773–775.

[15] Balicas, L., Brooks, J. S., Storr, K., Uji, S., Tokumoto, M., Tanaka, H., Kobayashi, H., Kobayashi, A., Barzykin, V., and Gor'kov, L. P. Superconductivity in an organic insulator at very high magnetic fields. *Phys. Rev. Lett. 87* (Jul 2001), 067002.

[16] Bardeen, J., Cooper, L. N., and Schrieffer, J. R. Theory of superconductivity. *Phys. Rev. 108*, 5 (Dec 1957), 1175–1204.

[17] Bastien, G., and Knebel, G. *Private Communication*.

[18] Bauer, E., Buhler-Paschen, S., and Prokofiev, A. *Highly Correlated Electron Systems, SCES 2005, Vienna*. 2006.

[19] Bayrakci, S., Keimer, B., and Tennant, D. Magnon-mediated thermal transport in antiferromagnets: the link to momentum-resolved magnon lifetime data. *ArXiv e-prints 1302.6476* (Feb. 2013).

[20] Behnia, K., Taillefer, L., Flouquet, J., Jaccard, D., Maki, K., and Fisk, Z. Thermal conductivity of superconducting UPt_3. *Journal of Low Temperature Physics 84* (1991), 261–278.

[21] Bel, R., Behnia, K., Proust, C., van der Linden, P., Maude, D., and Vedeneev, S. I. Test of the wiedemann-franz law in an optimally doped cuprate. *Phys. Rev. Lett. 92* (Apr 2004), 177003.

[22] Bennett, A. J., and Rice, M. J. Exact solutions of boltzmann's equation for combined electron-electron electron-impurity scattering. *Phys. Rev. 185* (Sep 1969), 968–970.

[23] Berk, N. F., and Schrieffer, J. R. Effect of ferromagnetic spin correlations on superconductivity. *Phys. Rev. Lett. 17* (Aug 1966), 433–435.

[24] Blagoev, K. B., Engelbrecht, J. R., and Bedell, K. S. Effect of ferromagnetic spin correlations on superconductivity in ferromagnetic metals. *Phys. Rev. Lett. 82* (Jan 1999), 133–136.

[25] Blount, E. I., and Varma, C. M. Electromagnetic effects near the superconductor-to-ferromagnet transition. *Phys. Rev. Lett. 42* (Apr 1979), 1079–1082.

[26] Buschow, K. H. J., Bruck, E., van Wierst, R. G., de Boer, F. R., Havela, L., Sechovsky, V., Nozar, P., Sugiura, E., Ono, M., Date, M., and Yamagishi, A. Specific heat and magnetic behavior of UTGe compounds. *Journal of Applied Physics 67*, 9 (1990), 5215–5217.

[27] Butchers, M. Spin density in UCoGe. In *XRMS10* (2010).

[28] Canepa, F., Manfrinetti, P., Pani, M., and Palenzona, A. Structural and transport properties of some UTX compounds where T = Fe, Co, Ni and X = Si, Ge. *Journal of Alloys and Compounds 234*, 2 (1996), 225 – 230.

[29] Cao, G., Xu, S., Ren, Z., Jiang, S., Feng, C., and Xu, Z. Superconductivity and ferromagnetism in $EuFe_2(As_{1-x}P_x)_2$. *Journal of Physics: Condensed Matter 23* (2011), 464204.

[30] Carra, P., Thole, B. T., Altarelli, M., and Wang, X. X-ray circular dichroism and local magnetic fields. *Phys. Rev. Lett. 70* (Feb 1993), 694–697.

[31] Chakal'skii, B., Azhazha, V., Red'ko, N., and Shalyt, S. Thermal conductivity of vanadium at low temperatures. *JETP Letters 23* (1976), 468.

[32] Chandrasekhar, B. S. A note on the maximum critical field of high-field superconductors. *Applied Physics Letters 1*, 1 (1962), 7–8.

[33] Clogston, A. M. Upper limit for the critical field in hard superconductors. *Phys. Rev. Lett. 9* (Sep 1962), 266–267.

[34] Coleman, P. *Heavy Fermions: Electrons at the Edge of Magnetism.* John Wiley & Sons, Ltd, 2007.

[35] Cuoco, M., Gentile, P., and Noce, C. Coexistence of ferromagnetism and singlet superconductivity via kinetic exchange. *Phys. Rev. Lett. 91* (Nov 2003), 197003.

[36] Custers, J., Gegenwart, P., Neumaier, K., Wilhelm, H., Oeschler, N., Ishida, K., Kitaoka, Y., Geibel, C., and Steglich, F. Quantum criticality in $YbRh_2Si_2$. *Journal of Physics: Condensed Matter 15*, 28 (2003), S2047.

[37] Custers, J., Gegenwart, P., Wilhelm, H., Neumaier, K., Tokiwa, Y., Trovarelli, O., Geibel, C., Steglich, F., C., P., and P., C. The break-up of heavy electrons at a quantum critical point. *Nature 424* (2003), 524.

[38] de la Mora, P., and Navarro, O. Electronic structure of the ferromagnetic superconductor UCoGe from first principles. *Journal of Physics: Condensed Matter 20*, 28 (2008), 285221.

[39] de Visser, A., Huy, N. T., Gasparini, A., de Nijs, D. E., Andreica, D., Baines, C., and Amato, A. Muon Spin Rotation and Relaxation in the Superconducting Ferromagnet UCoGe. *Phys. Rev. Lett. 102* (Apr 2009), 167003.

[40] Deguchi, K., Osaki, E., Ban, S., Tamura, N., Simura, Y., Sakakibara, T., Satoh, I., and Sato, N. K. Absence of Meissner State and Robust Ferromagnetism in the Superconducting State of UCoGe: Possible Evidence of Spontaneous Vortex State. *Journal of the Physical Society of Japan 79*, 8 (2010), 083708.

[41] Dikin, D. A., Mehta, M., Bark, C. W., Folkman, C. M., Eom, C. B., and Chandrasekhar, V. Coexistence of superconductivity and ferromagnetism in two dimensions. *Phys. Rev. Lett. 107* (Jul 2011), 056802.

[42] Divis, M. Electronic structure and magnetism of UCoGe from first principles. *Physica B: Condensed Matter 403*, 13-16 (2008), 2505 – 2508.

[43] Dong, J. K., Tokiwa, Y., Bud'ko, S. L., Canfield, P. C., and Gegenwart, P. Anomalous Reduction of the Lorenz Ratio at the Quantum Critical Point in YbAgGe. *Phys. Rev. Lett. 110* (Apr 2013), 176402.

[44] Doniach, S. The kondo lattice and weak antiferromagnetism. *Physica B+C 91*, 0 (1977), 231 – 234.

[45] Erskine, J. L., and Stern, E. A. Calculation of the M_{23} magneto-optical absorption spectrum of ferromagnetic nickel. *Phys. Rev. B 12* (Dec 1975), 5016–5024.

[46] Fay, D., and Appel, J. Coexistence of p-state superconductivity and itinerant ferromagnetism. *Phys. Rev. B 22* (Oct 1980), 3173–3182.

[47] Felner, I., and Asaf, U. Superconductivity and weak ferromagnetism in $Eu_{1.4}Ce_{0.6}Ru_{1-x}Fe_xSr_2Cu_2O_{10-\delta}$. *Physica C: Superconductivity 292* (1997), 97 – 103.

[48] Felner, I., Asaf, U., Levi, Y., and Millo, O. Coexistence of magnetism and superconductivity in $R_{1.4}Ce_{0.6}RuSr_2Cu_2O_{10-\delta}$ (R=Eu and Gd). *Phys. Rev. B 55* (Feb 1997), R3374–R3377.

[49] Ferstl, J., Geibel, C., Weickert, F., Gegenwart, P., Radu, T., Luhmann, T., and Steglich, F. Tuning $YbRh_2Si_2$ to a non-magnetic state by La-doping. *Physica B: Condensed Matter 359-361* (2005), 26 – 28.

[50] Fertig, W. A., Johnston, D. C., DeLong, L. E., McCallum, R. W., Maple, M. B., and Matthias, B. T. Destruction of Superconductivity at the Onset of Long-Range Magnetic Order in the Compound $ErRh_4B_4$. *Phys. Rev. Lett. 38* (Apr 1977), 987–990.

[51] Fischer, O., Decroux, M., Roth, S., Chevrel, R., and Sergent, M. Compensation of the paramagnetic effect on H_{c2} by magnetic moments: 700 kG superconductors. *Journal of Physics C: Solid State Physics 8*, 21 (1975), L474.

[52] Fischer, y. H. Properties of high field superconductors containing localized magnetic moments. *Helvetica Physica Acta 45* (1972), 331–397.

[53] Flouquet, J. On the heavy fermion road. *eprint arXiv:cond-mat/0501602* (Jan. 2005).

[54] Franz, R., and Wiedemann, G. Uber die Wame-Leitungsfahigkeit der Metalle. *Annalen der Physik 165*, 8 (1853), 497–531.

[55] Friedemann, S., Paschen, S., Geibel, C., Wirth, S., Steglich, F., Kirchner, S., Abrahams, E., and Si, Q. Comment on "Zeeman-Driven Lifshitz Transition: A Model for the Experimentally Observed Fermi-Surface Reconstruction in $YbRh_2Si_2$". *Phys. Rev. Lett. 111* (Sep 2013), 139701.

[56] Friedemann, S., Westerkamp, T., Brando, M., Oeschler, N., Gegenwart, P., Krellner, C., Geibel, C., MaQuilon, S., Fisk, Z., Steglich, F., and Wirth, S. Magnetic and Electronic Quantum Criticality in $YbRh_2Si_2$. *Journal of Low Temperature Physics 161*, 1-2 (2010), 67–82.

[57] Fujimori, S., Ohkochi, T., Kawasaki, I., Yasui, A., Takeda, Y., Okane, T., Saitoh, Y., Fujimori, A., Yamagami, H., Haga, Y., Yamamoto, E., Tokiwa, Y., Ikeda, S., Sugai, T., Ohkuni, H., Kimura, N., and Ōnuki, Y. Electronic structure of heavy fermion uranium compounds studied by core-level photoelectron spectroscopy. *Journal of the Physical Society of Japan 81*, 1 (2012), 014703.

[58] Fulde, P., and Ferrell, R. A. Superconductivity in a strong spin-exchange field. *Phys. Rev. 135* (Aug 1964), A550–A563.

[59] Gasmi, M., Khene, S., and Fillion, G. Coexistence of superconductivity and ferromagnetism in nanosized YBCO powders. *Journal of Physics and Chemistry of Solids 74* (2013), 1414 – 1418.

[60] Gasparini, A., Huang, Y. K., Hartbaum, J., v. Löhneysen, H., and de Visser, A. Thermal expansion of the superconducting ferromagnet UCoGe. *Phys. Rev. B 82* (Aug 2010), 052502.

[61] Gegenwart, P., Custers, J., Geibel, C., Neumaier, K., Tayama, T., Tenya, K., Trovarelli, O., and Steglich, F. Magnetic-field induced quantum critical point in $YbRh_2Si_2$. *Phys. Rev. Lett. 89* (Jul 2002), 056402.

[62] Gegenwart, P., Si, Q., and Steglich, F. Quantum criticality in heavy-fermion metals. *Nature Physics 4*, 3 (MAR 2008), 186–197.

[63] Gegenwart, P., Tokiwa, Y., Westerkamp, T., Weickert, F., Custers, J., Ferstl, J., Krellner, C., Geibel, C., Kerschl, P., Müller, K.-H., and Steglich, F. High-field phase diagram of the heavy-fermion metal $YbRh_2Si_2$. *New Journal of Physics 8*, 9 (2006), 171.

[64] Greenside, H. S., Blount, E. I., and Varma, C. M. Possible coexisting superconducting and magnetic states. *Phys. Rev. Lett. 46* (Jan 1981), 49–53.

[65] Gruenberg, L. W., and Gunther, L. Fulde-Ferrell Effect in Type-II Superconductors. *Phys. Rev. Lett. 16* (May 1966), 996–998.

[66] Hackl, A., and Vojta, M. Hackl and Vojta Reply:. *Phys. Rev. Lett. 111* (Sep 2013), 139702.

[67] Haigh, C. W. The theory of atomic spectroscopy: jj coupling, intermediate coupling, and configuration interaction. *Journal of Chemical Education 72* (1995), 206.

[68] Hardy, F., Huxley, A., Flouquet, J., Salce, B., Knebel, G., Braithwaite, D., Aoki, D., Uhlarz, M., and Pfleiderer, C. (P,T) phase diagram of the ferromagnetic superconductor URhGe. *Physica B: Condensed Matter 359-361*, 0 (2005), 1111 – 1113.

[69] Hardy, F., and Huxley, A. D. p-Wave Superconductivity in the Ferromagnetic Superconductor URhGe. *Phys. Rev. Lett. 94* (Jun 2005), 247006.

[70] Harris, R., and Grant, M. Thermal conductivity of a kinetic ising model. *Phys. Rev. B 38* (Nov 1988), 9323–9326.

[71] Hasselbach, K., Taillefer, L., and Flouquet, J. Critical point in the superconducting phase diagram of UPt_3. *Phys. Rev. Lett. 63* (Jul 1989), 93–96.

[72] Hassinger, E., Aoki, D., Knebel, G., and Flouquet, J. Pressure-phase diagram of UCoGe by ac-susceptibility and resistivity measurements. *Journal of Physics: Conference Series 200*, 1 (2010), 012055.

[73] Hattori, K., and Tsunetsugu, H. p-wave superconductivity near a transverse saturation field. *Phys. Rev. B 87* (Feb 2013), 064501.

[74] Hattori, T., Ihara, Y., Nakai, Y., Ishida, K., Tada, Y., Fujimoto, S., Kawakami, N., Osaki, E., Deguchi, K., Sato, N. K., and Satoh, I. Superconductivity Induced by Longitudinal Ferromagnetic Fluctuations in UCoGe. *Phys. Rev. Lett. 108* (Feb 2012), 066403.

[75] Hattori, T., Ishida, K., Nakai, Y., Ohta, T., Deguchi, K., Sato, N., and Satoh, I. Weakly first-order behavior in ferromagnetic transition of UCoGe revealed by ^{59}Co-NQR studies. *Physica C: Superconductivity 470, Supplement 1* (2010), S561 – S563.

[76] Hegger, H., Petrovic, C., Moshopoulou, E. G., Hundley, M. F., Sarrao, J. L., Fisk, Z., and Thompson, J. D. Pressure-Induced Superconductivity in Quasi-2D $CeRhIn_5$. *Phys. Rev. Lett. 84* (May 2000), 4986–4989.

[77] Herrmannsdörfer, T., Skrotzki, R., Wosnitza, J., Köhler, D., Boldt, R., and Ruck, M. Structure-induced coexistence of ferromagnetic and superconducting states of single-phase Bi_3Ni seen via magnetization and resistance measurements. *Phys. Rev. B 83* (Apr 2011), 140501.

[78] Hess, C., Baumann, C., Ammerahl, U., Büchner, B., Heidrich-Meisner, F., Brenig, W., and Revcolevschi, A. Magnon heat transport in $(Sr,Ca,La)_{14}Cu_{24}O_{41}$. *Phys. Rev. B 64* (Oct 2001), 184305.

[79] Hess, C., Ribeiro, P., Buchner, B., ElHaes, H., Roth, G., Ammerahl, U., and Revcolevschi, A. Magnon heat conductivity and mean free paths in two-leg spin ladders: A model-independent determination. *Phys. Rev. B 73* (Mar 2006), 104407.

[80] Hill, H. H. *Plutonium and Other Actinides*. No. ptie. 1 in Nuclear metallurgy. AIME, 1970.

[81] Hill, R. W., Proust, C., Taillefer, L., Fournier, P., and Greene, R. L. Breakdown of fermi-liquid theory in a copper-oxide superconductor. *Nature 414*, 6865 (Dec. 2001), 711–715.

[82] Horsley, J. A. Relationship between the area of L2,3 x-ray absorption edge resonances and the d orbital occupancy in compounds of platinum and iridium. *The Journal of Chemical Physics 76*, 3 (1982), 1451–1458.

[83] Huang, K., Hamlin, J. J., Baumbach, R. E., Janoschek, M., Kanchanavatee, N., Zocco, D. A., Ronning, F., and Maple, M. B. Ferromagnetic quantum critical point in $UCo_{1-x}Fe_xGe$. *Phys. Rev. B 87* (Feb 2013), 054513.

[84] Huxley, A., Sheikin, I., Ressouche, E., Kernavanois, N., Braithwaite, D., Calemczuk, R., and Flouquet, J. UGe_2: A ferromagnetic spin-triplet superconductor. *Phys. Rev. B 63* (Mar 2001), 144519.

[85] Huy, N., and de Visser, A. Ferromagnetic order in U(Rh,Co)Ge. *Solid State Communications 149* (2009), 703 – 706.

[86] Huy, N. T., de Nijs, D. E., Huang, Y. K., and de Visser, A. Unusual Upper Critical Field of the Ferromagnetic Superconductor UCoGe. *Phys. Rev. Lett. 100*, 7 (Feb 2008), 077002.

[87] Huy, N. T., Gasparini, A., de Nijs, D. E., Huang, Y., Klaasse, J. C. P., Gortenmulder, T., de Visser, A., Hamann, A., Goerlach, T., and von Loehneysen, H. Superconductivity on the border of weak itinerant ferromagnetism in UCoGe. *Phys. Rev. Lett. 99* (2007), 067006.

[88] Ihara, Y., Hattori, T., Ishida, K., Nakai, Y., Osaki, E., Deguchi, K., Sato, N. K., and Satoh, I. Anisotropic Magnetic Fluctuations in the Ferromagnetic Superconductor UCoGe Studied by Direction-Dependent ^{59}Co NMR Measurements. *Phys. Rev. Lett. 105* (Nov 2010), 206403.

[89] Ishida, K., MacLaughlin, D., Okamoto, K., Kawasaki, Y., Kitaoka, Y., Nieuwenhuys, G., Bernal, O., Koda, A., Higemoto, W., Kadono, R., Geibel, C., and Steglich, F. μSR and low-temperature antiferromagnetism in the ordered non-Fermi-liquid compound $YbRh_2Si_2$. *Physica B: Condensed Matter 329-333, Part 2* (2003), 589 – 590.

[90] Ishida, K., MacLaughlin, D. E., Young, B.-L., Okamoto, K., Kawasaki, Y., Kitaoka, Y., Nieuwenhuys, G. J., Heffner, R. H., Bernal, O. O., Higemoto, W., Koda, A., Kadono, R., Trovarelli, O., Geibel, C., and Steglich, F. Low-temperature magnetic order and spin dynamics in $YbRh_2Si_2$. *Phys. Rev. B 68* (Nov 2003), 184401.

[91] Ishida, K., Okamoto, K., Kawasaki, Y., Kitaoka, Y., Trovarelli, O., Geibel, C., and Steglich, F. $YbRh_2Si_2$: Spin Fluctuations in the Vicinity of a Quantum Critical Point at Low Magnetic Field. *Phys. Rev. Lett. 89* (Aug 2002), 107202.

[92] Ishikawa, M., and Fischer, . Destruction of superconductivity by magnetic ordering in $Ho_{1.2}Mo_6S_8$. *Solid State Communications 23* (1977), 37 – 39.

[93] Jaccarino, V., and Peter, M. Ultra-high-field superconductivity. *Phys. Rev. Lett. 9* (Oct 1962), 290–292.

[94] Jacobsson, P., and Sundqvist, B. Thermal conductivity and electrical resistivity of gadolinium as functions of pressure and temperature. *Phys. Rev. B 40* (Nov 1989), 9541–9551.

[95] Jaric, M. V., and Belić, M. Mean-field theory of ferromagnetic superconductors. *Phys. Rev. Lett. 42* (Apr 1979), 1015–1019.

[96] Jarlborg, T., Freeman, A. J., and Watson-Yang, T. J. Electronic Structure and Reentrant Magnetism in Superconducting $ErRh_4B_4$. *Phys. Rev. Lett. 39* (Oct 1977), 1032–1034.

[97] Jullien, R., and Coqblin, B. Temperature dependence of the thermal conductivity in nearly magnetic metals: Application to plutonium. *Journal of Low Temperature Physics 19*, 1-2 (1975), 59–74.

[98] Kaiser, A. B. Localized spin fluctuations in nearly-magnetic dilute alloys: Thermal resistivity and lorenz number. *Phys. Rev. B 3* (May 1971), 3040–3045.

[99] Kambe, S., Suderow, H., Fukuhara, T., Flouquet, J., and Takimoto, T. Spin-Fluctuation Mediated Thermal Conductivity Around the Magnetic Instability of $CeNi_2Ge_2$. *Journal of Low Temperature Physics 117* (1999), 101–112.

[100] Kartschagin, W., and Tschetwerikowa, E. Zur frage nach der magnetischen drehung der polarisationsebene primarer rontgenstrahlen. *Zeitschrift fur Physik 39*, 12 (1926), 886–900.

[101] Khodel, V., Yakovenko, V., and Zverev, M. Flattening of single-particle spectra in strongly correlated electron systems and the violation of the wiedemann-franz law. *JETP Letters 86*, 12 (2008), 772–778.

[102] Kim, K.-S., and Pépin, C. Violation of the wiedemann-franz law at the kondo breakdown quantum critical point. *Phys. Rev. Lett. 102* (Apr 2009), 156404.

[103] Kimura, N., Ito, K., Aoki, H., Uji, S., and Terashima, T. Extremely High Upper Critical Magnetic Field of the Noncentrosymmetric Heavy Fermion Superconductor $CeRhSi_3$. *Phys. Rev. Lett. 98* (May 2007), 197001.

[104] Klamut, P. W. Superconductivity and magnetism in the ruthenocuprates. *Superconductor Science and Technology 21*, 9 (2008), 093001.

[105] Klemm, R. A., Lorscher, C., Zhang, J., and Gu, Q. Upper critical field of p - wave ferromagnetic superconductors with orthorhombic symmetry. *Journal of Physics: Conference Series 400*, 2 (2012), 022055.

[106] Knafo, W., Matsuda, T. D., Aoki, D., Hardy, F., Scheerer, G. W., Ballon, G., Nardone, M., Zitouni, A., Meingast, C., and Flouquet, J. High-field moment polarization in the ferromagnetic superconductor UCoGe. *Phys. Rev. B 86* (Nov 2012), 184416.

[107] Knebel, G., Aoki, D., and Flouquet, J. Antiferromagnetism and superconductivity in cerium based heavy-fermion compounds. *Comptes Rendus Physique 12*, 5-6 (2011), 542 – 566.

[108] Knebel, G., Boursier, R., Hassinger, E., Lapertot, G., Niklowitz, P. G., Pourret, A., Salce, B., Sanchez, J. P., Sheikin, I., Bonville, P., Harima, H., and Flouquet, J. Localization of 4f state in $YbRh_2Si_2$ under magnetic field and high pressure: Comparison with $CeRh_2Si_2$. *J. Phys. Soc. Jpn. 75*, 11 (NOV 2006), 114709.

[109] Kobayashi, T. C., Hori, A., Fukushima, S., Hidaka, H., Kotegawa, H., Akazawa, T., Takeda, K., Ohishi, Y., and Yamamoto, E. Pressure–Temperature Phase Diagram and Superconductivity in UIr. *Journal of the Physical Society of Japan 76*, 5 (2007), 051007.

[110] Kolodziejczyk, A., Sarkissian, B. V. B., and Coles, B. R. Magnetism and superconductivity in a transition metal compound: Y_4Co_3. *Journal of Physics F: Metal Physics 10* (1980), L333.

[111] Kolodziejczyk, A., Wiendlocha, B., Zalecki, R., Tobola, J., and Kaprzyk, S. Superconductivity, weak itinerant ferromagnetism and electronic band structure of Y_9Co_7. *Acta Physica Polonica, A 111* (2007), 513–526.

[112] Kotegawa, H., Harada, A., Kawasaki, S., Kawasaki, Y., Kitaoka, Y., Haga, Y., Yamamoto, E., Ōnuki, Y., Itoh, K. M., Haller, E. E., and Harima, H. Evidence for Uniform Coexistence of Ferromagnetism and Unconventional Superconductivity in UGe_2: A ^{73}Ge-NQR Study under Pressure. *Journal of the Physical Society of Japan 74* (2005), 705–711.

[113] Kubert, C., and Hirschfeld, P. J. Quasiparticle transport properties of d-wave superconductors in the vortex state. *Phys. Rev. Lett. 80* (Jun 1998), 4963–4966.

[114] Kuper, C. G., Revzen, M., and Ron, A. Ferromagnetic superconductors: A vortex phase in ternary rare-earth compounds. *Phys. Rev. Lett. 44* (Jun 1980), 1545–1548.

[115] Larkin, A. I., and Ovchinnikov, I. U. N. Inhomogeneous state of superconductors. *Soviet Physics JETP 20* (1965), 762–769.

[116] Lausberg, S., Hannaske, A., Steppke, A., Steinke, L., Gruner, T., Pedrero, L., Krellner, C., Klingner, C., Brando, M., Geibel, C., and Steglich, F. Doped $YbRh_2Si_2$: Not Only Ferromagnetic Correlations but Ferromagnetic Order. *Phys. Rev. Lett. 110* (Jun 2013), 256402.

[117] Leggett, A. J. A theoretical description of the new phases of liquid ^{3}He. *Rev. Mod. Phys. 47* (Apr 1975), 331–414.

[118] Levy, F., Sheikin, I., Grenier, B., and Huxley, A. Magnetic field-induced superconductivity in the ferromagnet URhGe. *Science 309* (2005), 1343–1346.

[119] Li, S. Y., Taillefer, L., Wang, C. H., and Chen, X. H. Ballistic Magnon Transport and Phonon Scattering in the Antiferromagnet Nd_2CuO_4. *Phys. Rev. Lett. 95* (Oct 2005), 156603.

[120] Lowell, J., and Sousa, J. B. Mixed-state thermal conductivity of type II superconductors. *Journal of Low Temperature Physics 3* (1970), 65–87.

[121] Lussier, B., Ellman, B., and Taillefer, L. Anisotropy of Heat Conduction in the Heavy Fermion Superconductor UPt_3. *Phys. Rev. Lett. 73* (1994), 3294–3297.

[122] Machida, K., and Ohmi, T. Phenomenological Theory of Ferromagnetic Superconductivity. *Phys. Rev. Lett. 86* (Jan 2001), 850–853.

[123] Machida, Y., Itoh, A., So, Y., Izawa, K., Haga, Y., Yamamoto, E., Kimura, N., Onuki, Y., Tsutsumi, Y., and Machida, K. Twofold Spontaneous Symmetry Breaking in the Heavy-Fermion Superconductor UPt_3. *Phys. Rev. Lett. 108* (Apr 2012), 157002.

[124] Machida, Y., Tomokuni, K., Izawa, K., Lapertot, G., Knebel, G., Brison, J.-P., and Flouquet, J. Verification of the Wiedemann-Franz Law in $YbRh_2Si_2$ at a Quantum Critical Point. *Phys. Rev. Lett. 110* (Jun 2013), 236402.

[125] Machida, Y., Tomokuni, K., Ogura, C., Izawa, K., Kuga, K., Nakatsuji, S., Lapertot, G., Knebel, G., Brison, J.-P., and Flouquet, J. Thermoelectric Response Near a Quantum Critical Point of β-$YbAlB_4$ and $Yb_2Rh_2Si_2$: A Comparative Study. *Phys. Rev. Lett. 109* (Oct 2012), 156405.

[126] Maki, K., and Won, H. How to probe p-wave superconductivity? *Physica B: Condensed Matter 281-282* (2000), 975 – 976.

[127] Malone, L., Howald, L., Pourret, A., Aoki, D., Taufour, V., Knebel, G., and Flouquet, J. Thermoelectricity of the ferromagnetic superconductor UCoGe. *Phys. Rev. B 85* (Jan 2012), 024526.

[128] Martinez-Samper, P., Rodrigo, J., Rubio-Bollinger, G., Suderow, H., Vieira, S., Lee, S., and Tajima, S. Scanning tunneling spectroscopy in MgB_2. *Physica C: Superconductivity 385* (2003), 233 – 243.

[129] Mathur, N., Grosche, F., Julian, S., Walker, I., Freye, D., Haselwimmer, R., and Lonzarich, G. Magnetically mediated superconductivity in heavy fermion compounds. *Nature 394*, 6688 (JUL 2 1998), 39–43.

[130] Matsuda, Y., and Shimahara, H. Fulde–Ferrell–Larkin–Ovchinnikov State in Heavy Fermion Superconductors. *Journal of the Physical Society of Japan 76* (2007), 051005.

[131] Matthias, B. T., and Suhl, H. Possible explanation of the "coexistence" of ferromagnetism and superconductivity. *Phys. Rev. Lett. 4* (Jan 1960), 51–52.

[132] Matthias, B. T., Suhl, H., and Corenzwit, E. Ferromagnetic superconductors. *Phys. Rev. Lett. 1* (Dec 1958), 449–450.

[133] Matthias, B. T., Suhl, H., and Corenzwit, E. Spin exchange in superconductors. *Phys. Rev. Lett. 1* (Aug 1958), 92–94.

[134] Maxwell, E., and Strongin, M. Filamentary structure in superconductors. *Phys. Rev. Lett. 10* (Mar 1963), 212–215.

[135] McHale, P., and Monthoux, P. Sensitivity of the superconducting transition temperature to changes in the spin-fluctuation spectral weight. *Phys. Rev. B 67* (Jun 2003), 214512.

[136] Meul, H. W., Rossel, C., Decroux, M., Fischer, O., Remenyi, G., and Briggs, A. Observation of magnetic-field-induced superconductivity. *Phys. Rev. Lett. 53* (Jul 1984), 497–500.

[137] Mineev, V. P. Superconducting states in ferromagnetic metals. *Phys. Rev. B 66* (Oct 2002), 134504.

[138] Mineev, V. P. Magnetic field dependence of pairing interaction in ferromagnetic superconductors with triplet pairing. *Phys. Rev. B 83* (Feb 2011), 064515.

[139] Mineev, V. P. Phase diagram of UGe_2: Whether there are quantum phase transitions ? *Journal of Physics: Conference Series 400* (2012), 032053.

[140] Mineev, V. P., and Champel, T. Theory of superconductivity in ferromagnetic superconductors with triplet pairing. *Phys. Rev. B 69* (Apr 2004), 144521.

[141] Misiorek, H., Mucha, J., Jezowski, A., Paderno, Y., and Shitsevalova, N. Thermal conductivity of rare-earth element dodecaborides. *Journal of Physics: Condensed Matter 7*, 47 (1995), 8927.

[142] Miyake, A., Aoki, D., and Flouquet, J. Field Re-entrant Superconductivity Induced by the Enhancement of Effective Mass in URhGe. *Journal of the Physical Society of Japan 77* (2008), 094709.

[143] Monthoux, P., and Lonzarich, G. p-wave and d-wave superconductivity in quasi-two-dimensional metals. *Phys. Rev. B 59*, 22 (JUN 1 1999), 14598–14605.

[144] Monthoux, P., Pines, D., and Lonzarich, G. G. Superconductivity without phonons. *Nature 450* (2007), 1177–1183.

[145] Moriya, T., and Takimoto, T. Anomalous properties around magnetic instability in heavy electron systems. *Journal of the Physical Society of Japan 64*, 3 (1995), 960–969.

[146] Moriya, T., and Ueda, K. Antiferromagnetic spin fluctuation and superconductivity. *Reports on Progress in Physics 66*, 8 (2003), 1299.

[147] Nachtrab, T., Bernhard, C., Lin, C., Koelle, D., and Kleiner, R. The ruthenocuprates: natural superconductor-ferromagnet multilayers. *Comptes Rendus Physique 7*, 1 (2006), 68 – 85.

[148] Nagamatsu, J., Nakagawa, N., Muranaka, T., Zenitani, Y., and Akimitsu, J. Superconductivity at 39K in magnesium diboride. *Nature 410* (2001), 63–64.

[149] Neto, M. B. S., Neto, A. H. C., Kim, J. S., and Stewart, G. R. d-f hybridization and quantum criticality in weakly-itinerant ferromagnets. *Journal of Physics: Condensed Matter 25*, 2 (2013), 025601.

[150] Nowik, I., Felner, I., Ren, Z., Cao, G. H., and Xu, Z. A. Coexistence of ferromagnetism and superconductivity: magnetization and Mossbauer studies of $EuFe_2(As_{1-x}P_x)_2$. *Journal of Physics: Condensed Matter 23* (2011), 065701.

[151] Oeschler, N., Hartmann, S., Pikul, A., Krellner, C., Geibel, C., and Steglich, F. Low-temperature specific heat of $YbRh_2Si_2$. *Physica B: Condensed Matter 403* (2008), 1254 – 1256.

[152] Ohta, T., Hattori, T., Ishida, K., Nakai, Y., Osaki, E., Deguchi, K., Sato, N. K., and Satoh, I. Microscopic Coexistence of Ferromagnetism and Superconductivity in Single-Crystal UCoGe. *Journal of the Physical Society of Japan 79* (2010), 023707.

[153] Ohta, T., Nakai, Y., Ihara, Y., Ishida, K., Deguchi, K., Sato, N. K., and Satoh, I. Ferromagnetic Quantum Critical Fluctuations and Anomalous Coexistence of Ferromagnetism and Superconductivity in UCoGe Revealed by Co-NMR and NQR Studies. *Journal of the Physical Society of Japan 77* (2008), 023707.

[154] Onnes, H. Further experiments with liquid helium. c. on the change of electric resistance of pure metals at very low temperatures. *Comm. Phys. Lab. Univ. Leiden 119,120,122* (1911).

[155] Ortenburger, I., and Sparks, M. Spin-wave contribution to low-temperature specific heat of yttrium iron garnet in zero applied fields. *Phys. Rev. 133* (Feb 1964), A784–A786.

[156] Paglione, J., Tanatar, M. A., Hawthorn, D. G., Hill, R. W., Ronning, F., Sutherland, M., Taillefer, L., Petrovic, C., and Canfield, P. C. Heat Transport as a Probe of Electron Scattering by Spin Fluctuations: The Case of Antiferromagnetic $CeRhIn_5$. *Phys. Rev. Lett. 94* (Jun 2005), 216602.

[157] Pai, R. V., and Mishra, S. G. Disorder effects in transport properties of weak itinerant-electron ferromagnets. *Phys. Rev. B 48* (Oct 1993), 10292–10303.

[158] Pan, B. Y., Guan, T. Y., Hong, X. C., Zhou, S. Y., Qiu, X., Zhang, H., and Li, S. Y. Specific heat and thermal conductivity of ferromagnetic magnons in Yttrium Iron Garnet. *EPL 103* (2013), 37005.

[159] Park, T., Lee, H., Martin, I., Lu, X., Sidorov, V. A., Gofryk, K., Ronning, F., Bauer, E. D., and Thompson, J. D. Textured Superconducting Phase in the Heavy Fermion $CeRhIn_5$. *Phys. Rev. Lett. 108* (Feb 2012), 077003.

[160] Paschen, S., Luhmann, T., Wirth, S., Gegenwart, P., Trovarelli, O., Geibel, C., Steglich, F., Coleman, P., and Si, Q. Hall-effect evolution across a heavy-fermion quantum critical point. *Nature 432*, 7019 (Dec. 2004), 881–885.

[161] Paulsen, C., Hykel, D. J., Hasselbach, K., and Aoki, D. Observation of the Meissner-Ochsenfeld Effect and the Absence of the Meissner State in UCoGe. *Phys. Rev. Lett. 109* (Dec 2012), 237001.

[162] Petrovic, C., Pagliuso, P., Hundley, M., Movshovich, R., Sarrao, J., Thompson, J., Fisk, Z., and Monthoux, P. Heavy-fermion superconductivity in $CeCoIn_5$ at 2.3 K. *J. Phys.: Condens. Matter 13* (2001), L337–L342.

[163] Pfau, H., Daou, R., Lausberg, S., Naren, H. R., Brando, M., Friedemann, S., Wirth, S., Westerkamp, T., Stockert, U., Gegenwart, P., Krellner, C., Geibel, C., Zwicknagl, G., and Steglich, F. Interplay between Kondo Suppression and Lifshitz Transitions in $YbRh_2Si_2$ at High Magnetic Fields. *Phys. Rev. Lett. 110* (2013), 256403.

[164] Pfau, H., Hartmann, S., Stockert, U., Sun, P., Lausberg, S., Brando, M., Friedemann, S., Krellner, C., Geibel, C., Wirth, S., Kirchner, S., Abrahams, E., Si, Q., and Steglich, F. Thermal and electrical transport across a magnetic quantum critical point. *Nature 484* (2012), 493–497.

[165] Pfleiderer, C. Superconducting phases of f-electron compounds. *Rev. Mod. Phys. 81* (2009), 1551–1624.

[166] Pfleiderer, C., Uhlarz, M., Hayden, S. M., Vollmer, R., Lohneysen, H. v., Bernhoeft, N. R., and Lonzarich, G. G. Coexistence of superconductivity and ferromagnetism in the d-band metal $ZrZn_2$. *Nature 412* (2001), 58–61.

[167] Phillips, N. E., and Matthias, B. T. Heat capacity of ferromagnetic superconductors. *Phys. Rev. 121* (Jan 1961), 105–107.

[168] Pospisil, J., Prokes, K., Reehuis, M., Tovar, M., Vejpravova, J. P., Prokleska, J., and Sechovsky, V. Influence of Sample Preparation Technology and Treatment on Magnetism and Superconductivity of UCoGe. *Journal of the Physical Society of Japan 80* (2011), 084709.

[169] Pourret, A., Knebel, G., Matsuda, T. D., Lapertot, G., and Flouquet, J. Magnetic Polarization and Fermi Surface Instability: Case of $YbRh_2Si_2$. *Journal of the Physical Society of Japan 82* (2013), 053704.

[170] Prokes, K., de Visser, A., Huang, Y. K., Fok, B., and Ressouche, E. Anomalous spin distribution in the superconducting ferromagnet UCoGe studied by polarized neutron diffraction. *Phys. Rev. B 81* (May 2010), 180407.

[171] Proust, C., Behnia, K., Bel, R., Maude, D., and Vedeneev, S. I. Heat transport in $Bi_{2+x}Sr_{2-x}CuO_{6+\delta}$: Departure from the Wiedemann-Franz law in the vicinity of the metal-insulator transition. *Phys. Rev. B 72* (2005), 214511.

[172] Raymond, S., and Huxley, A. Spin dynamics of the ferromagnetic superconductor UGe_2. *Physica B: Condensed Matter 350* (2004), 33 – 35.

[173] Reid, J.-P., Tanatar, M. A., Daou, R., Hu, R., Petrovic, C., and L., T. Wiedemann-Franz law and non-vanishing temperature scale across the field-tuned quantum critical point of $YbRh_2Si_2$. *ArXiv e-prints: 1309.6315* (2013).

[174] Ren, Z., Tao, Q., Jiang, S., Feng, C., Wang, C., Dai, J., Cao, G., and Xu, Z. Superconductivity Induced by Phosphorus Doping and Its Coexistence with Ferromagnetism in $EuFe_2(As_{0.7}P_{0.3})_2$. *Phys. Rev. Lett. 102* (Apr 2009), 137002.

[175] Ronning, F., Capan, C., Bauer, E., Thompson, J., Sarrao, J., and Movshovich, R. Pressure study of quantum criticality in $CeCoIn_5$. *Phys. Rev. B 73* (2006), 064519.

[176] Roth, s. Coexistence of superconductivity and magnetic order. *Applied physics 15*, 1 (1978), 1–11.

[177] Roth, S., Ibel, K., and Just, W. Neutron scattering experiment on the coexistence of superconductivity and ferromagnetism. *Journal of Physics C: Solid State Physics 6*, 23 (1973), 3465.

[178] Roussev, R., and Millis, A. J. Quantum critical effects on transition temperature of magnetically mediated p-wave superconductivity. *Phys. Rev. B 63* (Mar 2001), 140504.

[179] Sakarya, S., van Dijk, N. H., and Brück, E. Determination of the magnetic domain size in the ferromagnetic superconductor UGe_2 by three-dimensional neutron depolarization. *Phys. Rev. B 71* (May 2005), 174417.

[180] Samsel-Czekala, M., Elgazzar, S., Oppeneer, P., Talik, E., Walerczyk, W., and Troć, R. The electronic structure of UCoGe by ab initio calculations and XPS experiment. *Journal of Physics: Condensed Matter 22* (2010), 015503.

[181] Sarrao, J. L., Morales, L. A., Thompson, J. D., Scott, B. L., Stewart, G. R., Wastin, F., Rebizant, J., Boulet, P., Colineau, E., and Lander, G. H. Plutonium-based superconductivity with a transition temperature above 18K. *Nature 420*, 6913 (Nov. 2002), 297–299.

[182] Saxena, S., Agarwal, P., Ahilan, K., Grosche, F., Haselwimmer, R., Steiner, M., Pugh, E., Walker, I., Julian, S., Monthoux, P., Lonzarich, G., Huxley, A., Sheikin, I., Braithwaite, D., and Flouquet, J. Superconductivity on the border of itinerant-electron ferromagnetism in UGe_2. *Nature 406* (2000), 587–592.

[183] Saxena, S. S., and Littlewood, P. B. Superconductivity: Iron cast in exotic role. *Nature 412*, 6844 (July 2001), 290–291.

[184] Scharnberg, K., and Klemm, R. A. Upper critical field in p-wave superconductors with broken symmetry. *Phys. Rev. Lett. 54* (Jun 1985), 2445–2448.

[185] Schuberth, E., Tippmann, M., Kath, M., Krellner, C., Geibel, C., Westerkamp, T., Klingner, C., and Steglich, F. Magnetization measurements on $YbRh_2Si_2$ at very low temperatures. *Journal of Physics: Conference Series 150* (2009), 042178.

[186] Schuberth, E., Tippmann, M., Krellner, C., and Steglich, F. New magnetically ordered phases in $YbRh_2Si_2$. *Physica Status Solidi (B) 250* (2013), 482–484.

[187] Schütz, G., Wagner, W., Wilhelm, W., Kienle, P., Zeller, R., Frahm, R., and Materlik, G. Absorption of circularly polarized x rays in iron. *Phys. Rev. Lett. 58* (Feb 1987), 737–740.

[188] Seyfarth, G., Brison, J. P., Méasson, M.-A., Flouquet, J., Izawa, K., Matsuda, Y., Sugawara, H., and Sato, H. Multiband Superconductivity in the Heavy Fermion Compound $PrOs_4Sb_{12}$. *Phys. Rev. Lett. 95* (2005), 107004.

[189] Shakeripour, H., Petrovic, C., and Taillefer, L. Heat transport as a probe of superconducting gap structure. *New Journal of Physics 11*, 5 (2009), 055065.

[190] Sheikin, I., Huxley, A., Braithwaite, D., Brison, J. P., Watanabe, S., Miyake, K., and Flouquet, J. Anisotropy and pressure dependence of the upper critical field of the ferromagnetic superconductor UGe_2. *Phys. Rev. B 64* (Nov 2001), 220503.

[191] Shimahara, H. Structure of the Fulde-Ferrell-Larkin-Ovchinnikov State in Two-Dimensional Superconductors. *Journal of the Physical Society of Japan 67* (1998), 736–739.

[192] Shimizu, K., Kimura, T., Furomoto, S., Takeda, K., Kontani, K., Onuki, Y., and Amaya, K. Superconductivity in the non-magnetic state of iron under pressure. *Nature 412*, 6844 (July 2001), 316–318.

[193] Slooten, E., Naka, T., Gasparini, A., Huang, Y. K., and de Visser, A. Enhancement of Superconductivity near the Ferromagnetic Quantum Critical Point in UCoGe. *Phys. Rev. Lett. 103* (Aug 2009), 097003.

[194] Smith, R. P., Sutherland, M., Lonzarich, G. G., Saxena, S. S., Kimura, N., Takashima, S., Nohara, M., and Takagi, H. Marginal breakdown of the fermi-liquid state on the border of metallic ferromagnetism. *Nature 455*, 7217 (Oct. 2008), 1220–1223.

[195] Sologubenko, A. V., Felder, E., Gianno, K., Ott, H. R., Vietkine, A., and Revcolevschi, A. Thermal conductivity and specific heat of the linear chain cuprate Sr_2CuO_3: Evidence for thermal transport via spinons. *Phys. Rev. B 62* (Sep 2000), R6108–R6111.

[196] Sologubenko, A. V., Jun, J., Kazakov, S. M., Karpinski, J., and Ott, H. R. Thermal conductivity of single-crystalline MgB_2. *Phys. Rev. B 66*, 1 (Jun 2002), 014504.

[197] Sologubenko, A. V., Zhigadlo, N. D., Karpinski, J., and Ott, H. R. Thermal conductivity of Al-doped MgB_2: Impurity scattering and the validity of the Wiedemann-Franz law. *Phys. Rev. B 74* (2006), 184523.

[198] Sonin, E. B., and Felner, I. Spontaneous vortex phase in a superconducting weak ferromagnet. *Phys. Rev. B 57* (Jun 1998), R14000–R14003.

[199] Starace, A. F. Potential-Barrier Effects in Photoabsorption. I. General Theory. *Phys. Rev. B 5* (Mar 1972), 1773–1784.

[200] Steglich, F., Aarts, J., Bredl, C. D., Lieke, W., Meschede, D., Franz, W., and Schäfer, H. Superconductivity in the Presence of Strong Pauli Paramagnetism: $CeCu_2Si_2$. *Phys. Rev. Lett. 43* (Dec 1979), 1892–1896.

[201] Steglich, F., Gegenwart, P., Geibel, C., Hinze, P., Lang, M., Langhammer, C., Sparn, G., and Trovarelli, O. Non-fermi-liquid effects in stoichiometric 4f-electron metals at ambient pressure. *Physica B: Condensed Matter 280* (2000), 349 – 353.

[202] Steven, E., Kiswandhi, A., Krstovska, D., Brooks, J. S., Almeida, M., Goncalves, A. P., Henriques, M. S., Luke, G. M., and Williams, T. J. Robust properties of the superconducting ferromagnet UCoGe. *Applied Physics Letters 98* (2011), 132507.

[203] Stöhr, J. Exploring the microscopic origin of magnetic anisotropies with X-ray magnetic circular dichroism (XMCD) spectroscopy. *Journal of Magnetism and Magnetic Materials 200* (1999), 470 – 497.

[204] Stock, C., Broholm, C., Demmel, F., Van Duijn, J., Taylor, J. W., Kang, H. J., Hu, R., and Petrovic, C. From Incommensurate Correlations to Mesoscopic Spin Resonance in $YbRh_2Si_2$. *Phys. Rev. Lett. 109* (Sep 2012), 127201.

[205] Stock, C., Sokolov, D. A., Bourges, P., Tobash, P. H., Gofryk, K., Ronning, F., Bauer, E. D., Rule, K. C., and Huxley, A. D. Anisotropic Critical Magnetic Fluctuations in the Ferromagnetic Superconductor UCoGe. *Phys. Rev. Lett. 107* (Oct 2011), 187202.

[206] Suhl, H. Simultaneous onset of ferromagnetism and superconductivity. *Phys. Rev. Lett. 87* (Sep 2001), 167007.

[207] Suhl, H., Matthias, B. T., and Walker, L. R. Bardeen-Cooper-Schrieffer Theory of Superconductivity in the Case of Overlapping Bands. *Phys. Rev. Lett. 3* (1959), 552–554.

[208] Sumiyama, A., Oda, Y., Nagano, H., Ōnuki, Y., Shibutani, K., and Komatsubara, T. Coherent Kondo State in a Dense Kondo Substance: $Ce_xLa_{1-x}Cu_6$. *Journal of the Physical Society of Japan 55* (1986), 1294–1304.

[209] Tachiki, M., Matsumoto, H., Koyama, T., and Umezawa, H. Self-induced vortices in magnetic superconductors. *Solid State Communications 34*, 1 (1980), 19 – 23.

[210] Tada, Y., Fujimoto, S., Kawakami, N., Hattori, T., Ihara, Y., Ishida, K., Deguchi, K., Sato, N. K., and Satoh, I. Spin-Triplet Superconductivity Induced by Longitudinal Ferromagnetic Fluctuations in UCoGe: Theoretical Aspect. *Journal of Physics: Conference Series 449*, 1 (2013), 012029.

[211] Takada, S. Superconductivity in a Molecular Field. II: Stability of Fulde-Ferrel Phase. *Progress of Theoretical Physics 43*, 1 (1970), 27–38.

[212] Takahashi, Y. First-order magnetic phase transitions in anisotropic itinerant electron ferromagnets. *Journal of the Physical Society of Japan 79*, 8 (2010), 083707.

[213] Takeda, Y., Saitoh, Y., Okane, T., Yamagami, H., Matsuda, T. D., Yamamoto, E., Haga, Y., Ōnuki, Y., and Fisk, Z. Separation of magnetic properties at uranium and cobalt sites in UCoAl using soft x-ray magnetic circular dichroism. *Phys. Rev. B 88* (Aug 2013), 075108.

[214] Tanatar, M. A., Paglione, J., Nakatsuji, S., Hawthorn, D. G., Boaknin, E., Hill, R. W., Ronning, F., Sutherland, M., Taillefer, L., Petrovic, C., Canfield, P. C., and Fisk, Z. Unpaired Electrons in the Heavy-Fermion Superconductor $CeCoIn_5$. *Phys. Rev. Lett. 95* (Aug 2005), 067002.

[215] Tanatar, M. A., Paglione, J., Petrovic, C., and Taillefer, L. Anisotropic violation of the Wiedemann-Franz law at a quantum critical point. *Science 316* (2007), 1320–1322.

[216] Tateiwa, N., Kobayashi, T. C., Hanazono, K., Amaya, K., Haga, Y., Settai, R., and Onuki, Y. Pressure-induced superconductivity in a ferromagnet UGe_2. *Journal of Physics: Condensed Matter 13*, 1 (2001), L17.

[217] Thole, B. T., Carra, P., Sette, F., and van der Laan, G. X-ray circular dichroism as a probe of orbital magnetization. *Phys. Rev. Lett. 68* (Mar 1992), 1943–1946.

[218] Tokiwa, Y., Gegenwart, P., Weickert, F., Küchler, R., Custers, J., Ferstl, J., Geibel, C., and Steglich, F. Suppression of the Kondo state in $YbRh_2Si_2$ by large magnetic fields. *Journal of Magnetism and Magnetic Materials 272-276, Supplement* (2004), E87 – E88.

[219] Tritt, T. *Thermal Conductivity: Theory, Properties, and Applications*. Physics of Solids and Liquids. Springer, 2004.

[220] Troc, R., and Tran, V. Magnetic properties of UT(Si, Ge) series. *Journal of Magnetism and Magnetic Materials 73*, 3 (1988), 389 – 397.

[221] Troc, R., Wawryk, R., Miiller, W., Misiorek, H., and Samsel-Czekala, M. Bulk properties of the UCoGe Kondo-like system. *Philosophical Magazine 90*, 16 (2010), 2249–2271.

[222] Trovarelli, O., Geibel, C., Langhammer, C., Mederle, S., Gegenwart, P., Grosche, F., Lang, M., Sparn, G., and Steglich, F. Non-Fermi-liquid effects at ambient pressure in the stoichiometric heavy-fermion compound $YbRh_2Si_2$. *Physica B: Condensed Matter 281-282* (2000), 372 – 373.

[223] Trovarelli, O., Geibel, C., Mederle, S., Langhammer, C., Grosche, F. M., Gegenwart, P., Lang, M., Sparn, G., and Steglich, F. $YbRh_2Si_2$: Pronounced Non-Fermi-Liquid Effects above a Low-Lying Magnetic Phase Transition. *Phys. Rev. Lett. 85* (2000), 626–629.

[224] Ueda, K., and Moriya, T. Contribution of spin fluctuations to the electrical and thermal resistivities of weakly and nearly ferromagnetic metals. *Journal of the Physical Society of Japan 39*, 3 (1975), 605–615.

[225] van der Laan, G., Moore, K. T., Tobin, J. G., Chung, B. W., Wall, M. A., and Schwartz, A. J. Applicability of the spin-orbit sum rule for the actinide $5f$ states. *Phys. Rev. Lett. 93* (Aug 2004), 097401.

[226] van der Laan, G., and Thole, B. T. X-ray-absorption sum rules in jj-coupled operators and ground-state moments of actinide ions. *Phys. Rev. B 53* (Jun 1996), 14458–14469.

[227] Vejpravova-Poltierova, J., Pospisil, J., Prokleska, J., Prokes, K., Stunault, A., and Sechovsky, V. Low magnetic field phase diagram of UCoGe. *Phys. Rev. B 82* (Nov 2010), 180517.

[228] Vekhter, I., and Houghton, A. Quasiparticle thermal conductivity in the vortex state of high- T_c cuprates. *Phys. Rev. Lett. 83* (Nov 1999), 4626–4629.

[229] Volovik, G. Superconductivity with lines of gap nodes - density of nodes in the vortex. *JETP LETTERS 58* (1993), 469–473.

[230] Vorontsov, A. B., and Vekhter, I. Unconventional superconductors under a rotating magnetic field. I. Density of states and specific heat. *Phys. Rev. B 75*, 22 (Jun 2007), 224501.

[231] Wagner, D. K., Garland, J. C., and Bowers, R. Low-temperature electrical and thermal resistivities of tungsten. *Phys. Rev. B 3* (May 1971), 3141–3149.

[232] Wakeham, N., Bangura, A. F., Xu, X., Mercure, J.-F., Greenblatt, M., and Hussey, N. E. Gross violation of the Wiedemann-Franz law in a quasi-one-dimensional conductor. *Nat. Commun. 2* (2011), 396–.

[233] Wang, Z., Mao, W., and Bedell, K. Superconductivity near itinerant ferromagnetic quantum criticality. *Phys. Rev. Lett. 87* (Nov 2001), 257001.

[234] Watanabe, H., and Ogata, M. Fermi-surface reconstruction without breakdown of kondo screening at the quantum critical point. *Phys. Rev. Lett. 99* (Sep 2007), 136401.

[235] White, G. K. Thermal conductivity of silver at low temperatures. *Proceedings of the Physical Society. Section A 66*, 9 (1953), 844.

[236] Wiendlocha, B., Tobola, J., Kaprzyk, S., and Kolodziejczyk, A. Electronic structure, magnetism, and spin fluctuations in the superconducting weak ferromagnet Y_4Co_3. *Phys. Rev. B 83* (Mar 2011), 094408.

[237] Wilhelm, F., Jaouen, N., Rogalev, A., Stirling, W. G., Springell, R., Zochowski, S. W., Beesley, A. M., Brown, S. D., Thomas, M. F., Lander, G. H., Langridge, S., Ward, R. C. C., and Wells, M. R. X-ray magnetic circular dichroism study of uranium/iron multilayers. *Phys. Rev. B 76* (Jul 2007), 024425.

[238] Wirth, S., Ernst, S., Cardoso-Gil, R., Borrmann, H., Seiro, S., Krellner, C., Geibel, C., Kirchner, S., Burkhardt, U., Grin, Y., and Steglich, F. Structural investigations on $YbRh_2Si_2$: from the atomic to the macroscopic length scale. *Journal of Physics: Condensed Matter 24* (2012), 294203.

[239] Yelland, E. A., Barraclough, J. M., Wang, W., Kamenev, K. V., and Huxley, A. D. High-field superconductivity at an electronic topological transition in URhGe. *Nat. Phys. 7* (2011), 890–894.

[240] Yelland, E. A., Hayden, S. M., Yates, S. J. C., Pfleiderer, C., Uhlarz, M., Vollmer, R., Lohneysen, H. v., Bernhoeft, N. R., Smith, R. P., Saxena, S. S., and Kimura, N. Superconductivity induced by spark erosion in $ZrZn_2$. *Phys. Rev. B 72* (Dec 2005), 214523.

[241] Yelon, W. B., and Berger, L. Magnon Heat Conduction and Magnon-Electron Scattering in Fe-Ni. *Phys. Rev. Lett. 25* (Oct 1970), 1207–1210.

[242] Yin, Y., Liu, H., Xie, L., Su, T., Teng, M., and Li, X. Coexistence of Superconductivity and Ferromagnetism in $La_{2-x}Sr_xCuO_4$ Nanoparticles. *The Journal of Physical Chemistry C 117* (2013), 3028–3035.

[243] Yuan, H. Q., Singleton, J., Balakirev, F. F., Baily, S. A., Chen, G. F., Luo, J. L., and Wang, N. L. Nearly isotropic superconductivity in (Ba,K)Fe_2As_2. *Nature 457* (2009), 565–568.

Résumé des Chapitres en Français

Chapitre 1: Contexte Scientifique

Ce chapitre explique pourquoi les composés dits à fermions lourds sont très étudiés à basses températures, car ils présentent des propriétés très intéressantes et très diverses d'un composé à l'autre. Une explication rapide des notions de point critique quantique et de supraconductivité non conventionnelle est également donnée. La fin du chapitre donne le contexte scientifique sur la coexistence de la supraconductivité et du ferromagnétisme, avec la présentation des trois composés fermions lourds supraconducteurs ferromagnétiques existants: UGe_2, URhGe et UCoGe. Ce dernier est le composé étudié dans cette thèse. Le second composé étudié, $YbRh_2Si_2$, sera décrit lors du dernier chapitre. Le plan de la thèse est donné à la fin de cette partie.

Chapitre 2: Techniques Expérimentales

Les deux cryostats à dilution utilisés sont décrits dans ce chapitre. Le premier était en état de marche lors de mon arrivée, mais le second fut complètement remis en état. J'explique les travaux que j'ai effectués dessus avant de pouvoir l'utiliser. Je décrits ensuite les mesures de transport utilisées: la résistivité électrique et la conduction thermique. Cette deuxième méthode est expliquée plus en détail, car elle est délicate à mettre en œuvre. Ce chapitre se termine sur la description de la ligne ID12 à l'ESRF à Grenoble pour les mesures de XMCD.

Chapitre 3: Premiers Résultats sur UCoGe

Ce chapitre montre les résultats obtenus sur les mesures du champ critique de UCoGe et par XMCD. Les champs critiques, mesurés avec le champ magnétique selon les axes **b** et **c** par conduction thermique, ont certaines caractéristiques similaires aux champs critiques mesurés par résistivité: la courbure positive ($\mathbf{H}//\mathbf{c}$) et le début du renforcement de la température critique à fort champ ($\mathbf{H}//\mathbf{b}$), même si les mesures n'ont été faites que jusqu'à 8.5T. Ces résultats, obtenus sur deux échantillons de qualités très différentes, prouvent leurs caractères intrinsèques. La pente du champ critique presque verticale proche de la température supraconductrice ($\mathbf{H}//\mathbf{b}$), mesurée par conduction thermique, rend nécessaire le fait de finir de mesurer le champ critique à fort champ et selon l'axe **a**.

Les mesures de XMCD, faites à 3K jusqu'à 17T, ont été faites avec le champ selon l'axe **c** et **b**. Le possible ferrimagnétisme observée à fort champ n'est pas validé, les mesures montrant que le moment porté par le cobalt est parallèle au champ, et donc à l'aimantation totale. Les mesures $\mathbf{H}//\mathbf{b}$, elles aussi en accord avec les mesures macroscopiques d'aimantation, n'ont

pas montré de comportements particuliers, et l'absence d'anomalies vers 10T (maximum du renforcement de la température supraconductrice) n'est pas visible, sans doute à cause de la haute température de mesure ou d'un désalignement de l'axe **b** par rapport à la direction du champ.

Chapitre 4: Mesures de Conduction Thermique sur UCoGe

Ce chapitre montre le principal travail que j'ai fourni durant cette thèse: les mesures de conduction thermique dans UCoGe. Etant donné que les propriétés observées dépendent de la qualité de l'échantillon, plusieurs ont été mesurés dans les mêmes conditions pour séparer les effets extrinsèques des effets intrinsèques. L'étude de la phase normale a montré qu'il existe des canaux supplémentaires de chaleur supplémentaires à ceux causés par les électrons et les phonons à basse température. Dans la phase paramagnétique, ils présentent une sensibilité au champ similaire aux fluctuations magnétiques détectées par RMN. Ces fluctuations sont donc suspectées d'être responsables de cette contribution supplémentaire. Dans la phase ferromagnétique, selon la direction du courant de chaleur, une grande anisotropie de cette contribution supplémentaire est visible, avec une surprenante augmentation de son intensité à basse température. Les études dans la phase supraconductrice ont montré que UCoGe est un supraconducteur avec plusieurs gaps supraconducteurs.

Chapitre 5: $YbRh_2Si_2$

Ce dernier chapitre fait tout d'abord l'état de l'art de ce composÃl' relativement bien étudié. Les mesures de conduction thermique, déjà faites dans différents groupes, veulent clarifier la situation sur la possible violation de la loi de Wiedemann-Franz proche du point critique quantique à très basse température. Pour cela, des mesures à très basses températures ont été effectuées sous champ, jusqu'à 4T. Il a été mis en évidence l'impossibilité de pouvoir conclure de manière définitive sur la validité ou la violation de la loi, mais aucun comportement particulier n'a été observé proche du point critique quantique et l'intégralité de nos résultats peut être interprétée supposant sa validité. Un nouveau régime semble apparaître à partir de 0.5T, et demande à être étudié plus en détail avec de nouvelles mesures.

Annexes

En annexes sont donnés différents modèles pour reproduire les contributions supplémantaires. Ces modèles souffrent cependant d'un manque de bases théoriques.

Abstract

Thermal conductivity measurements have been performed at low temperatures and under field in the superconducting ferromagnet UCoGe and in the weak antiferromagnet $YbRh_2Si_2$. In both systems, the magnetic fluctuations have an important role in their properties, and it appeared that they contribute as a heat channel, seen by thermal conductivity at low temperatures. In UCoGe, the extra contribution due to the magnetic fluctuations have the same field dependence as the one measured by NMR, and, unexpectedly, a new heat channel appears at very low temperatures. Furthermore, thermal conductivity measurements in the superconducting state have confirmed the multigap superconductivity of UCoGe. XMCD measurements have also been performed in UCoGe. In $YbRh_2Si_2$, the very low temperature thermal conductivity measurements have shown that an extra contribution appears at very low temperature, which avoids to conclude definitively about the violation or the validation of the Wiedemann-Franz law at the quantum critical point, even if the results can be interpreted supposing its validation.

Keywords: Unconventionnal Superconductivity, Magnetism, Thermal Conductivity, Very Low Temperatures, UCoGe, $YbRh_2Si_2$

Résumé

Les mesures de conduction thermique ont été effectuées à basses températures dans le supraconducteur ferromagnétique UCoGe et dans le composé faiblement antiferromagnétique $YbRh_2Si_2$. Les fluctuations magnétiques sont un élément important dans les propriétés de ces deux composés, et sont responsables d'un canal de chaleur à basses températures. Dans UCoGe, la contribution supplémentaire causée par les fluctuations magnétiques ont la même dépendance en champ magnétique que celles vues par RMN. Etonnamment, un nouveau canal de chaleur apparaît à très basses températures. Les mesures dans l'état supraconducteur ont confirmé la caractère multigap de UCoGe. Des mesures de XMCD ont également faites dans UCoGe. Dans $YbRh_2Si_2$, les fluctuations magnétiques sont suspectées d'être responsables d'un canal de chaleur visible à très basses températures, empêchant de pouvoir conclure sur la violation ou la validité de la loi de Wiedemann-Franz au niveau du point critique quantique. Cependant, les résultats peuvent être interprétés sans avoir recours à sa violation.

Mots-clès: Supraconductivité Non Conventionnelle, Magnétisme, Conduction Thermique, Très Basses Températures, UCoGe, $YbRh_2Si_2$